Universite Pierre et Marie Curie

Ecole doctorale 127: Astronomie et Astrophysique de Paris

Institut d'Astrophysique de Paris

Ph.D Thesis

candidate : **Charlotte Welker**

defended on : **September,17th 2015**

to obtain the degree of : **Ph.D in Astrophysics**

Field/subfield : **Astrophysics/galaxy formation and evolution**

Flipping Pancakes:

How gas inflows and mergers shape galaxies in their cosmic environment.

Ph.D advisors

M. Pichon Christophe	*Pr., IAP*
M. Devriendt Julien	*Dr., Oxford University*
M. Dubois Yohan	*Dr., IAP*

Referees

Ms. Sijacki Debora	*Dr, University of Cambridge*
M. Naab Thorsten	*Dr, Max Planck Institute for Astrophysics*

Examiner

M. Semelin Benoit	*Dr., Observatoire de Paris LERMA*

Invited members

M. Aussel Hervé	*Dr., AIM*
M. Ilbert Olivier	*Dr., LAM*

To my parents, my brothers, my wife Amandine and to all my dearest friends teaching physics in high-school who ever questioned the purpose of their endeavor.

Acknowledgements

First and foremost, I would like to thank sincerely Christophe Pichon and Julien Devriendt for their sustained interest in my work and their careful supervising in every aspect of my Ph.D all along those three years. More specifically, I would like to thank Christophe Pichon for his unfailing eagerness to design new projects that would help the development of my skills, his high and constantly renewed expectations, and for the stimulating discussions we had that greatly helped me relate my work to the most theoretical aspects of galactic dynamics. I am also deeply indebted to Julien Devriendt who always provided me with the insightful complementary opinions and scrupulous revisions that ultimately proved necessary to the development and achievement of my projects to their full potential.

Eventually, I would like to express my gratitude to both of them not only for their most acute scientific advising and technical help in the design and achievement of specific projects but also for their great commitment in helping the overall construction of my professional career, in all its academic requirements and networking aspects.

I would also like to address a special thank to Yohan Dubois for his constant availability and his eagerness to share his expertise on baryonic physics, not to mention help me solve most of the technical difficulties I encountered in the course of my Ph.D. I greatly benefited from his enthusiastic contribution to my supervision, especially in the development of my numerical skills.

A special thank to Sandrine Decara-Codis who shared my room and not only contributed to its calm and friendly atmosphere, but also gave me powerful scientific insights through informal conversations with this great skill of hers to make even the most elaborated theory look trivial. As a young female member of a field still vastly dominated by men, I greatly appreciated the inspiring presence of a self-confident and successful female scientist by my side.

I must express my gratitude to my colleagues and co-authors Sebastien Peirani, Sugata Kaviraj, Elisa Chisari and Thierry Sousbie who constantly paid attention to my work and to the progress of my Ph.D, contributing to it with enthusiasm whenever they could. Special thanks also to Stephane Arnouts and Valerie de Lapparent for the interest in my results they expressed in many occasions and for their strong support and fruitful comments, which greatly renewed my own interest in observational Astrophysics.

Last but not least, I would like to thank my family and friends for their unstinting support, and especially my beloved wife Amandine Ravel d'Estienne who stood by my side everyday, comforted me when I had doubts and took care of me so that I could get time to focus on my Ph.D. She shared even my worst moments while I owe her the best and gave me confidence all along the way.

Declaration

I declare that this thesis is the outcome of my own work, except where explicitly referring to the work of others. No part of it has ever been or is currently being submitted for the validation on any other degree, qualification or diploma than the one explicitly mentioned in first page.

All this research was carried out in collaboration with my supervisors Christophe Pichon, Julien Devriendt and Yohan Dubois.

Chapter 2, sections 2 to 4, has already been published in the form of two related papers: "Dancing in the dark: galactic properties trace spin swings along the cosmic web.", Dubois Y., Pichon. C., Welker, C. et al., in The Monthly Notices of the Royal Astronomical Society, 444, 1453-1468, and " Mergers drive spin swings along the cosmic web", Welker, C., Devriendt, J., Dubois, Y., Pichon, C., Peirani, S, in The Monthly Notices of the Royal Astronomical Society: Letters, 445, L46-L50.

Chapter 3, sections 2 to 6, is to be submitted to The Monthly Notices of the Royal Astronomical Society under the title: "Caught in the rhythm: how satellites settle into a plane around their central galaxy.", Welker, C., Dubois, Y., Pichon, C., Devriendt, J., Chisari, E., to be submitted to MNRAS, 2015.

Chapter 4, sections 2 to 5, has been submitted in March, 2015 to The Monthly Notices of the Royal Astronomical Society: "The rise and fall of stellar discs across the peak of cosmic star formation history: mergers versus smooth accretion.", Welker,C., Dubois,Y., Devriendt, J., Pichon, C., Kaviraj, S., Peirani, S.

Resumé

L'importance des interactions entre les galaxies et leur environnement à plus grande échelle pour comprendre leur évolution constitue une pierre angulaire de la théorie actuelle de formation des structures. Cependant, derrière cette idée très générale se cache en réalité une longue liste de processus physiques. En effet, les galaxies grandissent au sein d'intenses courants de gaz à haut redhsift et acquièrent du moment angulaire grâce aux couples de marée exercés par les grandes échelles, tout en fusionnant avec d'autres galaxies. Aucun de ces mécanismes ne peut être appréhendé indépendamment de la distribution de matière à grande échelle, fortement anisotrope, constituée d'un réseau étendu de vides délimités par des murs, eux-mêmes segmentés par des filaments de haute densité dans lesquels la matière s'écoule en direction des noeuds compacts où ils se croisent. La géométrie et la dynamique d'une telle structure influent fortement sur les écoulements cosmiques, notamment les flux de gaz et de galaxies en migration vers les noeuds de la "toile cosmique" ainsi définie. Cela modifie en conséquence la distribution des galaxies et de leurs propriétés, observées à différents redshifts. Cette thèse explore certaines de ces corrélations entre les échelles galactiques et extra-galactiques dans la simulation cosmologique hydrodynamique Horizon-AGN, afin d'éclairer nos connaissances sur les origines des propriétés observées des galaxies, à l'aide d'un échantillon statistiquement représentatif. Dans une première partie, j'analyse l'orientation du moment angulaire des galaxies et retrouve une tendance déjà mesurée sur les halos de matière noire qui les abritent: les galaxies jeunes et peu massives ont un moment angulaire préférentiellement aligné avec la direction de leur filament le plus proche tandis que les galaxies plus vieilles et plus massives présentent un moment angulaire d'avantage perpendiculaire à cette même direction. Cette dichotomie est reliée aux mécanismes par lesquels les galaxies accroissent leur masse, tout d'abord par accrétion diffuse de gaz, dans des régions à forte vorticité présentes au coeur des filaments, puis lors de fusions avec d'autres galaxies au cours de leur dérive le long de ces mêmes filaments, ce qui entraine une conversion substantielle de moment orbital en moment angulaire intrinsèque. Je quantifie ces effets dans Horizon-AGN, et montre que les fusions majeures comme mineures peuvent provoquer d'importantes bascules du moment angulaire galactique sur

des échelles de temps de l'ordre de quelques centaines de millions d'années. J'étudie par la suite la distribution des galaxies satellites autour de leur hôte plus massive et mets de nouveau à jour des corrélations non négligeables avec la direction du filament voisin. Toutefois, cette tendance est en compétition avec une autre selon laquelle les satellites finissent par aligner leur orbites avec le plan de leur galaxie centrale, entrant alors en co-rotation, une tendance qui se révèle particulièrement importante dans les parties les plus internes du halo ($r < r_{\rm vir}$), même lorsque le plan galactique est très mal aligné avec la direction du plus proche filament. En dernier lieu, J'étudie plus précisément l'impact des fusions galactiques caractérisées par différents rapports de masses ainsi que de l'accrétion diffuse sur la taille et sur la forme des galaxies lors du pic de formation stellaire a l'échelle cosmique. Mes principaux résultats apportent une confirmation statistique au scénario invoquant des fusions mineures à faible composante gazeuse pour interpréter la perte de compacité des sphéroïdes entre $z \sim 2 - -3$ et $z \sim 1$. Ils apportent également des preuves substantielles de la tendance de l'accrétion diffuse de gaz à $z > 1$ à reformer des disques pourvu que ceux-ci restent confinés dans la région riche en vorticité qui les contenait initialement.

Mots clé : astrophysique numérique, simulation, formation des galaxies, évolution galactique, structures a grande échelle, fusions, accrétion.

Abstract

The importance of interactions with the larger scale environment in driving their evolution is a central tenet of structure formation theory. However, this general idea actually encompasses a long list of physical processes. Indeed, galaxies grow from intense gas inflows at high-redshift and acquire spin through tidal torques on larger scales while merging with one another at the same time. None of this processes can be considered independently from the large scale distribution of matter, which is strikingly anisotropic, consisting of an extended network of voids delimited by sheets, themselves segmented by high-density filaments within which matter flows towards compact nodes where they intersect. Such a structure imprints its geometry and dynamics on cosmic flows, especially gas inflows and migrating galaxies - which drift along this so-called "cosmic web" - ultimately shapes the distribution of galaxies and galactic properties observed at all redshifts. This work investigates some of these correlations between galactic and extra-galactic scales in the hydrodynamical cosmological simulation Horizon-AGN to shed light on the origins of galactic properties through a statistically representative analysis. In a first part of this thesis I analyze the spin orientations of galaxies and recover a trend already documented for dark halo hosts: young small galaxies have a spin preferentially aligned to the direction of their closest filament while older more massive counterparts more likely display a perpendicular orientation. This dichotomy can be related to the way galaxies acquire mass, first from diffuse gas accretion in vorticity rich regions in the vicinity of filaments, then through mergers along filaments, which leads to a substantial conversion of orbital momentum into intrinsic angular momentum. I quantify these affects in Horizon-AGN , showing that both minor and major mergers can drive important spin swings on timescales of the order of a few hundred million years. I further investigate the distribution of satellite galaxies around a more massive central host and find it to be also fairly correlated to the direction of the surrounding filament. However, this trend is in competition with a tendency for satellites to eventually align their orbits in the central galactic plane and start co-rotating, a trend that proves significant in the inner parts of the halo ($r < 0.5\, r_{\rm vir}$) even when such a galactic plane is strongly misaligned with the direction of its closest filament. Finally, I study with greater

precision the impact of mergers of various mass ratios and of diffuse accretion processes on the size and morphology of galaxies at the peak of cosmic star formation history. The main results of this study include a statistical validation of the gas-poor minor merger scenario to interpret the loss of compacity of spheroids between $z \sim 2-3$ and $z \sim 1$ and substantial evidence that diffuse gas accretion at $z > 1$ tend to (re)-form disks, up to the point where the galaxy grows out of the coherent vorticity region it is embedded in.

Keywords: computational astrophysics, galaxy formation, galaxy evolution, large-scale structure, mergers, accretion

Contents

Introduction **17**

0.1 Structure formation in the early universe: linear perturbation theory 18

0.2 Spherical collapse and Press-Schechter theory 20

0.3 The cosmic web 22

0.4 Galactic morphologies 24

0.5 Structure of this Thesis 26

1 Numerical Methods **27**

1.1 Simulating the universe on cosmological scales 28

1.1.1 RAMSES: basic features 28

1.1.2 Small-scale physical recipes for realistic galactic dynamics. 32

1.2 Structure detection and identification in Horizon-AGN 35

1.2.1 Haloes and galaxies: Structure identification and merging 35

1.2.2 Synthetic galaxies in Horizon-AGN 37

1.2.3 The numerical cosmic web 40

2 Galactic spin alignments induced by the cosmic web **45**

2.1 Orientation of dark haloes in the cosmic web 46

2.1.1 The spin of dark haloes: a mass segregated distribution 46

2.1.2 Tidal Torque Theory 47

2.1.3 A dynamical scenario 49

2.1.4 Mergers versus smooth accretion 50

2.1.5 From haloes to galaxies . . . 51
2.2 Tracing galactic spin swings in the cosmic web . . . 53
2.2.1 Numerical Methods . . . 53
2.2.2 Evolution tracers . . . 57
2.2.3 Alignments in Horizon-AGN . . . 60
2.2.4 Comparison to observations . . . 64
2.3 How mergers drive spin swings in the cosmic web . . . 64
2.3.1 Tracking mergers in Horizon-AGN . . . 64
2.3.2 Mergers, stellar mass and spin in Horizon-AGN: close-up case studies . . . 66
2.3.3 Mergers and smooth accretion on spin orientation . . . 69
2.3.4 Mergers and smooth accretion on acquisition of spin. . . . 72
2.4 Conclusion . . . 76

3 Orientation of satellites galaxies: massive hosts versus the cosmic web 79

3.1 An overview of satellite galaxies . . . 80
3.1.1 The formation of satellite galaxies in CDM cosmology . . . 80
3.1.2 The distribution of satellite galaxies . . . 86
3.2 Satellites in Horizon-AGN . . . 90
3.2.1 Identifying central galaxies and satellites . . . 90
3.2.2 Tracing the evolution of satellites in the halo: synthetic colors. . . . 92
3.3 Statistical properties of the orientation of satellites . . . 94
3.3.1 Methods and variables . . . 94
3.3.2 Results . . . 99
3.4 A dynamical scenario : satellites migrating into the halo. . . . 108
3.4.1 Scenario . . . 108
3.4.2 Corotation of satellites . . . 108
3.4.3 Evolution of satellites within the halo . . . 110
3.5 Implications for observations. . . . 115
3.5.1 Color selection . . . 116

3.5.2 Signal on smaller scales . . . 120
3.5.3 Effects of the shape of the central host and high-z alignments. . . . 121
3.6 Conclusion. . . . 125

4 The rise and fall of stellar disks at $z > 1$ 129

4.1 Inflows and galaxy encounters: an overview . . . 130
4.1.1 Disc galaxies: evolution of the Hubble sequence with redshift . . . 131
4.1.2 Violent Disc Instability: the path to compact spheroids . . . 132
4.1.3 Mergers . . . 133
4.1.4 Dry or wet mergers? Extended spheroids and massive disks. . . . 135
4.2 Characterizing different types of mergers in Horizon-AGN . . . 138
4.2.1 Characterizing the morphology of galaxies . . . 141
4.2.2 Gas content of high-z galaxies . . . 142
4.2.3 Merger rates: from observations to simulation . . . 145
4.3 Size growth of galaxies . . . 147
4.3.1 Galactic stellar density . . . 147
4.3.2 Galactic half-mass radius . . . 150
4.3.3 Impact of initial gas fraction and morphology . . . 152
4.4 Impact on morphologies . . . 154
4.4.1 Smooth accretion . . . 154
4.4.2 Mergers . . . 157
4.5 Conclusion . . . 160

Conclusion 163

4.6 Main results . . . 163
4.7 Prospects . . . 165
4.7.1 Sorting out the merger zoo . . . 165
4.7.2 Gas inflows: feeding galaxies into diverse morphologies ? . . . 166
4.7.3 Distribution of satellites . . . 167

Bibliography **171**

Introduction

Understanding the mechanisms that drive the formation and evolution of galaxies and lead to their observed diversity is a long-standing issue. Over the past decades major improvements in observational and computational astrophysics have led to substantial changes from the simple initial picture of galaxies as isolated islands arising from the collapse of smooth spherical self-gravitating clouds of particles. The formation scenarios have grown in complexity, progressively leading to the now standard evolutionary track in which small haloes of dark matter form first and hierarchically merge into more massive structures at later times (Press & Schechter, 1974). Galaxies then form as gas collapses into the center of such haloes, radiatively cools and starts forming stars (White & Rees, 1978). First scenarios suggested the formation of a hot corona of gas around galaxies in formation —as a result of the virial shock undergone by the collapsing gas— that would subsequently cool radiatively and rain isotropically over the galaxy. It has since been realized that dense enough gas would never shock-heat to temperatures where Bremsstrahlung dominates cooling but rather cool first by atomic transitions, leading to a scenario where forming galaxies are actually being fed by cooling gas streams (Binney, 1977; Dekel & Birnboim, 2006) .The later evolution of these galaxies has been progressively completed with internal mechanisms such as supernova outbursts (Dekel & Silk, 1986; Kauffmann *et al.* , 1999; Benson *et al.* , 2003) and central black holes activity (Binney & Tabor, 1995; Ciotti & Ostriker, 1997; Silk & Rees, 1998; King, 2003) able to channel out matter and energy so as to prevent overcooling trends measured in simulations (Cole, 1991; White & Frenk, 1991) and heat the gas so as to reconcile the observed low star formation rates of most massive galaxies with the hierarchical model which claims they form last (Bower *et al.* , 2006; Croton *et al.* , 2006; Cattaneo *et al.* , 2006; Sijacki *et al.* , 2007).

Although these so-called *feedback* processes are intrinsic and prove crucial to explain the observed properties of galaxies in the Local universe, perhaps the most striking aspect in this change of paradigm remains the complete and definite rule-out of the "isolated islands" picture. Both the hierarchical model and the origin of the galactic stellar component from cooling gas streams imply that galaxies mostly form and evolve from interactions between other collapsed objects and gas

inflows shaped by the underlying dark matter distribution on larger-scales. This naturally ties up the fate of galaxies to the geometry of the matter distribution on larger scales.

Interestingly, both theory and observations altogether found it to be strikingly anisotropic even on scales > 1 Mpc, drawing a large-scale "cosmic web" made of clustered halos, filaments, sheets and voids. Zel'dovich (1970); Shandarin & Zeldovich (1989); Bond *et al.* (1996) predicted the planar collapse of matter into walls, then into filaments, themselves draining matter into intersection nodes as a direct consequence of the inherent structure of the initial gaussian density field, and Bond *et al.* (1996) completed this picture explaining how galaxies and dark haloes are woven in such filaments. The extension of the Center for Astrophysics redshift survey (Huchra *et al.* , 1983) then provided spectacular observational evidence (de Lapparent *et al.* , 1986; Geller & Huchra, 1989) for this picture - further confirmed in the Sloan Digital Sky Survey (SDSS) [1] (Doroshkevich *et al.* , 2004) - and triggered a renewed interest for such large-scale galaxy surveys (Colless *et al.* , 2001).

This underlying anisotropy imprints the geometry of matter flows (gas and satellites) and therefore has major consequences on the outcome of gas accretion onto galaxies and of galaxy mergers. Moreover, Tidal Torque Theory (Peebles, 1969; White, 1984; Porciani *et al.* , 2002b) also predicts a strong tidal influence of extragalactic scales on haloes and galaxies, accounting for most of their orbital momentum at high-redshift. As a result there exists a tight connection between the geometry and dynamics of the cosmic web on the one hand, and the properties of galaxies on the other hand, which simulations on cosmological scales are especially well-suited to analyze.

In this thesis, we use the cosmological hydrodynamical simulation Horizon-AGN (Dubois *et al.* , 2014) to further investigate this connection. More specifically, we analyze the orientation of the intrinsic angular momentum of large sample of galaxies in a wide range of redshifts, how it arises from mergers and gas inflows, and how these mechanisms relate it to the underlying filamentary structure. In a similar fashion, we analyze the distribution of satellite galaxies around their central host, and eventually we characterize in detail the impact of mergers and diffuse accretion on the sizes and morphology go galaxies.

0.1 Structure formation in the early universe: linear perturbation theory

According to the standard hot Big Bang model, the universe emerged from an inflationary phase (epoch of accelerated expansion) the last stage of which lasted for less than 10^{-32} s and resulted in a

[1] http://www.sdss.org/science

flat and nearly homogeneous universe with the exception of small density perturbations of quantum origin. After this phase, the (less accelerated) expansion went on, causing the temperature to drop progressively and resulting in the successive formation of protons and neutrons, then light elements within less than 20 minutes. Past this epoch, the universe expanded adiabatically for about 380 000 years before the temperature dropping under $\sim 3000\,\mathrm{K}$ caused radiation (photons) and matter (hydrogen) to decouple, hence insuring the free streaming of the photons and the subsequent transparency of the universe.

The dynamics of this universe is well described in general relativity and in the Friedmann-Lemaitre-Robertson-Walker metric by the Friedmann equation:

$$H^2(t) = \left(\frac{\dot{a}}{a}\right)^2 = \frac{8\pi G\rho}{3} - \frac{k}{a^2} + \frac{\Lambda}{3}\,, \tag{1}$$

with $H(t)$ the Hubble parameter, $a(t)$ the scale factor, G the gravitational constant, Λ the dark energy related cosmological constant and k the curvature ($k = 0$ for a flat universe). The first term encompasses the contribution from both matter density ρ_m and radiation density ρ_r. This latter can be conveniently re-written as:

$$H^2(t) = \left(\frac{\dot{a}}{a}\right)^2 = H_0^2\left[\frac{\Omega_{m,0}}{a^3(t)} + \frac{\Omega_{r,0}}{a^4(t)} - \frac{\Omega_k}{a^2(t)} + \Omega_\Lambda\right]\,, \tag{2}$$

with the cosmological parameters: $\Omega_{m,0} = \rho_{m,0}/\rho_{c,0}$, $\Omega_{r,0} = \rho_{r,0}/\rho_{c,0}$, $\Omega_k = H_0^2/k$ and Ω_Λ that characterize the contribution from matter density ρ_m, radiation density ρ_r, curvature k and dark energy respectively. The subscript 0 indicates that quantities are taken at present time and $\rho_c = 3H^2(t)/(8\pi G)$ is the critical density. Such a set of parameters therefore defines the cosmology of the universe and needs to be fitted from observations and used as an input in simulations.

Comparing how each component in the equation scales with $a(t)$, one can distinguish three successive eras: the early universe where radiation is the most important form of energy, then a later phase that is matter-dominated, eventually leading to the contemporary universe where dark energy takes over. As the previously mentioned density perturbations start to grow after the matter-radiation equality, their subsequent evolution under gravity in an expanding universe is well described in the linear regime with the linearised Euler equations and the Poisson equation. Defining the density contrast $\delta(\mathbf{x}, t)$:

$$\rho(\mathbf{x}, t) = \rho_m(t)[1 + \delta(\mathbf{x}, t)]\,, \tag{3}$$

One gets

$$\frac{\partial \delta}{\partial t} + \frac{1}{a}\nabla.\mathbf{v} = 0\,, \tag{4}$$

$$\frac{\partial \mathbf{v}}{\partial t} + \frac{\dot{a}}{a}\mathbf{v} = -\frac{1}{a}\nabla\phi\,, \tag{5}$$

$$\nabla^2\phi = 4\pi G\bar{\rho}a^2\delta\,, \tag{6}$$

which leads to the perturbation equation:

$$\frac{\partial^2\delta}{\partial t^2} + 2\frac{\dot{a}}{a}\frac{\partial\delta}{\partial t} = \frac{3}{2}\Omega_{m,0}H_0^2\frac{\delta}{a^3}\,, \tag{7}$$

which admits the following general solution in an Einstein-de Sitter Universe with ($k = 0, \Lambda = 0, \Omega_m = 1$):

$$\delta = A(\mathbf{x})D_+(t) + B(\mathbf{x})D_-(t) \simeq A(\mathbf{x})D_+(t)\,, \tag{8}$$

as the decaying mode becomes rapidly negligible, with the growth factor $D_+ \propto a$ in a matter dominated universe.

The growth of these density perturbations is thought to give rise to all the structures observed in the current universe from the cosmic web to virialised haloes and galaxies. Initially, in their early post-inflation form, they are to a large extent gaussian distributed, hence fully characterized by their initial power spectrum (in Fourier modes k):

$$P_i(k) = Ck^{n_s}\,, \tag{9}$$

with $n_s = 0.96 \simeq 1$. This yields to the important conclusion that corresponding fluctuations for the gravitational potential are scale invariant in good approximation, hence distribute equally on all spatial scales. The subsequent evolution of this power spectrum is encapsulated in the transfer function $T(k)$ such that:

$$P(k) = P_i(k)T^2(k). \tag{10}$$

0.2 Spherical collapse and Press-Schechter theory

The evolution of these perturbations is however not fully described in the linear regime, as perturbations later enter a non-linear regime when particle orbits start to cross and invalidate the one-flow approximation. In particular, density peaks later collapse into virialised haloes and galaxies. This collapse is well described by the spherical collapse model which consists in solving the Friedmann equation for an over dense sphere of radius r in a flat universe. This successfully describes the competition between the global expansion of the universe that tends to spread particles apart, and the gravitational potential that tend to collapse them into one point.

This allows to calculate the turnover radius $r_{\rm max} = 6r_i/10\delta_i$, which is the maximum radius the sphere reaches before it begins to shrink as gravity takes over and the density contrast above which a sphere will collapse to a point $\delta_{\rm col} = 1.686$ (for $\Lambda = 0$. $\Omega_\Lambda = 0.7$ leads to $\delta_{\rm col} = 1.676$). In reality, the over density is not smooth but rather composed of particles which do not accumulate in one point but shell-cross and reach virial equilibrium. In this case, the same model predicts that the ratio between the density inside the sphere at virial equilibrium and the average background density at time of collapse will be:

$$\frac{\rho(t_{\rm virial})}{\bar{\rho}(t_{\rm collapse})} = 18\pi^2 \simeq 178\,, \tag{11}$$

assuming that $\Lambda = 0$. Interestingly, this provides a well justified criterium to discriminate collapsed structures in simulations. Fully developed galaxies will later form at the center of virialised dark haloes from the accumulation of cold dense gas streaming to the core of the haloes and forming stars. Note that a non-zero cosmological constant, this ratio is actually redshift dependent (Bryan & Norman, 1998).

Another neglected aspect of the collapse stems from the non-sphericity of density peaks and will be developed in Chapter 1. Noticeably haloes and pro to-galaxies acquire angular momentum through misalignments between their tensor of inertia (ellipticity) and the eigenvectors of the tidal tensor that describes gravitational tidal interactions on large scales. This ability of galaxies to acquire rotation can have a major impact on their subsequent morphology.

Following on this analysis, it is therefore of interest to derive the statistics of collapsed structures, especially the fraction of haloes of a given mass M at a given time. In order to understand when and with which rate over-dense clouds smoothed on a typical scale R (hence enclosing a typical mass $M \sim 4\pi R^3/3$) will collapse, Press & Schechter (1974) investigated the evolution of such smoothed gaussian random fields describing the smoothed density contrast δ.

The mass of such a cloud smoothed on scale R is :

$$M(\mathbf{r}) = \int \rho(\mathbf{x}) W(\mathbf{x}+\mathbf{r}, R) d^3\mathbf{x}\,, \tag{12}$$

with $W(\mathbf{r}, R)$ a window function sharply decreasing for $r > R$.

This smoothing washes away fluctuations on scales smaller than R. The corresponding smoothed gaussian random field takes the form:

$$p(\delta)d\delta = \frac{1}{\sqrt{2\pi}\sigma_M} \exp\left[-\frac{\delta^2}{2\sigma_M^2}\right] d\delta\,, \tag{13}$$

with $\sigma_{\rm M}$ the variance in mass fully determined by the power spectrum $P(k)$ and the smoothing function W. This quantity decreases with M in a ΛCDM universe.

Therefore remarking that fluctuations above the threshold $\delta_{\rm col}(t)$ correspond to virialized structures and that $\delta_{\rm col}(t) = \delta_{\rm col}/D_+(t)$ increases with time t, Press & Schechter (1974) derived the differential number density of haloes (modulo a factor of 2 to account for the fact that voids can be gravitationally bound to over-densities hence collapse simultaneously):

$$\frac{dn}{d\ln M} = \sqrt{\frac{2}{\pi}}\frac{\bar{\rho}_m}{M}\frac{d\ln\sigma_M^{-1}}{d\ln M}\nu\exp\left(-\frac{\nu^2}{2}\right), \tag{14}$$

with $\nu = \delta_{col}(t)/\sigma_M$.

In the ΛCDM paradigm, this therefore implies that more massive haloes - that correspond to more extended lagrangian patches of matter - collapse later in time. This prediction is the backbone of the *hierarchical formation model* according to which small-mass structures form first from fluctuations on smaller scales, then further coalesce into more massive structures. Massive haloes then most likely correspond to mergers of smaller - previously collapsed - haloes, and later merge themselves into even bigger clusters.

0.3 The cosmic web

For nearly two decades, this result appeared to be in stark contrast with the *pancake model* proposed by Zel'dovich (1970) and Shandarin & Zeldovich (1989) to describe the outcome of a non-spherical collapse and predicting the "cosmic web" agencing of matter on largest scales in a ΛCDM universe. In both observations (de Lapparent *et al.* , 1986; Doroshkevich *et al.* , 2004) and N-body simulations (Efstathiou *et al.* , 1985; Springel *et al.* , 2006), matter on largest scales appears to be distributed in compact nodes connecting high density filaments, themselves segmenting lower density sheets which enclose under-dense voids.

Assuming the validity of the now famous Zeldovich approximation (Zel'dovich, 1970; Hidding *et al.* , 2014) for the displacement field ψ - that maps eulerian coordinates to lagrangian ones in the linear regime -, these authors established that such structures correspond to the ongoing compression of matter along each eigenvector of the deformation tensor

$$D_{ij} = -\frac{\partial\psi_i}{\partial q_j}, \tag{15}$$

the fast (since not slowed down by gravity) expansion of voids confining matter into sheets, that then feed matter into filaments, themselves draining matter into nodes. As the Zeldovich approximation reduces the displacement field ψ to a potential vector field, the scalar potential of which is simply proportional to the underlying gravitational potential, a major result of this theory is that the Universe large-scale structure is framed by the planar local collapse of over densities. However, In such a theory, smallest structures arise from the fragmentation of bigger ones, hence form last.

These approaches were reconciled by Bond *et al.* (1996) remarking that these theories are valid on different scales and in different regimes: smoothing out the initial density contrast to recover only somewhat "long wave-length" fluctuations that have not yet entered the non-linear regime, The Zeldovich pancaking successfully explain the anisotropy in the distribution of matter on largest scales. However, it is not an accurate description of the non-linear regime of structure formations once individual orbits have shell-crossed and ruled out the hypothesis that allows to describe δ as a single-flow fluid.

The non-linear regime is then better described by the Press-Schechter formalism. However, one should notice that the non-linear collapse regime is first entered where the overdensity is initially the highest, hence at narrow peaks of the unsmoothed density field. On these short wave-length scales, we therefore recover the hierarchical picture in which smaller structures form first then merge into bigger ones.

The apparent discrepancy between these two approaches hence disappears when high order statistics of the initial random field are analyzed in details, more specifically in the vicinity of "rare" peaks. This reveals that 1) the long wavelength fluctuations act as a background that constrains the distribution of shorter wavelength peaks, which tend to be enhanced by the background leading to collapsed structures that lie near the crests of the long waves 2) rare peaks on a given scale tend to enhance the density contrast in between them, therefore constraining the position of a proto-filament (Bond *et al.* , 1996).

More generally, the main point raised by Bond *et al.* (1996) is that the field of initial perturbations already has a geometrical structure and a globally interconnected organization, an aspect largely overseen in the Zel'dovich approach. Hence, the universe large-scale structure is actually framed by the *interplay* between the planar collapse and the inherent structure of the gaussian initial density and velocity shear fields.

This leads to the following picture at time t: the perturbations of the initial density field in a given wavelength range - that has not yet reached the critical density of non-linear collapse - is subject to quasi-linear pancaking whose geometry is imprinted in the inherent structure of the gaussian density field on these scales, especially the position of the rare peaks. This generates a cosmic web made of overdense collapsing peaks and fast expanding voids where matter is being drained into denser and denser regions at their intersection. This background anisotropy constrain the distribution of density peaks of smaller wavelength (Kaiser, 1984) simultaneously entering the non-linear clustering regime, which drives a "bottom-up" clustering on these smaller scales. The distribution that emerges from this process is that of a filamentary network made of hierarchically clustered haloes and galaxies woven in the linear cosmic web, more and more massive collapsed

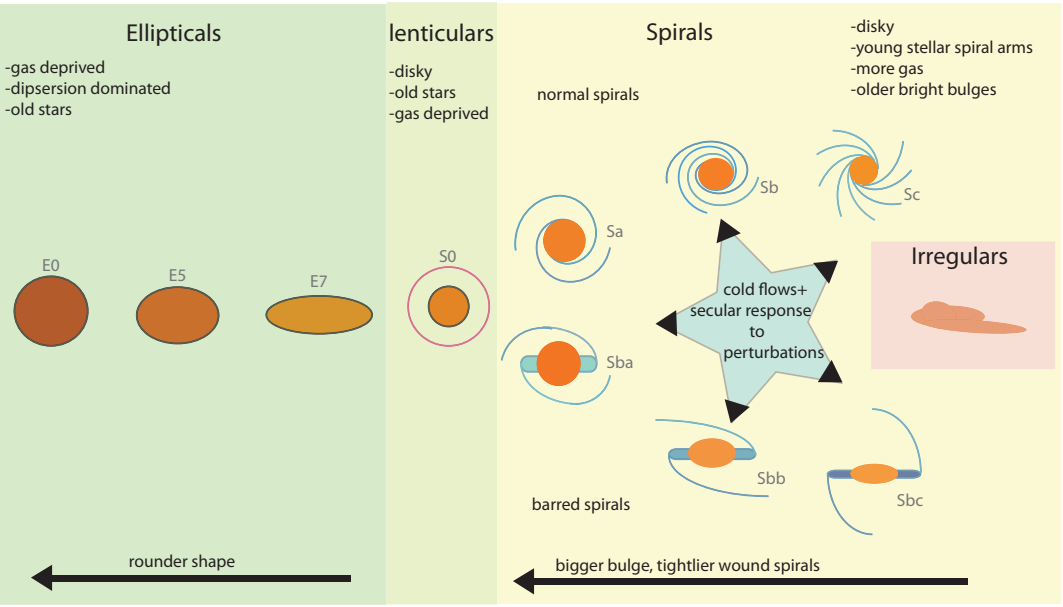

Figure 1: Illustration of the Hubble sequence with main features for the three distinct branches: elliptical, normal spirals and barred spirals.

objects appearing, as larger and larger wavelengths progressively enter the non-linear collapse regime, hence as haloes and galaxies along the filaments migrate towards nodes and merge.

This naturally raises the question of the influence of such an anisotropic environment on the formation and evolution of galaxies, more specifically on their observed properties such as their mass, size and morphology.

0.4 Galactic morphologies

The morphological diversity of galaxies in the Local Universe is remarkable. They come in a variety of sizes and shapes and can have as few as 10 million stars or as many as 10 trillion (the Milky Way has about 200 billion stars). In 1926, Edwin Hubble classified them in the now famous "Hubble Sequence" fork diagram (Hubble, 1936) depending on their overall shape (ellipsoid, spheroid or disk), the presence or not of a central bar, inner structure patterns (tightly wound spirals, double spirals) and importance of the bulge (bulge dominated, disk dominated). This fork diagram is presented in Fig .1 and distinguishes three branches:

Ellipticals: Elliptical galaxies show very little substructure and display roughly ellipsoidal shapes, sorted out in the Hubble tuning fork diagram from the quasi-spheroidal ones (E0) on the left to the most flattened ones on the right (E7). It should be noted however that elliptical galax-

ies from E4 to E7 do show a faint bulge/disc dichotomy. They tend to contain very little gas and dust and host old (red) stars. They are believed to form either from the relaxation of unstable disks (Elmegreen *et al.* , 2008; Dekel *et al.* , 2009; Ceverino *et al.* , 2012) at high redshift, or later through mergers of either disk progenitors (Toomre & Toomre, 1972; Schweizer, 1982; Cretton *et al.* , 2001; Naab & Burkert, 2003; Naab *et al.* , 2006b; Qu *et al.* , 2011). Their masses are extremely diverse, ranging from the smallest to the largest of all observed galaxies ($10^6 M_\odot$ to $10^{13} M_\odot$).

Normal spirals: Spirals are galaxies characterized by a disk shape, which comprises a bulge of somewhat old stars and a thin outskirt of younger stars. They display spiral patterns, the winding strength of which can be more or less pronounced, from floculent (Sc) to grand-design (Sa). They are classified (from left to right) in the Hubble diagram from the most tightly wound with largest bulge to the loosest arms with smallest bulge. In the local Universe, they occupy a narrow intermediate galactic mass range ($10^9 M_\odot$ to $10^{11} M_\odot$).

Barred spirals: Barred spirals (Sb) display spiral arms that originate from a central bar rather than directly from the center of mass of the galaxy. They are otherwise very similar to normal spirals in the Hubble diagram.

Irregular galaxies with less distinctive features and corresponding to disturbed systems eventually add up to the picture, as well as lenticulars which are disk structures with no distinctive spiral pattern.

Although from the very publication of this diagram Hubble insisted that it should be considered a static classification, favoring no temporal evolution, the continuous transformation from the left to the right of the sequence led astrophysicists to question the origin of this diversity and to suspect transformations from one type to the other. Over the last decades, many new mechanisms have piled up to the list of possible transformation channels from spirals to lenticulars, lenticulars to ellipticals, or spirals to ellipticals.

An aspect of this work, developed in Chapter 3 is to investigate some of the most promising of these accretion mechanisms to explain the build-up of disks and ellipticals at high redshift (and their subsequent loss of compacity).

0.5 Structure of this Thesis

This thesis investigates the interplay between galaxies and their anisotropic environment, more specifically through a close analysis of the contrasting impacts of diffuse accretion processes and mergers on the mass, spin, shape and size of galaxies and on the spatial distribution of their satellites. This analysis was performed in the state-of-the-art cosmological hydrodynamical simulation Horizon-AGN
(Dubois *et al.* , 2014) run with the eulerian code RAMSES (Teyssier, 2002). Chapter 1 briefly describes the main features of the code and the Horizon-AGN simulation, and gives further details on the numerical methods used to identify haloes, galaxies, and large-scale cosmic web features such as filaments. Chapter 2 presents results I have obtained relative to the spin orientation of galaxies in the cosmic web. In particular, it identifies specific galactic properties as tracers of spin alignment trends. It further analyzes the ability of galaxy mergers to trigger galactic spin swings and of smooth accretion to build-up the galactic spin parallel to its closest filament. While this study is performed at $z > 1$, Chapter 3 focuses on the distribution of satellites around their central galaxy at redshift $0.3 < z < 0.8$. More specifically, it investigates the tendency of satellites to align within the filament in which their central host is embeddded and analyses their related tendency to align in the galactic plane of their host. In this chapter we also discuss important consequences of such alignment trends for prospective observations. Chapter 4 presents results I have obtained concerning the impact of mergers of various mass ratios and diffuse accretion processes on the morphology and size of galaxies at the peak of cosmic star formations history. In particular, I discuss the statistical efficiency of gas-poor mergers in driving the loss of compacity expected for spheroidal galaxies between $z \sim 2 - 3$ and $z = 1$. I correlate these results with previous findings on the impact of the filamentary structure on the statistics of mergers and diffuse accretion.

Chapter 5 Concludes and discusses prospects.

Chapter 1

Numerical Methods

Throughout the last decades, numerical simulations have progressively acquired a leading role in the study of galactic formation and evolution. Ever since pure dark matter N-body cosmological simulations imposed themselves as the main theoretical driving force to establish the ΛCDM paradigm (by allowing to perform theoretical measurements of the 2 point correlation function which can be compared quantitatively with that measured in galaxy surveys), important efforts have been made to implement new physics in computational astrophysics. At the heart of this rapid development lies the fact that, while the dark matter dynamics drives the formation of the cosmic web, a full understanding of the formation of galaxies in such a structure requires to successfully integrate additional baryonic processes to the description.

Indeed, since galaxies grow from intense star formation in regions where gas has cooled radiatively and later undergo a long list of strongly non-linear processes on small scales, from mergers to feedback from supernovae and supermassive black holes, deriving reliable analytical predictions for the outcome of such events proves extremely difficult. In this context, simulations implementing effective models to describe such mechanisms stand out as ideal tools to understand the diversity of galaxies on cosmic scales and their interplay with their anisotropic environment.

Over the last few years, the increase in computing performance has given birth to the first generation of *"full-physics" cosmological hydrodynamical simulations*: high-resolution simulations of large cosmic volumes (up to ∼100 Mpc scale) including not only the evolution of the dark matter component but also the hydrodynamics of the gas and numerous non-linear processes such as star formation or feedback. Horizon-AGN [1] (Dubois *et al.* , 2014) is one of these simulated universes, along with others such as MareNostrum, MassiveBlack-II, Eagle and Illustris (Devriendt *et al.* , 2010a; Khandai *et al.* , 2015; Schaye *et al.* , 2015; Vogelsberger *et al.* , 2014; Genel *et al.* , 2014).

[1] http://www.horizon-simulation.org

Each of these includes its own implementation of hydrodynamics and specific non-linear small scale processes.

In this first chapter, I describe the genesis and the main features of the simulation HORIZON-AGN in which I analyzed the interplay between the cosmic web and galaxies. Let me consecutively develop the main numerical tools I used to identify the galaxies and compute their physical properties.

1.1 Simulating the universe on cosmological scales

In practice, simulating a universe consists in computing iteratively the evolution of a set of well-suited initial conditions (at redshift $z \simeq 50$) for dark matter density under specific physical forces and in a specific cosmology. Dark matter is modeled with macro particles, each of which actually corresponds to considerable amounts of real dark matter particles. Initially evenly distributed on a mesh that covers the whole simulated volume, these particles are first applied a Zeldovich boost accordingly to the initial density contrast at their initial position. They are subsequently left to move and interact under gravitational forces only as their small cross-sections make them non-collisional in good approximation. Diverse methods have been developed to further include gas and follow its dynamics and transformation into star particles. More specifically, the HORIZON-AGN simulation is run with the Adaptive Mesh Refinement code RAMSES (Teyssier, 2002), which is further described in the next sub-sections.

HORIZON-AGN adopts a standard ΛCDM cosmology with total matter density $\Omega_{\rm m} = 0.272$, dark energy density $\Omega_\Lambda = 0.728$, amplitude of the matter power spectrum $\sigma_8 = 0.81$, baryon density $\Omega_{\rm b} = 0.045$, Hubble constant $H_0 = 70.4\,{\rm km\,s^{-1}\,Mpc^{-1}}$, and $n_s = 0.967$ compatible with the WMAP-7 cosmology (Komatsu, 2011). The values of this set of cosmological parameters are compatible with those of the recent Planck results within a ten per cent relative variation (Planck Collaboration *et al.* , 2014). The chosen size of the simulation box is $L_{\rm box} = 100\,h^{-1}\,{\rm Mpc}$ with 1024^3 dark matter (DM) particles, which results in a DM mass resolution of $M_{\rm DM,res} = 8 \times 10^7\,{\rm M_\odot}$. The initial conditions have been produced with the MPGRAFIC software (Prunet *et al.* , 2008), which efficiently generates gaussian random fields from an input power spectrum. The simulation was run down to $z = 0.05$ and used 10 million CPU hours.

1.1.1 RAMSES: basic features

In RAMSES, the cosmological expansion is accounted for using the super-comoving coordinate system described in Martel & Shapiro (1998). This amounts to a rescaling of the variables - for a non-zero cosmological constant universe - depending on the scale factor $a(t)$, the cosmological

parameters and a specific time variable - the conformal time - derived from the Friedman equation. Such a coordinate system has the major advantage of preserving the standard form of the fluid equations obtained in a non-expanding universe. As a consequence, one should bear in mind that in RAMSES (as in other cosmological simulations) expansion is a taken into account as a background evolution, therefore not influenced by the internal dynamics of particles.

1.1.1.1 Turning on gravity

In this background, particles (dark matter: DM and later stars) form collisionless systems governed by gravitational forces, each particle following the equation of motion:

$$\frac{\mathrm{d}\mathbf{x_p}}{\mathrm{dt}} = \mathbf{v_p}\,, \tag{1.1}$$

$$\frac{\mathrm{d}\mathbf{v_p}}{\mathrm{dt}} = -\nabla\phi\,, \tag{1.2}$$

where $\mathbf{x_p}$,$\mathbf{v_p}$ and ϕ are the position, the velocity and the gravitational potential respectively. The direct computation of all the inter-particle forces is very costly. RAMSES therefore resorts to an adaptive Particle-Mesh method which computes the gravitational force on a non-uniform grid and can be described as follows:

- Particles of mass m_p are given an extension by means of a cloud shape function $S(\mathbf{x})$ (a Cloud-in-Cell in RAMSES, i.e. a grid-sized top hat function) and assigned to all the grid cells i (of size Δx) they overlap through the assignment function

$$W(x) = \int_{x_i-\Delta x/2}^{x_i+\Delta x/2} S(\mathbf{x})dx\,, \tag{1.3}$$

- This allows to convert the distribution of particles into a discrete density computed on the grid:

$$\rho_i = \frac{1}{\Delta x^3}\sum_{p=1}^{N} m_p W(x)W(y)W(z)\,, \tag{1.4}$$

- ϕ can then be derived from the Poisson equation: $\nabla^2\phi = 4\pi G\rho$. Since the grid is not uniform, RAMSES solves iteratively the diffusion equation:

$$\frac{\partial\phi}{\partial\tau} = \nabla^2\phi - 4\pi G\rho\,, \tag{1.5}$$

  until a stable solution is found (Bodenheimer *et al.* , 2007). This is performed discretizing (finite differencing) this equation on the grid and isolating the potential in cell i at time τ_{n+1}, $\phi_i(\tau_{n+1})$ as a function of the density in cell i and of the potential at time τ_n in the neighboring cells.

- Then the force $-\nabla\phi$ calculated on the grid is interpolated at each particle position
- Positions and velocities are updated.

Details about the solver and convergence control methods can be found in Teyssier (2002).

1.1.1.2 Hydrodynamics

Additionally, RAMSES computes the dynamics of the gas. Unlike particles, fluid elements are subject to compression and pressure. In Astrophysics, viscosity is relevant on unresolved scales hence fluid dynamics are governed by the stress-free Euler equations with gravity source term, which extend the conservation equations for mass, momentum and energy:

$$\frac{\partial \rho}{\partial t} + \nabla.(\rho \mathbf{u}) = 0\,, \tag{1.6}$$

$$\frac{\partial \rho \mathbf{u}}{\partial t} + \nabla.(\rho \mathbf{u} \times \mathbf{u}) = -\nabla P - \rho \nabla \phi\,, \tag{1.7}$$

$$\frac{\partial E}{\partial t} + \nabla(\mathbf{u}[E+P]) = 0\,, \tag{1.8}$$

with ρ, u and P the density, stream velocity and pressure of the fluid. Note that this latter equation 1.8 actually becomes

$$\frac{\partial E}{\partial t} + \nabla(\mathbf{u}[E+P]) = H - C\,, \tag{1.9}$$

when taking into heating and cooling processes which will be described in section 1.1.2.1.

RAMSES is an eulerian code. As such, it solves the Euler system on a grid where gas is represented as fluid cells by computing the fluxes at the interface of each cell, as opposed to lagrangian codes (Smoothed-Particle-Hydrodynamics techniques) which discretize mass rather than space and therefore split the gas into massive extended interacting particles. A major advantage of eulerian codes is their great ability to capture complex instabilities and shocks, however at the expense of strict mass conservation.

The evolution of the gas is therefore followed using a second-order unsplit Godunov scheme see (Godunov, 1959, see). To briefly describe this method, let us focus on the simple case where all the source terms: gravity, cooling or heating can be neglected. the Euler equations simplify as:

$$\frac{\partial \mathbf{Q}}{\partial t} + \frac{\partial \mathbf{F}}{\partial \mathbf{x}} = 0\,, \tag{1.10}$$

with $\mathbf{Q} = (\rho, \rho u, E)$ the conservative variables and $\mathbf{F} = (\rho u, \rho u u + P, u[E+P])$ the fluxes.

Assuming that the gas is ideal, monoatomic and in adiabatic evolution it further simplifies to:

$$\frac{\partial \mathbf{Q}}{\partial t} + \mathbf{A}\frac{\partial \mathbf{Q}}{\partial \mathbf{x}} = 0\,, \tag{1.11}$$

which can be solved finding the eigenvalues of the jacobian matrix $\mathbf{A}$, and therefore allows to understand the Euler system as the propagation of a given superposition of hydrodynamical waves. In Horizon-AGN , the gas follows an equation of state for an ideal monoatomic gas with an adiabatic index of $\gamma = 5/3$.

For simplification, let us consider a unidimensional uniform grid. One can show that integrating equation 1.10 over cell of size Δx and time step Δt and using the divergence theorem yields to

$$\mathbf{Q}_i^{n+1} = \mathbf{Q}_i^n - \frac{\Delta t}{\Delta x}(\mathbf{F}_{i+1/2} - \mathbf{F}_{i-1/2}) \,, \tag{1.12}$$

with $\mathbf{Q}_i^n$ the average value of $\mathbf{Q}$ over cell i at time step n and $\mathbf{F}_{i\pm1/2}$ the half-step Godunov fluxes computed from the inter-cell riemann solutions for $\mathbf{Q}$: $\mathbf{Q}_{i\pm1/2}$. This allows for an iterative calculation of $\mathbf{Q}$ and $\mathbf{F}$ at each timestep in any cell of the grid providing that one can properly estimate the inter-cell variables and Godunov fluxes.

The scheme used in ramses is second-order meaning that $\mathbf{Q}$ (hence $\mathbf{Q}_{i\pm1/2}$) is actually reconstructed everywhere in a cell using a piecewise linear interpolation rather than simply equated to the average value over the cell previously calculated, in order to avoid diffusion. There is a variety of ways to reconstruct such states and compute the corresponding Godunov fluxes. Horizon-AGN relies on the HLLC Riemann solver (Toro & Speares, 1994), which makes strict assumptions on the propagation direction and velocity of the former identified hydrodynamical waves, then reconstructs the interpolated variables from their cell-centered values. It further imposes limitations on the slope of the linear interpolation using the MinMod Total Variation Diminishing scheme to prevent spurious oscillations at cell interfaces in regions where the gradient of $\mathbf{Q}$ is steep.

The reader may refer to Teyssier (2002) for more technical information on these methods.

1.1.1.3 Adaptive mesh refinement

ramses is an adaptive mesh refinement code, which means that the grid is not uniform but rather refines or de-refines automatically (i.e. splits one cell into 8 sub-cells) in dense regions from one time step to the next so as to naturally adapt to the local density and successfully follow the dynamics of the gas and particles in the highly non-linear regions. In Horizon-AGN , the initial mesh is refined up to $\Delta x = 1\,\mathrm{kpc}$ (7 levels of refinement). This is done according to a quasi-Lagragian criterion: if the number of DM particles in a cell is more than 8, or if the total baryonic mass in a cell is 8 times the initial DM mass resolution, a new refinement level is triggered. In order to keep the minimum cell size approximately constant in physical units, a new maximum level of refinement is allowed every time the expansion scale factor doubles (i.e. at $a_{\mathrm{exp}} = 0.1$, 0.2, 0.4 and 0.8).

1.1.2 Small-scale physical recipes for realistic galactic dynamics.

Once the dynamics is computed for the gas and the particles, simulating a physical universe still requires to compute the non-linear physics that govern small scales of the Universe. Since our resolution is limited to $1\,kpc$, many of these processes actually occur on typical scales smaller than the smallest cell in the simulation. They are consecutively labeled as "sub-grid processes", hence only modeled through their effective impact on cell scales. Let us review all such processes implemented in Horizon-AGN .

1.1.2.1 Gas cooling and heating

Photons interact with electrons -either bound in an atom or free- in many ways that can impact the overall energy of the system. Specifically, photons can excite bound electrons to either higher energy bound states which will soon after decay radiating away the excess energy, or to unbound states which may lead to the subsequent recombination of the electron with another photon (ionization/recombination). Free electrons can also transfer their kinetic energy to background photons through two channels: bremsstrahlung (fly-by braking) or inverse Compton scattering (head-on collision). These processes, each of which dominates in a specific temperature range, therefore reduce the internal energy of the gas. This loss of energy $\dot{e}$ therefore depends on the number density of protons $n_{\rm p}$ and electrons $n_{\rm e}$:

$$\dot{e} \propto n_{\rm e} n_{\rm p}\,. \tag{1.13}$$

In the temperature range $10^4 - -10^5\,\mathrm{K}$, gas is at ionization equilibrium, leading to a plasma where the number density of electrons and the proton number density are related through specific coefficients that account for the rates of spontaneous emission, absorption and stimulated emission respectively. The loss of energy writes $\dot{e} = f_{\rm cool}(T) n_{\rm p} n_{\rm e}$ where $f_{\rm cool}(T)$ is a cooling rate that encapsulates the efficiency of each process at a given temperature T.

In Horizon-AGN , gas is allowed to cool by H and He cooling with a contribution from metals assuming a solar composition by implementing the cooling rate from the Sutherland & Dopita (1993) model down to $10^4\,\mathrm{K}$. This leads to add the cooling term C in the energy equation of the Euler system. Metallicity is modelled as a passive variable for the gas and its amount is modified by the injection of gas ejecta during supernovae explosions and stellar winds. Various chemical elements synthesised in stars are released by stellar winds and supernovae: O, Fe, C, N, Mg and Si. However, it is important to remind that they do not contribute separately to the cooling curve (the ratio between each element is taken to be solar for simplicity) but can be used to probe the distribution of the various metal elements

Quasars and hot massive stars are also thought to produce an intense UV radiation able to heat the gas from very high redshift (Haehnelt *et al.* , 2001; Dunkley *et al.* , 2009). In order to model this effect, heating from a uniform UV background is triggered in Horizon-AGN after redshift $z_{\rm reion} = 10$ following the frequency-integrated ionization and photo-heating rates computed from the spectra of quasars in Haardt & Madau (1996). This adds the heating term H in the energy equation of the Euler system. .

1.1.2.2 Star formation and stellar feedback

Stars form from the collapse of giant molecular clouds or ultra-dense infrared dark clouds (under Jeans instability) emerging from the cooling of high-density gas. This suggests that the star formation rate must be a function of the local gas density, a relationship that reveals surprisingly tight in observations (Kennicutt (1998)) which found it to be close to $\dot{\rho_{star}} \propto \rho_{gas}^{3/2}$. This behavior can be understood as the result of the star formation rate following a Schmidt law:

$$\dot{\rho}_{\rm star} = \epsilon_* \rho / t_{\rm ff} \,, \tag{1.14}$$

where $\dot{\rho}_{\rm star}$ is the star formation rate density, $\epsilon_* = 0.02$ (Kennicutt, 1998; Krumholz & Tan, 2007) the constant star formation efficiency, and $t_{\rm ff}$ the local free-fall time of the gas:

$$t_{\rm ff} = \frac{3\pi}{32 G \rho}. \tag{1.15}$$

This is how star formation is modeled in Horizon-AGN .

However, observations also reveal that stars form only in regions where the gas density exceeds a given threshold that corresponds to the transition from atomic hydrogen to molecular hydrogen(Kennicutt, 1998; Wong & Blitz, 2002). Following on this behavior, although with some corrections to overcome the limited resolution of the simulation, star formation in Horizon-AGN is allowed in regions which exceed a gas Hydrogen number density threshold of $n_0 = 0.1\,{\rm H\,cm^{-3}}$. In such regions, at each time step, a small fraction of gas is converted into star particles the density of which is given by the Schmidt law, and whose individual masses are multiple of the minimum mass $M_* = \rho_0 \Delta x^3 \simeq 2 \times 10^6\,{\rm M_\odot}$. The multiple is drawn from a Poissonian random process (Rasera & Teyssier, 2006; Dubois & Teyssier, 2008).

The gas pressure is artificially enhanced above $\rho > \rho_0$ assuming a polytropic equation of state $T = T_0(\rho/\rho_0)^{\kappa-1}$ with polytropic index $\kappa = 4/3$ to avoid excessive gas fragmentation and mimic the effect of stellar heating on the mean temperature of the interstellar medium (Springel & Hernquist, 2003).

As massive stars ($M > 8\,M_\odot$) grow a stable iron core, they begin to contract. Their inner

core collapses under gravity and increases its density up to the point where it reaches the Fermi quantum degeneracy pressure. Passed this point, the inner core undergoes an extremely rapid collapse owing to the dissociation of its iron nuclei that allows the protons to capture electrons and form neutrons, hence decreases the Fermi pressure. This phase produces intense fluxes of neutrinos. It stops abruptly due to repulsive strong force when the density reaches the point where it violates the Pauli's principle applied to neutrons. This generates a shock wave which washes away the energy of the supernova, therefore released in the interstellar medium. This kind of supernovae is labeled *Type II*: it ejects $\sim 5\,\mathrm{M}_\odot$ in the interstellar medium with a total kinetic energy $K \sim 10^{51}$erg and radiates $\sim 10^{49}$erg on a month timescale.

Another major type of supernovae (*Type Ia*) is consecutive to the accretion of a companion star by a white dwarf whose electronic pressure has reached the Fermi limit. This drives explosions that release huge amounts of thermal energy and leave no remnant.

This feedback from stars is explicitly taken into account assuming a Salpeter (1955) initial mass function with a low-mass (high-mass) cut-off of $0.1\,\mathrm{M}_\odot$ ($100\,\mathrm{M}_\odot$), as described in details in Kimm 2012 (DPhil Thesis). Specifically, the mechanical energy from supernovae type II and stellar winds is taken from STARBURST99 (Leitherer *et al.* , 1999, 2010), and the frequency of supernovae type Ia explosions is computed following Greggio & Renzini (1983).

1.1.2.3 Feedback from black holes

Supermassive black holes forming at the center of galaxies can also radiate considerable amount of energy either thermally or through strong outflows of accelerated ionized material locked in a thin bipolar jet.

In HORIZON-AGN , the same "canonical" Active Galactic Nuclei (AGN) feedback modelling than the one presented in Dubois *et al.* (2012b) is used. Black holes (BHs) are created where the gas mass density is larger than $\rho > \rho_0$ with an initial seed mass of $10^5\,\mathrm{M}_\odot$. In order to avoid the formation of multiple BHs in the same galaxy, BHs are not allowed to form at distances less than 50 kpc from each other. The accretion rate onto BHs follows the Bondi-Hoyle-Lyttleton rate $\dot{M}_{\rm BH} = 4\pi\alpha G^2 M_{\rm BH}^2 \bar{\rho}/(\bar{c}_s^2 + \bar{u}^2)^{3/2}$, where $M_{\rm BH}$ is the BH mass, $\bar{\rho}$ is the average gas density, $\bar{c}_s$ is the average sound speed, $\bar{u}$ is the average gas velocity relative to the BH velocity, and α is a dimensionless boost factor with $\alpha = (\rho/\rho_0)^2$ when $\rho > \rho_0$ and $\alpha = 1$ otherwise (Booth & Schaye, 2009) in order to account for our inability to capture the colder and higher density regions of the inter-stellar medium. The effective accretion rate onto BHs is capped at the Eddington accretion rate: $\dot{M}_{\rm Edd} = 4\pi G M_{\rm BH} m_{\rm p}/(\epsilon_{\rm r}\sigma_{\rm T} c)$, where $\sigma_{\rm T}$ is the Thompson cross-section, c is the speed of light, $m_{\rm p}$ is the proton mass, and $\epsilon_{\rm r}$ is the radiative efficiency, assumed to be equal to $\epsilon_{\rm r} = 0.1$ for

the Shakura & Sunyaev (1973) accretion onto a Schwarzschild BH.

The AGN feedback is a combination of two different modes, the so-called *radio* mode operating when $\chi = \dot{M}_{\rm BH}/\dot{M}_{\rm Edd} < 0.01$ and the *quasar* mode active otherwise. The quasar mode consists of an isotropic injection of thermal energy into the gas within a sphere of radius Δx, and at an energy deposition rate: $\dot{E}_{\rm AGN} = \epsilon_{\rm f}\epsilon_{\rm r}\dot{M}_{\rm BH}c^2$. In this equation, $\epsilon_{\rm f} = 0.15$ is a free parameter chosen to reproduce the scaling relations between BH mass and galaxy properties (mass, velocity dispersion) and BH density in our local Universe (see Dubois *et al.* , 2012b). At low accretion rates, the radio mode deposits AGN feedback energy into a bipolar outflow with a jet velocity of $10^4\,{\rm km\,s^{-1}}$. The outflow is modelled as a cylinder with a cross-sectional radius Δx and height $2\,\Delta x$ following Omma *et al.* (2004) (more details are given in Dubois *et al.* (2010). The efficiency of the radio mode is larger than the quasar mode with $\epsilon_{\rm f} = 1$.

1.2 Structure detection and identification in HORIZON-AGN

1.2.1 Haloes and galaxies: Structure identification and merging

identification Haloes and galaxies are identified from DM particles and star particles respectively using HaloMaker (Tweed *et al.* , 2009, based on) with the AdaptaHOP algorithm (Aubert *et al.* , 2004). This subsection only summarizes the main features of the algorithm.

This method identifies structures from the particle positions only, no further correction is performed based on the velocities. Its great advantage is however its ability to detect sub-structures. It first computes the density at each particle position by finding its N nearest neighbors and integrating their contribution to the local density using the standard SPH (smoothed particle hydrodynamics) spline kernel (Monaghan (1992). A total of 20 neighbours were used to compute the local density of each particle in our post-processing of HORIZON-AGN .

Then the algorithm hops from one particle to its highest density neighbor until it reaches a local maximum. Once all the local maxima of the field are found, a peak patch around each maximum is defined as the set of particles above a well-suited density threshold ($\rho/\bar{\rho} > \rho_{\rm th}$ where $\bar{\rho}$ is the average of the total matter density) that share this local maximum. In the following work, I chose $\rho_{\rm th} = 178$ to identify clear collapsed, virialised structures: haloes and galaxies. At this point, detected overdensities still need to be discriminated into main structures and sub-structures of various levels.

It is performed first identifying the saddle points between interfacing patches. The connecting saddle point between two patches is identified as the particle of highest density among all their

saddle points. Those saddle points are used to create branches connecting all the local maxima in a group of adjacent patches with saddle point densities higher than $\rho_{\rm th}\bar{\rho}$. It allows to build a hierarchy of nodes, where each node contains all the particles in the group whose associated density is enclosed between two values. For a connex group of interfacing patches, the lowest level (0) node is constituted of all the particles in the group with associated density higher than the threshold $\rho_{\rm th}\bar{\rho}$ and lower than the lowest saddle point detected (if any). Particles with density above this value are splitted into two level 1 nodes depending on their proximity to the two local maxima associated to this saddle point. This operation is repeated iteratively over all saddle points in the group in ascending order of their density: Particles in level 1 nodes are splitted into higher level nodes if their density is higher than that of the lowest of the remaining saddle points adjacent to the patch of the maximum they have been temporarily assigned to.

Physical structures correspond to the highest level -"leaf-" nodes, which are nodes that cannot be further splitted. Structures and sub-structures of various hierarchical levels are then recovered collapsing this node structure tree along the branch containing the most massive leaf node ("MSM" technic). This defines the main structure. This operation is then repeated with the most massive remaining leaf node, whose branch is collapsed down to the the lowest level node not assigned yet, and then again until all leaf nodes are assigned a substructure hierarchical level. A force softening (minimum size below which substructures are considered irrelevant) of ~ 2 kpc is applied to discard small fluctuations or clumps as substructures.

Moreover, only structures with a minimum number of particles (fixed as an input parameter to 50, 100 or 1000 in this work) are identified as haloes or galaxies.

The center of a structure is then identified as the particle of highest density, its inertia tensor is computed from the positions of its particles, which allows to infer its axis ratios when assuming its shape to be ellipsoidal. Mass is then computed in concentric ellipsoids with axis (a_i, b_i, c_i) and same axis ratios until the enclosed particles verify the condition:

$$\frac{||2E_k + E_p||}{||E_k + E_p||} < 0.2\,. \tag{1.16}$$

This determines the viral mass $m_{\rm vir}$ and the virial radius $R_{\rm vir} = (a_i b_i c_i)^{1/3}$.

Merger trees The updated version devised by Tweed *et al.* (2009) allows to build merger trees (with the TreeMaker module) for all galaxies or haloes from a collection of time-ordered snapshots. These trees are hierarchical networks through which a galaxy (or halo) identified in snapshot n is connected to its progenitors in snapshot $n-1$ and its child structures at time set $n+1$. The tree is computed using the following set of rules:

- Each (sub)structure i at step n can only have 1 son at step $n+1$. Fragmentation is neglected.
- Tracking the identities of the star (DM) particles, the mass m_{ij} shared by a (sub)structure i of mass m_i at step n and a (sub)structure j of mass m_j at step $n+1$ is computed
- The son of i is identified as the (sub)structure j that maximizes m_{ij}/m_i.
- Conversely, a (sub)structure i of mass m_i at step n is a progenitor of the (sub)structure j of mass m_j at step $n+1$ if, and only if j is the son of i.
- The main progenitor of j is the (sub)structure i that maximizes m_{ij}/m_j

A new progenitor of a galaxy n_g in snapshot n is therefore any galaxy in snapshot $n-1$, then identified as a main or sub-structure, whose material (or a significant amount of it) is found in the galaxy n_g in snapshot n and not further identified as a relevant substructure. This method thus naturally tracks the last stage of the merging process when the material of the smallest progenitor has completely dissolved into its more massive host.

1.2.2 Synthetic galaxies in Horizon-AGN

Applying this identification process in HORIZON-AGN and selecting only galactic structures identified with more than 50 particles, I produce catalogues of around $\sim$ 150 000 galaxies and $\sim$ 300 000 haloes at each snapshot of the simulation for redshifts $0 < z < 5$. For each galaxy or halo, HaloMaker produces a list of all the particles (star or DM) in the structure with their position, age, mass and velocity, along with some global properties such as the total mass of the structure or its virial radius.

These data allow to compute numerous more elaborate properties such shape parameters (inertia tensor, bulge-to-disc ratios, triaxiality) or rest-frame colors from AB magnitudes. The computation of such specific properties will be detailed in each chapter when relevant to the study. However, a few general comments can be made prior to a more detailed analysis:

- Although the limited resolution used for the hydrodynamics and intense AGN feedback prevent the formation of very thin disks with well defined spiral patterns, HORIZON-AGN recovers a wide morphological diversity for galaxies at all redshifts with disk, ellipticals and spheroids, covering a wide range of masses and colors. A few examples are presented on Fig. 1.1 .
- The mass function in HORIZON-AGN is compatible with observations down to lowest redshifts although it tends to overestimate the low-mass range by a factor $\simeq 3$ as can bee seen on Fig.. 1.2. It should be noted however that the rate of AGN feedback and supernovae feedback

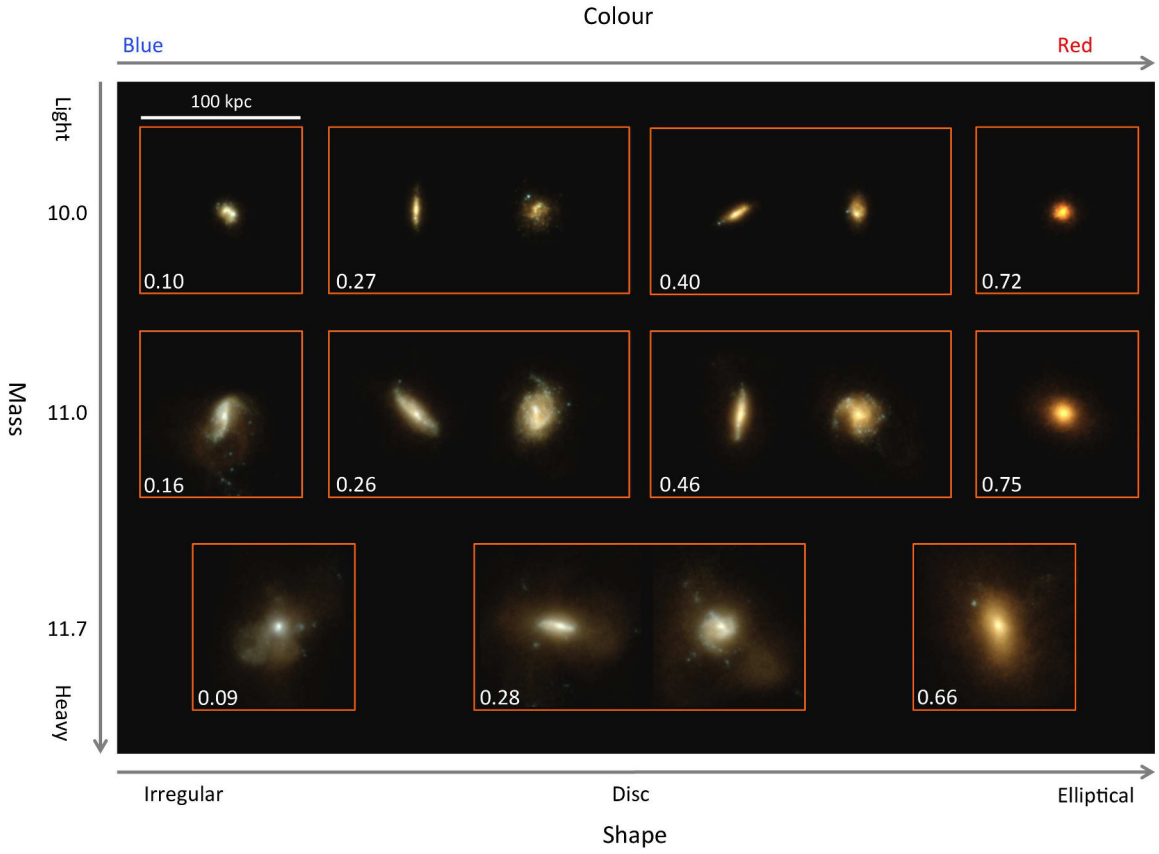

Figure 1.1: Stellar emission of a sample of galaxies in the HORIZON-AGN simulation at $z = 1.3$ observed through rest-frame u-g-i filters. Extinction by dust is not taken into account. Each vignette size is 100 kpc vertically. The numbers on the left of the figure indicate the galaxy stellar mass in log solar mass units. The number in the bottom left of each vignette is the g-r rest frame colour, not corrected for dust extinction. Disc galaxies (galaxies in the centre of the figure) are shown edge-on and face-on.

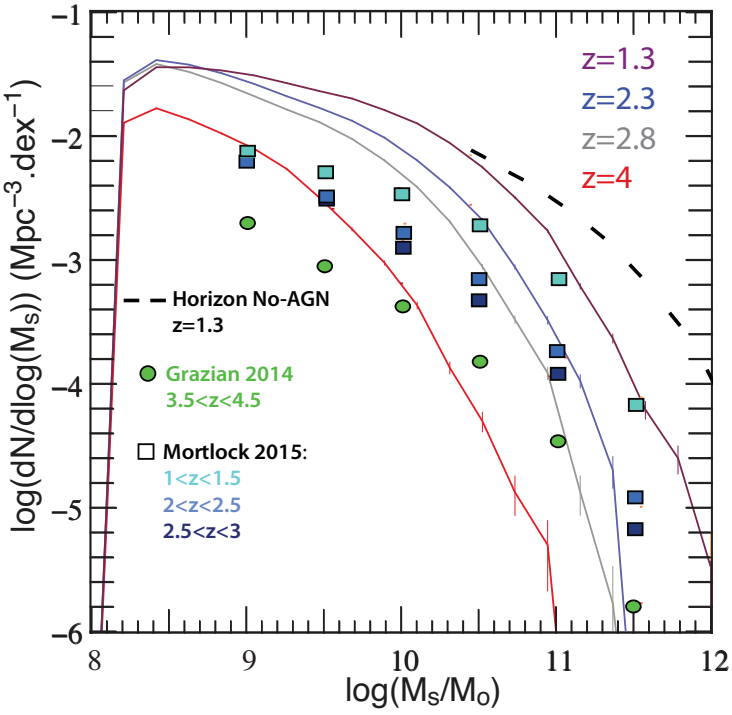

Figure 1.2: Galaxy stellar mass function in HORIZON-AGN , for $z = 4$ to $z = 1.3$. N is the number density of galaxies, M_s the stellar mass (together with Horizon-noAGN for comparison). The sharp cut-off at $M_s = 10^8\,\mathrm{M}_\odot$ corresponds to our completeness detection threshold. 1-σ poissonian error bars are over plotted as vertical lines. Observational points from CANDELS-UDS and GOODS surveys are rescaled from best fits in Mortlock *et al.* (2015) and Grazian *et al.* (2014) and overplotted. While mass functions are consistent at the high mass end, HORIZON-AGN overshoots the low-mass end by about a factor 3 in this redshift range.

are tuned so as to bend the mass function in the high-mass and low-mass range respectively and obtain this compatible mass function.

- HORIZON-AGN features the large-scale pattern of the cosmic web, with filaments and walls surrounding voids and connecting halos, the gas following very closely the distribution of the underlying dark matter on largest scales. A projected map of half the simulation volume and a smaller sub-region are shown in Fig. 1.3.

Gas density, gas temperature and gas metallicity are depicted in Fig. 1.3. Massive halos are filled with hot gas, and feedback from supernovae and AGN pours warm and metal-rich gas in the diffuse inter-galactic medium.

As demonstrated in Dubois *et al.* (2013a), the modelling of AGN feedback is critical to create early-type galaxies and provide the sought morphological diversity in hydrodynamical cosmological simulations (see e.g. Croton *et al.* , 2006, for semi-analytical models).

1.2.3 The numerical cosmic web

I briefly recalled in introduction how theoretical models of structure formation and numerical simulations have predicted that the amplification of small density fluctuations from the early Universe under gravitational instability leads to the formation of this large-scale "cosmic web" made of clustered halos embedded in filaments, sheets and voids. Although this filamentary layout is visually compelling, tracking its influence on the properties of galaxies on smaller scales requires the development of a robust mathematical framework, able to provide strict definitions of such patterns (filaments, sheets, voids) then identify them in simulations and observations from the density field of matter or gas (or even galaxies themselves in observations).

Over the past decade, numerous attempts in this direction have led to an important diversification of such geometry extractors. In this work, I chose to use what might be the most robust -both theoretically and numerically- and the most promising one towards the unification of extractors in simulations and observations: the DisPerse ridge extractor devised by Sousbie (2013), and a slightly older version from Sousbie *et al.* (2009)

In the following, a brief description is provided of the successive generations that have led to the fully developed and most up-to-date method I used. For a full description of the mathematical framework involved, the reader may refer to Novikov *et al.* (2006); Sousbie *et al.* (2008); Sousbie *et al.* (2009, 2010).

Let us consider a gaussian random field ρ describing the matter density in the universe (or a

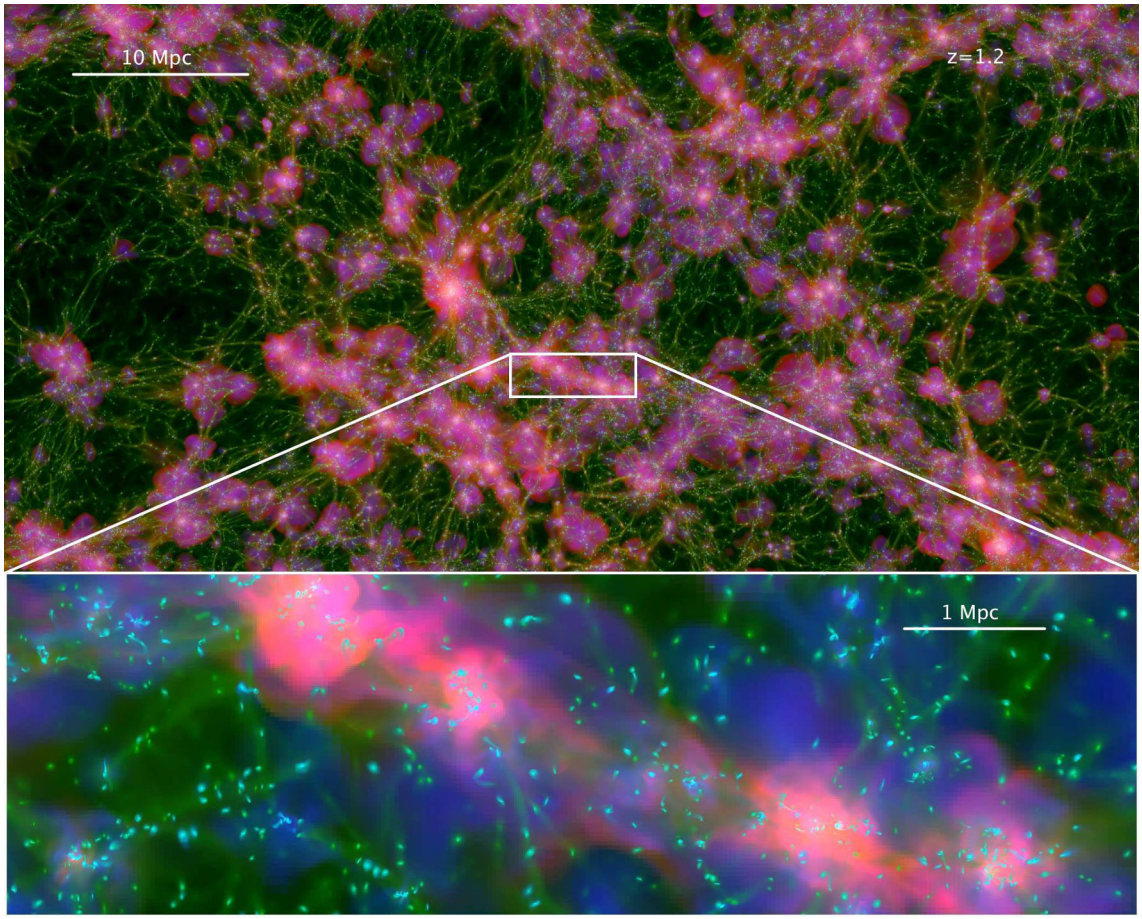

Figure 1.3: Projected maps of the HORIZON-AGN simulation at $z = 1.2$ are shown. Gas density (green), gas temperature (red), gas metallicity (blue) are depicted. The top image is $100\,h^{-1}$ Mpc across in comoving distance and covers the whole horizontal extent of the simulation and $25\,h^{-1}$ Mpc comoving in depth. The bottom image is a sub-region where one can see thin cosmic filaments as well as a thicker filaments several Mpc long bridging shock-heated massive halos and surrounded by a metal-enriched intergalactic medium. Physical scales are indicated on the figures in proper units.

simulated/observed volume).

Let us first restrain this description to 2D and then define peak patches (void patches) as the regions of space containing all the points converging to the same local maximum (local minimum) while going along the field lines in the direction (opposite direction) of the gradient $\nabla\rho$. The skeleton of overdense regions can be seen as the borders of the void patches, that is to say the ridges of the density field . One can show that it passes through all the saddle points and the local maxima.

The skeleton can therefore be rigorously defined as the ensemble of pairs of stable fields lines departing from saddle points and connecting them to local maxima. The skeleton field lines can thus be drawn by going along the trajectory with the following motion equation:

$$\frac{d\mathbf{r}}{dt} = \mathbf{v} = \nabla\rho\,, \tag{1.17}$$

starting from the saddle points, and with initial velocity parallel to the major axis of the local curvature. This definition can be extended to three dimensional fields. One should note however that this dependance on nearby saddle points means that such a skeleton is by very definition non-local.

First techniques developed in this framework proposed to by-pass this difficulty with a local Taylor expansion (second order approximation) of the density field around extremas and saddle points. At leading order, back in a three dimensional field, this therefore leads to define the skeleton as the set of points which satisfy:

$$\mathbf{H}.\nabla\rho = \lambda_1\nabla\rho\,, \tag{1.18}$$

$$\lambda_3 < 0,\, \lambda_2 < 0\,, \tag{1.19}$$

with

$$\mathbf{H} = \frac{\partial^2\rho}{\partial x_i \partial x_j}\,, \tag{1.20}$$

the Hessian tensor of the field, and $\lambda_3 < \lambda_2 < \lambda_1$ its eigenvalues (axis of the local curvature). While the first condition arises from a constrained extremalization of the gradient $\nabla\rho$ to select the most relevant field lines from one point to another, the second condition is enforced so that the skeleton traces only the ridges of the distribution.

Since this *local skeleton* is based on a local second-order approximation of the density field, its properties can be understood through the properties of its gradient and hessian tensor only.

The eigenvalues of $\mathbf{H}$ define the local curvature of ρ at any point, thus separating space into distinct regions depending on the sign of these eigenvalues. Let N_- be the number of negative eigenvalues:

- Nodes are located at maxima of the density field and have $N_- = 0$
- Filaments are passing through saddle points that have $N_- = 1$ ("filament-type saddle point")
- Walls are located around saddle points that have $N_- = 2$ ("pancake-type saddle point")
- Voids are located at minima of ρ and have $N_- = 3$.

This characterization of typical extremas and saddle points is theoretically robust and allows for a better understanding of how large-scale structures are deeply imprinted in the initial matter density field, but it implies to compute such a "skeleton" locally, at the expense of its connectivity.

Building on this first idea, two versions of the ridge extractor I used were designed and greatly improved the identification of these structures by producing a fully connected network of filaments ("skeleton"). Both are based on Morse theory results (Jost (1995)), i.e. the definition of sheets as the interface (boundaries) of void patches, and filaments as the interface of sheets. Therefore they identify iteratively voids, sheets from voids and filaments from sheets:

- The first version: "the skeleton" (Sousbie *et al.* (2009)) is based on the watershed technique and consists in a probabilistic extraction of patches in a sufficiently sampled and smoothed density field (to ensure differentiability). For each pixel, probabilities of belonging to specific patches are calculated and the pixel is later assigned to the highest probability patch. When enough neighboring pixels belong to different patches, skeleton segments are created from the edges of such pixels, and their extremities are later adjusted to ensure the differentiability of the skeleton.
- the second version: DisPerse (Sousbie *et al.* (2010) requires no smoothing and directly operates on a distribution of particles (would it be a noisy one). It computes a discrete density field from a Delaunay tessellation on the particles then - extending Morse theory to deal with discrete fields - identifies the relevant ridge lines connecting maxima through filament-type saddle points above a given *persistence* threshold. The concept of persistence encompasses the robustness of topological features in the field (such as number of components, of holes, or tunnels) to an increasing excursion threshold (i.e. when looking only at values of the field above a certain threshold). It proceeds via pairing critical points together as persistence pair, and measuring their relative height (the persistence of the pair) to decide if they are significant enough to represent a robust underlying topological feature of the field, or if they are an artifact of sampling. This second version hence naturally deals with noisy observational data.

Both versions were found to give similar results in HORIZON-AGN on scales considered.

Chapter 2

Galactic spin alignments induced by the cosmic web

Over the past ten years, several numerical investigations (e.g. Aragón-Calvo *et al.* , 2007; Hahn *et al.* , 2007; Paz *et al.* , 2008; Sousbie *et al.* , 2008) have reported that large-scale structures, i.e. cosmic filaments and sheets, influence the direction of the intrinsic angular momentum (AM) – or *spin*– of haloes, in a way originally predicted by Lee & Pen (2000). It has been speculated that massive haloes have AM perpendicular to the filament and higher spin parameters because they are the results of major mergers (Aubert *et al.* , 2004; Peirani *et al.* , 2004; Bailin & Steinmetz, 2005). On the other hand, low-mass haloes acquire most of their mass through smooth accretion, which explains why their AM is preferentially parallel to their closest large-scale filament (Codis *et al.* , 2012; Laigle *et al.* , 2015).

In this chapter, after a brief review of the results established for dark haloes and further precision on the numerical methods I used, I revisit these significant findings using the cosmological hydrodynamical Horizon-AGN simulation for redshifts $z > 1$ (around the peak of cosmic star formation history). First, I show that that this trend extends to simulated galaxies displaying a wide morphological diversity: the AM of low-mass, rotation-dominated, blue, star-forming galaxies is preferentially aligned with their filaments, whereas high-mass, velocity dispersion-supported, red quiescent galaxies tend to possess an AM perpendicular to these filaments. These theoretical predictions have recently received their first observational support (Tempel & Libeskind, 2013). Analysing Sloan Digital Sky Survey (SDSS) data (Aihara *et al.* , 2011), these authors uncovered a trend for spiral galaxies to align with nearby structures, as well as a trend for elliptical galaxies to be perpendicular to them. Then, in a second part, I emphasize both exploring the physical mechanisms which drive halo's and galactic spin swings and on quantifying how much mergers and smooth accretion re-orient these spins relative to cosmic filaments. In particular, I analyse the

effect of mergers and smooth accretion on AM's orientation and magnitude for haloes and galaxies.

This chapter reproduces results published in Dubois *et al.* (2014) and Welker *et al.* (2014).

2.1 Orientation of dark haloes in the cosmic web

Let us first summarize the theoretical and numerical results that first allowed for a better understanding of the orientation the orientation of dark haloes (more specifically the orientation of their spin) in the cosmic web.

2.1.1 The spin of dark haloes: a mass segregated distribution

The consensus that has emerged from the aforementioned studies is that the orientation of the spin of the dark haloes is imprinted by the geometry of the surrounding large scale structures, more specifically the nearby cosmic filaments, following two distinct mass dependent trends:

- low-mass haloes tend to display a spin parallel to the nearest large-scale filament.
- more massive haloes are more likely to have a spin orthogonal to the nearest filament.

This is not an absolute trend but a mild -though compelling- statistical effect, therefore better described by the evolution of the excess probability ξ of given deviations angles. While previous works had pointed out strong hints of such a mass-segregation, Codis *et al.* (2012) made the first robust quantitative estimation of such an angular distribution and confirmed with high relevancy the existence of a smooth transition from alignment to perpendicularity as the halo mass increases. Studying the orientation of 40 millions dark haloes in the cosmological N-body simulation 4π and making use of the same state-of-the-art filament detection methods presented in Chapter 1(Sousbie *et al.* (2009)), they constrained the estimation of the halo transition mass around $5\ 10^{12}\ M_{\odot}$ and the highest alignment excess probability for the cosine of the angle between the halo spin and the direction of its filament around $\xi = 20\%$.

They suggest a scenario involving the winding around of cosmic flows conjoint to the filamentary collapse to justify the spinning of small haloes parallel to their filament, and relying on Tidal Torque Theory (Hoyle, 1949; Peebles, 1969; Doroshkevich, 1970; White, 1984; Porciani *et al.* , 2002a,b) (possibly relayed through mergers) to flip more massive haloes perpendicular to it. In the next sections, the predictions of Tidal Torque Theory are presented with its subsequent improvements and develop the most up-to-date version of this scenario.

2.1.2 Tidal Torque Theory

Haloes - and therefore galaxies- acquire most of their angular momentum at an early stage of structure formation, in the linear regime, from environmental tidal torques from the nearby density fluctuations (Hoyle, 1949; Peebles, 1969). This angular momentum transfer results from the misalignment of their inertia tensor with the tidal shear tensor which induces, to the first non-vanishing order, a coupling between the quadrupole moment of the halo mass and the tidal field exerted by the neighboring density fluctuations (Doroshkevich, 1970; White, 1984). In contrast, only little angular moment is tidally exchanged after the haloes decouple from expansion and start to collapse.

This therefore leads to the halo angular momentum:

$$L_i(t) = a(t)^2 \dot{D}_+(t) \epsilon_{ijk} \, T_{jl} \, I_{lk} \, , \tag{2.1}$$

with the antisymmetric tensor ϵ_{ijk}, the expansion factor $a(t)$, the growth rate $D_+(t)$, the *tidal tensor* or *shear tensor*:

$$T_{ij} = D_{ij} - \frac{1}{3} D_{ij} \delta_{ij} \, , \tag{2.2}$$

defined as the traceless part of the deformation tensor:

$$D_{ij} = \frac{\partial^2 \Phi}{\partial q_i \partial q_j} \, , \tag{2.3}$$

and quadrupolar inertia tensor:

$$I_{ij} = \rho_0 \; a_0^3 \int_\Gamma q'_i q'_j \mathrm{d}^3 q' \, , \tag{2.4}$$

where Γ is the lagrangian volume of the proto-halo and $q' = q - \bar{q}$, the bar standing for the average over Γ. Note that only the traceless part of I_{ij} leads to a non-zero term. The q_i are the eulerian spatial coordinates and Φ is related to the gravitational potential ϕ through :

$$\Phi(\mathbf{q}) = \frac{\phi(\mathbf{q}, t)}{4\pi G \bar{\rho}(t) a(t)^2 D_+(t)} \, . \tag{2.5}$$

An interesting aspect of this expression is that it relates the geometry on small scales - through the inertia tensor- to the tidal tensor that probes the matter distribution on somewhat larger scales. This formalism is therefore well suited to explore the connection between the spin alignment trends and the cosmic web geometry. In the following, I briefly summarize the analysis performed in (Porciani *et al.* , 2002b).

First, let us assume that $\mathbf{T}$ and $\mathbf{I}$ are uncorrelated. Although this is a questionable assumption in the scope of structure growth from density perturbations, this provides a qualitative understanding

of the alignment trends. In a frame where $\mathbf{T}$ is diagonal, one finds:

$$L_i \propto (\lambda_j^{\mathrm{T}} - \lambda_k^{\mathrm{T}}) I_{jk} \,, \tag{2.6}$$

$$\tag{2.7}$$

with $\lambda_3^{\mathrm{T}} < \lambda_2^{\mathrm{T}} < \lambda_1^{\mathrm{T}}$ the corresponding eigenvalues of $\mathbf{T}$ and i, j, k cyclic permutations of $1, 2, 3$. Since $\mathbf{I}$ is supposed independent of $\mathbf{T}$, averaging over all the possible rotation matrix from the $\mathbf{T}$ to $\mathbf{I}$ frame, one gets:

$$\langle |L_i| \rangle \propto |\lambda_j^{\mathrm{T}} - \lambda_k^{\mathrm{T}}| \; \langle |I_{jk}| | i_1, i_2, i_3 \rangle = |\lambda_j^{\mathrm{T}} - \lambda_k^{\mathrm{T}}| \; f(i_1, i_2, i_3) \,, \tag{2.8}$$

where $i_1 > i_2 > i_3$ are the eigenvalues of $I_{i,j}$ and $f(i_1, i_2, i_3)$ is a function independent of the L_i component considered. As a consequence the largest component of the angular momentum is $L_2 \propto |\lambda_1^{\mathrm{T}} - \lambda_3^{\mathrm{T}}|$. In linear structure formation theory, for a lagrangian patch in the vicinity of a filament-type saddle point, the second eigenvector of $\mathbf{T}$ points towards the proto-wall and orthogonally to the local proto-filament. It is therefore expected that the haloes will display a spin preferentially aligned to the direction of the wall and orthogonal to the filament. As a purely linear prediction, it can only be expected to affect the largest scales of the halo hierarchy at low redshift i.e. the most massive ones.

Porciani *et al.* (2002a) found a good agreement between this prediction and massive haloes in N-body simulations, although both the spin amplitude and the alignment the trend were found to be much weaker than expected. They directly related that to the fact that $\mathbf{T}$ and $\mathbf{I}$ are actually strongly correlated, the typical initial configuration being a prolate proto-halo lying perpendicular to a large-scale high-density ridge, with the surrounding voids inducing compression along its major and intermediate inertia axes. However this result remains at odds with the trends found for low-mass haloes.

Anisotropic TTT To better understand the observed trends in simulations, Codis *et al.* (2015) developed an analytical theory of these correlations in the lagrangian framework, from the gaussian random field that describes initial matter density perturbations.

Defining a typical proto-filament within a proto-wall (i.e. the preferential environment where galaxies form) as a specific elliptical saddle-point of the initial density field (a filament-type saddle point), these authors derived analytical estimations of the tidal field everywhere in such a constrained large scale background. They further estimated the constrained inertia tensor (estimated through an appropriate normalization of the inverse hessian) of lagrangian patches at elliptical peaks of the density field ("proto-haloes"), in the vicinity of such an anisotropic environment.

This allowed them to extend the prediction of Tidal Torque Theory to map the mean spin expectations in this geometry .

In the direct vicinity of the saddle point, they found a mean spin aligned with the direction of the filament, with a symmetric distribution in four quadrants of alternate sign around the ridge line. Moving away from the saddle point in the direction of the filament, they predicted a flip of the mean spin orthogonally to the filament in these regions. These patterns arise from the fact that the tidal tensor and the inertia tensor of the proto-halo feel differently the large scale anisotropic features of the local density field that are predominantly the filament + the wall when close to the saddle point, and the filament + the density gradient towards the node when moving away from the saddle point in the direction of the filament. These misalignments then generate the angular momentum of the proto-halo as predicted by Tidal Torque Theory and lead to the observed distribution.

A simple use of a Press-Schechter like theory with background split prescription (Press & Schechter (1974); Peacock & Heavens (1990); Paranjape & Sheth (2012)) allowed them to relate this spatial evolution to the mass evolution detected in simulations for virialised structures at lower redshift: they mapped the mean mass of haloes formed in a given locus around this geometry, and recovered the transition mass between the two trends (spin aligned/ spin orthogonal) as more massive haloes form further from the saddle point than low-mass ones.

These results provide a good understanding of the distribution of spin on large (linear) scales of the cosmic web available for embedded future haloes. However, understanding the way it effectively persists in the hierarchical build up of evolved virialised haloes and possibly transfers to smaller scale, non-linear, virialised structures (including baryonic structures) requires a more detailed scenario.

2.1.3 A dynamical scenario

Such a scenario requires to analyze the dynamical evolution of structures over cosmic time and is therefore developed in the eulerian framework. It was first suggested qualitatively by Codis *et al.* (2012) for dark haloes and further developed in the scope of recent works such as Laigle *et al.* (2015), then extended to galaxies and tested in further details in Dubois *et al.* (2014) and Welker *et al.* (2014).

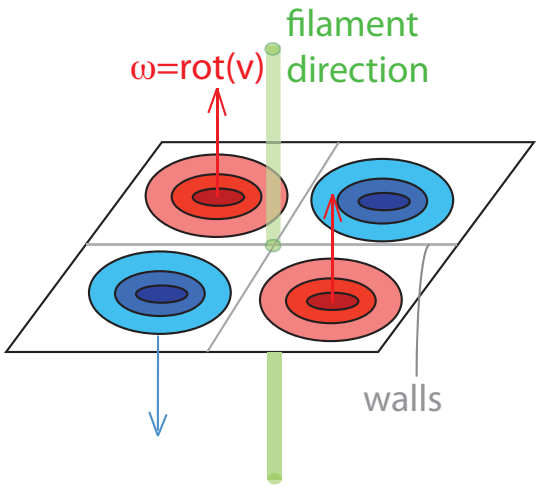

Figure 2.1: Sketch of the quadrupolar vorticity distribution in the vicinity of a filament.

2.1.4 Mergers versus smooth accretion

It relies on the interplay between two competing processes for the mass acquisition of virialised structures: mergers and smooth accretion.

Smooth accretion: I define smooth accretion as the diffuse accretion of material - dark matter, gas and possibly small amounts of stellar material- onto a halo (or galaxy). Unlike mergers, it is a continuous steady process that progressively builds up the structure In the vicinity of filament, smooth accretion follows a specific geometrical pattern.

Indeed simulations reveal that, after gravitational collapse has started, the coherent large scale spin quadrants analyzed in Codis *et al.* (2015) translate into near-filament regions where newly formed vorticity is concentrated and aligned with the initial spin, following a similar quadrupolar geometry (Laigle *et al.* (2015)) as represented on Fig .2.1. Small haloes embedded in these vorticity quadrants and accreting material from them therefore build up their angular momentum parallel to their neighboring filament from vorticity transfer (see also Pichon *et al.* (2011)). This coherent acquisition is efficient up to the point where vorticity-fed haloes grow out of their quadrant over the neighboring quadrants of opposite sign, therefore canceling out the overall vorticity transfer. This defines a transition mass $M_{\rm trans}$ around 5×10^{12} $\mathrm{M}_\odot$ for haloes.

Mergers: Above this limit, mergers likely dominate the spin acquisition. When two extended virialised structures (haloes or galaxies) come close to each other and bind in the gravitational potential of one another, they experience strong tidal disturbances which profoundly redistribute

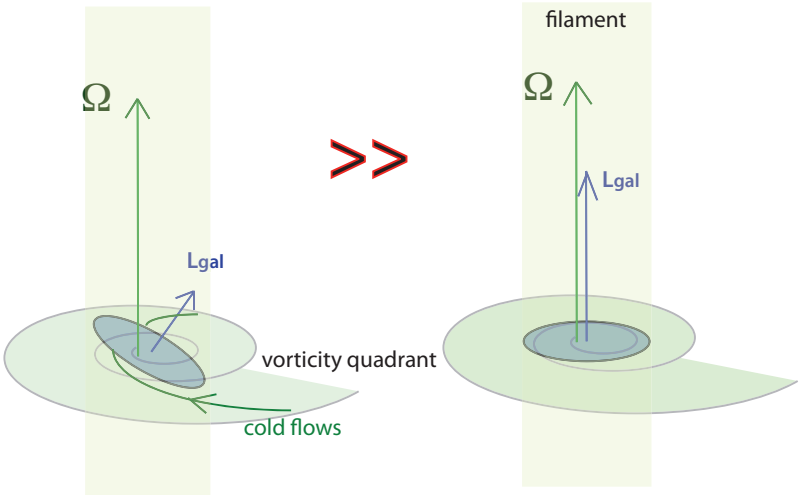

Figure 2.2: Sketch of the angular momentum build-up from vorticity transfer for low-mass haloes (and possibly galaxies: through "cold flows").

the orbits of their particles (dark matter or stars) and lead to rapid energy transfers to the dispersive component. Through this process of dynamical friction and violent relaxation (See Chapters 3 and 4 for further details), the two structures end up merging with one another therefore forming a new, more massive structure of increased dispersion. Specific features vary with the mass ratio between the two structures but such mergers drive the formation (collapse) of massive haloes and galaxies in the universe (see for instance Lotz *et al.* , 2010b,a).

The orientation of the spin of massive haloes is therefore driven by mergers. A simple explanation of the observed trend is therefore that pairs of merging haloes convert a significant amount of their orbital momentum into intrinsic momentum of the remnant, this component being dominant in its total intrinsic momentum. Moreover, tidal torque theory and standard structure formation theory naturally predict that mergers occur along the filament between pairs of drifting haloes. Indeed, since haloes flow along filaments as large scale structures collapse, and since mergers consequently correspond to the late (hence closer to the cosmic nodes) collapse of large lagrangian patches with a predicted spin orthogonal to the filament, their orbital momentum is also most likely orthogonal to the filament, which naturally explains the orthogonal spin orientation of their massive remnants.

2.1.5 From haloes to galaxies

Though alignment trends found in simulations are compelling for dark haloes they allow for no direct observation. A natural question arising from such theories is therefore whether, how and to

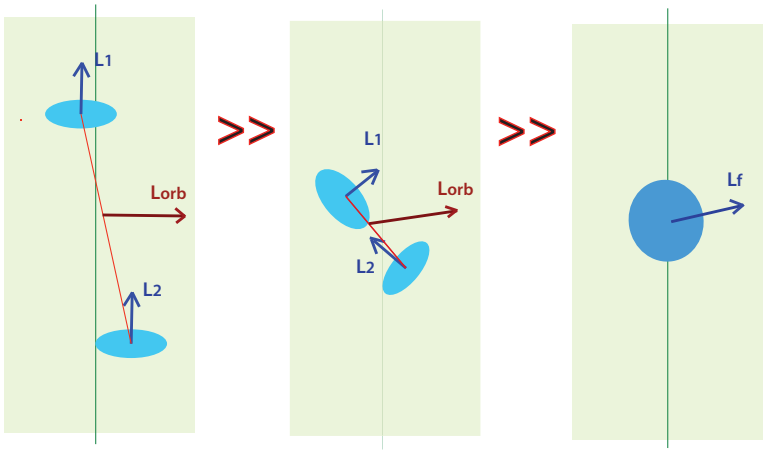

Figure 2.3: Sketch of the angular momentum build-up from orbital momentum transfer for high-mass haloes (and possibly galaxies).

what extent such trends cascade down to galactic scales and apply to baryonic matter.

Such questions are *a priori* difficult to answer since galaxies form on much smaller, highly non linear scales and grow from gas accretion, which, unlike dark matter, can shock and consecutively dissipate very effectively energy and redistribute angular momentum on dynamical (as opposed to secular) scales, even in the process of a smooth steady accretion. Most of the orbital momentum available from the infalling gas might thus be lost at the galactic virial scale when the radial density gradient rises to the point where the inflowing gas undergoes a interface shock (the "virial shock").

A major concern is therefore the fate of the gas flowing from the vorticity quadrant into an embedded galaxy, especially whether or not it lingers as coherent orbital momentum rich inflows down to the core of such a galaxy. Over the past decade, the behavior of these gas inflows has been studied in numerous zoom-in simulations including various physical effects. Unlike previously suggested, it was found that, at high redshift, multi-phase turbulence on the galactic virial scale allows for the partial conservation of coherent inflows in the form of cold streams (labeled as "cold flows") that survive the virial shock. (Birnboim & Dekel (2003); Dekel & Birnboim (2006); Brooks *et al.* (2009b)).

Danovich *et al.* (2012) studied the feeding of massive galaxies at high redshift through cosmic streams using the Horizon-MareNostrum simulation by Devriendt (2011). They found that galaxies are fed by one dominant stream (with a tendency to be fed by three major streams), streams tend to be co-planar (in the stream plane), and that there is a weak correlation between spin of the galaxy and spin of the stream plane at the virial radius, which suggests an angular momentum exchange at the interface between streams and galaxies (see also Tillson *et al.* , 2012;

Danovich *et al.* , 2015).

A key process that further drives the preservation or mixing of such streams is the level of active feedback from the galaxy: while intense feedback from central black holes (AGN feedback) seems to blow them away (Dubois *et al.* , 2012b; Nelson *et al.* , 2015), supernovae feedback lowers the amount of AGN feedback needed to form realistic synthetic galaxies and only triggers a partial fragmentation of cold flows that mostly preserves their orbital momentum (Powell *et al.* , 2011).

Recent observations - through specific emission lines in the line of sight of background quasars- of cold flow candidates flowing onto galaxies (Crighton *et al.* , 2013; Pisano, 2014) further strengthen the idea that the vorticity transfer identified for low-mass haloes might also be efficient for low-mass galaxies to the point of statistical observability.

Similarly, galaxy mergers might lead to a preferential orientation of the spin of massive galaxies perpendicular to their nearby filament if however they do not lose most of their orbital momentum to the host halo of the main progenitor (through dynamical friction, a process more thoroughly described in Chapter 2).

The main goals of the work presented here is to evaluate to what extent one can recover such alignment trends for fully developed galaxies the state-of-the-art cosmological hydrodynamical simulation Horizon-AGN and to quantify more carefully the proposed scenario in which galaxies form in the vorticity-rich neighborhood of filaments, and migrate towards the nodes of the cosmic web as they convert their orbital angular momentum into spin.

2.2 Tracing galactic spin swings in the cosmic web

2.2.1 Numerical Methods

2.2.1.1 Identifying and segmenting galaxies

Galaxies are identified with the already presented AdaptaHOP finder (Aubert *et al.* , 2004, updated to its recent version by Tweed *et al.* , 2009 for building merger trees) which directly operates on the distribution of star particles. Let us recall that a total of 20 neighbours are used to compute the local density of each particle, a local threshold of $\rho_t = 178$ times the average total matter density is applied to select relevant densities, and the force softening (minimum size below which substructures are considered irrelevant) is ~ 2 kpc. Only galactic structures identified with more than 50 particles are considered. It allows for a clear separation of galaxies including those in the process of merging. Catalogues of around $\sim 150\,000$ galaxies are produced for each redshift analysed in this chapter from $z = 3$ to $z = 1.2$.

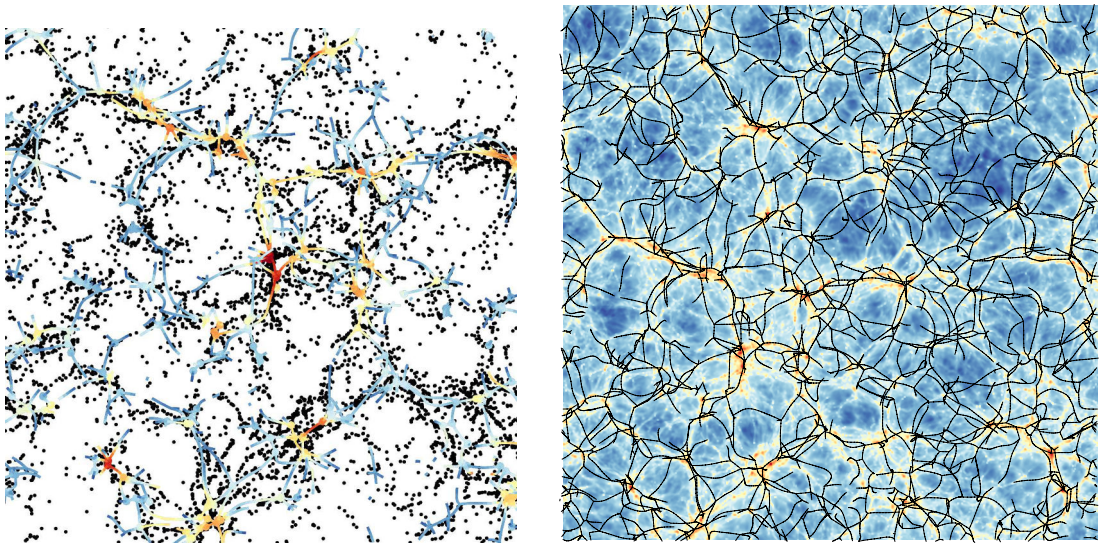

Figure 2.4: Top: projection along the z-axis of the HORIZON-AGN gas skeleton (colour coded by logarithmic density as red-yellow-blue-white from high density to low density) at redshift $z = 1.83$ of a slice of $25\,h^{-1}$ Mpc on the side and $10\,h^{-1}$ Mpc thickness. Galaxies are superimposed as black dots. The clustering of the galaxies follows the skeleton quite closely. *Bottom:* larger view of the skeleton on top of the projected gas density. This work quantifies orientation of the galaxies relative to the local anisotropy set by the skeleton.

2.2.1.2 Defining a relevant network of filaments with Skeleton

In order to quantify the orientation of galaxies relative to the cosmic web, I use the geometric three-dimensional ridge extractor described in Chapter 1 (the so-called "skeleton"), which is well suited to identify filaments. A gas density cube of 512^3 pixels is drawn from the simulation (whole box) and gaussian-smoothed with a length of $3\,h^{-1}$ Mpc comoving chosen so as to trace large-scale filamentary features relevant to galaxy nesting and consecutive anisotropic infall and tidal torquing. This length can be varied around this value with a Mpc amplitude with little effect on the observed trends. It was checked that our results were not sensitive to how many such segments were considered to define the local direction of the skeleton.

The two different implementations of the skeleton, based on "watershed" and "persistence" were implemented, without significant difference for the purpose of this investigation.

Fig. 2.4 shows a slice of $25\,h^{-1}$ Mpc of the skeleton colour coded by logarithmic density, along with galaxies contained within that slice. The clustering of the galaxies follows quite closely the skeleton of the gas, i.e. the cosmic filaments. Note that, on large-scales, the skeleton built from the gas is equivalent to that built from the dark matter particles as the gas and dark matter trace each other closely. To study the orientation of the spin of these galaxies relative to the

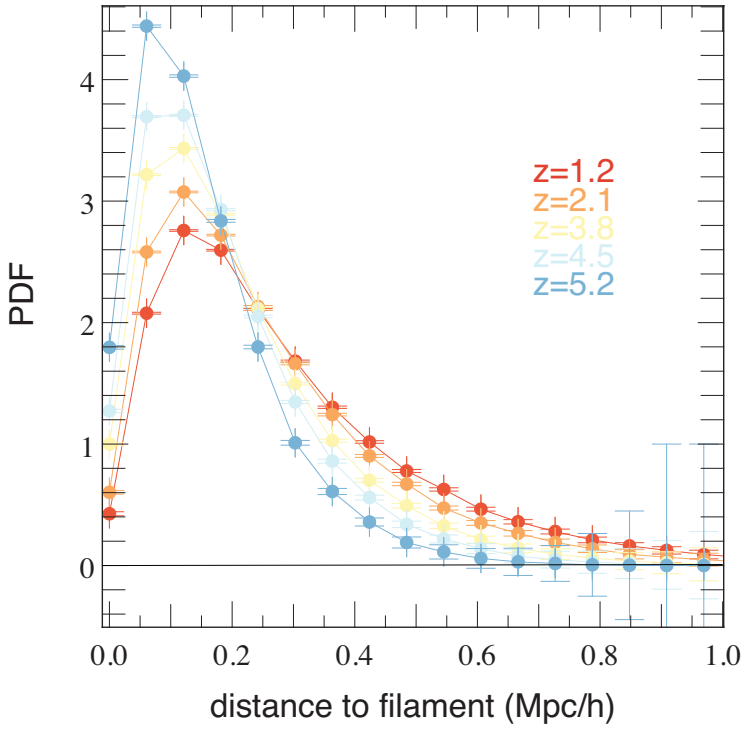

Figure 2.5: PDF of the distance to the nearest identified filament for galaxies in Horizon-AGN at 5 successive redshifts between $z = 5.2$ and $z = 1.2$.

direction of the nearest skeleton segment, an octree is built from the position of the mid-segment of the skeleton, which speeds up the association of the galaxy position to its nearest skeleton segment.The orientation of the relevant segment of the skeleton is then used to define the relative angle between the filament and the spin of the galaxy. The segments are also tagged with their curvilinear distance to the closest node (where different filaments merge), which allows for a more careful study of the evolution of this (mis)alignment with the distance to nearest node of the cosmic web.

Note that all galaxies/haloes are associated with one single filament. The very definition of such filament (ridge line) relies on a smoothing scale for the density field. The smoothing scale here is set so as to trace reasonably well the galaxy/halo distribution. As a consequence most galaxies are "close" to the ridge line they are assigned to, and only a few galaxies happen to be in voids. Fig. 2.5 confirms that most galaxies are within less than 0.5 Mpc away for their filament segment.

It was also checked that large-scale filaments, defined from the skeleton, do not show any alignment with the grid of the simulation.

2.2.1.3 Kinematics

The AM –or spin– of a galaxy (halo) is defined as the total angular momentum of the star (DM) particles it contains and is measured with respect to the densest of these star (DM) particles (centre of the structure):

$$\mathbf{L}_{\rm s} = \Sigma_i m_i(\mathbf{r_i} - \mathbf{r}_{\rm cm}) \times (\mathbf{v_i} - \mathbf{v}_{\rm cm})\,, \tag{2.9}$$

with $\mathbf{r_i}$, m_i and $\mathbf{v_i}$ the position, mass and velocity of particle i, and center of mass *cm*. Similarly, let us define the specific angular momentum (sAM) of the structure as $\mathbf{l}_{\rm s} = \mathbf{L}_{\rm s}/M_{\rm s}$, with $M_{\rm s}$ the total mass of the structure.

2.2.1.4 Dealing with grid-locking effects

A major concern when analyzing the orientation of spins in an AMR simulation is the amplitude of grid locking. Indeed, as gas fluxes are computed on a cartesian grid, this can favor orientations of *galaxy* spins along cartesian axes of the box, at least for a certain range of galaxy mass. The tendency to align with the grid was therefore tested prior to any further analysis in Horizon-AGN . I found that while the spin of the less massive galaxies are clearly aligned with the grid, no obvious alignment is seen for the high-mass galaxies. Lighter galaxies are preferentially locked with the grid because they are composed of very few grid elements: the gaseous disc of a galaxy with $\sim 10^9\,{\rm M}_\odot$, embedded in a halo of mass $\sim 10^{11}\,{\rm M}_\odot$, tends to be aligned with one of the cartesian axes due to the anisotropic numerical errors. However, for more massive galaxies, the grid-locking is absent due to a larger number of resolution elements to describe those objects. This result is consistent with that of Hahn *et al.* (2010) and Danovich *et al.* (2012).

Since low-mass galaxies (within halo of mass $< 5 \times 10^{11}\,{\rm M}_\odot$) show some preferential alignment along the x, y and z axis of the simulation box, the effect of grid-locked galaxies on the galaxy-filament different alignment signals was evaluated removing galaxies whose spin is comprised within less than 10 degrees of any of the cartesian planes of the box. I systematically found that the alignment signal without grid-locked galaxies is comparable to the case where all galaxies are accounted for.

This behaviour was expected as it was also checked that filaments do not suffer from grid-locking (coherently with the fact that such large scale structures are mostly determined by the dark matter collapse, dark matter particles evolving independently from the grid). The effect of grid-locking on low-mass galaxies is limited to some extra noise to the alignment measurement. Thus, the signal obtained below for alignment of low-mass galaxies, while probably under-estimated, is a robust trend. The same is true for high-mass galaxies that do not suffer from spurious grid-locking.

2.2.2 Evolution tracers

This work aims not only to check if one can recover the alignment transition documented for haloes but also to understand how one can trace such swings in observations and how it relates to the dynamical evolution of galaxies. In Dubois *et al.* (2014), I then computed multiple synthetic properties for all the simulated galaxies identified such as: rest-frame colors, age, specific star formation rates or various morphology tracers. In the following section, I present two such tracers that relate well to the dynamical evolution of galaxies (and therefore correlate with their stellar mass).

2.2.2.1 Colors

Rest-frame colors are efficient tracers of the age of galaxies in observations. Indeed, as the emission spectrum of stars in a galaxy is directly dependent on their age, colors are a direct tracer of the star formation activity - which varies over cosmic time- in a galaxy and of the aging of its stars. Expectedly, strong colour and metallicity (curvilinear) gradients were found by Gay *et al.* (2010) towards and along the filaments and nodes of the cosmic web in the Horizon-MareNostrum simulation (Devriendt *et al.* , 2010b), which however did not display much morphological diversity.

In this study, it was therefore of great interest to compute synthetic absolute AB magnitudes and rest-frame colors for all the identified galaxies. To perform such a spectral synthesis, one needs to resort to models, more specifically stellar population models.

A single stellar population consists of all stars in a galaxy born at the same time (in an assumed "starburst") and having the same initial element composition (metallicity). Single stellar population models use them as building blocks for any more complex stellar population. However, in the same SSP, stars of different masses follow different evolutionary tracks. Such models therefore derive isochrones - lines that connect the points belonging to the various theoretical evolutionary tracks at the same age- from stellar evolution theory. Stellar spectra for stars at any evolutionary stage (i.e. any set of parameters including age, metallicity and mass) are compiled in libraries from both theoretical predictions and observations. Providing that the initial mass function(IMF) - defined as the mass distribution for a population of newly born stars (i.e. in a starburst)- is known, one can therefore calculate the full spectral energy distribution of an SSP of age t by integrating the stellar spectra over the isochrone, and the full energy spectra of a galaxy by integrating over all the SSPs.

I did so following the methodology below:

- I use single stellar population models from Bruzual & Charlot (2003) and assume a Salpeter Initial Mass Function (IMF). In Horizon-AGN , due to the coarse discretization of time and sub-galactic scales, each star particle corresponds to an SSP, the age, total mass and metallicity of which is known with precision. I therefore infer the corresponding integrated SSP spectrum of each star particle.

- Since each star particle contributes to a flux per frequency that depends on its mass, age, and metallicity,the sum of the contribution from all stars is then passed through the u, g, r, and i filters from the SDSS. Fluxes are expressed as rest-frame quantities (i.e. that do not take into account the red-shifting of spectra). I also neglect the contribution to the reddening of spectra from internal (interstellar medium) or external (intergalactic medium) dust extinction.

- The rest frame colors $g-r$, $u-r$ and $r-i$ are then computed from the calculated fluxes F_r, F_i and F_g as for instance $g-r=-2.5\ \log(F_g/F_r)$

Once the flux in each waveband is obtained for a star particle, I also build two-dimensional projected maps of 256x256 pixels from single galaxies (satellites are excised with the galaxy finder), and I can sum up the total contribution of their stars to the total luminosity.

2.2.2.2 Morphology

Like in observations, galaxies in Horizon-AGN display a wide variety of morphologies. However, although this is an intuitive visual concept, the morphology of a galaxy is hard to define quantitatively. A rather efficient way to do that in observations consists in quantifying the amount of rotational support and dispersion support of the stellar material in a galaxy, and then sort the galactic morphologies with the respect to the ratio between those two components. Let $V_{\rm rot}$ be an estimation of the average rotation component (around the spin axis) of star velocities and σ the dispersion component of such a collection of velocities, then $V_{\rm rot}/\sigma$ allows for a reasonable estimation of the galactic morphology.

In simulations, such an estimation can be performed on the 3D stellar distribution or on the 2D projected quantities so as to mimic observations. I first compute it in 3D with the following definition:

- Let $\mathbf{e_z}$ be the direction of the spin of a given galaxy. In the galactic rest-frame with adapted spherical coordinates $(\mathbf{e_r}, \mathbf{e}_\theta, \mathbf{e}_\phi)$ where $\mathbf{e_z}$ corresponds to the $\theta = 0$, $V_{\rm rot}$ is the mass averaged

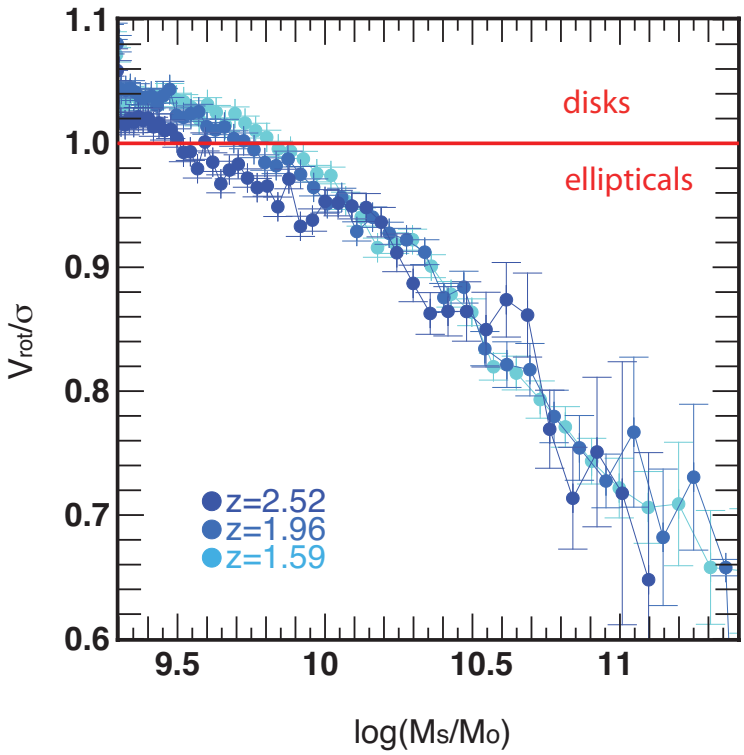

Figure 2.6: Evolution of $V_{\rm rot}/\sigma$ with respect to stellar mass for three different redshifts. low-mass galaxies are rotation supported while their high-mass counterparts are dispersion supported.

ϕ-projected component of the star velocities:

$$V_{\rm rot} = \sqrt{\frac{\sum_i \, m_i \, (\mathbf{v_i}.\mathbf{e}_\phi)^2}{\sum_i m_i}}\,, \tag{2.10}$$

- σ corresponds to the non-rotational component:

$$\sigma = \sqrt{\frac{\sum_i \, m_i \, (\mathbf{v_i} - (\mathbf{v_i}.\mathbf{e}_\phi))^2}{\sum_i m_i}}\,. \tag{2.11}$$

With these definitions, one can therefore distinguish two main morphologic categories: dispersion supported galaxies with $V_{\rm rot}/\sigma < 1$ (i.e. ellipticals, spheroids) and rotation supported galaxies with $V_{\rm rot}/\sigma > 1$ (i.e. disky structures). Fig. 2.6 displays the average evolution of this parameter with stellar mass for $1.5 < z < 2.5$. A similar estimation was also computed on projected quantities using 256x256 projected maps of galaxies, leading to similar results. Further details can be found in Dubois *et al.* (2014).

One can see that this morphology tracer is fairly well correlated to the galactic stellar mass, low-mass galaxies being rotation supported while their high-mass counterparts are dispersion supported. This correlation with mass holds for other tracers: colors, age, specific star formation rates were

also found to be correlated to the mass of the galaxy. These correlations allow to sort galaxies into two distinct groups related to the stage they have reached in their dynamical build-up: young, star forming, blue rotation supported structures and older, redder, rotation supported structures where star formation is somewhat quenched. The details of these results can be found in Dubois *et al.* (2014).

Note that this conclusion is obtained for galaxies at rather high redshifts ($1 < z < 5$), prior to the rebuilding of massive disks from orbital momentum rich wet mergers (such as grand design spirals) observed at z=0. It is therefore predictable that young galaxies newly born at the intersection of cold gas streams are disky structures since only the rotation (orbital) component of the gas velocity can survive multi-stream shocks, leading the gas to consecutively settle on a plane - determined by the conservation of angular momentum of the in falling material- and form stars.

It is also noticeable that, for galaxies in Horizon-AGN , $V_{\rm rot}/\sigma$ never reaches values much higher than the unity, when one would expect a thin disk to reach at least several unities. The reason is two-fold. First it is a resolution problem: the gas is computed one a grid of 1 kpc maximum initial resolution, and only in densest regions, which therefore drastically limits the settling of the gas in a disk forming a young galaxy. Moreover, AGN feedback also limits the flattening of more massive galaxies and the build-up of massive disks at lower redshifts. Horizon-noAGN, a similar simulation where AGN activity is turned off was found to lead to the build-up of many more massive thin disks at $z < 1$.

2.2.3 Alignments in Horizon-AGN

2.2.3.1 Recovering the mass segregation

Fig. 2.7, *Left panel* shows the PDF of $\mu = \cos\theta$ with θ the angle between the spin of the galaxy and the direction of its nearest filament for all galaxies with a stellar mass $M > 10^{8.5}{\rm M}_\odot$ at $z = 1.83$.

The choice of the cosine statistics is natural since the analysis is performed on the three-dimensional (3D) kinematics. This arises from the fact that I am willing to compare angular distributions (say $P(\theta)$) around a given axis to the 3D distribution $P_{\rm u}(\theta)$ one would expect in the absence of any angular bias: if angles were uniformly distributed on the sphere. Given a radius r_0, the standard definitions of the polar and azimuth angles θ and ϕ in an adapted spherical coordinate system, and $dS(\theta,\phi)$ the corresponding elementary surface, the probability density function $\rho_{\rm u}$ for this latter writes:

$$dP_{\rm u}(\theta) = \rho_{\rm u}(\theta)d\theta = \int_{\phi=0}^{\phi=2\pi} \frac{dS(\theta,\phi)}{4\pi r_0^2} = \int_{\phi=0}^{\phi=2\pi} \frac{r_0^2 \sin\theta d\theta d\phi}{4\pi r_0^2} = \frac{1}{2}\sin\theta d\theta = \frac{-1}{2} d(\cos\theta)\,. \quad (2.12)$$

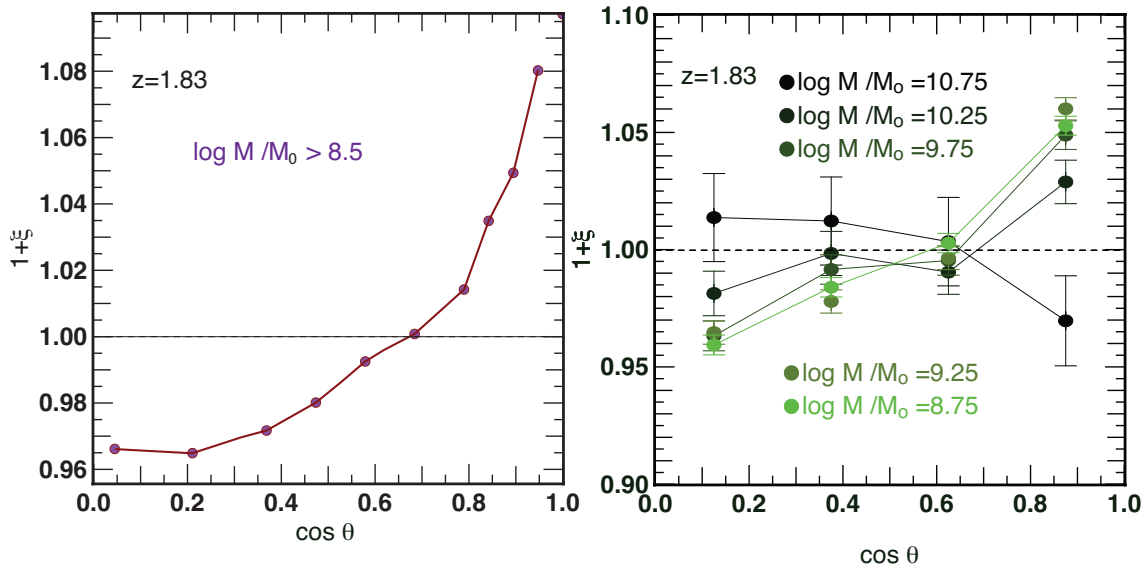

Figure 2.7: *Left panel* PDF of $\mu = \cos\theta$ with θ the angle between the spin of the galaxy and the direction of its nearest filament for all galaxies with a stellar mass $M > 10^{8.5}\mathrm{M}_\odot$ at $z = 1.83$. The uniform PDF is represented by a dashed line. *Right panel* PDF of $\mu = \cos\theta$ for different mass bins. Low mass galaxies tend to have a spin aligned to the nearest filament while more massive ones tend to display a spin perpendicular to the nearest filament.

Thus one gets $\rho_\mathrm{u}(\theta) \propto \sin\theta$ but $\rho_\mathrm{u}(\cos\theta) \propto cste$. The uniform probability density function is flat with respect to $\cos\theta$, which allows for an easy direct comparison.

One can notice that I recover on average the alignment trend expected for low-mass galaxies: the distribution peaks for values close to $\mu = 1$ revealing an excess alignment of the spin of galaxies with their nearest filament. The maximum excess probability is 8% and is observed in 20° cone around the nearby filament. On the contrary, the orthogonal orientation is disfavored. As a conclusion, galaxies seemingly tend to align their spin with the nearest filament.

However, the whole sample is largely dominated by low masses, which implies that the observed trend actually corresponds to the orientation of low-mass galaxies. To probe the evolution of this trend with stellar mass, Fig. 2.7, *Right panel* displays the PDF of $\mu = \cos\theta$ for different mass bins. It reveals a transition between two different trends: while low-mass galaxies have indeed a spin aligned with the nearest filament, this trend decreases as stellar mass increases bending closer to the uniform PDF down to the point where it flips across the uniform PDF. Hence most massive galaxies are more likely to have a spin orthogonal to the filament, although at this level of significance it is not entirely clear whether this latter orientation is strictly orthogonal or more random. The transition mass between these two trends is confidently bracketed between $M_\mathrm{trans,min} = 10^{0.25}\mathrm{M}_\odot$ and $M_\mathrm{trans,max} = 10^{0.75}\mathrm{M}_\odot$. This is consistent with the transition mass found for dark haloes in

Codis *et al.* (2012) accounting for stellar to dark matter mass ratio and redshift difference. As a conclusion, although the effect is fainter for galaxies, I recover the mass segregated alignment trend already described for dark haloes. However, mass is not a quantity easily measurable in observations, but rather derived from more specific measurements such as the observed luminosity, or related to more specific galactic properties such as morphology and color. It is therefore essential to test whether one can recover an orientation segregation similar to that found for the stellar mass for such galactic properties.

2.2.3.2 Relating tracers to the dynamical scenario

Fig. 2.8 displays the PDF of $\mu = \cos\theta$ for all galaxies with a stellar mass $M > 10^9 \mathrm{M}_\odot$ at $z = 1.83$, for different $V_{\rm rot}/\sigma$ bins. I select only galaxies with a stellar mass $M > 10^9 \mathrm{M}_\odot$ so as to ensure that I am considering structures with at least a few hundreds particles, which limits the shape noise associated with poor resolution. Bins are then chosen to compromise between the strict comparison to unity and the scarcity of the highest value sample. As expected, galaxies with the highest values of $V_{\rm rot}/\sigma$ (which corresponds to rotation supported disks) display a clear tendency to align their spin with the nearest filament, the amplitude being directly comparable to the same trend for low-mass galaxies. On the contrary, galaxies with $V_{\rm rot}/\sigma < 1.0$ (dispersion supported) do not follow such a trend and there is even hints for spin flips orthogonal to the filament.

In Dubois *et al.* (2014), projected quantities $V_{\rm rot}^{\rm max}\sigma^{\rm max}$ are also computed from maximum values estimated on a 256x256 projected map of each galaxy, and used to bin the PDF of $\mu = \cos\theta$. This shows a more clear-cut spin flip between disks and ellipsoids.

Now considering rest-frame colors on Fig. 2.9 which shows the PDF of $\mu = \cos\theta$ for galaxies with a stellar mass $M > 10^{8.5} \mathrm{M}_\odot$, at $z = 1.83$, for different $g-r$ and $r-i$ color bins, I can further confirm the two trends already described. Red galaxies (with $g - r > 0.34$ or $r - i > 0.17$) tend have a spin flipped orthogonal to the filament while their bluer counterparts most likely have a spin aligned to it.

The typical amplitude of the maximum excess probabilities is around $\xi = 5\%$ in order, once again much smaller than values found for dark haloes ($\xi \propto 20\%$), which is expected since galaxies are more evolved and subject to much more complex baryonic physics. However, Our results remain statistically significant and confirm that these spin orientations inherited from the large scale structures pervade down to galactic scales and may be reasonably detectable in observations.

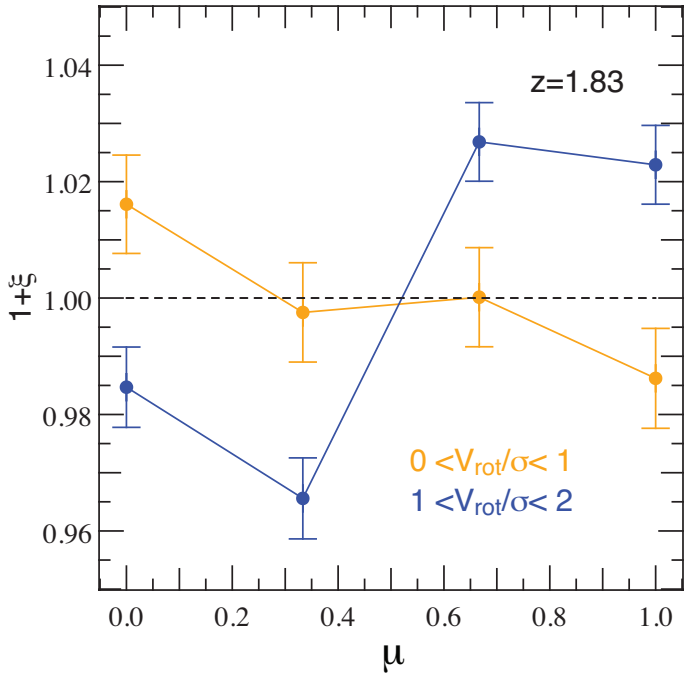

Figure 2.8: PDF of $\mu = \cos\theta$ with θ the angle between the spin of the galaxy and the direction of its nearest filament for all galaxies with a stellar mass $M > 10^9 \mathrm{M}_\odot$ at $z = 1.83$, for different $V_{\rm rot}/\sigma$ bins.

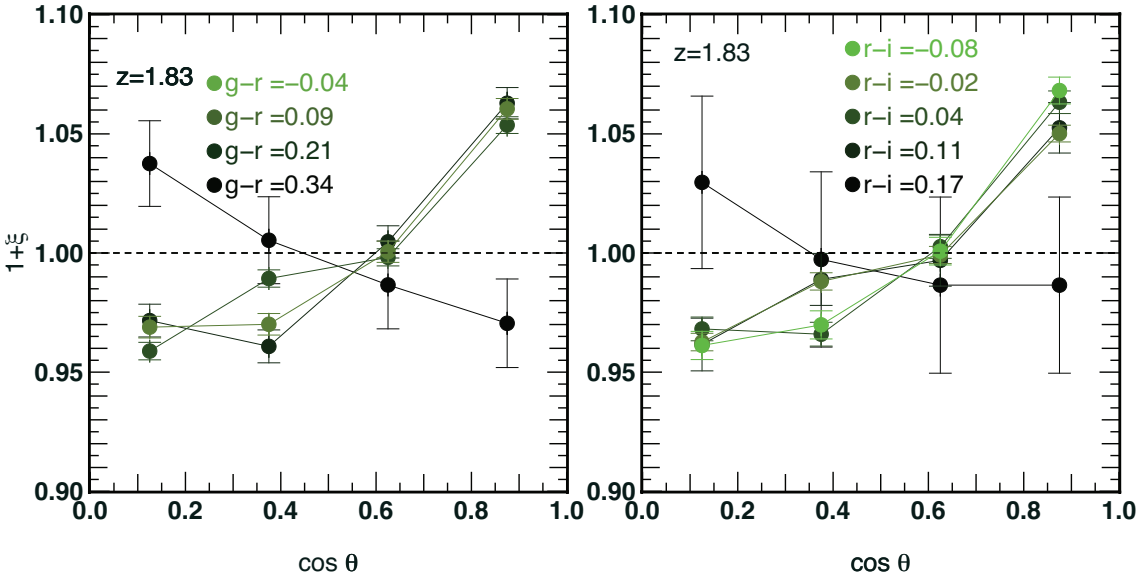

Figure 2.9: PDF of $\mu = \cos\theta$ with θ the angle between the spin of the galaxy and the direction of its nearest filament for all galaxies with a stellar mass $M > 10^9 \mathrm{M}_\odot$ at $z = 1.83$, for different $g - r$ and $r - i$ color bins.

2.2.4 Comparison to observations

It is of interest to notice that recent observations in the SDSS (Sloan Digital Sky Survey: Aihara *et al.* (2011)) by Tempel & Libeskind (2013) now support the segregated orientations I described in this section. Although those early investigations must be taken with precaution as the morphological classification method they used is different from ours, and as their filament detection relies on a specific method of local statistical inference, their results suggest that spiral galaxies align their spin to filaments while ellipticals bend it perpendicular to the same filaments.

These encouraging results should be followed by new investigations in deep field surveys such as VIPERS (Guzzo *et al.* , 2014), which in addition will apply the same filament detection technic -robust even when applied to scarce, low completeness data- than the one presented in this work.

More tracers -all correlated to stellar mass- are found to follow the exact same trends in Dubois *et al.* (2014) and pave the way towards new possible observational analysis. These results boil down to the following conclusions: young blue rotation supported low-mass galaxies are more likely to display a spin aligned with the filament they are embedded in while older redder dispersion supported massive galaxies tend to orient their spin orthogonal to the filament. The evolution spin-filament trend for the whole mass range (i.e. dominated by small masses as in Fig. 2.7, *Left panel*) is also found to decrease with cosmic time and with proximity to cosmic nodes, which is consistent with the aging and building up of more and more massive galaxies and with the idea that galaxies merge while drifting along filaments (which destroys alignment), and with the strong colour (curvilinear) gradients found by Gay *et al.* (2010).

Thus, It seems that the late collapse of more and more massive galaxies follows remarkably well the predictions of the Tidal Torque Theory. Is this spin-oriented collapse efficiently mediated by smooth accretion in vorticity rich regions then galaxy mergers? This is the question I investigate in Section .2.3.

2.3 How mergers drive spin swings in the cosmic web

2.3.1 Tracking mergers in Horizon-AGN

I also identify galaxies and haloes with the AdaptaHOP finder (Aubert *et al.* , 2004), which this time operates on the distribution of star particles for galaxies and DM particles for haloes respectively with the same parameters than previously. Unless specified otherwise, only structures with a minimum of $N_{\rm min} = 100$ particles are considered, which typically selects objects with masses larger than $2 \times 10^8\,{\rm M}_\odot$ for galaxies and $8 \times 10^9\,{\rm M}_\odot$ for DM haloes. Catalogues containing up to

$\sim$ 180 000 galaxies and more than $\sim$ 300 000 DM haloes are produced for each redshift output analysed for $1.2 < z < 3.8$. It is important to note that, although sub-structures may remain, they are sub-dominant in our sample.

The galaxy (halo) catalogues are then used as an input to build merger trees with TreeMaker (Tweed *et al.* , 2009). Any galaxy (halo) at redshift z_n is connected to its progenitors at redshift z_{n-1} and its child at redshift z_{n+1}. I build merger trees for 18 outputs from $z = 1.2$ to $z = 3.8$ equally spaced in redshift. On average, the redshift difference between outputs corresponds to a time difference of 200 Myr (range between 100 and 300 Myr). I reconstruct the merger history of each galaxy (halo) starting from the lowest redshift z and identifying the most massive progenitor at each time step as *the galaxy* or *main progenitor*, and the other progenitors as *satellites*. Moreover, I double check that the mass of any child contains at least half the mass of its main progenitor to prevent misidentifications. Note that the definition of mergers (vs smooth accretion) depends on the threshold used to identify objects as any object composed of fewer particles is discarded and considered as smooth accretion. Finally, in order to get rid of objects too contaminated by grid-locking effects (grid/spin alignment trend for the smallest structures, see Dubois *et al.* , 2014), I exclude galaxies with $M_{\rm s} < 10^9\,{\rm M}_\odot$ and haloes with $M_{\rm h} < 10^{11}\,{\rm M}_\odot$ from our *main progenitor* sample for spin analysis. Satellites, however, can be smaller structures, which is why I adopt a low object identification mass threshold, and select more massive *main progenitors* afterwards. This two-step procedure allows for a clear separation of main progenitors and satellites (which means that very minor mergers can be detected even for small galaxies in the sample) and avoids significant signal loss.

Let us define the mass fraction of an object that is accreted via mergers:

$$\delta m = \Delta m_{\rm mer}(z_n)/M(z_n)\,. \tag{2.13}$$

In this expression, $M(z_n)$ is the total stellar (DM) mass of a galaxy (halo) at redshift z_n and $\Delta m_{\rm mer}(z_n)$ is the stellar (DM) mass accreted by this galaxy (halo) through mergers between redshifts z_{n-1} and z_n. In this chapter I will mostly focus on three subclasses of mergers characterized by different mass ratios:

- very minor mergers with $1\% < \delta m < 5\%$,
- minor mergers with $5\% < \delta m < 10\%$
- and major mergers $\delta m > 10\%$.

It is important to notice that these definitions might not follow exactly corresponding definitions in observational studies which often limit major mergers to $\delta m > 20\%$ based upon observability.

However, all measurements presented below were also carried out for mergers with $\delta m > 20\%$ and even $\delta m > 30\%$, which did not show significant variations from the $10\% < \delta m < 20\%$ sample. For better visibility I therefore decided to restrict our higher cut to $\delta m > 10\%$ but it should be noted that results still hold for higher mass ratio cuts. Similarly I decided to present results for so-called "very minor mergers" with very low mass ratios -$1\% < \delta m < 5\%$- which might as well be tagged as "clumpy accretion" since it appears that the behavior of the spin for galaxies subjected to such events is closer to mergers than smooth stellar accretion conjoint to gas inflows.

When specified, I also use a higher detection threshold: $N_{\rm min} = 1000$. In such a situation the threshold is the same for galaxies and progenitors (which is around $M_{\rm s} = 10^9 {\rm M}_\odot$ for galaxies and $M_{\rm h} = 10^{11} {\rm M}_\odot$ for dark haloes, given that DM particles and stellar particles have different masses). It tends to discard small mergers for small galaxies and multiple simultaneous very small mergers in general (corresponding to clumpy accretion). Therefore, the focus is put on mergers (small to major) for massive galaxies ($M_{\rm s} > 10^{10} {\rm M}_\odot$) but only upper intermediate to major mergers for the smallest galaxies in the sample. This allows us to focus on well-resolved mergers, most likely one-to-one events along the cosmic web, discarding small mergers occurring between the smaller galaxies in formation caught in a given vorticity quadrant.

Note that, in all figures where haloes and galaxies are compared, the ratio of main progenitor minimal mass to satellite minimal mass is the same, so as to permit a fair comparison between both categories of objects.

2.3.2 Mergers, stellar mass and spin in Horizon-AGN: close-up case studies

Having defined the merger mass ratio, one can also define in a similar fashion the galactic merger fraction $f_{\rm merge}$ as the integrated stellar mass fraction acquired through mergers between $z_0 = 3.8$ and z_n:

$$f_{\rm merge} = \frac{\sum_{z_0}^{z_n} \Delta m_{\rm mer}(z_i)}{M(z_n)}\,. \tag{2.14}$$

This allows us to measure for each galaxy the stellar mass acquired through the different branches of the tree (satellites) quoted as a merger, the main progenitor being excluded from the calculation. The evolution of $f_{\rm merge}$ with stellar mass is presented on Fig. 2.10 at redshift $z = 1.83$. Fig. 2.10 shows that massive galaxies acquire a non-negligible fraction of their mass by mergers. (at least 1000 particles of star particles, up to 20 per cent at $z = 1.83$), while low-mass galaxies grow their stellar mass content almost exclusively by *in situ* star formation (e.g. De Lucia & Blaizot, 2007; Oser *et al.* , 2010). This definitely points towards a major role of mergers in the triggering of spin swings orthogonal to the filament, and justifies further analysis.

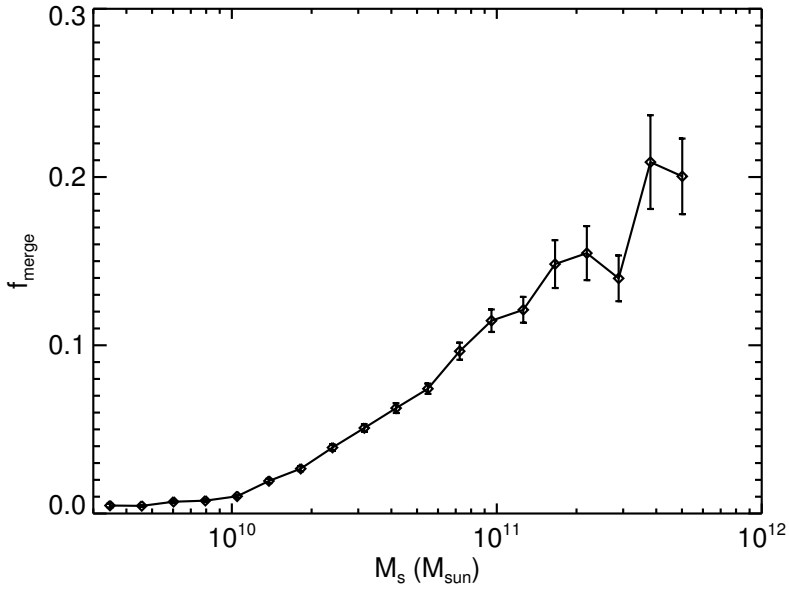

Figure 2.10: Average fraction of stellar mass gained through mergers as a function of the galaxy stellar mass at $z = 1.83$. The error bars are the standard errors on the mean. More massive galaxies have a larger fraction of galaxy mergers contributing to their stellar mass. Lower mass galaxies build up their stellar mass through in situ star formation only

Fig. 2.11 provides a more close-up observation following the spin six specific massive galaxies of various stellar masses ($1.7 \times 10^{11}\,\mathrm{M}_\odot$ (top left), $7.3 \times 10^{10}\,\mathrm{M}_\odot$ (top right), $3.8 \times 10^{10}\,\mathrm{M}_\odot$ (middle left), $4.8 \times 10^{10}\,\mathrm{M}_\odot$ (middle right), $1.2 \times 10^{11}\,\mathrm{M}_\odot$ (bottom left), $6.0 \times 10^{10}\,\mathrm{M}_\odot$ (bottom right) at $z = 1.83$) over the redshift range $1.8 < z < 3.8$. Let α be the angle between the direction of the spin of a galaxy at redshift z_n and its initial direction at redshift $z_0 = 3.8$. Fig. 2.11 follows the evolution of both $\cos\alpha$ (red curve) and the differential fraction of mass between two time steps coming from mergers δm (in blue) over 12 outputs.

One can notice that non-zero values of $\cos\alpha$, which correspond to rapid changes in spin direction ("flips"), are very well correlated to episodes of mass accretion through mergers, either minor or major mergers. In the absence of mergers, the galaxy spin maintains a steady direction, with negligeable drift over 2 Gyr. Once again, this is consistent with a scenario where galaxies acquire a spin orthogonal to their nearby filaments through mergers between progenitors drifting along the cosmic web. The following sections are dedicated to a more careful analysis of the efficiency of smooth accretion in building up galactic spins parallel to their filaments and of mergers in flipping them perpendicular by $\approx 90^{\mathrm{o}}$.

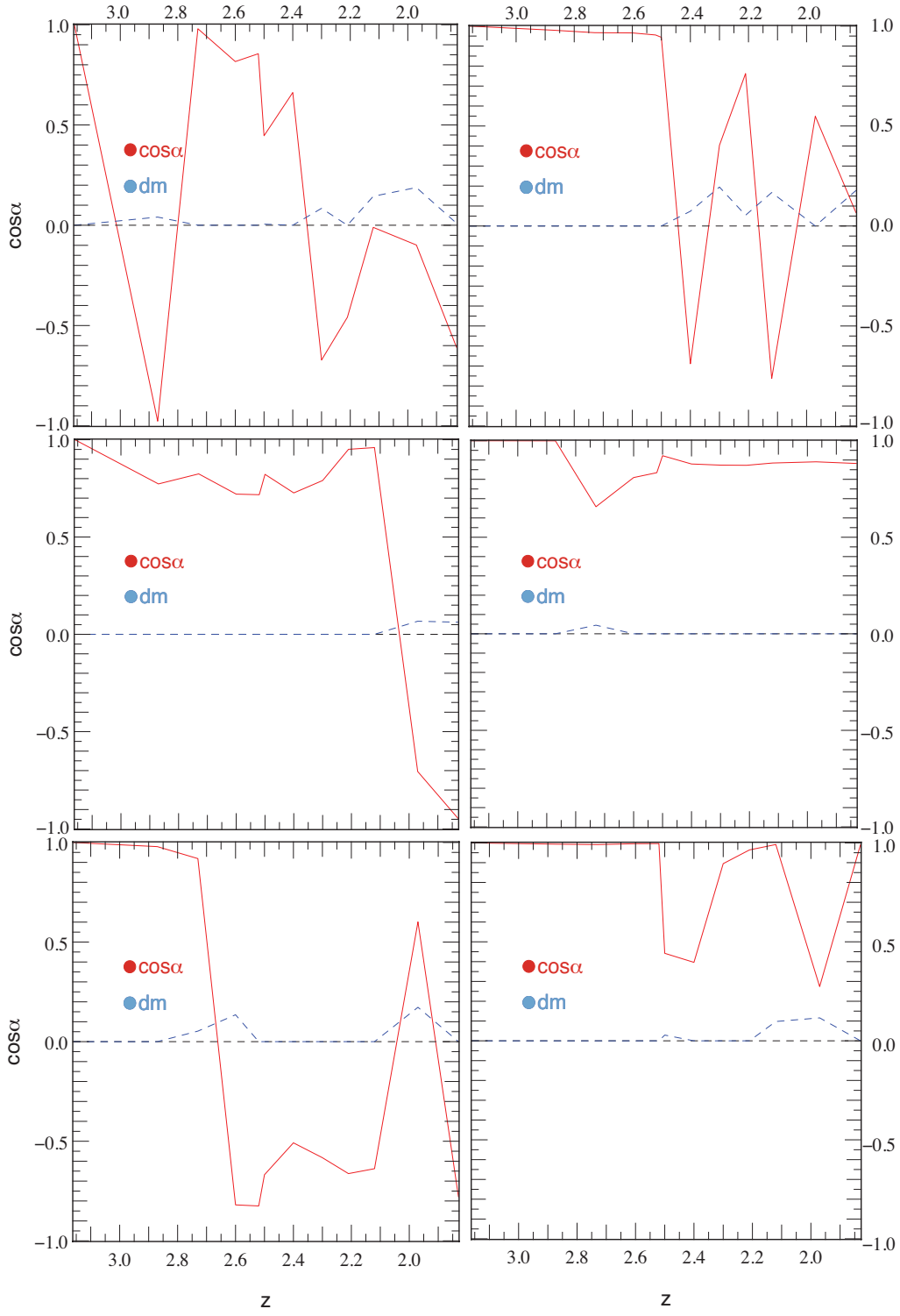

Figure 2.11: Examples of galaxies changing their spin direction during mergers with stellar mass $1.7 \times 10^{11}\,\mathrm{M}_\odot$ (top left), $7.3 \times 10^{10}\,\mathrm{M}_\odot$ (top right), $3.8 \times 10^{10}\,\mathrm{M}_\odot$ (middle left), $4.8 \times 10^{10}\,\mathrm{M}_\odot$ (middle right), $1.2 \times 10^{11}\,\mathrm{M}_\odot$ (bottom left), $6.0 \times 10^{10}\,\mathrm{M}_\odot$ (bottom right) at $z = 1.83$. $\cos\alpha$ (red curve) is the cosine of the angle between the spin of the galaxy at the current redshift and the initial spin measured at $z = 3.8$. The differential fraction of mass between two time steps coming from mergers $\delta m = \Delta m_{\mathrm{mer}}(z_n)/M(z_n)$ (in blue) is overplotted. Non-zero values correspond to rapid changes in spin direction. In the absence of mergers the galaxy spin has a steady direction.

2.3.3 Mergers and smooth accretion on spin orientation

Let us now also define the relative sAM variation of an object between simulation outputs $n-p$ and n as:

$$\delta\lambda_{\rm p} = \frac{l_{n+p-1} - l_{n-1}}{l_{n+p-1} + l_{n-1}}\,, \tag{2.15}$$

where l_n is the magnitude of the object sAM at redshift z_n. Fig. 2.12 (top panel) displays the Probability Distribution Function (PDF) of $\cos\Delta\alpha$, where $\Delta\alpha$ is the variation in the angle of the galaxy's AM between time outputs $n-1$ and $n+1$, for galaxies with different merger histories, i.e. different values of δm. We recall that the satellite detection threshold is set at $N_{\rm min} = 100$ particles, but that only main progenitors with masses $M_{\rm s} > 10^9\,{\rm M}_\odot$ (galaxies) and $M_{\rm h} > 10^{11}\,{\rm M}_\odot$ (haloes) are considered. From this figure, one can see that mergers are clearly the main drivers for galaxy spin swings, while the spins of galaxies without mergers tend to remain aligned between time outputs. Indeed, 91% of these latter see their spin stay within an angle of 25 deg over two time outputs (each separated by $\Delta z = 0.1$) whereas this happens only for 28% of galaxies with a merger mass fraction above 5% (this ratio even falls down to 10% with $N_{\rm min} = 1000$). Such a swing effect is sensitive to the merger mass fraction and, as one would expect, tends to be stronger for larger fractions. For $\delta m > 5\%$, 50% of the galaxy sample underwent a spin swing > 45 deg while this is true for only 18% of galaxies with $0\% < \delta m < 5\%$ and less than 2.5% of the no-merger ($\delta m = 0$) population. However, even mergers with low mass ratio (i.e. mergers where the satellite is less than twenty times lighter than the main progenitor) trigger important swings compared to the no-merger case. Only 58% of the galaxies which underwent a very minor merger ($0 < \delta m < 5\%$) maintain a spin within a cone of 25 deg over two time outputs (compared to 91% for non-mergers). This behavior is consistent with the well-known fact that when two galaxies merge, the remnant galaxy acquires a significant fraction of AM through the conversion of the orbital angular momentum of the pair rather than simply inheriting the AM of its progenitors.

A similar analysis for DM haloes confirms that they qualitatively follow the same behavior as galaxies but with quantitative variations due to the fact they are velocity dispersion-supported structures rather than rotationally supported ones. More specifically, one can see from Fig. 2.12 that unlike galaxies, even haloes defined as non-mergers ($\delta m = 0$) exhibit noticeable spin swings (see also Bett & Frenk, 2012). This can be attributed to the net AM of haloes resulting from random motions of DM particles (by opposition to ordered rotational motion of star particles for galaxies): even a small amount of AM brought in coherently by smooth accretion or mergers will be enough to noticeably influence the direction of the halo spin vector. Note that large-scale tidal torques also apply more efficiently to haloes than galaxies due to the larger spatial extent of the former, and it

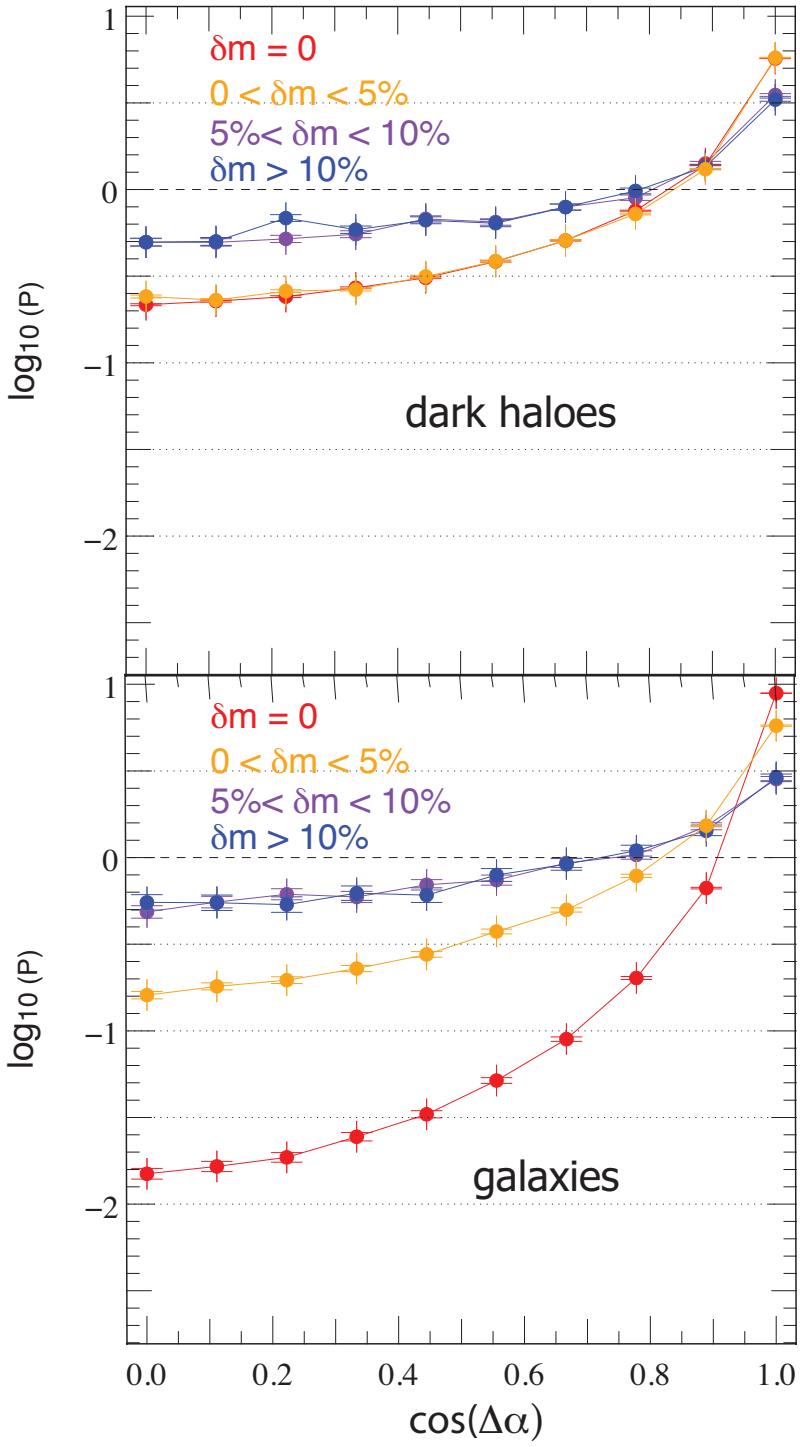

Figure 2.12: Logarithm of the PDF of $\cos\Delta\alpha$, the cosine of the spin swing angle for galaxies (top panel) and haloes (bottom panel) between time steps $n-1$ and $n+1$, for objects with different merger histories. The dashed line corresponds to the uniform PDF, i.e. no preferred orientation. The dotted lines show the threshold below which the population in the bin is 30%, 10%, 3% and 1% of the sample considered. δm is the mass fraction accreted through mergers between two consecutive time outputs. $\delta m = 0$ corresponds to the no merger case, i.e. pure smooth accretion. Mergers are responsible for spin swings; haloes are more sensitive to smooth accretion.

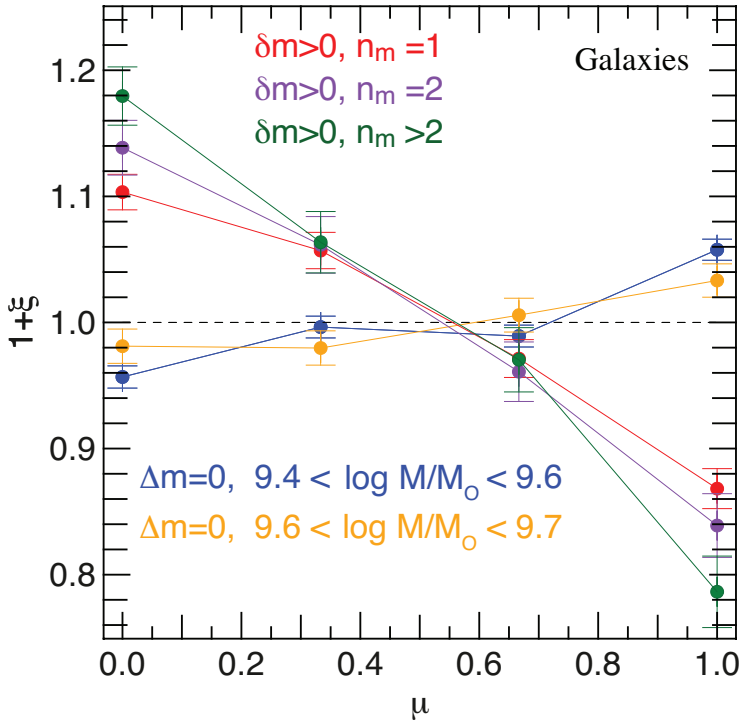

Figure 2.13: PDF of μ, the cosine of the angle between the galactic spin and its filament for different galaxy merger histories. This plot shows cumulative results for all simulation galaxies identified between $z = 3.16$ and $z = 1.71$. ξ is the excess probability with respect to a uniform distribution (dashed line). As before, δm is the fraction of mass accreted through mergers between two consecutive time outputs, and n_m is the total number of mergers a galaxy has undergone at the time of the measurement. $\Delta m = 0$, with Δm the cumulative merger fraction corresponds to the absence of mergers over the lifetime of the galaxy. The stronger the merger rate the stronger the misalignment. Subsequent mergers amplify the alignment.

can be speculated that these torques could also contribute to some of the quantitative differences I measure between AM alignment of haloes and galaxies.

Given that mergers account for the spin swings of galaxies, they should also be responsible for setting the orientation of their spins relative to the filament, at least for massive galaxies which do experience a significant amount of mergers. Our results are consistent with this scenario, as can be seen in Fig. 2.13 where I plot the PDF of μ, the cosine of the angle between the galactic AM and the direction of its filament, ξ being the excess probability with respect to a uniform distribution. It demonstrates that galaxies (each one being counted once after each merger) which have just merged tend to show a spin more perpendicular to filaments, and that the signal is stronger for galaxies which have experienced a larger number of mergers during their lifetime (from redshift of birth to the redshift of measurement). This is a strong argument in favour of orbital angular momentum transfer into spin since mergers are preferentially the result of galaxies encounters along

cosmic filaments, i.e., pairs with an orbital angular momentum that is orthogonal to the filament. Note that the excess probability $\xi \simeq 0.1 - 0.2$ of being perpendicular to their filament for galaxies undergoing mergers is larger than when the same galaxies are simply split in sub-samples according to their physical properties: mass, colour, activity, etc. ($\xi < 0.05$ in that case, see Dubois *et al.* , 2014).

In contrast, spins of galaxies with no merger are more likely to be aligned with their filament. Note that the threshold for structure detection here was set to $N_{\rm min} = 1000$ particles, which implies that "merger" galaxies are more clearly identified than "non-merger" ones in this figure. The alignment signal is therefore weaker, as expected. To emphasize this selection effect, the excess probability of alignment was analysed for galaxies split in different mass bins, the lowest two of which I plot in Fig. 2.13. Comparing both measurements, there is indeed tentative evidence that the excess probability of alignment is weaker for higher mass galaxies, which are more likely to have accreted "undetected" mergers. Note that the alignement signal is completely lost when considering that sub-sample of galaxies with masses above $10^{10}\,{\rm M}_\odot$. Further analysis confirms that lower thresholds ($N_{\rm min} < 1000$) attenuate the orthogonal misalignment and strengthen the alignment excess probabilities.

2.3.4 Mergers and smooth accretion on acquisition of spin.

Turning to the magnitude of the sAM, Fig. 2.14 shows the PDF of $\delta\lambda_2$ for both galaxies and haloes. We can see from this figure that mergers with mass ratios $5\% < \delta m < 10\%$ tend to increase the magnitude of the object sAM (curves are skewed towards positive $\delta\lambda_2$), and that this effect becomes stronger as the mass ratio increases, up to mass fractions around $\delta m > 10\%$ for which $\sim$75% of haloes and galaxies see their sAM magnitude increase – by a factor 2 or more for $\sim$25% of haloes and galaxies – between two consecutive time outputs.

This behaviour indicates that most mergers contribute constructively to the sAM of the collapsed structures. This is especially true for halo mergers where it can be understood as the conversion of orbital angular momentum into AM of the massive host. For very minor ($\delta m < 5\%$) to minor ($5\% < \delta m < 10\%$) galaxy mergers, satellites are most likely progressively stripped of their gas and stars and swallowed in the rotation plane of the central object, therefore increasing this later rotational energy. However, major mergers ($\delta m > 10\%$) – where an important part of the rotation energy can be converted to random motion energy through violent relaxation, intense star formation and feedback – can in fact contribute destructively to the sAM of the galaxy remnant. Indeed, those mergers induce wings in the PDF of $\delta\lambda_2$ corresponding to galaxies with increasing and decreasing sAM.

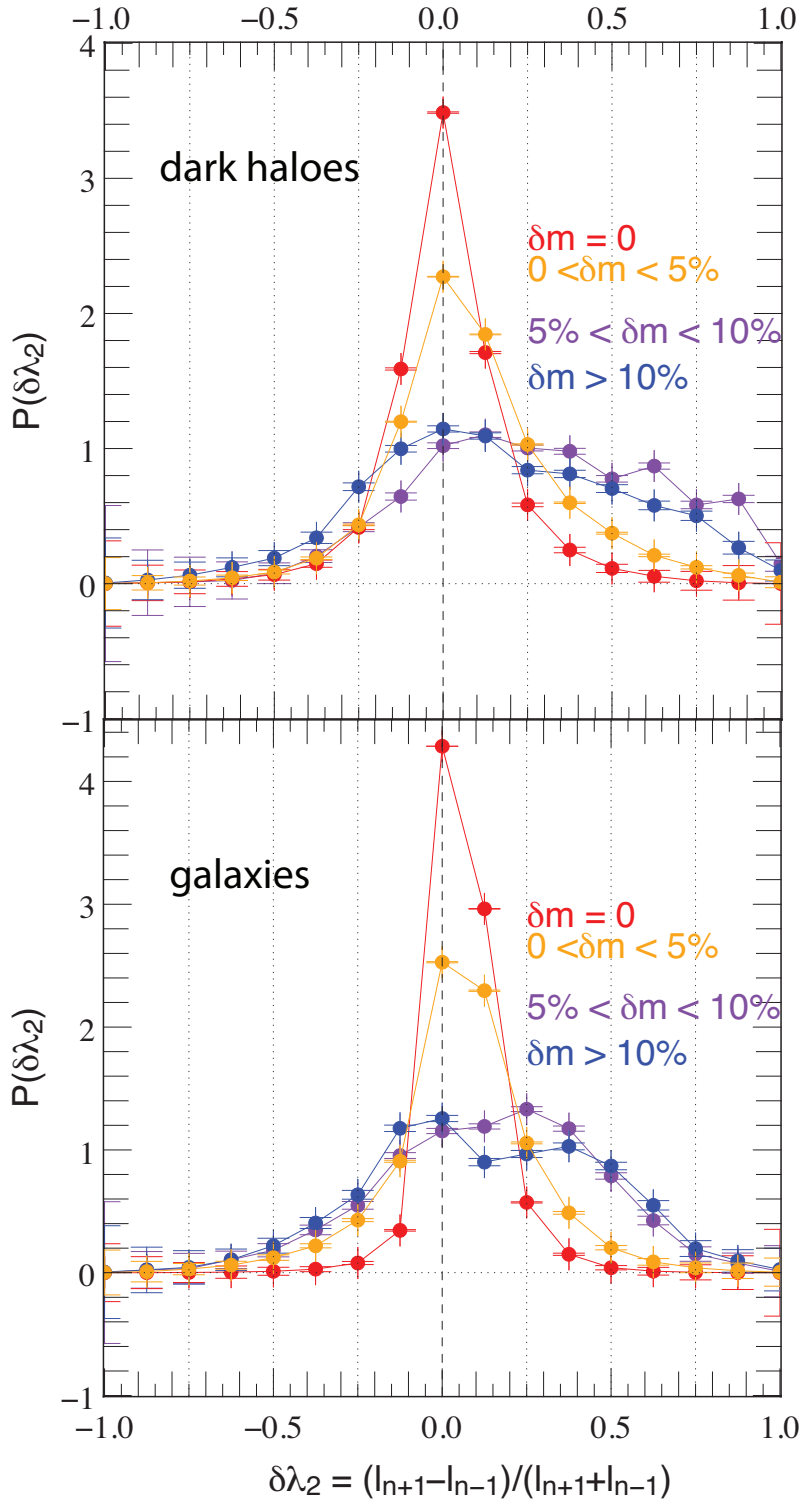

Figure 2.14: PDF of $\delta\lambda_2$ of the halo's (top panel) and galactic (bottom panel) sAM, for objects with different merger ratios. Positive values correspond to objects which acquire sAM through mergers, negative values correspond to objects which lose sAM. This plot shows results for the entire population of objects identified between $z = 3.8$ and $z = 1.2$. Mergers increase the sAM's magnitude.

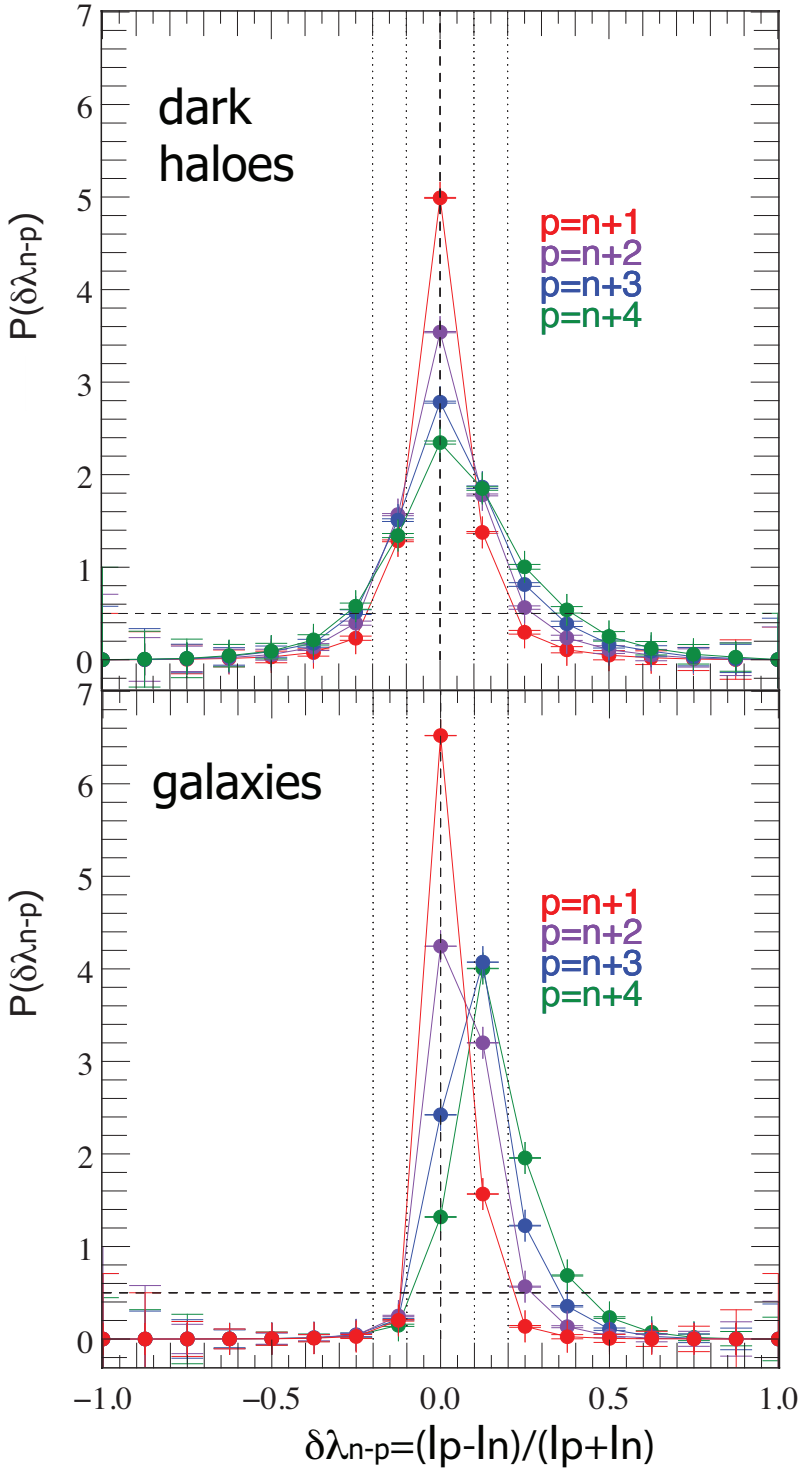

Figure 2.15: Same as Fig. 2.14 for objects which do not merge and for different lookback times. Secular accretion builds up the sAM of galaxies but not that of haloes.

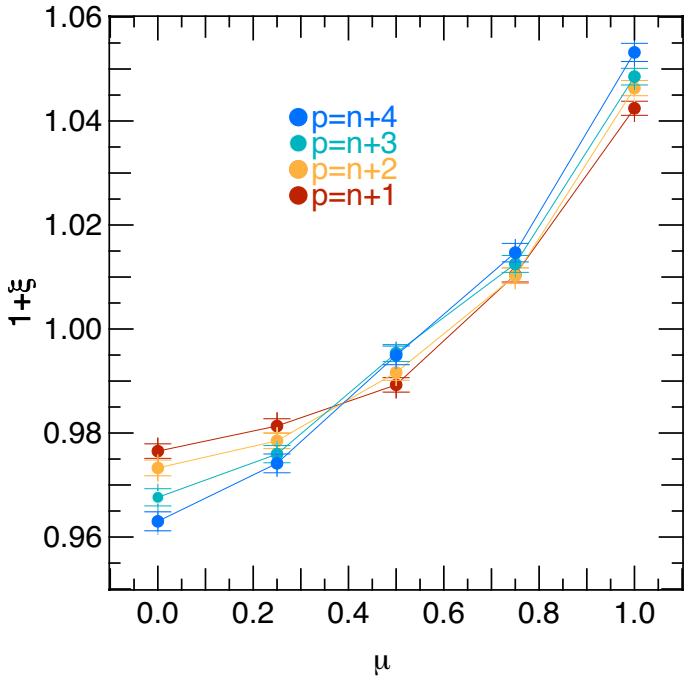

Figure 2.16: Same as Fig. 2.13 for galaxies which do not merge and for different lookback times (but samples of comparable size). In absence of merger, galaxies tend to re-align with their filament over time.

With $\delta m = 0$ the PDF bends towards positive $\delta\lambda_2$, suggesting that smooth gas accretion on galaxies, unlike smooth DM accretion on haloes tends to increase their sAM over time. In order to probe this (re)alignment process further, I present in Fig. 2.15 the evolution of the PDF of $\delta\lambda_{p-n} \equiv (l_p - l_n)/(l_p + l_n)$, where l_p is the sAM magnitude at redshift z_p and $p = n+1, n+2, n+3$ indicates different lookback time outputs, for haloes and galaxies. It appears clearly that while the halo distribution remains symmetric over time, the galaxy distribution shifts towards positive values with an average peak drift timescale of $t_{\delta\lambda} \simeq 5 - 10\,\mathrm{Gyr}$. I measure a similar trend for different galaxy mass bins up to $M_\mathrm{s} = 10^{11}\,\mathrm{M}_\odot$ (albeit with a slower drift for the most massive galaxies with $M_\mathrm{s} \approx 10^{11}\,\mathrm{M}_\odot$).

These findings favour the idea that cold gas (either cold streams or diffuse cooling gas) spins up galaxies over time. This secular gas accretion onto galaxies also (re)aligns the galaxy with its filament. This is demonstrated in Fig. 2.16, which is obtained via stacking for four successive time steps the relative orientation of the spins of galaxies to filaments when no merger occurs. It shows that the excess probability of alignment is amplified with time in the absence of mergers.

To sum up, Tempel & Libeskind (2013), found that spiral galaxies tend to have a spin aligned to their nearest filament while the spin of S0 galaxies are more likely to show an orthogonal

orientation. Dubois *et al.* (2014) argue that a transition mass can be associated to this change in spin orientation, which is reasonably bracketed between $\log(M_{\rm s}/{\rm M}_\odot) = 10.25$ and $\log(M_{\rm s}/{\rm M}_\odot) = 10.75$. These authors also point out that such a mass loosely corresponds to the characteristic mass at which a halo extent becomes comparable to that of the vorticity quadrant in which it is embedded within its host filament (Laigle *et al.* , 2015). Such a mass dependent scenario was first suggested by Hahn *et al.* (2007), and quantified by Codis *et al.* (2012) for DM haloes. The key idea which underpins all these studies is that lighter galaxies acquire most of their spin through secondary infall from their (aligned with the filament) vorticity rich environment, while more massive galaxies acquire a large fraction of theirs via orbital momentum transfer during merger events which mainly take place along the direction of the large scale filament closest to them. This section showed that galaxies without merger both realign to their host filament and increase their sAM, while successive mergers drive the remnant's spin perpendicular to it, and depending on the strength of the merger, decrease or redistribute the remnant's sAM magnitude. Hence it strongly favors the idea that cold/cooling flows feed low-mass disc galaxies (with anisotropic gas streams along the vorticity rich filaments, as advocated in Pichon *et al.* (2011), or possibly through smooth gas accretion from the spinning host halo) therefore enhancing their sAM magnitude over time.

2.4 Conclusion

Our analysis shows that the orientation of the spin of galaxies depends on various galaxy properties such as stellar mass, V/σ, colour and age:

- The spins of galaxies tend to be preferentially parallel to their neighbouring filaments, for low-mass, young, centrifugally supported, metal-poor, bluer galaxies.
- they tend to be perpendicular for higher mass, higher velocity dispersion, red, metal-rich old galaxies.

The alignment is the strongest, the closer to the filaments and further from the nodes of the cosmic web the galaxies are. This is in agreement with the predictions of Codis *et al.* (2012) for dark matter halos. I find a galactic transition mass, $M_{\rm tr,s} \simeq 3 \times 10^{10}\,{\rm M}_\odot$ which is also consistent with these authors' predictions for the corresponding halo transition mass. However, due to the weak galaxy-halo alignment (Dubois *et al.* (2014)), the amplitude of the correlation with cosmic filaments is somewhat weaker for galaxies than for halos. It also decreases with cosmic time, most likely due to mergers and quenching of cold flows and star formation. Hence our results suggest that galaxy properties can be used to trace the spin swings along the cosmic web.

This led us to analyse the variations of AM orientation and magnitude of galaxies and haloes as a function of their merger rates.

Our statistical analysis of merger trees, shows that the transition from the aligned to the misaligned case is dynamically triggered by mergers (the frequency of which increases with galaxy mass), which swing the spin of galaxies and have a strong impact on both the *orientation* and the *magnitude* of the AM. Our main findings are the following:

- the stronger the strength of the merger the larger the memory loss of the post-merger spin direction of dark haloes and galaxies;
- the alignment of the spin of an object with the cosmic web depends on its merger history: the more mergers contribute to its mass, the more likely its spin will be perpendicular to its filament;
- when the merger contribution to the mass of an object is negligible ($< 1\%$) the modulus of the sAM of *galaxies* still increases with time via smooth accretion. Moreover, the orientation of these spins drift towards (re-)alignment with the filament; this does not happen to the sAM of dark matter haloes, whose magnitude remains independent of time on average;
- mergers (with mass ratios $> 10\%$), like smooth accretion, also tend to build up the sAM modulus but of both haloes and galaxies in this case; on the other hand, they also produce a low sAM tail in the magnitude distribution.

Chapter 3

Orientation of satellites galaxies: massive hosts versus the cosmic web

An equally important impact of large scale structures on smaller scales is the impact of massive virialised structures on smaller scale virialised structures they host but do not strip apart. Indeed, in the previous chapter I studied how smoothly accreted - mostly gaseous - material and galaxy mergers could efficiently re-orient their spin of galaxies orthogonal to the filament their are embedded in. I explained that these results were consistent with similar trends for dark halo mergers and were a major source of correlation between the cosmic web geometry on large scales and the properties of virialised structures on small scales. However, in this description I focused on fully relaxed post-merger states of dark haloes and galaxies which necessarily induced a re-distribution of the dark matter/baryonic material into a new self-consistent structure over a few 100 Myrs.

Considering more closely the post-merger evolution of dark matter halos, features can be quite different. Indeed, when a massive dark halo accretes smaller halos, only gravitational forces are at stake. If those accreted haloes survive tidal stripping, they can give rise to a population of sub haloes evolving independently within the primary structure. Among them, the newly formed sub-haloes which managed to preserve their gas and possibly pre-existing stars host their own galaxy, which can therefore be defined as a satellite galaxy. The galaxy naturally formed by gas cooling and concentration at the pit of the potential well of the host halo prior to merging is called the central galaxy. This chapter focuses on understanding the interplay between these objects of similar structure and composition but formed at a different stage of the hierarchical evolution: satellites and their host's central galaxy.

This chapter reproduces results to be published in Welker *et al* (2015b) *in prep.*

3.1 An overview of satellite galaxies

This first section details the formation and evolution of satellites in standard CDM cosmology and further develops the reasons why they are the subject of great interest in observations..

3.1.1 The formation of satellite galaxies in CDM cosmology

Recall that, in the standard hierarchical model of structure formation, small dark haloes form first and progressively aggregate into more massive structures. Those dark haloes flow along the slowest direction of collapse predicted by the Zel'dovich paradigm of structure formation (Zel'dovich, 1970), therefore defining large-scale filaments of preferred accretion (Shandarin & Zeldovich, 1989; Sousbie *et al.* , 2008; Libeskind *et al.* , 2014) in which haloes and galaxies preferentially emerge (Bond *et al.* , 1996). When a low-mass dark halo flows towards a more massive companion under its gravitational influence, the two structures end up merging with one another. However, the outcome of such an event can fall in two different categories: either the smaller companion is stripped apart and its material redistributed in its host, or it manages to somewhat preserve its coherent structure, possibly its pre-existing gas and stars, and becomes a sub-halo, possibly hosting a satellite galaxy.

To understand how such a satellite halo can be either destroyed or preserved, let us focus on the processes that drives this evolution known as dynamical friction and tidal stripping.

3.1.1.1 Tidal and Ram Pressure Stripping

Let us a focus on a small dark halo orbiting in the gravitational potential of a much more massive host. In the rest frame of this host one can therefore compute the gravitational acceleration felt by the particles of the orbiting satellite. In the simplest model on Fig 3.1, *Panel a*, the massive host is modeled as a point-like mass M and the satellite as a spherical homogeneous mass m with radius r orbiting its host on a circular orbit of radius $R_{\rm s}$. The tidal acceleration on the edge of m (in point of shortest distance A) is therefore defined as the difference between the acceleration in A and the acceleration at the center of mass of the satellite S:

$$g_{\rm tidal} = \frac{G\,M}{R_{\rm s}^2} - \frac{G\,M}{(R_{\rm s}-r)^2} \approx \frac{2\,rGM}{R_{\rm s}^3} \quad \text{if} \quad r \ll R_{\rm s}\ . \tag{3.1}$$

Therefore, as a first approximation, if this acceleration exceeds the binding force per unit of mass Gm/r^2, the stars or dark matter particles orbiting the satellite at distance r will be stripped. This leads to define the tidal radius as:

$$r_{\rm t} = \left(\frac{m}{2M}\right)^{\frac{1}{3}} R_{\rm s}\,, \tag{3.2}$$

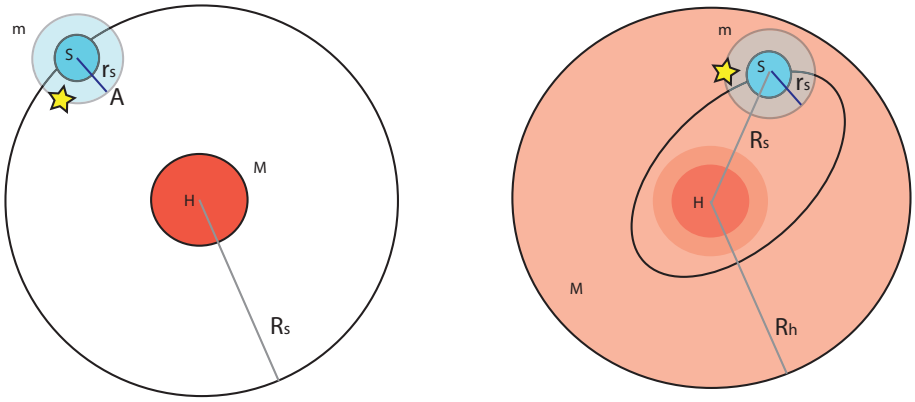

Figure 3.1: Sketch of the satellite-host system in the most simplistic model on *Panel a* and a more refined one taking into account the extension of the host halo and the eccentricity of the satellite's orbit on *Panel b*

the distance from the center of mass of the satellite above which its material will be stripped apart (von Hoerner, 1957).

Although this toy model provides a good understanding of the general process, it remains simplistic and does not allow to grasp the full complexity of tidal stripping. A straightforward correction consists in taking the centrifugal force associated with the centrifugal motion of the satellite, which leads to a corrected tidal radius:

$$r_{\rm t} = \left[\frac{m/M}{3+(m/M)}\right]^{\frac{1}{3}} R_{\rm s}\,. \tag{3.3}$$

Then again, the model in itself remains very simplistic.

Developing a more realistic model of tidal stripping of satellites requires to take into account the extension of the host halo, the eccentricity of the satellite's orbit, and possibly the orbits of the stars and dark matter particles within the satellite as presented on Fig 3.1, *Panel b*. In this model the tidal radius needs to be redefined as the instantaneous radius at which a particular star/particle within a satellite becomes bound instead to the host halo about which the satellite orbits. This radius therefore depends on four parameters: the potential of the host, the potential of the satellite, the orbit of the satellite and the orbit of the star within the satellite, all of these being time-dependent.

Few analytical works have tackled the whole complexity of this problem but many publications - both theoretical and numerical - have focused on different aspects and exposed the main features of tidal stripping:

- In the context of globular clusters, von Hoerner (1957) and King (1962) considered point mass potentials for the host and the satellite but suggested to deal with the eccentricity

of the cluster's orbit with a restricted definition of the tidal radius as the distance $r_{\rm t}$ from the center of m at which a point on line connecting centers of m and M experiences zero acceleration when m is located at the pericentric distance $R_{\rm p}$. This followed from the fact that the internal relaxation time of the cluster is greater than its orbital period for almost all observed globular clusters. In this case, star/particle orbits are assumed to be purely radial kepler orbits and the tidal radius reduces to $r_{\rm t} = (m/(M(3+e))1)^{1/3}\, R_{\rm p}$.

- Read *et al.* (2006) extended this analysis (for both point mass and power law potentials) to define two additional tidal radii for star/particles with prograde and retrograde circular orbits around the satellite, in which cases the coriolis force cannot be neglected. Noticing that the smallest radii are therefore found for coplanar orbits of the satellite and the star considered in a frame centered on the host and when the three bodies are aligned, they established analytically that prograde orbits are more easily stripped than radial ones, themselves more easily stripped than retrograde ones. As a result, tidal radii depend on the precise mass distribution of the satellite. This confirmed the predictions of numerous simulations (Toomre & Toomre, 1972; Keenan.D.W & Innanen, 1975; Kazantzidis *et al.* , 2004a).

- The fate of stripped stars has also been the object of numerous analytical works, from the restricted analysis of one single test star (Szebehely & Peters, 1967; Henon, 1997; Valtonen & Karttunen, 2006) to the precise description of tidal tails in angle-action variables (Helmi & White, 1999; Tremaine & Ostriker, 1999).

- Using N-body simulations, Choi *et al.* (2009) studied the dynamics of tidal tails made of stripped material and found that their morphology is considerably modified by the satellite's self gravity which tends to accelerate the trailing tail but decelerate the leading tail, furthermore displacing the radial velocities of the trails from that of the satellite orbit proportionally to the satellite mass.

- Eventually Chang *et al.* (2013) studied the dependence of the efficiency of tidal stripping on the satellite and the host central galaxy morphology, for satellite halos which contain a galaxy. They found that the removal of the stellar component only begins after 90% of the dark matter mass has been stripped and occurs very differently for disc, bulge+disc and pure bulge satellite galaxies. While the disc component is quickly removed (exponential mass loss) - completely after a few 100 Myr - especially when coplanar to the satellite orbit, remaining bulges are able to survive for several Gyr (power-law mass loss). This is consistent with previous result by Kazantzidis *et al.* (2004b) that satellites with high central densities mostly survive tidal stripping over several Gyr.

In addition, Mayer (2005) shows that intense stripping from ram pressure - the pressure $\rho_{\rm ext}v^2$ exerted on a satellite moving with the velocity v through the intergalactic medium of density $\rho_{\rm ext}$ is needed to account for a substantial removal of the gas component. As a consequence, a considerable amount of small dark haloes that accreted cold gas and started forming stars prior to merging with a more massive host are able to survive the stripping of their material and constitute a population of satellite galaxies.

3.1.1.2 Dynamical friction and orbital decay

Although this first exploration of tidal stripping explains how satellite galaxies can linger into their host, it does not explain how they migrate and distribute in the host halo. Indeed, once they are bound to their host, sub-halos do not remain on a definite orbit but rather spiral inwards rapidly over cosmic time. This process is called orbital decay and implies a transfer of energy and angular momentum to the host halo hence the existence of some drag force. The mechanism that makes this transfer possible is called dynamical friction and is briefly described in the following paragraph.

What is dynamical friction? The general idea behind dynamical friction is that individual stellar/DM encounters with a given satellite can perturb their trajectories, leading to a progressive diffusion in phase-space away from their initial orbits, over a typical timescale $t_{\rm relax}$ called the relaxation time. While $t_{\rm relax}$ is larger than the age of the universe for typical isolated galaxies, which can therefore be considered collisionless, this is not the case in the situation of satellite S moving across a much larger system H of much less massive field stars/DM particles.

In this situation, collisions between the satellite S (and its stars) and the particles of H leads to a transfer of energy from the relative orbital motion between S and H to the random motions of their constituent particles.

One way to take into account individual encounters requires to add up a collisional operator Γ to the Boltzmann equation which describes the effect of diffusion around a star in phase-space. The mathematical expression of Γ is rather complicated.

The mechanism of dynamical friction on a satellite can however conveniently be described in the framework of linear response theory (Weinberg, 1986, 1989; Colpi & Pallavicini, 1998) as a two step process, which regards the satellite as an external potential exciting a response density in the host system, itself exciting a response potential responsible for dynamical friction on the satellite. A seminal analysis is developed from a perturbative scheme in Tremaine & Weinberg (1984) and shows that this irreversible process can be interpreted as the result of numerous resonances between

the orbital frequencies of the satellite and the halo's particles. In a nutshell, the slower the relative orbital motion the stronger the cumulative effect of gravity.

This theory includes the effect of correlations between particles —restricted to self-correlations— which are needed to efficiently account for all the features of dynamical friction: the wake and tides associated to the satellite motion, the shift of the host stellar center of mass due to the stellar orbits perturbation and the orbital decay of satellites from outside their spherical host due to global tidal deformations excited by the orbital motion.

However, equations are quite complex and the mechanism of orbital decay can be understood in the restricted formalism developed by Chandrasekhar (1943).

Chandrasekhar local approximation This approximation assumes an infinite, homogeneous, isotropic stellar (point stars) background where self-gravity is turned off, in which case the frictional force simply arises from the uncorrelated superposition of binary short-lived encounters between the satellite of mass M at speed $\mathbf{v_s}$ and the field particles of the host (of mass $M_{\rm host}$). This reduces the drag force to a purely local friction term originating from a trailing wake of field particles, but linear response theory confirmed that this is indeed the dominant term providing that the satellite already lies in the background field, in which case this approach remains very predictive (Weinberg, 1989) . In this formalism the drag force can be expressed approximately as:

$$\mathbf{F}_\Delta = -4\pi \left(\frac{GM}{v_s}\right)^2 \ln\left(\frac{b_{\rm max}}{b_{90}}\right) \rho(< v_s) \, \frac{\mathbf{v_s}}{v_s}\,, \tag{3.4}$$

with $\rho(< v_s)$ the local density of field particles with speeds lower tan v_s, $b_{\rm max} \approx R$ the maximum impact parameter taken as the typical size of the host R and $b_{90} \approx G\ M/\langle v^2_{\rm star}\rangle^{1/2}$ the impact parameter leading to a 90 deg deflection.

A very short introduction to orbital decay Let us take the simple case of a satellite moving on a circular orbit with radius r_s in a spherical, isothermal halo with density $\rho(\mathrm{r}) = \mathrm{V}^2/(4\pi \mathrm{G r}^2)$ and a Maxwell-Boltzmann velocity distribution hence with dispersion $\sigma = V\sqrt{2}$. It is therefore straightforward to compute the rate at which the satellite loses orbital momentum:

$$\frac{dL_s}{dt} = r_s \frac{dv_s}{dt} = r_s \frac{F_\Delta}{M} = -0.428 \frac{GM^2}{r_s} \ln\left(\frac{b_{\rm max}}{b_{90}}\right), \tag{3.5}$$

$$\text{with} \quad \ln\left(\frac{b_{\rm max}}{b_{90}}\right) \approx \ln\left(\frac{M_{\rm host}}{M}\right) \quad \text{since} \quad V = \sqrt{\frac{GM_{\rm host}}{R}}.$$

Considering now that the satellite must recover the circular speed $v_s = V$, independent of radius, on its new orbit one gets:

$$\frac{d\mathbf{L_s}}{dt} = \mathbf{v_s} \times \frac{d\mathbf{r_s}}{dt}\,, \tag{3.6}$$

thus the satellite spirals inwards with the radius change:

$$r_s \frac{dr_s}{dt} \approx -0.428\,\frac{GM}{V}\ln\left(\frac{M_{\rm host}}{M}\right). \tag{3.7}$$

Therefore, as they orbit around their extended hosts, satellites lose angular momentum and energy to the background field and spiral inwards until they reach the center of their host after a dynamical friction time than can be estimated either this simplistic approach or from linear response theory.

Interplay between dynamical friction and tidal stripping. The processes of tidal stripping and dynamical friction do not occur independently but rather affect one another. Ample analytical and numerical studies have explored the fate of galaxy satellites bound to a spherical massive host under various hypothesis and noticeably found that eccentric orbits decay faster, and that the steady mass loss due to tidal stripping can increase the dynamical friction time by a factor three (Lynden-Bell & Kalnajs, 1972; Tremaine & Weinberg, 1984; Colpi *et al.* , 1999). Colpi *et al.* (1999) studied satellites with mass $M = 2\%\, M_{\rm host}$ and different density contrasts. They found tidal stripping to be systematically more efficient than dynamical friction: while satellites lose 60% of there mass after the first pericentric passage (1.5 Gyr), their orbital momentum is only decreased by 20%. They further estimated that satellites with high density contrasts could survive up to $6 - -8$ Gyr (4–5 pericenter passages) on eccentric orbits and that all satellites on peripheral orbits could survive much longer than 10 Gyr as the mass loss almost completely compensate the dynamical friction in this case. Moreover, satellites with small cores can survive up to a Hubble time within the primary. As an example, dwarf spheroidal satellites of the Milky Way, such as Sgr A and Fornax, have already suffered mass stripping, and with their present masses, the sinking times exceed 10 Gyr even if they are on very eccentric orbits (Colpi *et al.* , 1999). Linear response theory further confirms the numerical result that satellite orbits do not undergo any significant circularization through these processes (Colpi *et al.* , 1999).

Orbital decay from outside the host: torques form the central galaxy These processes explain well the fate of satellites once they have entered the halo. Nevertheless, significant effects can arise from the interaction between an external satellite and its central galaxy as the central galaxy - where stellar material is highly concentrated - can display a sharply distinct morphology from the overall morphology of the halo on large scales, imprinting only the morphology of the inner part of the halo.

This is however naturally described in the framework of linear response theory as the result of friction that arises from the tidal deformation induced by the external satellite on its self-gravitating host, which channels out energy and angular momentum from the satellite (Tremaine & Weinberg, 1984; Colpi, 1998) .

Noticeably, for eccentric orbits, the loss of stability is easier and corresponds to a pericentric distance smaller than a critical radius. The exchange of energy is then very effectively channeled through a quasi-resonance interaction. The bandwidth of effective energy transfer around the resonance is larger for more massive satellites which thus decay sooner and faster than their light counterparts for which the decay corresponds to a secular evolution.

3.1.2 The distribution of satellite galaxies

Theoretical predictions This first exploration of the processes that drive the evolution of satellite sub-haloes bound to a more massive host boil down to the following scenario: while satellites on very eccentric orbits and low density sub-haloes with few stars and gas are rapidly stripped apart and accreted down to the core of their host, highly concentrated sub-haloes hosting a galaxy revolve around their host along a wide range of eccentricities undistinguishable from that of the diffused dark matter component (Ghigna *et al.* , 1999), over long periods of time. They are only very progressively stripped of their gaseous and stellar material as they enter the inner regions of the halo.

As a consequence, one can expect the observed populations of satellite galaxies at low redshift to be excellent tracers of the underlying dark matter density of their host halo. Since numerous simulations in CDM cosmology have found that haloes display important deviations from sphericity and are therefore better described as ellipsoids (Barnes & Efstathiou, 1987; Warren *et al.* , 1992; Yoshida *et al.* , 2000; Meneghetti *et al.* , 2001; Jing & Suto, 2002), those satellites are therefore expected to be distributed anisotropically as a result of their host triaxiality (Wang *et al.* , 2005; Agustsson & Brainerd, 2010).

The properties of satellites are also expected to display a radial evolution consecutively to the progressive morphology dependent tidal stripping they undergo: while disks and star forming satellites will be most likely found in the outskirt of their host before any significant stripping and sinking has occurred, the inner regions will most likely host quenched spheroids deprived of their disk component as well as of their star forming gas (Agustsson & Brainerd, 2010; Yang *et al.* , 2006; Dong *et al.* , 2014).

Observations vs. Simulations: A biased distribution Although these predictions look pretty robust at first glance, many recent studies have exposed a discrepancy between simulations and observations, suggesting the existence of several biases in the satellite distribution.

Observationally, satellites have been successfully used as dynamical tracers to provide accurate dynamical masses for the haloes as well as constraints on the radial density distribution of dark matter (Zaritsky *et al.* , 1993; Brainerd & Specian, 2003; van den Bosch *et al.* , 2004). However, simulations predict two important spatial biases:

- First they found the radial distribution of halos to be much less concentrated at the center than the dark matter (Ghigna *et al.* , 2000; De Lucia *et al.* , 2004; Gao *et al.* , 2004; Mao, 2004; Nagai & Kravtsov, 2005). The discrepancy appears however much less pronounced in observations (van den Bosch *et al.* , 2005; Yang *et al.* , 2005), and recent measurements in the Illustris hydrodynamical simulation, based on moving-mesh techniques, seemingly recover these trends (Sales *et al.* , 2015).

- Second, many established the existence of an additional angular bias resulting from the preferential sustained accretion of sub-haloes along a cosmic filament (Aubert *et al.* , 2004; Knebe *et al.* , 2004; Wang *et al.* , 2005; Zentner *et al.* , 2005; Pichon *et al.* , 2011). These authors suggest that it would increase the tendency of satellites to align in the galactic plane of their host as -in the standard hierarchical model- this plane is most likely parallel to the filament direction since the massive host built up its spin from mergers along the filament. Recent observations in both the Local Group and the SDSS support this claim (Libeskind *et al.* , 2011; Lee *et al.* , 2014; Libeskind *et al.* , 2015; Tempel *et al.* , 2015).

One should notice that this latter effect seems by essence hard to distinguish from the anisotropy related to the mere triaxiality of the halo. Indeed, since the hierarchical build-up of massive host halos is not isotropic but partially the result of mergers, whose orientations are defined by the embedding filament, the population of massive hosts is thought to be dominated by halos with a spin flipped orthogonal to their host filament with no further evolution (van Haarlem & van de Weygaert, 1993; Tormen *et al.* , 1997; Bailin *et al.* , 2008; Paz *et al.* , 2011; Codis *et al.* , 2012; Zhang *et al.* , 2013). As a consequence, the elongation of the halo and filamentary infall share a unique direction. The tendency of their satellites to orbit in the central galactic plane is therefore not a mere tracer of the halo triaxiality but also naturally enhanced by the continuing infall (Aubert *et al.* , 2004; Knebe *et al.* , 2004; Wang *et al.* , 2005; Zentner *et al.* , 2005). Recent observations of planes of satellites for M31 or the Milky Way (Ibata *et al.* , 2013; Libeskind *et al.* , 2015) and the discovery of alignment trends in the SDSS, e.g., by Paz *et al.* (2008) and Tempel *et al.* (2015) which studied

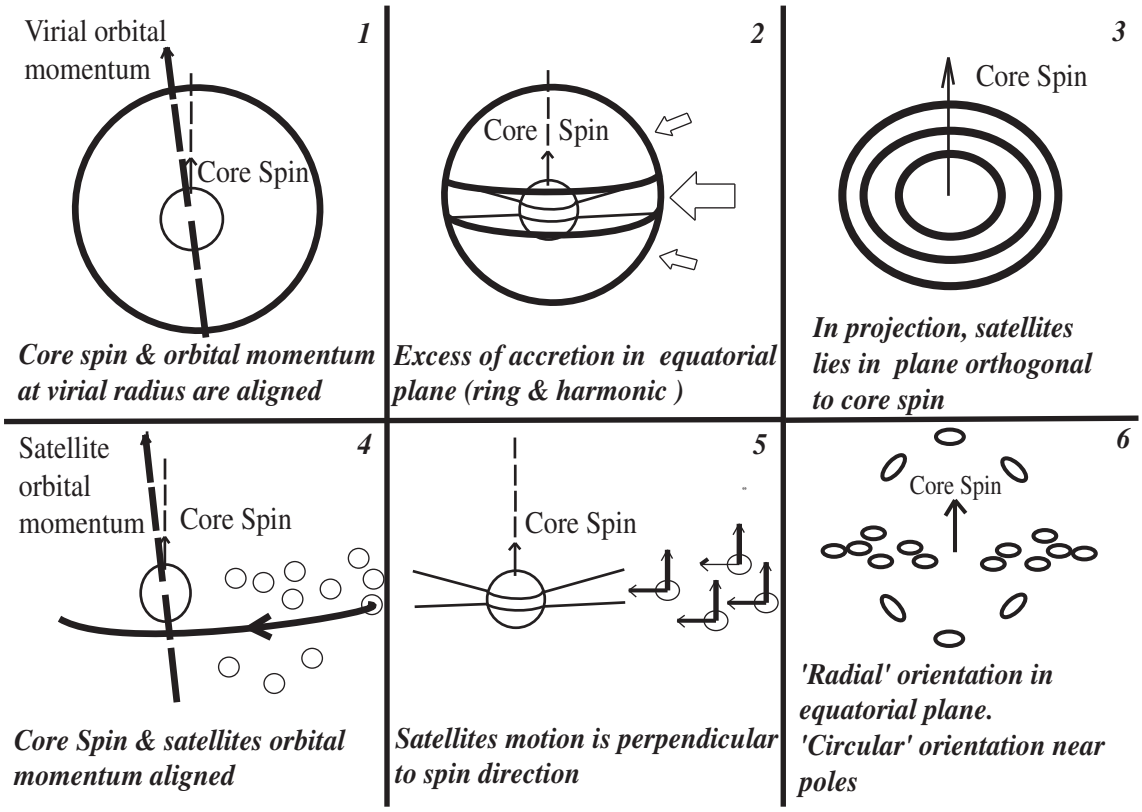

Figure 3.2: Illustration of the main features of anisotropic infall onto dark haloes discussed in Aubert *et al.* (2004): (1) The average orbital momentum measured on the virial sphere is mostly aligned with the spin embedded in the virial sphere. (2). On the virial sphere, an excess of ring-like or harmonic accretion in the equatorial plane is detected. (3) In projection, satellites lie preferentially in the projected equatorial plane of the halo. (4) The orbital momentum of satellites is preferentially aligned with the spin of the core halo. (5) The velocity vector of satellites (in the core s rest frame) is orthogonal to the direction of their spin. (6) In the equatorial plane, the projected orientation of satellites is more "radial", while near the direction of the spin a "circular" configuration of orientation seems to emerge. *courtesy of Aubert* et al. *(2004).*

the correlations between the alignment of satellites and the directions of the shear tensor, strongly support this claim.

One should note that results for dark matter find this concept of polar flow to be relevant for the diffuse component as well satellites. It is described in some details in Aubert *et al.* (2004). An illustration that summarizes the most significant findings of these authors can be found in Fig. 3.2. Using a suite of pure dark matter simulations, they explored the dynamical evolution of sub-haloes within their host halo. While the anisotropy of accretion they measure - strengthened in the equatorial plane of the halo for both satellites and the diffuse component - is consistent with a filamentary infall on haloes with a spin preferentially orthogonal to their nearby filament, they also detect a tendency of satellites to align their shape and synchronize their kinematic features with that of the core halo suggesting a specific dynamical influence of the host inner parts on those dense virialised structures.

Although it is still unclear how strongly this impacts the observed angular anisotropy and whether the alignment trends observed remain compatible with a mere asphericity of the halos (itself stimulated by the anisotropic infall), it remains important to make the distinction between a dynamical angular bias (sustained polar accretion, gravitational torques from the central disc and halo) and a purely geometrical angular anisotropy (related to the elongation of the halo) that affects the diffuse dark matter component equally, as illustrated on Fig. 3.3.

What's more, the triaxiality of a halo is distinct from the triaxiality of its central galaxy (van den Bosch *et al.* , 2002; Chen *et al.* , 2003; Sharma & Steinmetz, 2005; Dubois *et al.* , 2014), and predicting reliable correlations for them has proved a major difficulty for semi-analytical studies. More specifically, Kazantzidis *et al.* (2004b) and Dong *et al.* (2014) showed that the formation of a disc modifies only the shape and orientation of the inner halo, leaving the outer parts virtually intact.

This distribution of satellites in the galactic plane has since been confirmed by numerous observations at low and high redshifts (Sales & Lambas, 2004; Brainerd, 2005; Yang *et al.* , 2006; Sales *et al.* , 2009; Wang *et al.* , 2010; Nierenberg *et al.* , 2012), which focused on evaluating the alignment of satellites along the major axis of the host projection along the line of sight. Although Holmberg (1969) primarily found an alignment with the host *minor axis* and brought some confusion to the previous scenario - some studies even claiming the absence of any alignment trend (Hawley & Peebles, 1975; Phillips *et al.* , 2015) - subsequent studies -especially on large scales - were unable to confirm this so-called "Holmberg effect" with the exception of some specific cases in the Local Group (Pawlowski *et al.* , 2012; Forero-Romero & González, 2015) that have since been convincingly explained by large-scale tidal torques (Libeskind *et al.* , 2015). In particular, analysis

of galaxy groups in the Sloan Digital Sky Survey (SDSS, Abazajian *et al.* 2009) has confirmed this trend and established that the signal is stronger for massive red central galaxies, especially in the inner regions of the halo (Yang *et al.* , 2006). Note that alignments of nearby structures are common on multiple scales as there is also evidence of alignment trends between brightest cluster galaxies and groups/clusters on large scales (up to $100\,h^{-1}\,\mathrm{Mpc}$) as a consequence of hierarchical structure formation (Binggeli, 1982; Plionis & Basilakos, 2002; Hopkins *et al.* , 2005; Mandelbaum *et al.* , 2006; Hirata *et al.* , 2007; Okumura & Jing, 2009; Joachimi *et al.* , 2011; Smargon *et al.* , 2012; Singh & Mandelbaum, 2014). All of these alignment trends bring potential pollution to weak lensing surveys and therefore require in-depth study.

This chapter pursues two main goals:

- using a cosmological hydrodynamical simulation with all the prominent features of baryonic physics implemented to make testable statistical predictions for the satellites alignment to their host galaxy, without resorting to ad hoc prescriptions for the shape of such a galaxy. As such, I will show that these results add up to and confirm recent numerical results obtained by Dong *et al.* (2014).
- understanding whether the previously mentioned filament alignment trend is indeed distinctive from the coplanarity of satellites with their host galactic plane, and how the two correlate in different mass ranges and for different orientations of the host galaxy.

3.2 Satellites in Horizon-AGN

This study was carried out in the Horizon-AGN simulation, between redshift $z = 0.8$ and redshift $z = 0.3$ and briefly compared to higher results at higher redshifts ($1 < z < 2$).

3.2.1 Identifying central galaxies and satellites

As in previous chapters, haloes and galaxies were identified with the AdaptaHOP structure finder of the HaloMaker program (Tweed *et al.* , 2009; Aubert *et al.* , 2004), operating on dark matter particles for haloes and star particles for galaxies. The minimum number of particles for detected structures was set to $N_{\mathrm{min}} = 100$ - which typically selects stellar objects with masses larger than $2 \times 10^8 \mathrm{M}_\odot$ - but central galaxies were selected only among structures with a stellar mass $M_{\mathrm{g}} > 10^9 \mathrm{M}_\odot$ so as to detect satellites within a wide range of satellite-to-host mass ratios.

Catalogs were produced for six outputs of the simulation between for $0.3 < z < 0.8$ with a increment $\Delta z = 0.1$, which covers a period of 3.5 Gyr, with a typical time step of 700 Myr. This

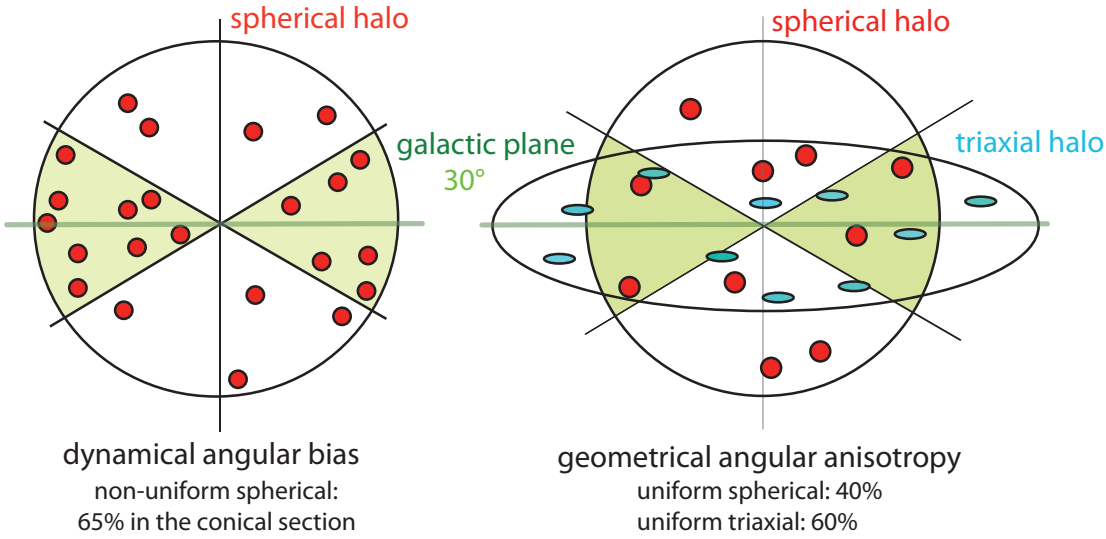

Figure 3.3: Sketch of the different angular biases that can be expected. Satellites are represented as red dots (spherical halo) and blue dots (elongated halo). *Right halo*: a dynamical process bends the satellites orbits towards a preferred plane. *Left halo*: While the corresponding spherical halo shows no angular anisotropy, a continuous transformation that breaks this sphericity leads to an effective anisotropy of the satellites distribution. Indicated fractions of satellites are relative to this specific illustration.

coarse time step allows for a substantial progress of satellites on their orbit. This allows us to stack the results from all the pairs in the 6 outputs and still remain consistent with observations stacked over independent redshift bins without being too disrupted by the time correlation between our snapshots.

Haloes were then matched to their central galaxy, identified as the most massive galaxy within a sphere of radius $0.25\,R_{\rm vir}$ around the center of mass of the halo, with $R_{\rm vir}$ its virial radius. Satellite galaxies were identified as all the galaxies within a sphere of a given radius R around the center of mass of the halo. In this selection, I considered only main haloes, galaxies within sub-haloes being therefore identified as satellites of the main halo. One can notice that, if R is chosen large enough, this selection will include galaxies hosted by other neighboring haloes. This method consistent with the idea that alignments along the major projected axis are expected to be detected on large scales as well, with haloes being themselves aligned with one another.

However, for reasons developed in the next section, this study focuses on the one-halo term and its interplay with the filament hosting the halo. Thorough studies of the two-halo term can be found in Chisari *et al.* (2015).

This leaves us with up to 180000 satellites and galaxies per snapshot, 10% to 15% of which

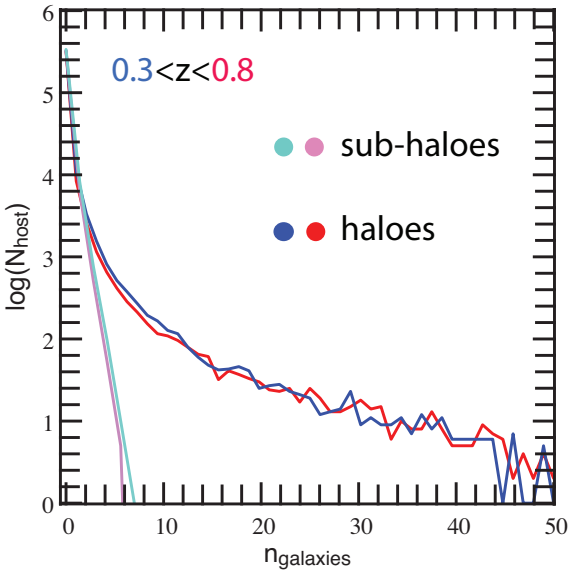

Figure 3.4: Log distribution of the number of galaxies per halo in HORIZON-AGN for main haloes and sub-haloes.

are identified as central galaxies. As an example, at $z = 0.3$, 16 000 galaxies are identified as centrals, 6622 haloes host at least 2 galaxies, 263 more than 30 galaxies and the richest one is a well-identified massive cluster in the simulation containing 678 galaxies.

For more details, Fig. 3.4 shows the distribution (in log scale) of the number of galaxies per halo in HORIZON-AGN for main haloes and sub-haloes, for the two extrema of the redshift range I study.

For complementary small-scale measurements, all non-central galaxies are also matched to their host sub-halo. This step is performed in a different way: I do not force a cut in radius but rather assign each galaxy to its closest halo structure, independently of its level in the hierarchical formation scheme.

3.2.2 Tracing the evolution of satellites in the halo: synthetic colors.

In this study, I want to follow the evolution of satellites within their hosts in order to develop a dynamical model for the distribution of satellites within dark haloes. This implies to be able to statistically trace the two main aspects of this evolution developed in the the first section:

- *the orbital decay* which leads to a distribution where satellites accreted earlier are found closer to the central galaxy. This is done computing the distance between the satellite and its host

- *the tidal stripping* which progressively deprives the satellite of its gas therefore quenching its star formation. This is done computing synthetic rest-frame colors derived from the AB magnitudes.

Indeed, I detailed in Chapter 2 how star formation from gas in a galaxy can be easily traced and allows for the estimation of the age and history of galaxies: the luminous spectrum of a star evolves as gas forms stars and as stars get old and consume their initial material into heavier chemical elements.

In a similar fashion to what was done in Chapter 2, in this work I use single star population models from Bruzual & Charlot (2003) and assume a Salpeter initial mass function to compute the flux for each star. The flux emitted from a galaxy can be seen as the sum of the contributions of all its star particles, each star contributing to a flux per frequency that depends on its mass, age and metallicity. This flux can therefore be passed through the u, g, r and i filters of the SDSS. It is therefore straightforward to calculate the rest-frame colors $g-r$, $u-r$ or $r-i$ from the calculated fluxes F_r, F_i and F_g as for instance $g-r=-2.5\ \log(F_g/F_r)$

This leads us to classify galaxies as red or blue depending on their colors: star forming galaxies containing lots of fast evolving high-mass stars at high temperature will emit hot radiation increasing the blue component of their spectrum, hence their $g-r$, $u-r$ and $r-i$ values to be lower than older quenched galaxies populated by old cooler stars emitting a redder radiation.

To decide which threshold to use in order to identify the galaxies and satellites in Horizon-AGN as red or blue, I studied the evolution of the color bi-modality in our sample. The bimodal aspect of the mass-color distribution in large samples of galaxies is a well-known feature of modern astronomy (Strateva *et al.* , 2001; Bell *et al.* , 2004; Ellis *et al.* , 2005; Baldry *et al.* , 2006; Driver *et al.* , 2006), with high-mass early-types residing on a well-defined sequence separate from a cloud of low-mass blue late-types. It has been established that galaxies progressively migrate from the blue cloud to the red sequence when their star formation slows down due to quenching resulting from intense feedback, stripping but mostly strangulation from their host (Kang *et al.* , 2005; van den Bosch *et al.* , 2008; Peng *et al.* , 2015).

In simulations, the color-diagrams do not show such a clear cut distinction. However, stacking over stellar masses allows us to recover the bimodal signal. The corresponding distributions for $g-r$, $r-i$ and $u-r$ in Horizon-AGN are presented on Fig. 3.5 for all the outputs studied in this chapter. Comparing the evolution of the peaks corresponding to the blue and red galaxies, one can clearly see the migration of blue galaxies into the red sequence over cosmic time.

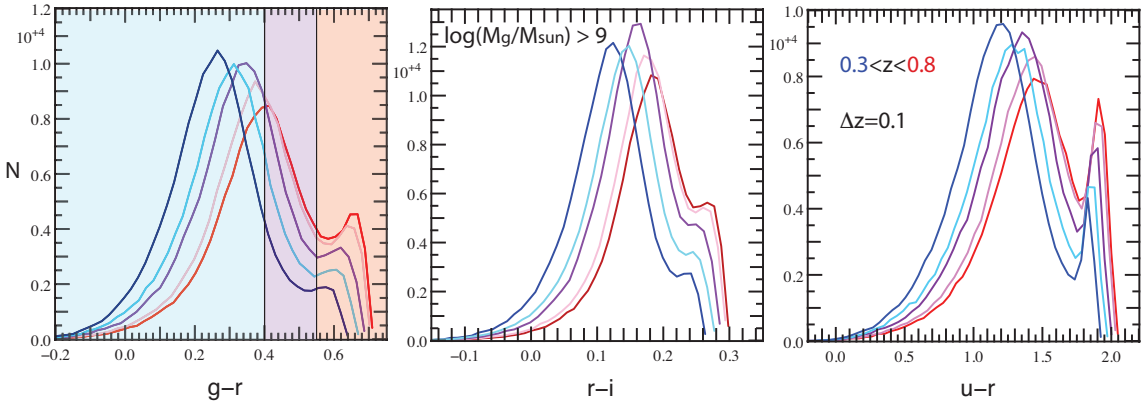

Figure 3.5: Distribution of the rest frame colors in Horizon AGN. Colored areas indicate the cuts chosen for the analysis in color bins in this paper.

The well contrasted peaks in our sample allow for the definition of three relevant bins corresponding to young star forming, intermediate and older quenched galaxies/satellites. The chosen bins are represented by specific colored areas on the first panel of Fig. 3.5 . I chose to carry out the following study with the $g-r$ color which is less sensitive to short timescale disruptions than the $u-r$ color where u encodes the highly energetic ultraviolet emission of new born stars. The cuts used to defined each population, $g-r<0.4$, $0.4<g-r<0.55$ and $g-r>0.55$, are defined in a compromising way so as to isolate the two peaks of the distribution and select populated enough samples for the analysis.

3.3 Statistical properties of the orientation of satellites

Once those synthetic galaxies are identified, I can calculate the kinematics of all satellites in the rest-frame of their host and perform a detailed analysis of the various alignment trends described in section.

3.3.1 Methods and variables

3.3.1.1 Kinematics

The kinematics are computed on the star particles for all galaxies and satellites in the sample. The angular momentum (AM) – or spin – of a galaxy is defined as the total AM of the star particles it contains and is measured with respect to the densest of these star particles (centre of the structure), which reveals an excellent estimation of the center of inertia and proves more relevant than the analytical center of mass for centrals at various stages of merging, hence including

a concentrated sub-structure:

$$\mathbf{L}_{\rm g} = \Sigma_i m_i (\mathbf{r_i} - \mathbf{r}_{\rm c}) \, (\mathbf{v_i} - \mathbf{v}_{\rm c}) \, , \tag{3.8}$$

with $\mathbf{r_i}$, m_i and $\mathbf{v_i}$ the position, mass and velocity of particle i, and center c. Notation $\mathbf{L}_{\rm g}$ is hereafter used for the AM of the central galaxy while $\mathbf{l}^{\mathbf{i}}_{\rm sat}$ designates the intrinsic AM of its i-th satellite. I also compute the total orbital AM of satellites $\mathbf{L}^{\rm orb}_{\rm sat}$ with similar definitions computed directly on the velocities and positions of satellites calculated before. Average angular velocities (for the central galaxy or its orbiting system of satellites) are defined as

$$\mathbf{v}_{\rm rot} = \frac{\Sigma_i m_i (\mathbf{r_i} \, \mathbf{v_i})}{\Sigma_i m_i r_i} \, , \tag{3.9}$$

with m_i, $\mathbf{r_i}$ and $\mathbf{v_i}$ the masses, radius and speeds of structures considered: star particles for the central galaxy, satellites for a system of satellites (replace $\mathbf{r_i}$, $\mathbf{v_i}$ and m_i by $\mathbf{r}^{\mathbf{i}}_{\rm s}$, $\mathbf{v}^{\mathbf{i}}_{\rm s}$ and $m^i_{\rm s}$). From now, I will use the notation $\mathbf{v}^{\rm gal}_{\rm rot}$ for the average angular velocity of the stellar material within the central galaxy, and $\mathbf{v}^{\rm sat}_{\rm orb}$ for the average orbital angular velocity of the system of satellites.

The position vector of each satellite in the rest frame of its central galaxy is defined as $\mathbf{r}_{\rm gs} = \mathbf{r_s} - \mathbf{r}_{\rm c}$ with $\mathbf{r_s}$ the position of the satellite. Its norm is $R_{\rm gs} = ||\mathbf{r}_{\rm gs}||$.

The inertia tensor of each galaxy is computed from its star particles' masses m_l and positions x^l (in the barycentric coordinate system of the galaxy):

$$\mathbf{I_{ij}} = \Sigma_l m^l (\delta_{ij} (x^l_k x^l_k) - x^l_i x^l_j) \, . \tag{3.10}$$

This inertia tensor is diagonalized, with its eigenvalues $\lambda_1 > \lambda_2 > \lambda_3$ being the moments of the tensor relative to the basis of principal axes $\mathbf{e_1}$, $\mathbf{e_2}$ and $\mathbf{e_3}$. Since the inertia tensor is a 3×3 real symmetric matrix, the analytical diagonalization is easily performed computing the determinant $Det(I_{ij} - \lambda)$ then solving the cubic equation in λ. The lengths of the semi-principal axes (with $a_1 < a_2 < a_3$) are derived from the moments of inertia:

$$\begin{aligned} a_3 &= (5/M_{0.5}) \sqrt{\lambda_1 + \lambda_2 - \lambda_3} \, , \text{ along } \mathrm{e}_3 \, , \\ a_2 &= (5/M_{0.5}) \sqrt{\lambda_1 + \lambda_3 - \lambda_2} \, , \text{ along } \mathrm{e}_2 \, , \\ a_1 &= (5/M_{0.5}) \sqrt{\lambda_3 + \lambda_2 - \lambda_1} \, , \text{ along } \mathrm{e}_1 \, . \end{aligned}$$

This allows for an easy estimation of the galactic shape using the triaxiality ratio $\tau = (a_2 - a_1)/(a_3 - a_2)$. Oblate structures (disky) have $\tau > 1$ while prolate structures (elongated) have $\tau < 1$.

For comparison with observations, I also define the corresponding projected quantities along the x-axis of the grid (labeled "X"). Definitions are similar for the positions and inertia tensor

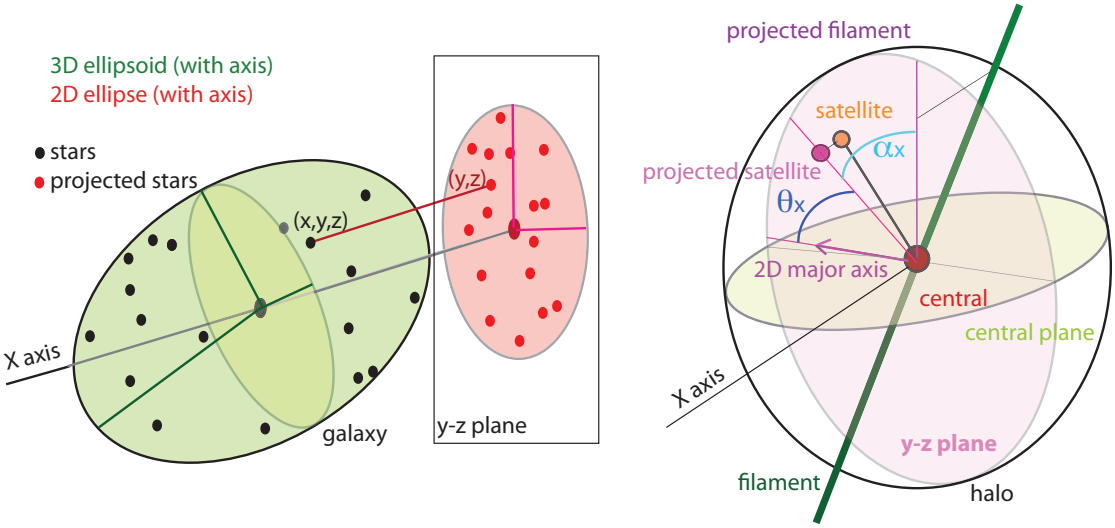

Figure 3.6: *Left panel*: 2D projection along the x axis of stellar positions and respective 3D and 2D ellipsoids that describe the shape of the galaxy. Axis of the respective inertia tensors are symbolized as colored segments, stars as black dots and their 2D projections as red dots. The bigger dots symbolize the highest density particle. In the case represented, the 3D major axis is nearly aligned with the x axis, hence the 2D major axis is still a reasonable tracer of the galactic plane. *Right panel*: Illustration of the 2D projected angles θ_X and α_X. All features in pink-purple shades are projections on the (y, z) plane containing the center of the central galaxy.

with summations restricted to the projected coordinates (y, z). This leads to the eigenvalues λ_1^X and λ_2^X, from which I derive the axis $a_1^X < a_2^X$. Fig. 3.6 illustrates the projection of stars on the 2D plane (y, z) of the grid and the consecutive calculation of the two-dimensional inertia tensor on the *left panel*. The *right panel* illustrates the definition of the projected angles α_X and θ_X which are the angles between the projected position vector of the satellite along the x-axis and direction of the projected filament and the 2D major axis respectively.

Each satellite has an individual orbital plane defined by $\mathbf{e}_\rho = \mathbf{r}_{\rm gs}/R_{\rm gs}$ and $\mathbf{e}_\theta = \mathbf{v}_{\rm ortho}/||\mathbf{v}_{\rm ortho}||$ the direction of the component of its velocity orthogonal to $\mathbf{r}_{\rm gs}$. The intersections, D_2 and D_3, of such a plane with the planes $(\mathbf{e_1}, \mathbf{e_2})$ and $(\mathbf{e_1}, \mathbf{e_3})$ of the central galaxy allow us to compute two orientation angles ζ_2 between D_2 and $\mathbf{e_2}$, and ζ_3 between D_3 and $\mathbf{e_3}$ respectively. Averaging these angles for all the satellites in the system, I obtain two angles that define the mean orbital plane for the whole system of satellites. This allows us to compute the *dispersion ratio*:

$$\frac{\sigma_{\rm plane}}{||\mathbf{L}_{\rm sat}^{\rm orb}||}, \tag{3.11}$$

with $\sigma_{\rm plane} = \sum_i ||\mathbf{j}_{\rm sat}^{\rm orb}||_i$ and $||\mathbf{j}_{\rm sat}^{\rm orb}||_i$ the norm of the projected orbital momentum of satellite i on the mean orbital plane of the whole system of satellites. This measures the dispersion of the satellites around a mean rotation plane. This parameter drops to zero if satellites are all rotating

in the same plane.

Similarly, I measure the *corotation ratio*:

$$\frac{|L_{\rm zc}|}{||\mathbf{L}_{\rm sat}^{\rm orb}||}\,, \tag{3.12}$$

with $L_{\rm zc}$ the projection of the total orbital momentum on the spin axis of the central galaxy.

3.3.1.2 Choice of variables: benefits and limitations

The objectives of this work are to investigate two specific alignment trends of satellites galaxies:

- **the tendency of satellites to lie in the galactic plane of their central host**: the *coplanar trend* . This can be analyzed computing either $\mu = \cos(\theta)$ the cosine of the angle between the satellite's position vector $r_{\rm gs}$ and the spin of the central, or $\mu_1 = \cos(\theta_1)$ the cosine of the angle between $r_{\rm gs}$ and the minor axis of the central (vector e_1). In this work, I mostly focus on this latter measurement which is more closely related to observational methods and gives a smoother signal.
- **the tendency of satellites to align within the nearest filament** - from which they flowed into the halo: the *filamentary trend*. To carry out this study, I compute $\nu = \cos(\alpha)$ the cosine of the angle between the satellite's position vector $r_{\rm gs}$ and the direction of the closest filament.

As in the previous chapter, the choice of the cosine statistics is natural since the analysis is performed on the three-dimensional (3D) kinematics since I want to compare angular distributions (say $P(\theta)$) around a given axis to the 3D unbiased angular distribution $P_{\rm u}(\theta)$: if angles are uniformly distributed on the sphere. Thus the uniform probability density function is $\rho_{\rm u}(\theta) \propto \sin\theta$ but is flat with respect to $\cos\theta$: $\rho_{\rm u}(\cos\theta) \propto cst$, which allows for an easy direct comparison.

It is however important to notice that a similar calculation in 2D (angles uniformly distributed on a circle) yields to $\rho_u^{2D}(\theta) \propto cst$, which implies that one should follow the PDF of θ when analyzing projected alignment trends that directly compare to observations. Thus, in this work I also analyze the PDF of the projected angles θ_X and α_X.

A somewhat more subtle effect that needs to be checked in order for this method to be relevant is whether or not, in a filament adapted spherical frame, the azimuth angle ($\alpha_{\rm 2D}$ on Fig. 3.7) is distributed randomly on the circle. Failure to fulfill this condition can mimic fake alignment signals for the cosine statistic since $\rho_{\rm u}(\cos\theta)$ cannot be assumed to be constant anymore. However, $\alpha_{\rm 2D}$ cannot be expected to be randomly distributed on the largest scales of the simulation as

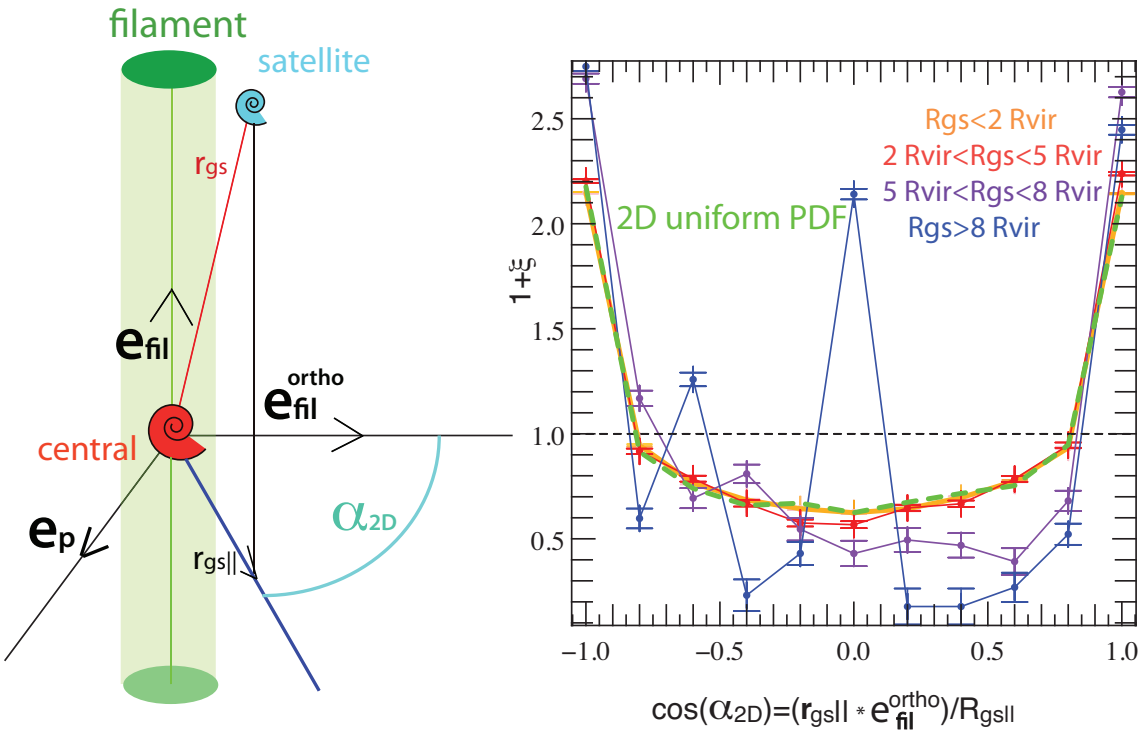

Figure 3.7: PDF of $\cos\alpha_{2D}$, the cosine of the angle between $\mathbf{e}_{\rm fil}^{\rm ortho} = \mathbf{e}_{\rm fil} \times \mathbf{x}$ and $\mathbf{r}_{\rm gs_{||}}$, the projection of $\mathbf{r}_{\rm gs}$ on the plane orthogonal to the filament (of norm $R_{\rm gs_{||}}$), with $\mathbf{e}_{\rm fil}$ the direction vector of the central galaxy's nearby filament and $\mathbf{x}$ the x direction of the grid, for all galaxies with $M_{\rm g} > 10^{10.5}\,{\rm M}_\odot$. The random circular distribution for $\cos\alpha_{2D}$ is over plotted in green. The satellite distribution can be considered random up to $R_{\rm gs} = 5\,R_{\rm vir}$. On larger scales, incomplete randomization of the wall directions in the simulated volume leads to significant deviations.

matter tend to be distributed in walls — the halo relevant scale of which is set by our cosmic web characterization — whose directions cannot be assumed to be random in the volume considered.

Fig. 3.7 shows the distribution of $\cos(\alpha_{2D})$, the angle between $\mathbf{e}_{\rm fil}^{\rm ortho} = \mathbf{e}_{\rm fil} \times \mathbf{x}$ and the projection of $\mathbf{r}_{\rm gs}$ on the plane orthogonal to the filament, with $\mathbf{e}_{\rm fil}$ the direction vector of the central galaxy's nearby filament and $\mathbf{x}$ the x direction of the grid. This distribution is restricted to the highest mass range studied: central galaxies with $M_{\rm g} > 10^{10.5}\,{\rm M}_\odot$. One can notice that for satellites within $R_{\rm gs} < 5\,R_{\rm vir}$, the signal is really well fitted by the 2D uniform PDF with a deviation inferior to 0.5% in ξ. However for satellites at larger distances, the PDF shows important deviations from the uniform PDF (up to 25%).

This naturally sets the maximal scale that can be probed with the 3D cosine statistic to $5\,R_{\rm vir}$ of the most massive halos.

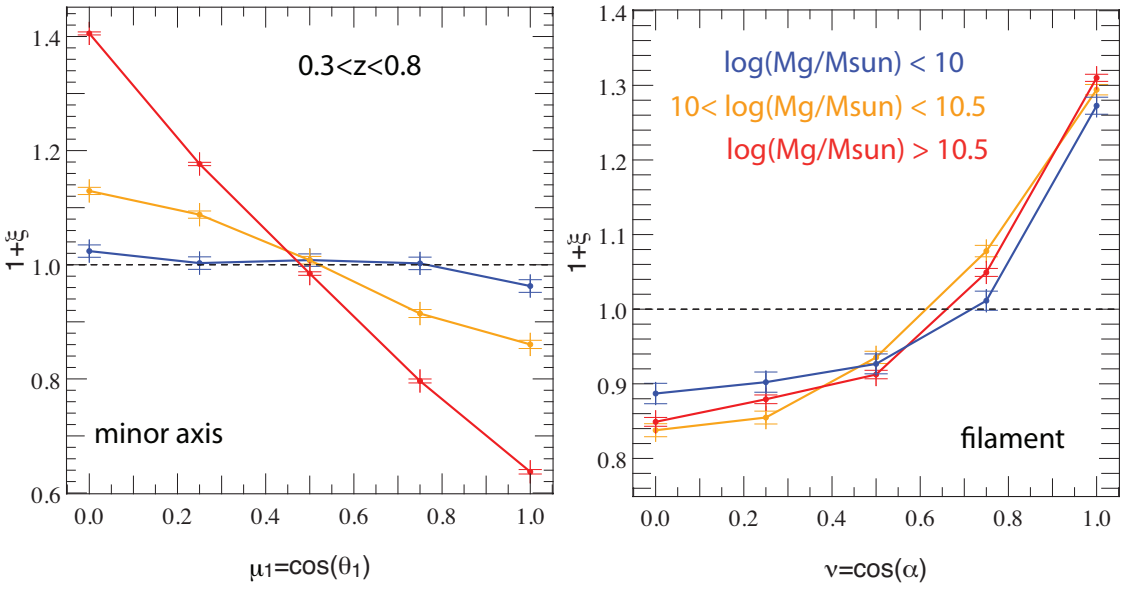

Figure 3.8: Left panel: excess PDF ξ of $\mu_1 = \cos\theta_1$, the angle between the minor axis of the central galaxy and the direction towards the center of mass of its satellites, for different central galaxy mass bins and between redshift $0.3 < z < 0.8$. Results are stacked for 6 outputs equally spaced in redshift. Satellites tend to distribute in the galactic plane of the central and this trend is stronger with the increasing mass of the central. Right panel: excess PDF of $\nu = \cos\alpha$, the cosine of the angle between the direction of the central's nearest filament axis and the direction towards the center of mass of its satellites. Satellites tend to be strongly aligned within the embedding filament.

3.3.2 Results

3.3.2.1 A mass segregated signal

Coplanar trend: Let me first analyze how the two trends evolve with respect to the stellar mass M_g of the central galaxy using the 3D kinematics.

Left panel of Fig. 3.8 shows the probability density function (PDF, ξ is the excess of probability density above 1) of $\mu_1 = \cos\theta_1$, where θ_1 is the non-oriented angle between the minor axis of the central galaxy and $\mathbf{r}_{gs}$ for different mass bins of the central galaxy. As explained in Section. 3.2.1, I accumulate the results of satellite distribution around central galaxies of the 6 Horizon-AGN outputs in the redshift range $0.3 < z < 0.8$ equally spaced in redshift bins and consider only satellites within $5\,R_{vir}$ of the halo host of the central. The main effect of this stacking is a smoothing of the signal. It was checked that results for individual snapshots are fully consistent with the stacked results, although with increased error bars.

Satellites have a tendency to lie in the galactic plane of the central galaxy, or equivalently, perpendicular to the minor axis of the galaxy as shown by the excess PDF ξ at $\mu_1 = 0$ (see

Aubert *et al.* , 2004, for the corresponding estimate for DM satellites). However, this conclusion does not hold for all central galaxies: while the distribution of satellites around their host is mostly random for low-mass centrals with $10^9\,\mathrm{M}_\odot < M_\mathrm{g} < 10^{10}\,\mathrm{M}_\odot$, the alignment strengthens as the central mass increases. For the most massive centrals, galaxy satellites clearly tend to be more distributed in the plane of the central galaxy.

For central galaxies with stellar mass $M_\mathrm{g} > 10^{10.5}\,\mathrm{M}_\odot$, the excess PDF at $\mu_1 = 0$ is $\xi = 40\%$, with 52% of satellites lying within a 33° cone ($\cos\theta_1 < 0.4$) around their projection on the galactic plane, as opposed to 40% for the uniform PDF (in dashed line). For intermediate central masses ($10^{10} < M_\mathrm{g} < 10^{10.5}\,\mathrm{M}_\odot$), the excess PDF at $\mu_1 = 0$ is $\xi = 13\%$, and 45% of satellites lie in the 33° cone. No substantial excess is found for lower masses ($\xi < 2\%$ at $\mu_1 = 0$). Thus the tendency of satellites to lie in the galactic plane of their host is directly correlated to its mass. Reasons for this can involve the mass segregation in the orientation of the galactic spins with respect to nearby filaments developed in the previous chapter, closely related mass-morphology correlations or gravitational torques of mass dependent strength.Codis *et al.* (2012); Dubois *et al.* (2014); Welker *et al.* (2014) and Laigle *et al.* (2015) confirmed that massive haloes and galaxies formed through mergers tend to display a spin orthogonal to their nearby filament (which is therefore contained in the galactic/rotation plane) while low-mass haloes/galaxies caught in the winding around of the cosmic flows in the vicinity of filaments are more likely to have a spin parallel to their filament.

In order to better discriminate these effects, one needs to analyze the correlations between this trend and the orientation of the closest filament. First, let us investigate the tendency of satellites to align with this very filament.

Filamentary trend: In the right panel of Fig. 3.8, one can see the excess PDF of $\nu = \cos\alpha$, the angle between the direction of the central's nearest filament axis and r_gs. Galaxy satellites tend to align in the filament axis direction of the central galaxy with $\xi \simeq 30\%$ rather independently of the central galaxy mass (slight increase of ξ with M_g). 27% of the satellites' vector positions are contained within a 37° cone around the filament ($\cos\alpha > 0.8$), as opposed to 20% for angles uniformly distributed on the sphere. This effect still holds even for the smallest host masses with a decrease in amplitude of less than 1%.

These trends are in line with statistical measurements of the orientation of the spin of galaxies in the cosmic web presented in the last chapter: low-mass young galaxies fed in vorticity rich regions at the vicinity of filaments (Laigle *et al.* , 2015) have their spin parallel to the filament their are embedded in, while older galaxies, more likely to be the products of mergers, are also more likely to

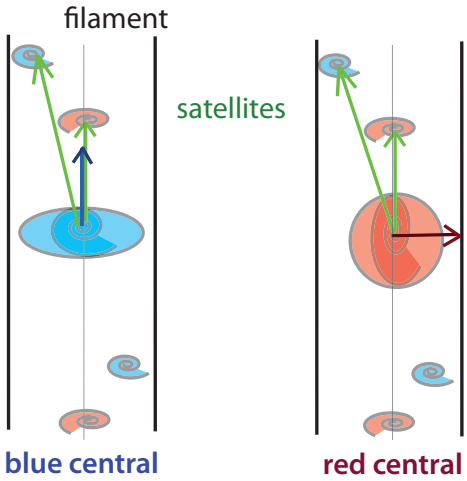

Figure 3.9: Sketch of the expected results for the *filamentary trend*. Satellite galaxies tend to be aligned within the nearest filament. they are consecutively orthogonal to the spin of older red (massive) galaxies, and more often aligned with the spin of young blue (low-mass) galaxies.

display a spin flipped orthogonal to the filament due to the transfers of orbital angular momentum during merger (Dubois *et al.* , 2014; Welker *et al.* , 2014).

The trends measured in Fig. 3.8 can therefore be explained by arguing that satellite galaxies tend to be distributed along the closest filament of the central. The alignment in the galactic plane is, thus, a direct consequence of:

- the dynamical angular bias: the fact that the galactic plane contains the ridge line defining the filament, therefore the preferential direction of the filamentary accretion. This corresponds to the case of the red central galaxy on the illustration in Fig. 3.9.
- the geometrical angular anisotropy: the fact that the host halo is mostly elongated in the direction of this very filament – which corresponds to the slowest compression axis of the shear tensor – resulting in an angular anisotropy tracing the halo density.

In this picture, the *coplanar trend* is a consequence of the *filamentary trend*. However, whether the first trend can be neglected when using satellites as tracers of the underlying DM density remains an open question. Moreover, the shape of central galaxies is not necessarily strongly correlated with the diffuse DM component on the outer parts of the halo: low-mass disc galaxies which can be responsible for additional gravitational torques (Kazantzidis *et al.* , 2004b; Dong *et al.* , 2014) and are most likely elongated orthogonally to the filament (Dubois *et al.* , 2014). Moreover I will show that many massive centrals in Horizon-AGN show a significant amount of misalignment between

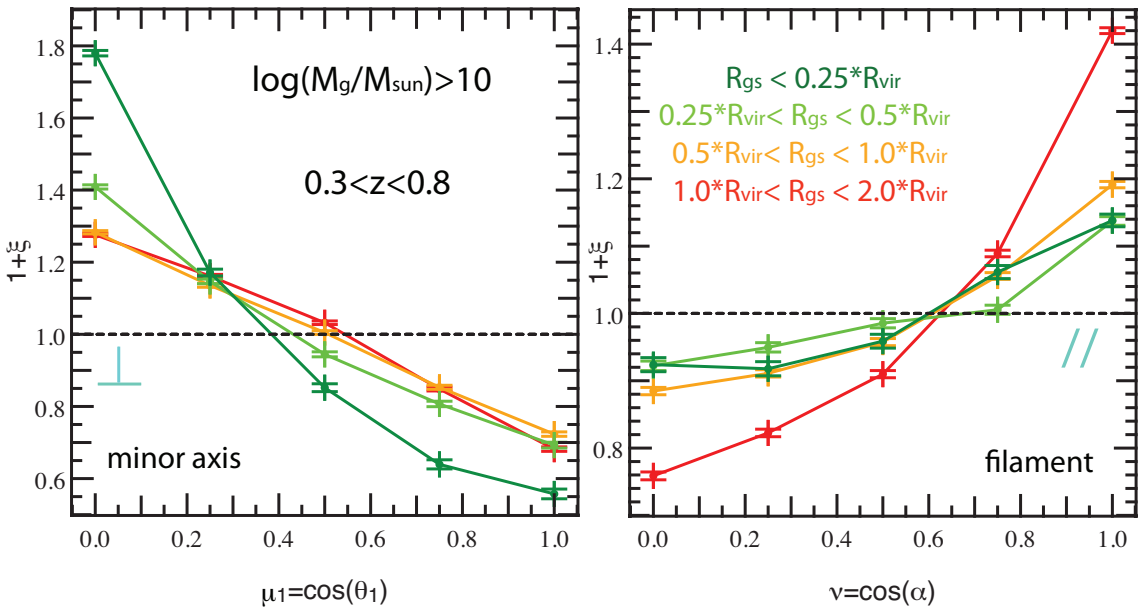

Figure 3.10: Same as Fig. 3.8 where samples are binned in distance from satellite to central $R_{\rm gs}$. Satellites close to the central galaxy tend to be distributed in the galactic plane with marginal alignment to the filament, while satellites in the outskirt of the host halo of the central are strongly aligned with the filament but the coplanarity with the central galaxy is weakened.

their galactic plane and the nearby filament. It is therefore important to study how this affects the two above described trends and to what extent those specific cases impact the general distribution.

3.3.2.2 The *filamentary* trend versus the *coplanar* trend

Quantifying the relative influence of the filament and the joint effect of dissipation in the halo and central galaxy torques (that also imposes the inner halo shape) is best achieved by noticing that these processes operate on different radial scales (Danovich *et al.* , 2015). Let me investigate how satellite galaxies distribute with distance to their central companion. Fig. 3.10 shows the excess PDF of $\mu_1 = \cos\theta_1$ (central galaxy minor axis) and $\nu = \cos\alpha$ (filament axis) for different bins of $R_{\rm gs} = ||\mathbf{r}_{\rm gs}||$, the distance from the satellite to the central galaxy.

One can see that, as the distance increases, the alignment in the galactic plane weakens progressively while the alignment with the filament is strengthened. For satellites in the vicinity of their host, within sphere of radius $R_{\rm gs} = 0.25\,R_{\rm vir}$, the *coplanar trend* is highly dominant with $\xi = 80\%$ at $\mu_1 = 0$, and with 60% of the satellites within a 33° conical flange around the galactic plane (40% for random), while the *filamentary trend* is reduced to a 12% excess within a 37° cone around the filament axis, hosting 23% of the satellites (20% for random).

In contrast, for satellites in the outskirt of the halo with $R_{\rm gs} > R_{\rm vir}$ the *filamentary trend* dominates with this same excess soaring to 41% at $\nu = 1$ hosting 28% of the satellites in a 37° cone around the filament axis (20% for random), and the amount of satellites within the galactic plane related 33° conical flange falls down to 48% (40% for random).

This investigation of satellite alignment with distance to the central galaxy shows that the *coplanar trend* is not a mere consequence of the *filamentary trend* as they exhibit competitive patterns, with the coplanarity being dominant in the vicinity of the central host, which is also the area and the filamentary orientation in the outskirt of the halo. Hence, the dynamical bias introduced by the *filamentary trend* can reach an amplitude comparable to that of the *coplanar trend* for satellites within $0.5\,R_{\rm vir} < R < R_{\rm vir}$ from their central galaxy.

In order to confirm that both trends are intrinsic and to better understand where and to what extent this competition occurs, Fig. 3.11 focuses on two sub-samples, which I select so as to preserve statistics:

- satellites whose central minor axis is *aligned* to the filament axis within a 37° cone ($\cos\theta_g > 0.8$), like the blue galaxy on the illustration of Fig. 3.9 ,
- satellites whose central minor axis is *perpendicular* to the filament axis within a 37° conical flange around the filament axis ($\cos\theta_g < 0.45$), like the red galaxy on the illustration of Fig. 3.9) .

In the first case (green lines), the coplanarity and filamentary trends are mutually exclusive, while in the second case they affect the distribution of satellites in similar ways and add up to one another. Fig. 3.11 shows the excess PDF ξ of $\mu_1 = \cos\theta_1$ and $\nu = \cos\alpha$ for both samples in different mass ranges for the central galaxy. Following the first sample of centrals, one can see that the coplanar trend dominates for the most massive central galaxies ($M_{\rm g} > 10^{10.5}\,{\rm M}_\odot$) with 43% of satellites in the galactic plane related 33° conical flange (40% for random), even though the filamentary trend has vanished. However, the coplanar trend disappears as the central mass decreases ($M_{\rm g} < 10^{10.5}\,{\rm M}_\odot$). In contrast, the filamentary trend is recovered for central galaxies with mass $M_{\rm g} < 10^{10.5}\,{\rm M}_\odot$, which shows a greater alignment to the filament (24% in the filament 37° cone instead of 20% for random).

Following the second sample of central galaxies whose minor axis is more perpendicular to the filament axis (orange lines), coplanarity and filamentary trends coexist in all mass bins. Both trends are strengthened for the most massive central galaxies ($M_{\rm g} > 10^{10.5}\,{\rm M}_\odot$), which confirms the distinct influences of the galactic plane and the filament in the orientation of satellites. The signals for this sample are significantly higher than signals obtained when the trends compete.

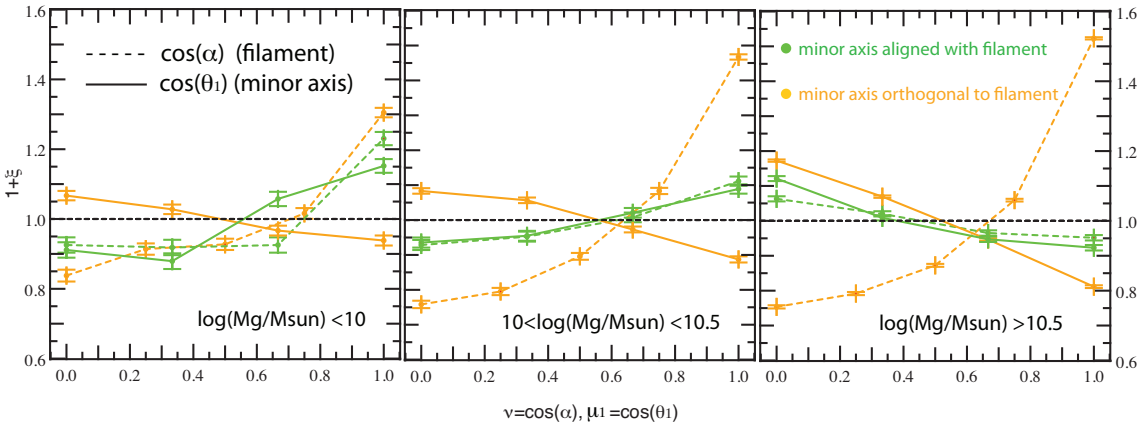

Figure 3.11: Evolution of the *filamentary trend* (dashed line) and the *coplanar trend* (solid line) for either central galaxy's minor axis aligned to the filament axis within a 37° cone (in green), or 2), or central galaxy's minor axis perpendicular to the filament axis within a 37° cone (in orange). From left to right panel, this shows three different central galaxy mass bins $M_{\rm g}$ as indicated in the panels. Following the green lines: the two trends compete in this case. The *coplanar trend* takes over for massive hosts while the *filamentary trend* is dominant for low mass hosts. Following the orange lines: the two trends add up in this case. Expectedly, the trends are strengthened for most massive hosts.

Corresponding satellite fractions are 46% for the 33° conical flange around the central galactic plane and 32% for the 37° cone around the spin axis of the central for the highest mass range.

Confirmation of the scale segregation inherent to this competition between the coplanarity and the filamentary trend can be found in Fig. 3.12. It shows the excess PDF of μ_1 and ν for different distances of satellites to the central galaxy similar to the one in Fig. 3.10 but restricted to the first sample, for which trends are mutually exclusive, as seen in Fig. 3.11. The transition between the filamentary trend far from the central galaxy and the coplanar trend in its vicinity is striking, with a 50% excess in the 37° cone around the filament axis (30% of satellites instead of 20% for random) at $R_{\rm gs} > 2\,R_{\rm vir}$ – and no detectable coplanarity with the central at that distance – that progressively decreases and turns to a 20% excess in a 33° conical flange orthogonal to the filament for $R_{\rm gs} < 0.25\,R_{\rm vir}$, associated to a $\xi = 70\%$ excess at $\mu_1 = 0$, corresponding to 59% of satellites in the 33° conical flange around the galactic plane (40% for random).

For further confirmation of this transition, Fig. 3.13 reproduces the analysis of Fig. 3.10 for three different central mass bins: $10^9 < M_{\rm g} < 10^{10}\,{\rm M}_\odot$, $10^{10} < M_{\rm g} < 10^{10.5}\,{\rm M}_\odot$ and $M_{\rm g} > 10^{10.5}\,{\rm M}_\odot$. The evolution of both trends with respect to the mass of the central is fully consistent with the strength of torques from the central and its average mass-dependent orientation in the cosmic web.

This confirms the general tendency already observed for all central galaxies with $M_{\rm g} > 10^{10}\,{\rm M}_\odot$

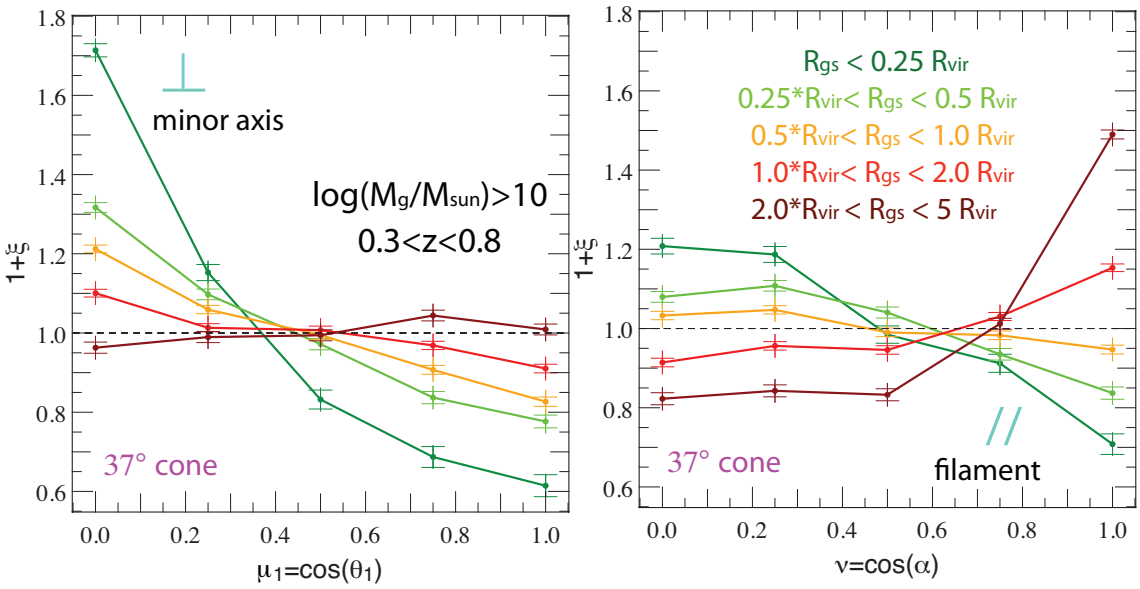

Figure 3.12: Same plot than Fig. 3.10 restricted to satellites whose host's minor axis is aligned to the nearest filament within a 37° cone, in which case the two trends compete. Results are stacked for $0.3 < z < 0.8$ for different radius R_{gs} (distance to the central galaxy) bins. Satellites close to their host tend to be distributed in the galactic plane hence orthogonally to the filament while satellites in the outskirt of the halo are strongly aligned with the filament but the coplanarity with their host is lost.

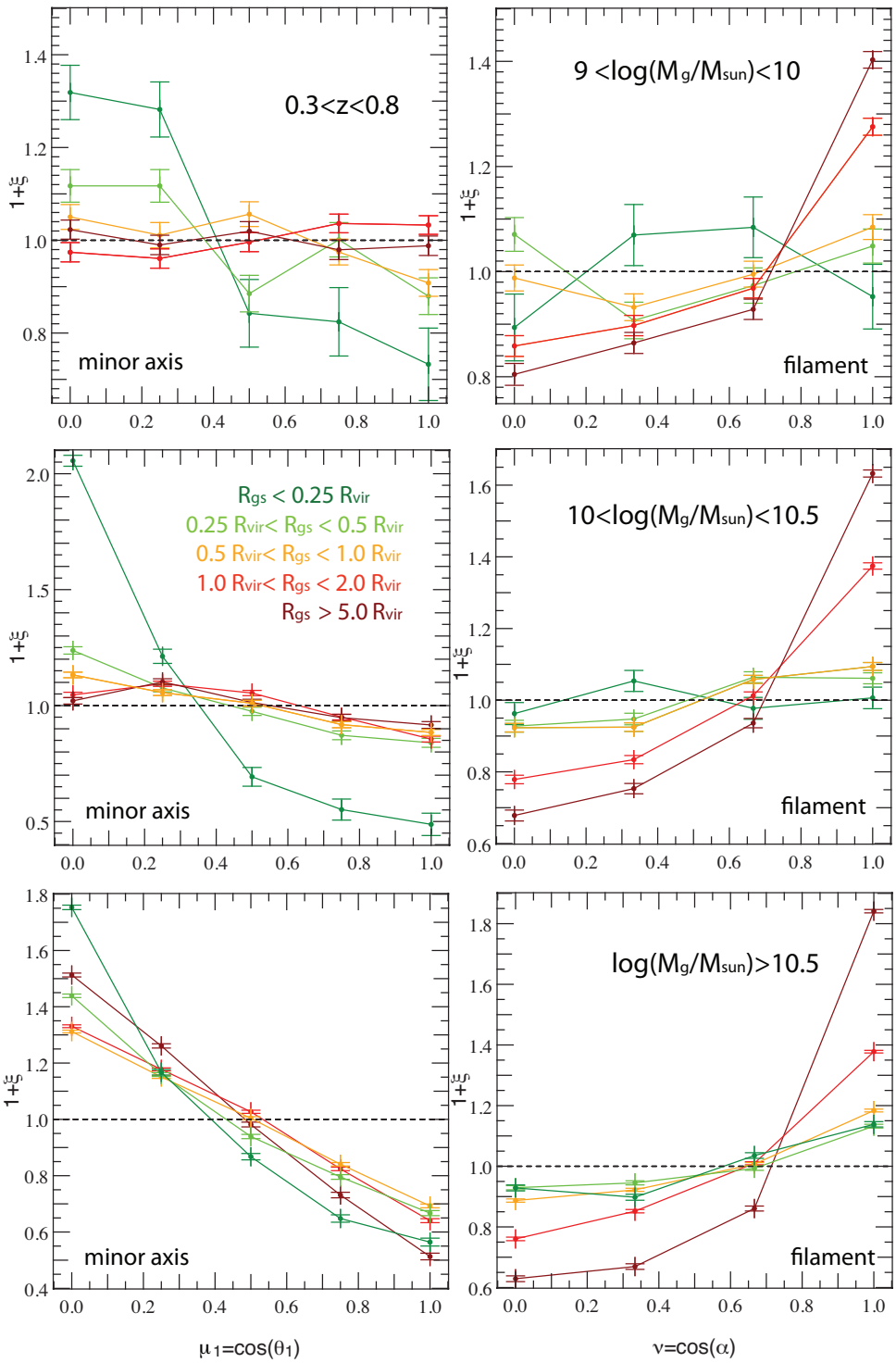

Figure 3.13: Same as Fig. 3.8 where samples are binned in distance, $R_{\rm gs}$, from satellite to central. This is plotted for three different central mass bins: $10^9 < M_{\rm g} < 10^{10}\,{\rm M}_\odot$ (top panels), $10^{10} < M_{\rm g} < 10^{10.5}\,{\rm M}_\odot$ (middle panels) and $M_{\rm g} > 10^{10.5}\,{\rm M}_\odot$ (bottom panels). Satellites close to the central galaxy tend to be distributed in the galactic plane with marginal alignment to the filament, while satellites in the outskirt of the host halo of the central are strongly aligned with the filament but the coplanarity with the central galaxy is weakened. Results are stacked for $0.3 < z < 0.8$.

in Fig. 3.10: satellites in the outskirt of the halo are aligned with the nearest filament. As they reach inner parts of the halo they deviate from the filament to align in the galactic plane of their central host. Specific features in each mass bin tend to confirm the general scenario:

- For low mass centrals, the *coplanar trend* is significantly weaker than for centrals with $M_{\rm g} > 10^{10}\,{\rm M}_{\odot}$ (for satellites within 0.25 $R_{\rm vir}$: $\xi = 30\%$ at $\cos\theta_1 = 0$ instead of $\xi \simeq 100\%$ for the two highest mass ranges). This is consistent with a weaker torquing of lower mass centrals. However, the flip from the *filamentary trend* to the *coplanar trend* is more distinctive than for higher mass bins, which is directly related to the fact that those small mass centrals are under the swing transition mass evaluated in Dubois *et al.* (2014), and therefore are more likely to have a minor axis aligned with the filament, in which case both trends compete.

- The *filamentary trend* in the outskirt of the halo is mildly affected by the mass of the centrals. As expected, it undergoes a little increase and persists at shorter distances from the host for high mass centrals for which *filamentary* and *coplanar* trends are more likely to add up to each other.

- For most massive central galaxies, the *coplanar trend* shows a general evolution very similar to that observed for lower masses but experiences a new increase – although somewhat limited – for satellites in the most outer parts of the halo ($R_{\rm gs} > 2\ R_{\rm vir}$). Satellites so distant can actually be satellites of a neighboring cluster. Thus, this trend is reminiscent of the Binggeli effect (Binggeli, 1982) that applies for massive clusters, which tend to align their rotation plane to that of their neighbours. This evolution is therefore a hint of the two-halo term and will be discussed in further details in an upcoming paper by Chisari *et al.* (2015).

An illustration of the evolution with distance to the central can be found in Fig. 3.19. The competition between the coplanar and filamentary trends may represent a real source of angular bias in the distribution of satellites since the filamentary trend generates a dynamical angular bias, which leads to either overestimate or underestimate the non-sphericity of the halo, inferred from the angular anisotropy in the distribution of its satellites assumed to be unbiased. None of these situations appears to be negligible since *aligned spin* galaxies with filament (angle smaller than 33°) represent 15% of all central galaxies with $M_{\rm g} > 10^{10}\,{\rm M}_{\odot}$, *orthogonal spin* galaxies (angle larger than 45°) 60% and moderate misalignment cases 25% (angle between 33° and 45°). This suggests that the contradictory results that have been claimed from observations since the Holmberg (1969) first results are mass and scale dependent, possibly as Zaritsky *et al.* (1997) suggested. The correct inference of a halo's non-sphericity from the distribution of its satellites would therefore depend on a reasonable estimate of the orientation of the nearby filamentary structure.

3.4 A dynamical scenario : satellites migrating into the halo.

3.4.1 Scenario

Considering our previous model of satellite migration down to the core of its halo through a combination of dynamical friction and tidal stripping, this evolution in distance provides some insights on the dynamical evolution satellites within their host halo. The main results of the previous section call for a dynamical scenario in which young star-forming satellites flow along the cold gas rich filament and plunge into the halo where their orbits can be progressively deviated from the filament by gravitational torquing from their host and angular momentum transfer from the halo which tend to flip it in the galactic plane. In effect, their fate is reminiscent of that of the cold gas at higher redhsift ($z > 1$), which pervade as cold flows down to the core of central galaxies in formation (Pichon *et al.* , 2011; Codis *et al.* , 2012; Tillson *et al.* , 2015). An important result is that high-redshift gas inflow in the frame of the galaxy is qualitatively double helix-like along its spin axis (Pichon *et al.* , 2011). It was generated via the same winding/folding process as the protogalaxy, and it represents the dominant source of filamentary infall at redshift $z \simeq 2-3$ which feeds the galaxy with gas with well aligned angular momentum (Pichon *et al.* , 2011; Danovich *et al.* , 2015).

Here I argue that the distribution of satellites in that frame at $z < 0.8$ somewhat traces that of the gas at $z > 1$, which is directly correlated with the idea that satellites have progressively formed in the gas streams, and which is of particular interest since the distribution of satellites can be observed. This is not completely obvious, as the gas, unlike the satellites, can shock in the CGM. In this picture, older quenched satellites in the vicinity of the halo end up rotating altogether in the galactic plane, which suggests that torquing from the disc dominates over the effect of shocks. To test this idea, let us further investigate the tendency of red and blue satellites to follow the *filamentary trend* and the *coplanar trend*, and their corotation with their host galaxy.

3.4.2 Corotation of satellites

To test the importance of the intrinsic torques of the central galaxy on its orbiting satellites, let us first study their rotation around the central galaxy. Fig. 3.14 shows the rescaled PDF $1 + 2\xi$ of $\cos\phi$, the cosine of the angle between the spin of the central galaxy and the total orbital momentum of its satellites in the rest-frame of their host, for $0.3 < z < 0.8$. I study the evolution with mass in the left panel, but also the evolution with distance to the host, $R_{\rm gs}$, in the middle panel.

Trends with mass and radius confirm the tendency of satellites to rotate in the galactic plane of their host with angular velocities of the same sign in the rest-frame of the host galaxy. This trend is observed for satellites of massive hosts ($M_{\rm g} > 10^{10}\,{\rm M}_\odot$) and within $2\,R_{\rm vir}$, increasing with the

mass of the host and decreasing with distance $R_{\rm gs}$. For satellites within a $R_{\rm gs} < 0.5\,R_{\rm vir}$ sphere around their host galaxy, I observe that 21.5% of them display an orbital angular momentum that remains within a 40° cone around the spin of their host and rotate in the same direction (12.5% for random). In contrast, counter-rotation is more unlikely in the vicinity of the central galaxy, with only 8% of the sample counter-rotating within a cone of 40°. (12.5% for random) The relative orientation of the satellite's orbital angular momentum and the spin of the central galaxy is close to the random distribution outside the halo of the central galaxy, where satellites motions are governed by the filamentary flow. Those results are consistent with the idea that the transfer of orbital angular momentum of satellites and intrinsic angular momentum of its host (halo and central galaxy), through dynamical friction and gravitationnal torques. This exchange of angular momentum drives the evolution of the orbital angular momentum satellites, which end up co-rotating in the galactic plane, as they are dragged deeper into the halo. This evolution shows that this second dynamical effect is qualitatively distinct from the *filamentary trend*, the later being dominant outside the halo. More massive central galaxies, and, therefore, halo hosts, influence the satellite orbital angular momentum more strongly: the excess probability at $\cos\phi = 1$ is 3 times higher for centrals with $M_{\rm g} > 10^{10.5}\,{\rm M}_\odot$ than for centrals with $M_{\rm g} < 10^{10}\,{\rm M}_\odot$.

To confirm this evolutionary picture, the right panel of Fig. 3.14 shows the PDF of $(v^{\rm sat}_{\rm orb} - v^{\rm gal}_{\rm rot})/(v^{\rm sat}_{\rm orb} + v^{\rm gal}_{\rm rot})$ for different distance bins, with $v^{\rm sat}_{\rm orb}$ and $v^{\rm gal}_{\rm rot}$ corresponding to the angular velocities of the system of satellites (i.e. the orbital velocity) and of the central galaxy, respectively. In the outer region of the halo, $R_{\rm gs} > 0.5\,R_{\rm vir}$, the average orbital velocity of satellites around their host is found to be lower than the angular velocity of the central host around its spin axis but $v^{\rm sat}_{\rm rot}$ increases in the inner part of the halo. Satellites therefore increase their angular velocity, synchronize with their host as they reach the inner halo and achieve corotation within $0.5\,R_{\rm vir}$ of the halo. Two effects are competing: conservation of angular momentum tend to increase the amount of rotational velocity as satellites goes deeper in the halo, but the dynamical friction enforces the orbital motions of satellites to synchronise with the rest of the material in the halo, and this effect is stronger in the densest regions of the halo, i.e. in the center.

However, the orbital angular momentum of satellites (not represented in Fig. 3.15) decreases for satellites closer to the host (by a factor 3 between $R_{\rm gs} < 5\,R_{\rm vir}$ and $R_{\rm gs} < 0.5\,R_{\rm vir}$). Comparing the ratios between $L_{\rm zc}$, the component of the orbital angular momentum aligned with the spin of the central galaxy (in the lower right panel) and the dispersion $\sigma_{\rm plane}$ (in the upper right panel), both normalised to total orbital angular momentum, one should notice on Fig. 3.15 *Left panel* that the relative importance of the aligned component increases for satellites closer to the host (from 60% to 70%) while om *Right panel* the relative amplitude of the dispersion between the satellite's

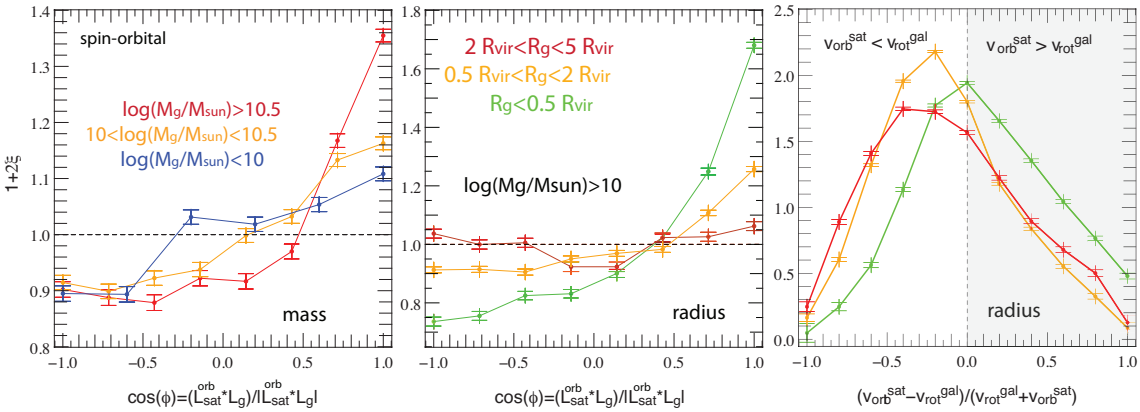

Figure 3.14: Twice the PDF of $\cos\phi$, the cosine of the angle between the spin of the central galaxy and the total orbital momentum of its satellites for $0.3 < z < 0.8$ for different mass bins (left panel) and radius $R_{\rm gs}$ bins (middle panel). For massive central galaxies, the orbital angular momentum of satellites tend to align with the galactic spin of the central, especially in its harbour. Right panel: excess PDF of $(v_{\rm orb}^{\rm sat} - v_{\rm rot}^{\rm gal})/(v_{\rm orb}^{\rm sat} + v_{\rm rot}^{\rm gal})$ for different radius bins, with $v_{\rm orb}^{\rm sat}$ and $v_{\rm rot}^{\rm gal}$ the angular velocities of the satellites system and of the host galaxy respectively. satellites increase their angular velocity and synchronize with their host as they reach the inner halo.

orbits drops from 120% to 20% between $2\,R_{\rm vir}$ and $0.25\,R_{\rm vir}$. This is consistent with the fact that orbits of satellites progressively become coplanar. On average satellites lose angular momentum as they are dragged deeper into the halo but these trends reveal a segregation between the different components of the satellite orbital angular momentum: the component aligned to the spin of the central galaxy is better preserved as satellites reach the inner parts of the halo.

I show in the next section that the evolution of satellites' age as traced by colours is also consistent with this mechanism. To trace the age of satellites I rely on the rest-frame colors computed from the AB magnitudes as described in section. 3.2.2.

3.4.3 Evolution of satellites within the halo

So far, I only followed the evolution of alignment trends with respect to distance to the host. Although it can be reasonably expected to trace the evolution in time of satellites entering a host halo, It was explained in section 3.1.1.2 that the radius decay of a given satellite depends on numerous parameters, including the eccentricity of its orbit. To further confirm the dynamical aspect of the previous trends, I analyze their evolution with respect to rest-frame colors of the satellites, used as tracers of their age and progressive strangulation from their host.

Fig. 3.16 *right panel* shows the PDF of $\cos\phi$, the angle between the spin of the central galaxy and the total orbital angular momentum of its satellites for $0.3 < z < 0.8$ and for different satellite $g - r$ color bins One can see that red satellites have an orbital plane better aligned with the

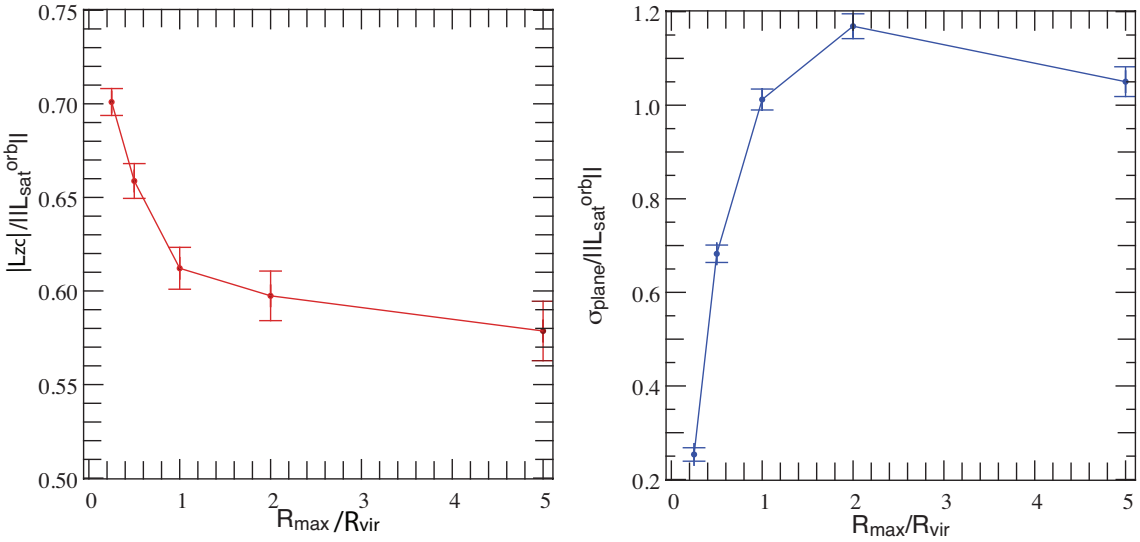

Figure 3.15: *Left panel:* Evolution of the orbital dispersion momentum $\sigma_{\rm plane}$ over the norm of the total satellite orbital momentum for systems of satellites enclosed in spheres of increasing radius around their central host. *Right panel:* Evolution of the ratio between the component of the satellite orbital momentum aligned to the spin of the central galaxy over the norm of the total satellite orbital momentum.

galactic plane on average than their blue counterparts (24% of the sample within the 33° cone around for $g-r>0.55$, and around 21.5% for $g-r<0.4$. Moreover, Fig. 3.16 *left panel* shows the average distance of satellites to the central as a function of their color for satellites within $5\,R_{\rm vir}$: red galaxies are closer to the central ($\simeq 1.3\,R_{\rm vir}$) than blue galaxies ($\simeq 0.9\,R_{\rm vir}$). Therefore, red satellites are more clustered around the central galaxies than blue satellites, as an effect of ram-pressure stripping and strangulation that respectively removes the gas from satellites and prevents further gas accretion onto them as they evolve in the hot pressurised atmosphere of the halo host of the central.

In conclusion, satellites orbits are closer to coplanarity with the central galaxy as they get closer to it and get progressively deprived of their star forming gas. Sketch orbits of such satellites are represented by blue lines on the illustration of Fig. 3.19.

As can be seen in the left panel of Fig. 3.17, I also found that satellites not only align their orbital plane to the galactic plane, but also align their spin (intrinsic angular momentum) with that of the central galaxy as they reach the inner parts of the halo. In fact, cuts in mass and distance $R_{\rm gs}$ lead to similar results as for $\cos\phi$, when applied to $\cos\chi$, the cosine of the angle between the host galaxy's spin and the satellite's spin, though the signal is weaker and rapidly decreasing with distance to the host. Nonetheless, within a $0.5\,R_{\rm vir}$ sphere around their host, satellites have a $\xi=9\%$ excess probability to stay within a 37° cone around the spin of their host (22% of the

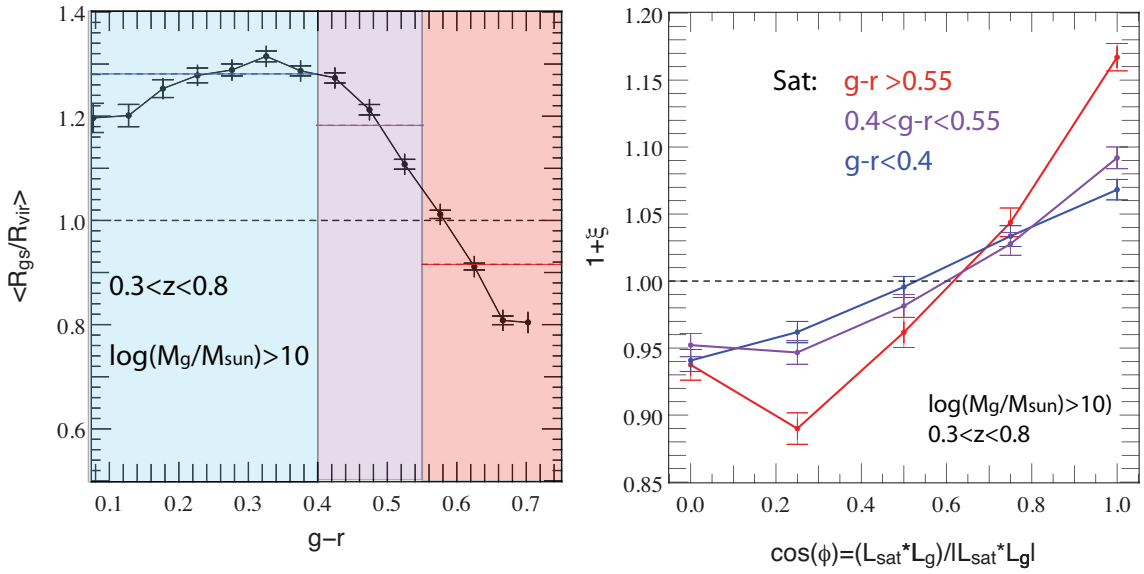

Figure 3.16: *Left panel*: evolution of the relative mean radius with g-r color. Our bins are represented as colored areas. Colored dashed lines indicate the average radius in each bin. The radius is constant for $-0.2 < g - r < 0.05$. However, satellites with $g - r < 0.05$ are marginal hence not represented. *Right panel*: PDF of $|\cos(\phi)|$, the cosine of the angle between the spin of the central galaxy and the total orbital momentum of its satellites in the rest frame of their host for $0.3 < z < 0.8$ and for different g-r color bins. For red quenched satellites, the orbital momentum of satellites tend to be aligned with the galactic spin. Blue star forming satellites do not follow such a trend.

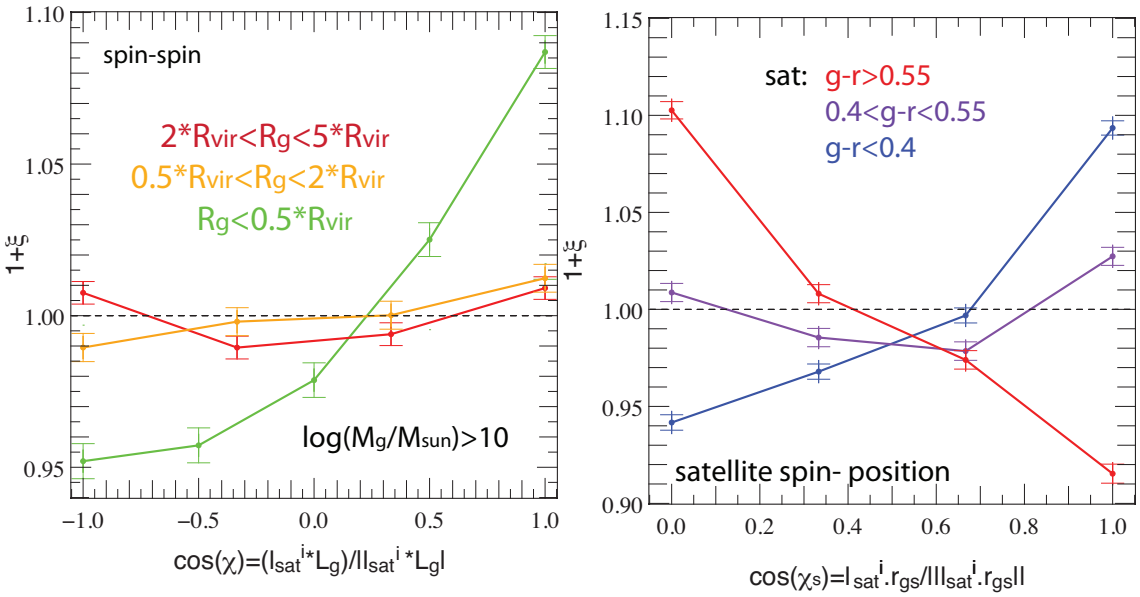

Figure 3.17: *Left panel* Twice the PDF of $\cos\chi$, the cosine of the angle between the spin of the central galaxy and the spin of the satellite for $0.3 < z < 0.8$ for different radius bins. satellites align their intrinsic angular momentum to to that of the host galaxies in the inner part of the halo. Blue satellites in the outskirt of the halo have a spin aligned with their position vector while red satellites in the inner parts have a rotation plane aligned with that of the galaxy. *Right panel* PDF of $\cos\chi_s$, the cosine of the angle between the spin of the satellite and its position vector for different satellites in $g-r$ color bins.

satellites). Although this effect is weaker than the previous trends, it statistically confirms the strength of angular momentum transfer from the halo and torques from the massive host in the fate of satellites plunging into the halo (in particular, this excess was also found to reach 18% for satellites within $0.25\,R_{\rm vir}$, 20% for most massive hosts with $M_{\rm g} > 10^{11}\,{\rm M}_{\odot}$). Note that this measurement is at least partially sensitive to grid-locking (i.e. tendency of spins to align with the grid on which the gas fluxes are computed; such effects will be discussed in great details in (Chisari *et al.* , 2015), which will analyse spin-spin correlations over a wide range of masses and separations.

To confirm such swings of the satellite rotation plane, let us show in the right panel of Fig. 3.17 the PDF of $\cos\chi_s$, the cosine of the angle between the spin of the satellite and its position vector for different color bins. I find that blue (outer) satellites have a spin preferentially aligned with their position vector, which is directly related to the fact that they are mostly small structures with spins aligned with the filament they are flowing from; while red (inner) satellites have a spin more likely to be perpendicular to their position vector, hence a rotation plane aligned with it.

In Fig. 3.18, I consider the orientation of the minor axis rather than the spin of the satellite for

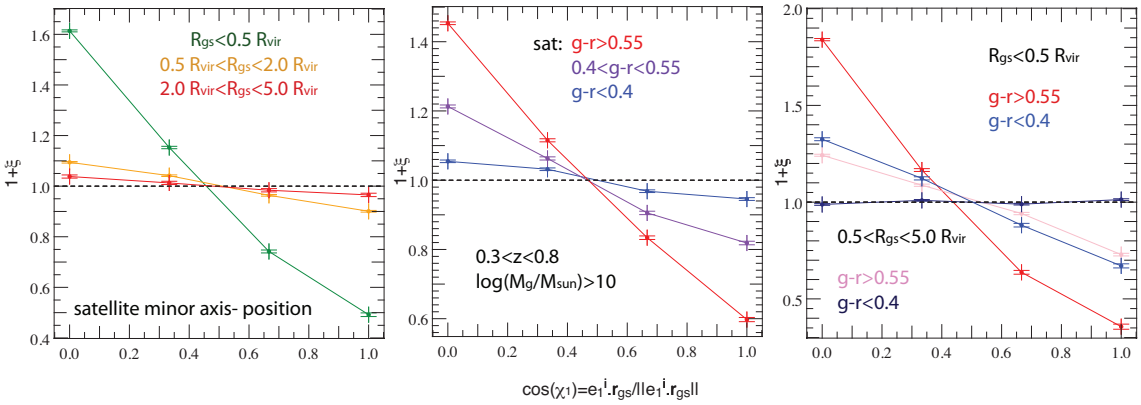

Figure 3.18: PDF of $\cos\chi_1$, the cosine of the angle between the minor axis of the satellite and its position vector for $0.3 < z < 0.8$ for different radius bins (*Left panel*), satellite $g-r$ color bins (*Middle panel*) and mixed bins (*Right panel*). satellites lingering in the halo align their minor axis to that of the host galaxies in the inner part of the halo.

different bins in distance and colors. This static geometrical parameter is more strongly sensitive to stripping and friction than the orientation of the satellite spin and no flip as clear as the one found for the spin is detected, but the evolution is globally similar and the tendency to display a minor axis orthogonal to the galactic plane for redder satellites in the inner parts of the halo is strengthened. It confirms the dynamical mechanism that bends the rotation plane of satellites in alignment with their orbital plane. As it progressively aligns itself with the central galactic plane, the rotation plane of satellites also end up aligned.

These torquing processes are consistent with theoretical predictions derived from linear response theory in Colpi (1998). They interpreted the orbital decay triggered not by the surrounding halo, but by the central galaxy (stellar material) itself on its external satellites, via near resonance energy and angular momentum transfers. This should lead noticeably to a circularization of orbits, and an alignment between the major axis of the satellite with $\mathbf{r}_{\rm gs}$, a result also found for dark haloes in N-body simulations by Aubert *et al.* (2004) and Faltenbacher *et al.* (2008). Note that Schneider *et al.* (2013) finds a fainter signal in observations from the GAMA survey, most likely associated with the misalignments between baryons and dark matter. However, while Schneider *et al.* (2013) claims that much of the signal could be reminiscent of filamentary accretion, our distance analysis, in strong agreement with Faltenbacher *et al.* (2008), underlines the importance of torques from the host, even for the baryonic component. Note however that Sifón *et al.* (2015) and Chisari *et al.* (2014) recently looked at ellipticity alignments around stacked clusters at lower redshift ($0.05 < z < 0.5$) and found residual systematic effects to be much smaller than the statistical uncertainties. As a consequence neither of them was able to recover a significant

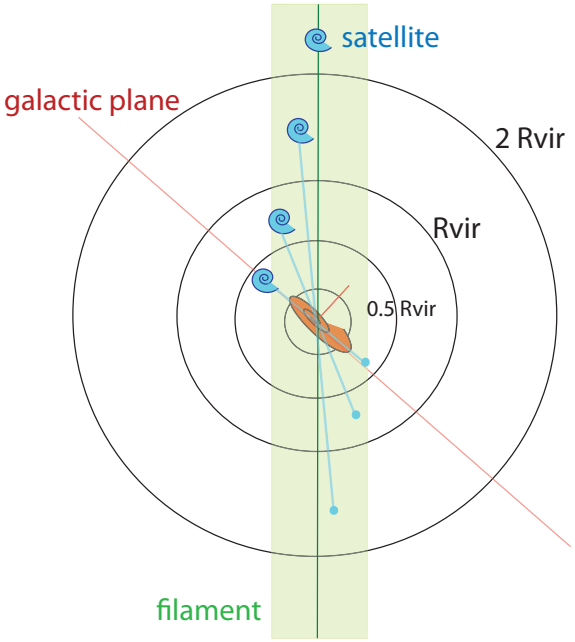

Figure 3.19: Sketch of the evolution of the alignment trends with distance to the center of the halo. On the outskirt of the halo, satellite galaxies are strongly aligned with the nearest filament. Probing deeper into the halo this trend weakens as the alignment of satellites in the galactic plane strengthens.

alignment signal. Although numerous observational limitations and selection effects affect such measurements, it suggests that satellite alignments in most massive clusters may be mostly damped in the local universe by non-linear evolution. This calls for thorougher studies of the dependence of these alignments with the morphology and mass of the central galaxy.

It is important to note that this tidal torquing from the central galaxy induces a dynamical angular bias that is *a priori* distinct from the geometrical anisotropy inherited from the large scale shear. However, it affects the dark matter component in the inner parts of the halo in a similar way, as established by several numerical works which showed that the shape of the inner halo ($R < R_{\rm vir}$) is strongly correlated to the shape of the central galaxy even though this correlation disappears on larger scales (Kazantzidis *et al.* , 2004b; Bailin *et al.* , 2005; Dong *et al.* , 2014). It may therefore preserve the quality of satellites as dark matter density tracers, providing that the *filamentary trend* has vanished.

3.5 Implications for observations.

In this last part I provide further insights about the signal that can be expected in observations and I relate our trends to existing observational studies. The interest is double: one wants to

make accurate predictions for prospective observational studies and one wants to confirm that the scenario developed in the previous section is compatible with existing observations.

3.5.1 Color selection

In most observational studies, the mass of galaxies and satellites is traced by their rest-frame colors. Fig. 3.20 shows three plots very similar to the mass segregation plots presented in the previous sections but with mass bins replaced by $g-r$ color bins for the central galaxy. Assuming that red central galaxies are indeed older and more massive than their blue counterparts, one would expect to observe the increase of the *coplanar trend* as $g-r$ increases. This is indeed the case, as can be seen on the first panel, which displays the PDF of $\mu_1 = \cos(\theta_1)$ for three different bins of color for the central galaxy. Red hosts with $g-r > 0.55$ tend to have their satellites aligned in their galactic plane, with 54% of satellites in the 33° cone around their projection on the galactic plane, which falls down to 46% for blue centrals with $g-r < 0.4$ (uniform: 40%). The *filamentary trend* is also observed in the *middle panel*, with excess probabilities similar to the trend with mass. The fact that blue centrals are more likely to be young galaxies with a spin parallel to the filament explains why blue hosts are subject to a slight decrease in the *filamentary trend* compared to red hosts: they are more likely to be found in a situation where both trends compete.

As a conclusion, color selection proves as efficient as mass selection to identify and quantify both trends, which is consistent with the steady evolution of the average mass in each color bin for all galaxies with $M_{\rm g} > 10^{10}\,{\rm M}_\odot$: *red* galaxies have an average mass of $8.8\times10^{10}\,{\rm M}_\odot$, while it falls down to $4.2\times10^{10}\,{\rm M}_\odot$ for the *intermediate* bin and $2.9\times10^{10}\,{\rm M}_\odot$ for the *blue* galaxies. Additionally, the *right panel* of Fig. 3.20, shows the PDF of $\mu = \cos(\theta)$, the angle between the spin of the central galaxy and the direction towards the center of mass of its satellites. While replacing the alignment to the minor axis by the alignment to the galactic spin does not change results qualitatively, one can see that the spin signal is significantly lower than the axis signal, with the already mentioned 54% falling down to less than 45%. This is a general trend that I tested on multiple PDFs presented in this paper, which suggests a significant impact of torquing from the central galaxy in the motion of satellites entering the halo and is also reminiscent of the fact that the spin can be significantly misaligned with both the minor axis of the galaxy and the spin of the host halo.

As will be made clear in the next section, the discrepancy between those two signals is highly dependent on the shape of the central galaxy, which can induce significant misalignments between the minor axis and the spin.

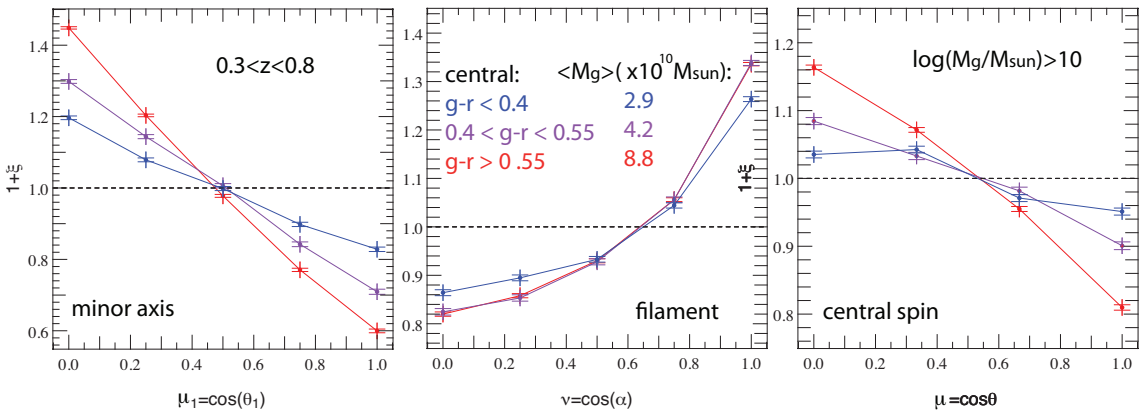

Figure 3.20: PDF of $\mu = \cos\theta$, the angle between the spin of the central galaxy and the direction towards the center of mass of its satellites, at $0.3 < z < 0.8$ for different central color bins. For massive red central galaxies, the satellites tend to be distributed in the galactic plane.

Fig. 3.21 shows similar results for the projected quantities along the x-axis of the grid. The right panel shows the PDF of θ_x the angle between the major axis of the projected central galaxy and the projected $\mathbf{r}_{\rm gs}$, at $0.3 < z < 0.8$ for different color bins. The left panel displays the PDF of α_x, the angle between the projected direction of the filament and the projected $\mathbf{r}_{\rm gs}$. Results are in good agreement with the observed signal found in the SDSS by Yang *et al.* (2006), although alignment trends seem to be slightly stronger in our case, taking into account the fact that our mass range is more biased towards small masses. Average values for θ_x in each color bin are specified on the right panel and confirm the steady evolution of the trend with $g - r$. This increase is sharper than that found in Yang *et al.* (2006), however the results remain completely consistent. I do not model dust extinction, which impacts our estimation of colors and might explain this deviation.

Nevertheless, it is interesting to notice that the projected estimation follows very closely the results in 3D, although it tends to slightly underestimate the alignment trends.

Finally, in Fig. 3.23 I use the three dimensional framework to test further observations by Yang *et al.* (2006) and simulations by Dong *et al.* (2014), which performed a detailed analysis of the alignments with respect to the colors of both the satellites and the hosts. Our results are the following:

- The *coplanar trend* is stronger for red hosts, especially red hosts with blue satellites (although the distinction is minor). This is most likely a mass effect due to more efficient torques, as the mass ratio $m^i_{\rm sat}/M_{\rm g}$ is smaller on average for blue satellites. It is important to remember that trends are more likely to add up in this case, as red centrals are often post-merger structures, hence have a higher chance of maintaining a spin orthogonal to their filament.Therefore, the

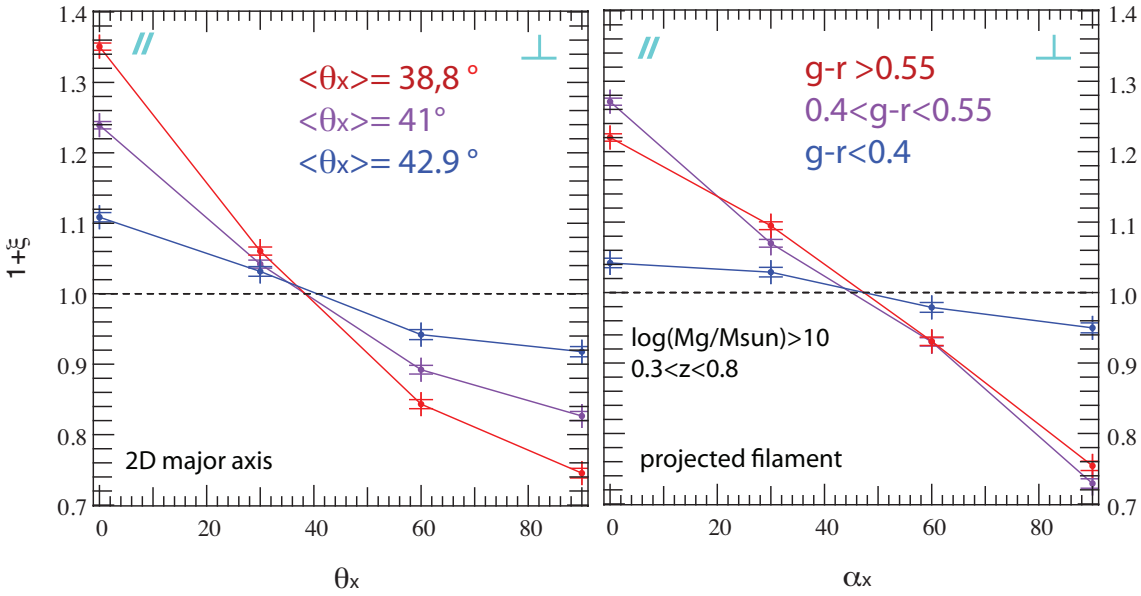

Figure 3.21: PDF of θ_x and α_x, the angles between the x-projected major axis of the central galaxy (left panel) / direction of the filament (right panel) and the x-projected $\mathbf{r}_{\rm gs}$, at $0.3 < z < 0.8$ for different color bins. For massive red central galaxies, the satellites tend to be distributed in the galactic plane. Projected signal is comparable to results in 3D.

distance to the filament is not crucial in this case, as satellites fall directly from the filament into the galactic plane.

- Blue hosts — younger and less massive — are more likely to have a spin parallel to their filament — which induces a competition between the *filamentary* and the *coplanar* trends — and less likely to efficiently torque their satellites into their rotation plane. Expectedly, the *coplanar* signal is weaker than the one for red hosts.

- Consistently, The signal is then slightly stronger for red satellites of blue hosts which are more evolved and on average closer to their host than blue satellites.

The same analysis in projection along the x-axis of the grid provides similar results and leads to a mean angle variation detail on Fig. 3.22. Those results are again consistent with Yang *et al.* (2006) which analyzed more specifically the alignments of satellites along the major axis of their host within the galactic plane. Although they found a red-red signal higher than the red-blue ones, their study focused on $R_{\rm gs} < R_{\rm vir}$ which left aside an important amount of possible blue satellites in alignment with the filament. However their general color and mass trends for the central galaxy are in good agreement with our results.

<θx> (°)		Rgs < Rvir	Rgs<5*Rvir
central	satellite		
red	red	40.0	38.9
red	blue	39.3	38.4
blue	red	41.9	41.9
blue	blue	42.1	43.1

Figure 3.22: Mean values (in degrees) for θ_x in different color bins for both satellites and central galaxies, and within two different radius from their host.

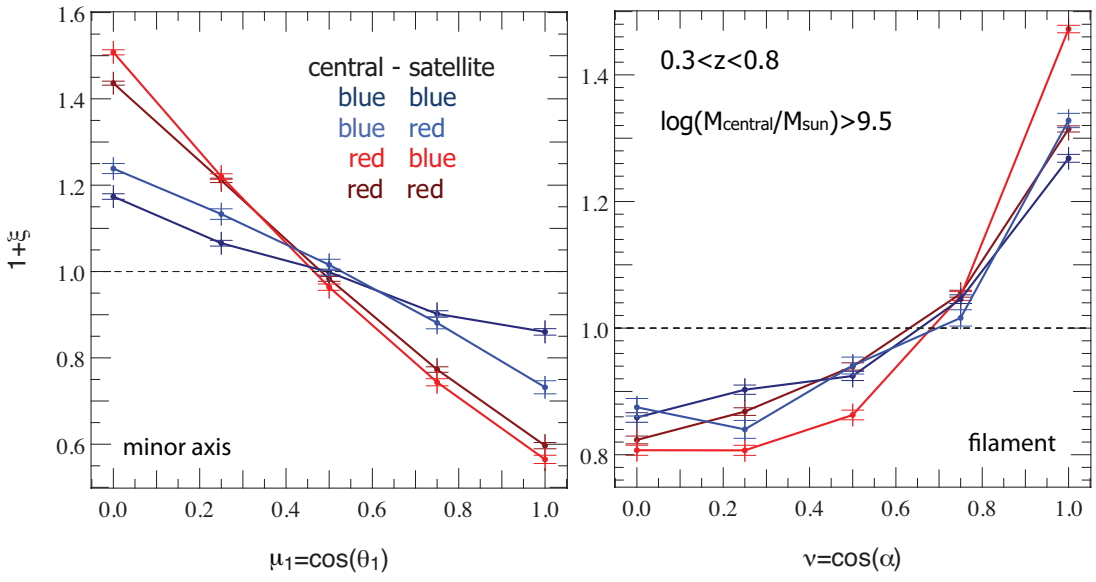

Figure 3.23: PDF of $\mu_1 = \cos(\theta_1)$ and $\nu = \cos(\alpha)$ for different color bins for both the hosts and the satellites. Blue galaxies are identified as structures with $g - r < 0.4$ and red galaxies as structures with $g - r > 0.55$.

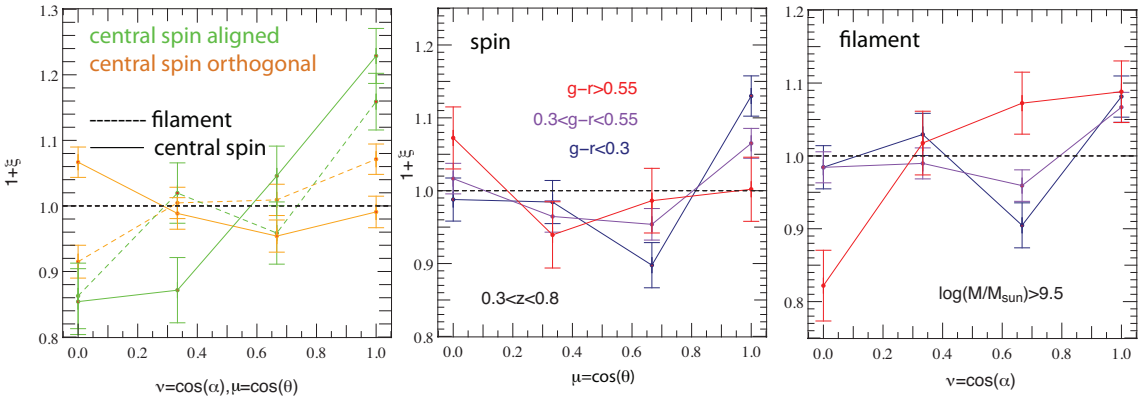

Figure 3.24: *Left panel* Evolution of the *filamentary trend* (dashed line) and the *coplanar trend* (solid line) for two sub-samples of the *sub-halo* satellites: 1) satellites whose host's minor axis is aligned to the nearest filament within a 37 deg cone (in *green*) 2) satellites whose host's minor axis is perpendicular to its nearest filament within a 37 deg cone (in *orange*). *middle and right panels* PDF of $\mu = \cos\theta$ (middle panel), the angle between the spin of the central galaxy and the direction towards the center of mass of its satellites, and $\beta = \cos\alpha$ (right panel) for $0.3 < z < 0.8$ and for different $g - r$ color bins. For massive red central galaxies, the satellites tend to be distributed in the galactic plane, which is consistent with an alignment with the filament.

3.5.2 Signal on smaller scales

Although much less populated (maximum in the simulation: six satellites), the sub-haloes in Horizon-AGN still offer reasonable statistics to track alignment trends on smaller scale. This was done for all sub-haloes in the simulation. Fig. 3.24 , middle and right panels, shows the corresponding color cuts for the *filamentary trend* and the *coplanar trend*. One can see that both trends exist at small scale with the same qualitative evolution as similar trends on halo scales, although with a much fainter signal ($\xi = 2.5\%$ in the best case, for red hosts.). The signal is found to be slightly higher at higher redshift, $1 < z < 2$ which tends to confirm the existence of such trends for sub-haloes.

Cuts in colors at an intermediate redshift ($z = 1.2$) are presented on Fig. 3.25 , which shows that while red galaxies tend to have their satellites distributed in the galactic plane, blue galaxies have them distributed along the direction of their spin. This is consistent with the previous results as more massive galaxies tend to be older and redder than their blue, younger hence smaller counterparts.

This result highlights the multi-scale nature of such alignment trends as the direct consequence of the scale invariance of the density fluctuation power spectrum in the primordial universe. Though our work is restricted to the one-halo term, similar results can be found on higher scales with nearby central galaxies aligning their galactic planes with one another, then gathering in clusters whose

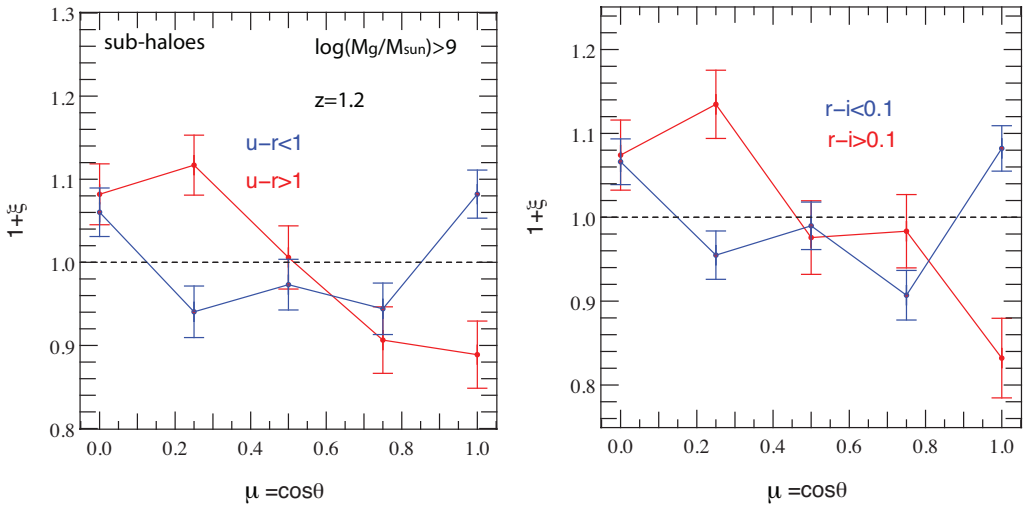

Figure 3.25: PDF of $\mu = \cos\theta$, the angle between the spin of the central galaxy and the direction towards the center of mass of its satellites in the same *sub-halo* at $z = 1.2$ for different color bins, for all galaxies with $M_g > 10^9\,M_\odot$. For massive red central galaxies, the local satellites tend to be distributed in the galactic plane.

major axis tend to align with each other as well (Binggeli effect: Binggeli (1982)).

Such intrinsic alignments of galaxy shapes are widely regarded as a contaminant to weak gravitational lensing measurements (Hirata *et al.* , 2004; Mandelbaum *et al.* , 2006; Hui & Zhang, 2008; Schneider & Bridle, 2010),. They play a particularly important role in upcoming cosmic shear measurements, potentially biasing constraints on the evolution of dark energy equation of state (Bernstein & Norberg, 2002; Schneider *et al.* , 2013; Codis *et al.* , 2015). In particular, the need to access information on nonlinear scales of cosmic shear power spectrum to constrain dark energy makes it particularly important to use numerical hydrodynamical simulations to study the mechanisms that lead to alignments (Tenneti *et al.* , 2015a). Coplanarity of satellites in the vicinity of a central massive galaxy can lead to an alignment signal that could contaminate lensing measurements. Similarly, coherent alignments of galaxies with the filaments that define the large-scale structure of the Universe can produce a contamination to cosmic shear. A complementary analysis to this work can be found in Chisari *et al.* (2015), which relates the shapes of the galaxies in the simulation and their correlations to currently available models for intrinsic alignments

3.5.3 Effects of the shape of the central host and high-z alignments.

The dependance of the alignment on the shape of the central host proves crucial to fully understand the amplitude of the signal, as trends show different features for oblate and prolate structures. Fig. 3.26 (upper panels) shows the evolution of the PDF of $\mu_1 = \cos\theta_1$ for oblate and prolate cen-

tral galaxies. The satellites's orthogonality to the minor axis is stronger for prolate structures, especially in the intermediate mass range. One should not deduce however that it corresponds to a better alignment in the galactic plane, as such a plane for prolate structures is poorly defined and more likely to be supported by the minor axis. Indeed, prolate structures show a significant amount of misalignment between their spin and minor axis, with more than 30% displaying a spin aligned to the major axis. Fig. 3.26 (lower panels) — which investigates the oblate and prolate alignment in the intermediate mass range for which the deviation is maximal — confirms this trend. Following the green lines which show the evolution of the PDF of $\mu_1 = \cos\theta_1$ and $\nu = \cos\alpha$ for satellites of central galaxies with a spin aligned to the filament, one can see that the alignment of satellites along the minor axis of their host and along the filament can not be straightforwardly deduced from the orientation of the spin for such prolate structures.

Finally, Fig. 3.27 shows the PDF of $\mu_3 = \cos\theta_3$ the cosine of the angle between $\mathbf{r}_{\rm gs}$ and the major axis of the central host for oblate hosts (dashed line) and prolate hosts (solid line). While oblate hosts display a certain degree of satellite alignment along their major axis, prolate hosts have their satellites strongly aligned with their major axis. This is consistent with a distribution of satellites tracing the underlying triaxiality of its host but is also reminiscent of the fact that this axis is more often aligned with the spin in the prolate case.

This shape dependence leads to a major difficulty when comparing two samples at very different redshifts. They correspond to different galactic populations — with great variations in the galactic shape distribution — due to subsequent evolution, especially from mergers between the two epochs. This therefore induces substantial changes in the angle between the minor axis and the galactic rotation plane. To overcome this difficulty I chose to compare the alignments with the galactic spin rather than the minor axis, and I computed the spin only on the star particles contained in the half-mass radius of each galaxy (defined as the radius which encompasses 50% of the total stellar mass). This limits the dispersion in shape and the misalignments with the host halo spin. Fig. 3.28 displays the PDF of $\mu = \cos(\theta)$, the angle between the spin of the central galaxy and the direction towards the center of mass of its satellites, for different mass bins, for both redshift ranges. Results are stacked for 10 outputs equally spaced in redshift between $z = 2$ and $z = 1$ and 6 outputs between $z = 0.3$ and $z = 0.8$. The low-redshift range is presented on the first panel and its high-redshift counterpart on the second.

Although this induces a loss a signal, Fig. 3.28 clearly shows a greater signal at $1 < z < 2$. As expected, the signal decreases with redshift as galaxies evolve non-linearly and merge with one another. While 75% of satellites lie within a cone of 45° around the minor axis of their central galaxy at high-redshift, this population only amounts to 64% of the sample at low-redshift. More

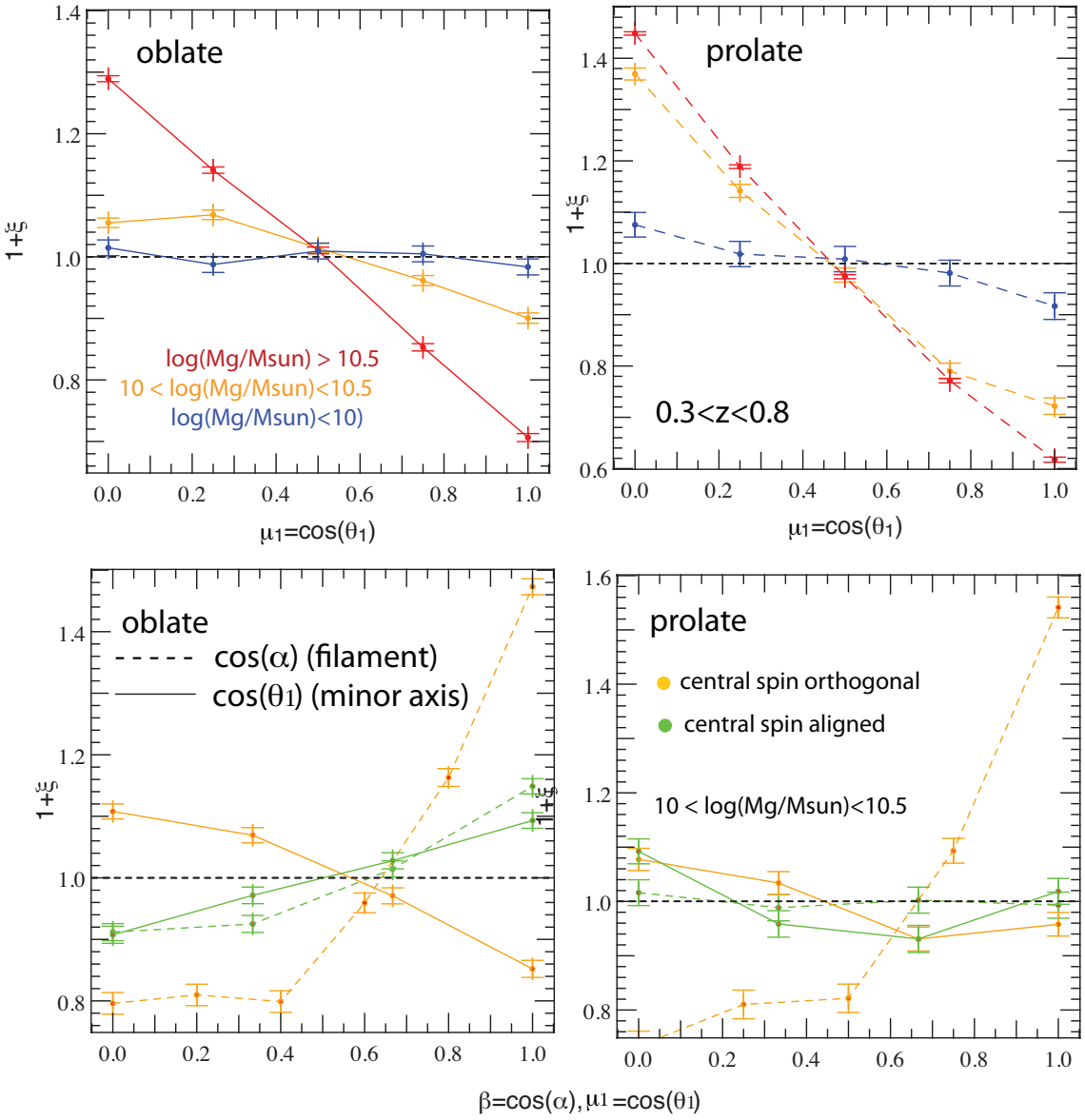

Figure 3.26: *Upper panels*: Mass cuts for the PDF of $\mu_1 = \cos\theta_1$ similar to those in Fig. 3.8 for oblate (left) and prolate (right) central galaxies. *Lower panels*: PDF of $\mu_1 = \cos\theta_1$ (solid line) and $\nu = \cos\alpha$ (dashed line) for central galaxies with a spin aligned to their filament (in green) and central galaxies with a spin orthogonal to their filament (in orange), for the intermediate mass range. Results for oblate centrals are presented on the *left* panel, for prolate centrals on the *right* one.

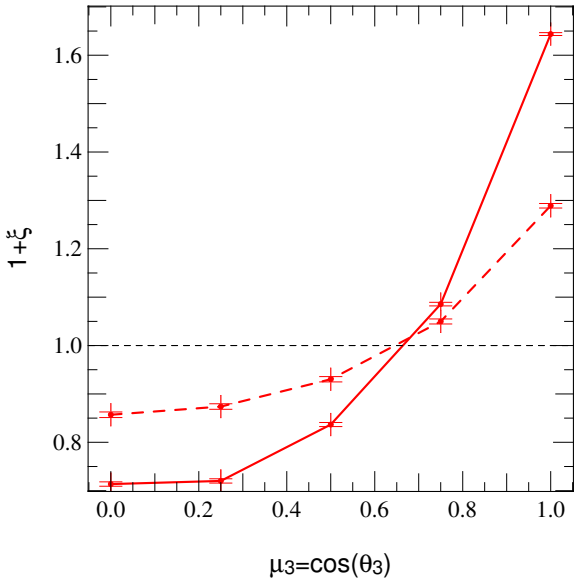

Figure 3.27: PDF of $\mu_3 = \cos\theta_3$ the cosine of the angle between $\mathbf{r}_{\rm gs}$ and the major axis of the central host for oblate hosts (dashed line) and prolate hosts (solid line). Prolate hosts have their satellites aligned along their major axis, which is consistent with the fact that this axis is more often aligned with the spin in this case. Oblate hosts display a certain degree of satellite alignment too, which is consistent with a distribution of satellites tracing the underlying triaxiality of its host.

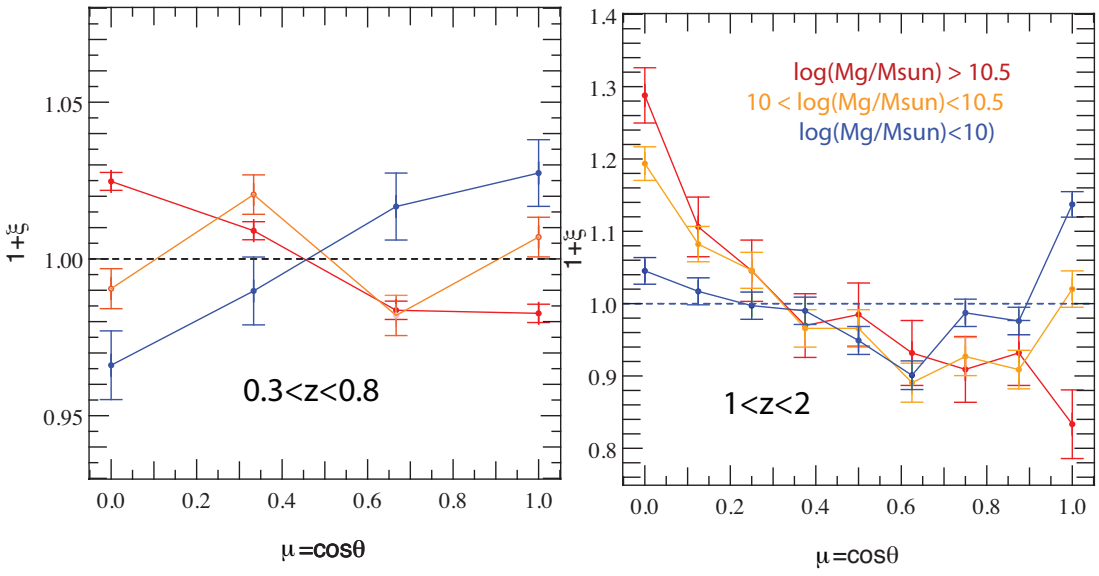

Figure 3.28: PDF of $\mu = \cos(\theta)$, the angle between the half-mass spin of the central galaxy and the direction towards the center of mass of its satellites, for different mass bins, for both redshift ranges. Results are stacked for 10 outputs equally spaced in redshift between $z = 2$ and $z = 1$ and 6 outputs between $z = 0.3$ and $z = 0.8$.For massive central galaxies, the satellites tend to be distributed in the galactic plane. The signal is stronger at higher redshift, for less evolved galaxies
.

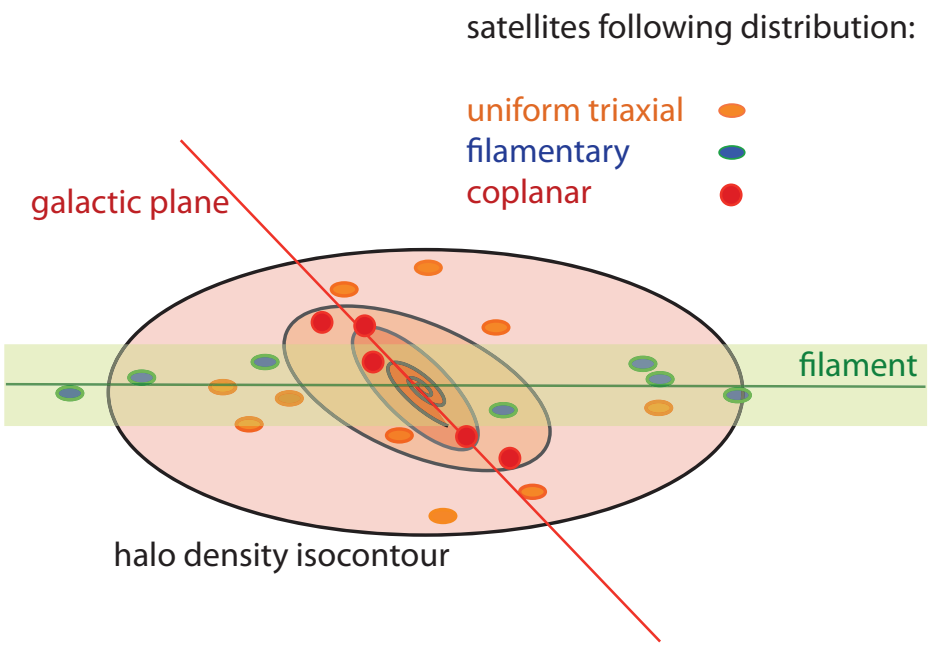

Figure 3.29: Illustrated summary of the three alignment trends that drive the fate of satellites in their host halo.

specifically, at $1 < z < 2$, 44% of satellites lie within a 33° cone around the minor axis, while it amounts to 26% for galaxies at $0.3 < z < 0.8$.

3.6 Conclusion.

The main results of this work are sketched on Fig. 3.29: the distribution of satellites in their host halo and around their host central galaxy arises from the superposition of three different effects:

- the tri-axiality of the halo, as identified by numerous numerical and observational studies
- the polar flow from the filament, which mostly affects young blue satellites in the outskirt of the halo, and leads to an overestimation of the halo's tri-axiality on large scales.
- the dissipation in the halo and torques from the central galaxy, which bend older inner redder satellite orbits close to coplanarity with the galactic plane, thus accordingly with the inner dark matter density profile.

The analysis of the radial and temporal evolution of those trends in Horizon-AGN strongly suggests that:

- The leading effect in the orientation of satellites is the tendency to align with the nearest filament. While stronger for satellites in the outskirt of the dark halo, this tendency decreases as the satellites are dragged deeper into the halo - where they exchange angular momentum as they are subject to the gravitational torques of the central galaxy - but not to the point where it becomes negligible, unless strong misalignment ($> 45°$) are found between the central galaxy's minor axis and the filament's direction.

- A secondary effect that becomes dominant in the inner parts of the halo is the tendency of satellites to eventually align with the central galactic plane. This effect can either compete or strengthen the alignment with the filament, depending on the orientation of the central galaxy. As expected, the signal is stronger for red massive centrals which are already more likely to have a spin orthogonal to the filament - therefore the filament lies in the galactic plane - as the two effects add up to one another in this case. On the contrary, low mass blue centrals with a minor axis aligned to their filament have satellites predominantly aligned with their filament.

- The alignment of satellites in both the filament and the galactic plane is consistently found to be stronger for red central galaxies, as it corresponds to massive centrals. The dependance of this *coplanar* trend on the $g - r$ color of satellites is also consistent with a dynamical scenario in which young (blue) satellites flowing from the filament progressively bend their orbits towards the central galactic plane (under its tidal influence) as they reach the inner parts of the halo and get deprived of their gas and stars through tidal stripping therefore becoming redder. This is likely to be observable.

- Around 40% of massive centrals with $M_{\rm g} > 10^{10}$ $\rm M_{\odot}$ display significant deviations from the spin-filament orthogonality ($> 30°$) and are therefore subject to such competing alignment trends, with an alignment to the filament predominant for blue satellites in the outskirt of the halo, and coplanarity with the central host taking over for older red satellites in the inner regions of the halo.

- The tendency for systems of satellites to align in the galactic plane is consistent with a tendency to align and synchronize their orbital momentum to the angular momentum of the central galaxies. I also find hints that satellites align their intrinsic AM to that of their host as they reach inner regions of the halo.

- This effect is occurring on multiples scales. Noticeably, similar trends are detected on the sub-halo scales and add up to other trends previously observed on larger scales, between central galaxies and even clusters. These intrinsic alignments may therefore represent a

worrisome source of contamination for upcoming 1% precision weak lensing surveys, as it correlates ellipticities of structures on virtually all scales and thus mimics the gravitational lensing shear (Chisari *et al.* , 2015).

In closing, this investigation has shown that the distribution of satellites cannot at face value be taken to simply trace the shape of the dark halo. One must also account for the dynamical bias induced by their flow within their embedding filament, which closely resembles that of the cold gas, even though the satellites population does not shock in the CGM (Circum Galactic Medium) which highlights their tidal origin. Given that such flow was identified at high redshift with tracer particles Dubois *et al.* (2012a); Danovich *et al.* (2015), it is interesting that it has a stellar counterpart at low redshift in the possibly observable satellite distribution via its colour variation.

Observationally, stacked satellite distributions relying on galactic surveys such as the SDSS could be used to compile a synthetic edge-on galactic disk and compare the corresponding flaring with predictions. The measured anisotropic infall and realignment within the virial radius have an impact on building up thick discs via cosmic accretion, and galactic warping.

Moreover, the development of models to quantify alignment trends is crucial for upcoming imaging surveys to achieve their goals of constraining the equation of state of dark energy and modifications to General Relativity. Surveys such as *Euclid*[1] (Laureijs *et al.* , 2011), the Large Synoptic Survey Telescope[2](Ivezic *et al.* , 2008) and WFIRST[3] (Spergel *et al.* , 2013). Hydrodynamical simulations are a promising tool to quantify "intrinsic alignments" in the nonlinear regime and provide estimates of contamination to future surveys (Tenneti *et al.* 2015b,a; Chisari *et al.* 2015). The results of simulations can be used to inform the parameters of an intrinsic alignment "halo model" (Schneider & Bridle, 2010), or nonlinear models that rely on perturbation theory power spectra (Blazek *et al.* , 2015).

However, our work shows that alignments of galaxies on small scales are the result of a complex dynamical interplay between the host galaxy, the satellites and the surrounding filamentary structure, and that alignment trends depend on the evolutionary stage of a galaxy (as probed by color) and on the orientation of the central with respect to the nearest filament. Morever, our work suggests that alignment trends exist for "blue discs", and that their significance is increased at the higher redshifts that will be typically probed by weak lensing surveys. While this alignment signal tends to be suppressed in projection, its potential contamination to lensing remains to be explored

[1] `http://sci.esa.int/euclid`
[2] `http://www.lsst.org`
[3] `http://wfirst.gsfc.nasa.gov/`

Chisari *et al.* (2015). Moreover, I have shown that alignments can transition between two regimes as satellites move from the surrounding filament into the gravitational well of the central galaxy. The *filamentary trend* implies a tangential aligment of discs around centrals, resulting in a tangential shear signal that adds to the galaxy-lensing in projection. The *coplanar trend* represents a net radial orientation of satellites and their host, suggesting that galaxy-lensing could be suppressed on the small scales in projection. Both trends would contribute to a cosmic shear measurement through correlation of intrinsic shapes and weak lensing (the 'GI' term Hirata *et al.* , 2004).

Chapter 4

The rise and fall of stellar disks across the peak of cosmic star formation history: mergers versus smooth accretion

In the last chapters, we studied in details how the anisotropy of the cosmic web drastically impacts the relative orientation of galactic spins, galactic planes, satellite orbits and cosmic filaments. We found that these orientations changes are consecutive to gas inflows, tidal interactions and mergers, the orientation of which is constrained by the large scale structures. Spins and separation vectors are vector quantities therefore easy to relate to the geometry of the cosmic web, but it is of great interest to also evaluate and understand to what extent such constrained mergers and gas inflows can modify more specific galactic properties, such as its shape or size. Indeed, the morphological diversity of galaxies in the Local Universe - qualitatively encompassed by the well-known Hubble Sequence - remains one of the most puzzling issues of modern astrophysics.

But while our present understanding of galaxy evolution derives mainly from the nearby ($z < 1$) Universe, the bulk of today's stellar mass formed around the broad peak of cosmic star formation history at $z \sim 2$ (e.g. Madau *et al.* , 1998; Hopkins & Beacom, 2006). Although it represents a significant epoch in the evolution of the observable Universe, the properties of galaxies remain largely unexplored at this epoch, as it has only recently become accessible by current observational facilities (CANDELS, GOODS, Herschel, ALMA, Chen *et al.* , 2014; Lin *et al.* , 2010; Cooper *et al.* , 2012; López-Sanjuan *et al.* , 2013).

As a result, what constitutes arguably the most important aspect of hierarchical galaxy formation and evolution is still being debated. Throughout the last decades, many processes - which will

be detailed in the following section- have been proposed to trigger specific galactic morphologies. Remaining issues consist in understanding to what extent mergers, as opposed to secular evolution driven by (cold) gas inflows, explain the diversity of galaxies?

Notwithstanding observational advances, large statistical studies remain difficult, both due to the fact that observational efforts rely on pencil-beam surveys that are susceptible to low-number statistics and cosmic variance but also that they are based on techniques that can differ significantly from study to study. Moreover, studies of galaxy merging at these redshifts are further complicated by the fact that normal star forming discs becomes more turbulent and irregular at earlier times, making them difficult to separate from genuine mergers (Kaviraj *et al.* , 2014b; Huertas-Company *et al.* , 2014).

With the advent of large-scale albeit fairly well resolved cosmological hydrodynamical simulations such as Horizon-AGN , it has recently become feasible to investigate these different physical processes in detail and with sufficient statistics, a necessary requirement to truly unravel the impact of galaxy environment on their properties.

In this last chapter, I review the morphological diversity of galaxies and its suspected origins, and following up on Chapter 1, I investigate the comparative role of mergers and smooth accretion of both gas and stars on defining and modifying the size and morphology of galaxies (see Fig 4.17) in Horizon-AGN . After careful evaluation of the accretion rates of different types of mergers as well as smooth accretion over cosmic history, I analyze the impact of both processes on the growth of galaxies in the cosmic web, with specific emphasis on the different role played by gas and stars dominated mergers (equivalent to the dry/wet dichotomy used in lower z studies). We then explore the competitive effects of smooth accretion and mergers on the morphology of galaxies and their correlation to the disk and spheroid abundances over the duration of the peak of cosmic star formation.

4.1 Inflows and galaxy encounters: an overview of morphological transformations and size evolution

We presented in Introduction the "Hubble Sequence" fork diagram which classifies the vast diversity of galactic morphologies depending on their overall shape (ellipsoid, spheroid or disk), density profile (bulge dominated, disk dominated) and inner structure patterns (tightly wound spirals, double spirals, central bar). It is now of interest to understand how galaxies evolve from one type into another and how it affect the specific ratio of each type.

4.1.1 Disc galaxies: evolution of the Hubble sequence with redshift

According to the now standard hierarchical paradigm - in which most massive galaxies form last - thick gas-rich disk galaxies form first at high redshift at the intersection of cold gas streams funneled through the cosmic filaments (Brooks *et al.* , 2009b; Agertz *et al.* , 2009; Dekel *et al.* , 2009; Pichon *et al.* , 2011; Danovich *et al.* , 2012, 2015). Gas streams shock and lose most of their mean velocities and angular momentum through tidal torquing with the exception of their orbital components which add up coherently, then settle in a rotating plane plane through the conservation of angular momentum and start to form stars.

Elliptical galaxies are generally believed to form later through galaxy mergers (Cretton *et al.* , 2001; Naab & Burkert, 2003; Naab *et al.* , 2006b; Qu *et al.* , 2011).

However, in the wake of modern deep field surveys (CANDELS, GOODS, Herschel, ALMA, Chen *et al.* , 2014; Lin *et al.* , 2010; Cooper *et al.* , 2012; López-Sanjuan *et al.* , 2013), and with the rise of high-performance cosmological simulations, this description has also progressively enriched with distinctive features for given types at different redshifts

Hammer *et al.* (2009) and Delgado-Serrano *et al.* (2010) compared nearby galaxies from the Sloan Digital Sky Survey (SDSS) and distant galaxies from the GOODS survey, which led to confirm the relevance of the Hubble sequence for $z > 1$ but revealed evolving type ratios. Such observations find an abundance of massive thin disks in the local universe, and measurements of disk ratios at redshifts $z = 1$ and $z = 0$ reveal an increase of the amount of disks with cosmic time, not observed for ellipticals, the amount of which remains roughly constant (Mortlock *et al.* , 2013; Hammer *et al.* , 2009). More noticeably, irregulars progressively disappear as the ratio of disks increases, suggesting the existence of a migration process from one type to the other (most likely mergers of gas rich pairs with high orbital momentum), hence the re-building of disks at $z < 1$.

These later massive thin disks seemingly form later at $z < 1$.

These studies also revealed that, if the broadly defined morphological types of the Hubble sequence hold at high and low redshifts, their specific features actually experience on-going evolution down to $z = 0$. Similar results were found by Mortlock *et al.* (2013) in the CANDELS survey. In particular, observational studies suggest that large fractions of star-forming galaxies around $z \sim 2$ are not razor thin spirals but rather show kinematics and visual morphologies consistent with systems dominated by turbulent discs (e.g. Forster Schreiber *et al.* , 2006; Shapiro *et al.* , 2008; Genzel & Burkert, 2008; Mancini *et al.* , 2011; Kaviraj *et al.* , 2013b). Consistently, disk galaxies in simulations are found to be much thicker, clumpier and much more turbulent at redshift $z > 2$ (Elmegreen *et al.* , 2008; Dekel *et al.* , 2009; Cacciato *et al.* , 2012; Ceverino *et al.* , 2012) - when

continuously fed with dense cold gas streams ("cold flows") reminiscent of the filamentary structure they are embedded in - than their counterparts (re)-built in the Local Universe which do not experience this type of collimated smooth accretion (Birnboim & Dekel, 2003; Dekel & Birnboim, 2008; Dubois *et al.* , 2013b).

Note that disks then develop typical spiral patterns (density waves) as a secular response to low amplitude perturbations (tidal, accretion related or internal such as supernovae feedback). Bars can also develop through secondary gravitational interactions between stellar orbits (not counterbalanced by their dispersion) and stir up specific spiral patterns.

4.1.2 Violent Disc Instability: the path to compact spheroids

This clumpy structure of early discs is a direct consequence of violent gravitational disk instability (Toomre, 1964) which arises when intense high density gas inflows trigger unstable density waves that ultimately lead to the fragmentation of the disk into massive clumps if centrifugal and dispersion ("pressure") forces are not able to counter balance their gravitational collapse. Those clumps grow in mass and drive inflows to the galactic center on dynamical timescales as they migrate inwards and drive transfers of angular momentum outwards (Bournaud *et al.* , 2007b; Elmegreen *et al.* , 2008; Ceverino *et al.* , 2010). In simulations, it efficiently drives the transformation of the disk into a compact spheroid ("red nugget") over a few hundreds Myr (Dekel *et al.* , 2009; Ceverino *et al.* , 2015). This mechanism is efficient at high redshift ($z > 1$) where gas cold flows are commonly found and related accretion intense but becomes extremely rare in the Local Universe where cold flows have dried out and feedback processes actively blow them away (Dubois *et al.* , 2013b; Cen, 2014; Nelson *et al.* , 2015).

Accordingly, recent observations confirm that many primordial spheroids that are forming the bulk of their stellar mass at $z \sim 2$ do not show the tidal features that would be expected from recent major mergers (Kaviraj *et al.* , 2013a). This therefore questions the statistical efficiency of disk building in cosmic flows at $z > 1$. This issue constitutes one of the main focus of this work. In contrast, possibly newly formed disks at $z < 1$ are predictably much less disturbed since cold flows are rare at these redshifts

Moreover massive spheroids are much less compact in the Local Universe than the previously mentioned "red nuggets" (e.g Trujillo *et al.* , 2006; van Dokkum *et al.* , 2008) .They are estimated to grow their size by a factor 5-6 between $z \sim 2 - 3$ and $z = 0$ for a fixed mass range (stellar mass $\sim 10^{11} M_{\odot}$) (Nipoti *et al.* , 2012; Huertas-Company *et al.* , 2013), which calls for yet another transformation process.

This latter issue constitutes another important focus of this work. To better understand which specific interactions could drive the formation of large massive spheroids, let us further develop the mechanisms through which galactic encounters drive morphological transformations in the next subsections.

4.1.3 Mergers

In the context of long encounters better described by the processes of dynamical friction and stripping presented in Chapter 2, galaxies can bind, progressively lose orbital momentum and energy and eventually merge with one another into a remnant structure with new features such as size and morphology. The frequency of such events scales as $\propto (1+z)$ for ΛCDM dark haloes with important uncertainties on the prefactor (Gottlöber *et al.* , 2001; Berrier *et al.* , 2006; Fakhouri & Ma, 2008; Stewart, 2009). This discrepancy is even stronger for galaxies in observations (Patton *et al.* , 2002; Bundy *et al.* , 2004; Lin *et al.* , 2004; Bridge & Carlberg, n.d.; Lotz *et al.* , 2008b). Such events are also believed to evolve from mere binding to complete relaxation over a wide range of timescales: from a few 100 Myr for minor mergers to more than 1 Gyr for mergers of equal mass progenitors (Lotz *et al.* , 2010b,a). However, even in such cases the elapsed time between first encounter and post merger structure is closer to $\propto 0.5$ Gyr. Moreover, strong morphological disturbances, such as strong asymmetries and double nuclei, which occur during the close encounter and final merger stages are believed to be short-lived and only apparent for only a few 100 Myr (Lotz *et al.* , 2008a). Specific extended tails can survive longer but are much fainter.

The outcome of such an event is however highly dependent on the mass ratio between the less massive and the most massive progenitor. Assuming galaxies to be collisionless self-gravitating systems of stars, one can get a first idea of the size evolution of the remnant in specific cases.

Minor mergers If the mass ratio between progenitors is small ($\sim 1/10$), mergers are tagged as *minor*. Although they are too faint to be observed, they might drive important morphological changes. Interestingly, size predictions can be derived from the virial theorem (Naab *et al.* , 2009; Hilz *et al.* , 2012). Using index $\zeta = i$ for the initial main progenitor, $\zeta = f$ for the final remnant and $\zeta = a$ for the accreted smaller system, and defining the respective masses M_ζ, gravitational radii $r_{\mathrm{g},\zeta}$ and mean square speeds of the stars $\langle v_\zeta^2 \rangle$, it yields to:

$$E_\zeta = -K_\zeta = \frac{1}{2} W_\zeta \tag{4.1}$$

$$= -\frac{1}{2} M_\zeta \langle v_\zeta^2 \rangle = -\frac{1}{2} \frac{G M_\zeta^2}{r_{\mathrm{g},\zeta}}. \tag{4.2}$$

Defining the mass ratio $\eta = M_{\rm a}/M_{\rm i}$ and the dispersion ratio $\epsilon = \langle v_{\rm a}^2\rangle/\langle v_{\rm i}^2\rangle$, and assuming the conservation of energy one gets:

$$E_{\rm f} = E_{\rm i} + E_{\rm a} \tag{4.3}$$

$$= -\frac{1}{2}M_{\rm f}\langle v_{\rm f}^2\rangle = -\frac{1}{2}M_{\rm i}\langle v_{\rm i}^2\rangle(1+\epsilon\eta)\,, \tag{4.4}$$

$$M_{\rm f} = M_{\rm i} + M_{\rm a} = (1+\eta)M_{\rm i}. \tag{4.5}$$

The following ratios are derived from the previous equations:

$$\frac{r_{\rm g,f}}{r_{\rm g,i}} = \frac{(1+\eta)^2}{(1+\epsilon\eta)}\,, \tag{4.6}$$

$$\frac{\langle v_{\rm f}^2\rangle}{\langle v_{\rm i}^2\rangle} = \frac{(1+\epsilon\eta)}{(1+\eta)}. \tag{4.7}$$

For a minor merger, if one can assume $\epsilon \ll 1$, then one obtains the scaling relation:

$$\frac{r_{\rm g,f}}{r_{\rm g,i}} \propto \left(\frac{M_{\rm f}}{M_{\rm i}}\right)^2\,, \frac{\langle v_{\rm f}^2\rangle}{\langle v_{\rm i}^2\rangle} \propto \left(\frac{M_{\rm f}}{M_{\rm i}}\right)^{-1}. \tag{4.8}$$

Hence the radius can increase by a factor 4 while the dispersion is decreased by a factor 2.This prediction might explain the increase in size of spheroids at $z < 2-3$.

However, this assumes that galaxies can be considered pure systems of stars, which is a somewhat crude approximation. Real galaxies are actually composite systems of stars, dark matter particles and gas. Noticeably, energy is not strictly conserved. Gas can shock thus lose angular momentum and energy, falling down to the pit of the potential well where it can form additional stars and lead to a strong contraction of the system.

We therefore expect the accuracy of this prediction to be highly dependent on the fraction of gas in the progenitors: while this theoretical size evolution may be reasonable for gas-poor mergers, it can be expected to overestimate the size growth triggered by gas-rich mergers.

Major mergers Similar predictions for major mergers (assuming $\epsilon \sim 1$) would lead to:

$$\frac{r_{g,f}}{r_{g,i}} \propto \frac{M_{\rm f}}{M_{\rm i}}\,, \frac{\langle v_f^2\rangle}{\langle v_i^2\rangle} \propto cst\,. \tag{4.9}$$

In this approximation, the radius is doubled through an equal size merger ($\eta \sim 1$) while the dispersion remains constant. However, one should keep in mind that evolution can be quite different when a merger occurs between two progenitors of comparable mass. In this process, the mechanism of violent relaxation is significant and strongly impacts the properties of the remnant. This mechanism introduced by Lynden-Bell (1967) and further refined by Nakamura (2000) describes the evolution of two interacting collisionless systems of stars when, as a consequence, the gravitational potential varies rapidly with time, which rules out the conservation of energy for single stars.

Full understanding of this phenomenon is actually a complex problem of collisionless statistical mechanics (see Lynden-Bell (1967) for more details) but main features consecutive to the non-conservation of single star energy can be described simply. The conservation equation for energy becomes:

$$\frac{d\epsilon}{dt} = \frac{\partial \phi}{\partial t}, \tag{4.10}$$

with ϵ the energy per unit of mass. The time dependent virial theorem therefore yields to:

$$\frac{1}{2}\frac{d^2 I}{dt^2} = 2K + W, \tag{4.11}$$

with I the inertia tensor, K and the kinetic energy of the system and W its potential energy. The rapid variations if ϕ will therefore drive back-and-forth transfers between the kinetic and the potential energies. Since in equilibrium, $I = 0$ and $K = -E$ with $E = K + W$, then away from equilibrium K and W vibrate around these values, which scatters the energy distribution of stars. As a result, tightly bound stars become even more bound and migrate into a dense core while some weakly bound stars gain enough energy to escape the galactic potential. The remnant therefore displays a dense core and fewer stars than the sum of the two initial systems.

Once again, it should be noted that real galaxies are not mere systems of stars but rather composite systems of stars, dark matter particles and gas, which may lead to significant variations in the expected features , especially since the gas can shock and fall down to the core of the remnant to form new stars. At $z > 2$, when the universe is dense and very rich of cold gas, gas-rich major mergers are thus expected to significantly add up to cold gas inflows to trigger intense central starbursts and drive the formation of compact spheroids (Wellons *et al.* , 2015).

Thus, a conclusion of this first investigation is that the fraction of gas in progenitor galaxies stands out as a key parameter to predict the outcome of a merger.

4.1.4 Dry or wet mergers? Extended spheroids and massive disks.

As a result, the significance of mergers, considered a cornerstone of the bottom-up growth of galaxies, has been heavily debated in recent work. They are certainly capable of inducing star formation, black hole growth and morphological transformations (e.g. Springel *et al.* , 2005), but it is not obvious that, *at* $z > 1$, mergers drive the evolution of galaxy properties like stellar mass, size and morphology (Shankar *et al.* , 2004; Law, 2009; Kaviraj *et al.* , 2013b) considering the steady

input of accreted streams of gas (Kereš *et al.* , 2005; Ocvirk *et al.* , 2008; Dekel *et al.* , 2009) and the gas-rich nature of galaxies (Tacconi *et al.* , 2010; Santini *et al.* , 2014).

Semi-analytical models and numerical simulations propose that mergers can account for the size increase of *local* early-type galaxies if they are mostly dry (gas poor) and minor mergers (Boylan-Kolchin *et al.* , 2006; Khochfar & Silk, 2006; Maller *et al.* , 2006; Naab *et al.* , 2006a, 2007; Bournaud *et al.* , 2007a; De Lucia, 2007; Guo & White, 2008; Hopkins *et al.* , 2009; Nipoti *et al.* , 2009; Feldmann *et al.* , 2010; Shankar *et al.* , 2013; Bédorf & Portegies Zwart, 2013). Dry minor mergers explain the loss of compactness of massive ellipticals at $z < 2$, where they are thought to take over smooth accretion processes (driving in-situ star formation) in terms of stellar mass increase rates (Oser *et al.* , 2010; Lackner *et al.* , 2012; Hirschmann *et al.* , 2012; Dubois *et al.* , 2013a; Lee & Yi, 2013). The dryness of low-redshift galaxies is ensured either by the environment (for satellites infalling in groups and clusters) or by the presence of a supermassive black hole (BH) at the center of massive galaxies which powers feedback from the active galactic nuclei (AGN) (Sijacki *et al.* , 2007; Di Matteo *et al.* , 2008; Booth & Schaye, 2009; Dubois *et al.* , 2012b). Together, these mechanisms allow for the formation of extended elliptical galaxies that would otherwise remain compact discs (Dubois *et al.* , 2013b; Choi *et al.* , 2014).

Multiple numerical studies also focused on a few idealised high resolution merger events to determine their impact on the morphology of the stellar component of galaxies (Bournaud *et al.* , 2004, 2005; Naab & Trujillo, 2006; Peirani *et al.* , 2010). They found that while major mergers, or multiple minor mergers of stellar disks tend to produce elliptical-like remnants, either disky or boxy depending on the amount of gas available (Cretton *et al.* , 2001; Naab & Burkert, 2003; Naab *et al.* , 2006b; Qu *et al.* , 2011), single minor mergers did not systematically destroy the primary disk but only thickened it (Quinn *et al.* , 1993; Walker *et al.* , 1996; Velazquez & White, 1999; Younger *et al.* , 2007). On the other hand, the steady input of cosmological gas accretion is able to rebuild the disc of galaxies (Brooks *et al.* , 2009a; Agertz *et al.* , 2009; Pichon *et al.* , 2011). Hence one needs to assess the relative importance of mergers versus smooth accretion driven by the cosmic environment and to study its induced morphological diversity.

Fig. 4.1 summarizes the main suspected dynamical mechanisms that drive transformations across the Hubble sequence. Recall that this does not imply however the existence of an "arrow of time" across the Hubble sequence as those processes occur on different timescales, with different frequencies and dominate at different epochs. Noticeably, while mergers are stochastic events with timescales ranging from 100 Myr to 2 Gyr, major mergers being scarce, violent disk instabilities arise from steady intense mass inputs and efficiently produce compact spheroids within a few 100 Myr at early stages of galaxy formation ($z > 2$). As a result, all types in the sequence are

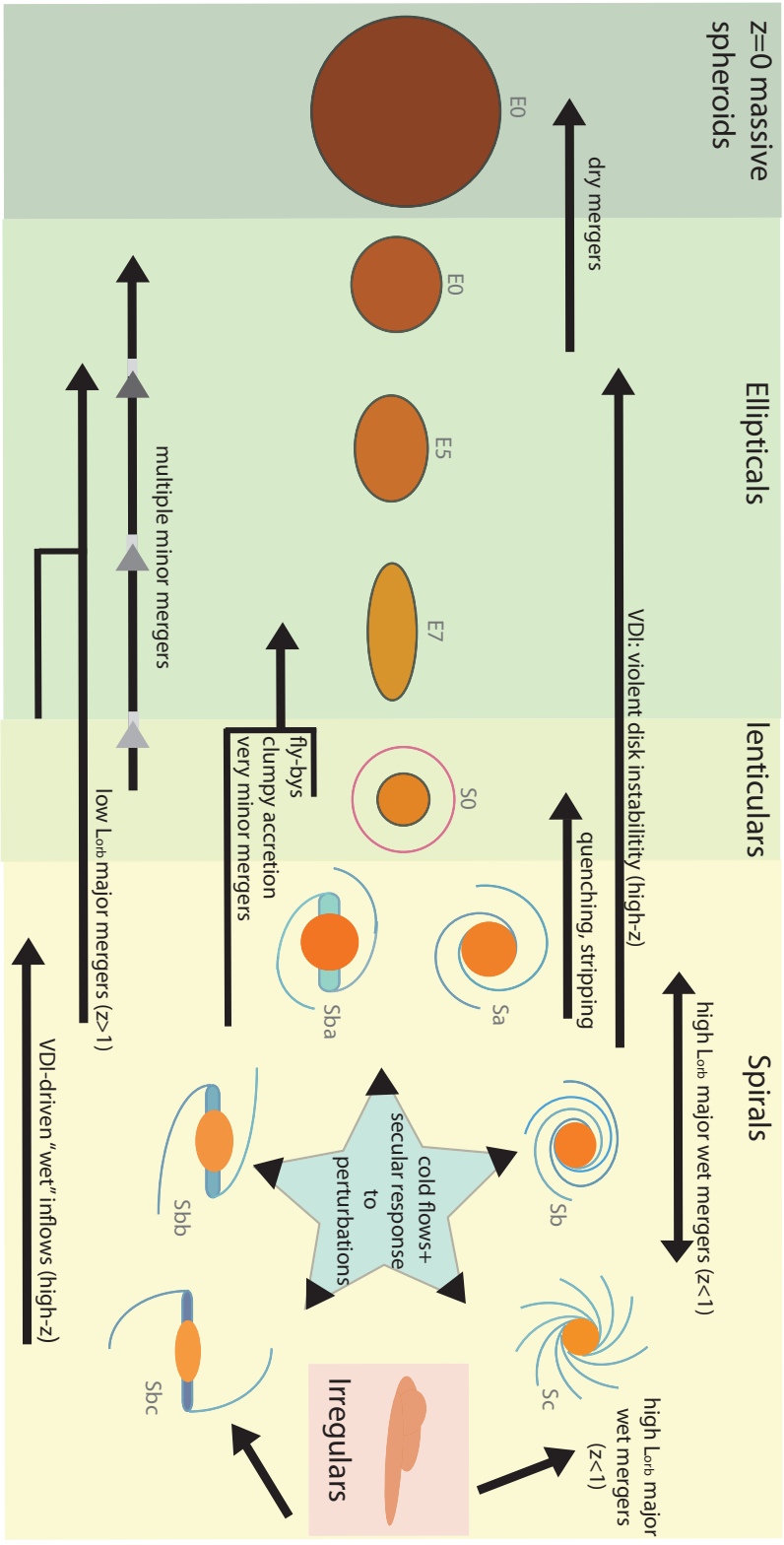

Figure 4.1: Illustration of the Hubble sequence with main suspected dynamical channels between the various morphologies

represented at any redshift from $z = 2 - 3$, but with varying features and ratios.

As stated in previous sections, this work is dedicated to understand the impact, competition and efficiency of only a few of these mechanisms at the peak of stellar formation history where they are believed to be dominant. In the simple framework I develop, I can classify them into two broad categories: smooth accretion processes (cold flows, clumpy accretion) and mergers (of various mass ratios and gas fraction).

4.2 Characterizing different types of mergers in Horizon-AGN

Similarly to what is done in previous chapters, galaxies are identified with the most massive sub-node method (Tweed *et al.* , 2009) of the AdaptaHOP halo finder (Aubert *et al.* , 2004) operating on the distribution of star particles with the same parameters than in Dubois *et al.* (2014). Unless specified otherwise, only structures with a minimum of $N_{\rm min} = 100$ particles are considered, which typically selects objects with masses larger than $2 \times 10^8\,{\rm M}_\odot$. Catalogues containing up to $\sim 150\,000$ galaxies are produced for each redshift output analysed ($1.2 < z < 5.2$). Although sub-structures may remain, these populations of galaxies are largely dominated by main structures.

Fig. 4.2 shows the evolution of the average stellar mass of galaxies with $M_{\rm s} > 10^{10}\,{\rm M}_\odot$ at $z = 1.2$, across the peak of cosmic star formation history. Note that the stellar mass growth of galaxies remains steady for most of the evolution. The knee at redshift $z = 1.5$ corresponds to a peak in the merger rate and smooth accretion observed at the same redshift (see Fig. 4.8), which is due to the extra level of refinement added at this particular redshift: as gas cells get refined, sub-cells are created where the density contrast is either enhanced or depleted, which triggers the formation of stars in the new densest sub-cells.

The purpose of this work is to better understand the underlying processes that lead to this steady growth, and how it affects the morphology of galaxies and their size evolution. To carry out such a study one needs to track the individual evolution of all the galaxies in the sample and find which progenitors have led to a specific galaxy.

Thus, I use the galaxy catalogues as an input to build merger trees with TreeMaker (Tweed *et al.* , 2009) with the same procedure that was described in Chapter 2. Any galaxy at redshift z_n is connected to its progenitors at redshift z_{n-1} and its child at redshift z_{n+1}. We use the merger tree of 22 outputs from $z = 1.2$ to $z = 5.2$ equally spaced in redshift. On average, the redshift difference between outputs corresponds to a time difference of 200 Myr (range between 100 and 300 Myr). We reconstruct the merger history of each galaxy starting from the lowest redshift z and identifying the most massive progenitor at each time step as *the galaxy* or *main progenitor*, and

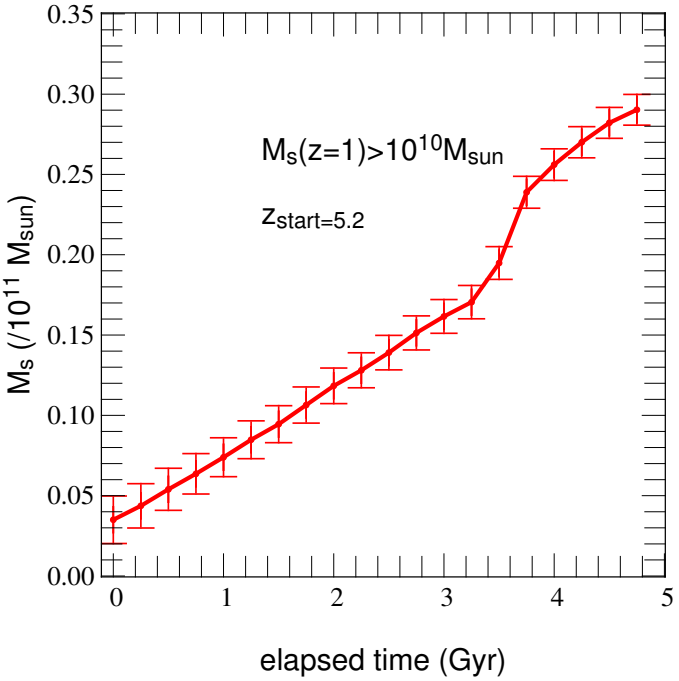

Figure 4.2: Evolution of the average stellar mass of galaxies with $M_{\rm s} > 10^{10}\,{\rm M}_{\odot}$ at $z = 1.2$.

the other progenitors as *satellites*. Moreover, we check that the mass of any child contains at least half the mass of its main progenitor to prevent misidentifications. Remember that such a definition of mergers (vs smooth accretion) depends on the threshold used to identify objects as any object below the chosen threshold is discarded and considered as smooth accretion.

We sort mergers in three categories depending on the mass fraction $\delta m = m_{\rm mergers}(z_{n-1\rightarrow n})/M_{\rm s}(z_n)$, where $m_{\rm mergers}(z_{n-1\rightarrow n})$ is the stellar mass accreted through mergers between z_{n-1} and z_n and $M_{\rm s}(z_n)$ the stellar mass of the merger product at z_n.

- *Major mergers* are defined as mergers with $\delta m > 20\%$,
- *Minor mergers* as mergers with $9\% < \delta m < 20\%$
- *Very minor mergers* with $4.5\% < \delta m < 9\%$.

Any merger with $\delta m < 4.5\%$ is discarded and counted as smooth accretion. This latest definition might seem questionable but this corresponds to the frequent accretion of very small stellar structures along varying directions which cannot be conceptually separated from a statistically smooth clumpy accretion process conjoint to accretion of gas streams. Furthermore, such events are neither observable nor discriminated from gas streams in observations. Eventually, they cannot be counted

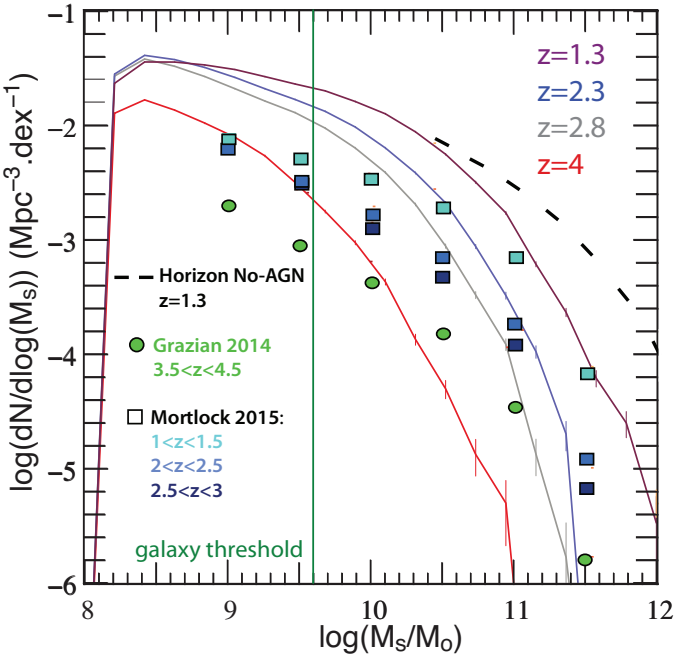

Figure 4.3: Galaxy stellar mass function in Horizon-AGN , for $z = 4$ to $z = 1.3$. N is the number density of galaxies, M_s the stellar mass (together with Horizon-noAGN for comparison). The sharp cut-off at $M_s = 10^8\,M_\odot$ corresponds to our completeness detection threshold. Observational points from CANDELS-UDS and GOOD-S surveys are rescaled from best fits in Mortlock *et al.* (2015) and Grazian *et al.* (2014) and overplotted. While mass functions are consistent at the high mass end, Horizon-AGN overshoots the low-mass end by about a factor 3 in this redshift range. The vertical green line shows the selection threshold for our main progenitors candidates, chosen to enable us to completely track their mergers with galaxies up to 20 times smaller.

as mergers since the merger sample is not complete for the whole range of *main progenitors* for this mass ratio: as explained in the next paragraph, I am not able to track smaller mergers for the low-mass galaxies in our sample since corresponding *satellite* masses are typically under the HaloMaker detection threshold. These bins are defined so as to be consistent with observational definitions of mergers using pairs of interacting galaxies, for which the observed mass ratio R is defined as $R = M_{\rm satellite}/M_{\rm galaxy}$ and where the subscripts indicate secondary and main progenitors respectively, as defined in the previous paragraph of this section. Our bins thus correspond to $R = 1:4$, $R = 1:10$ and $R = 1:20$.

In order to preserve completeness, I define a second threshold and exclude galaxies with $M_s < 5 \times 10^9\,M_\odot$ from the *galaxy* sample used in our analysis. *Satellites*, however, are allowed to be less massive, in order for us to still capture the whole range of merger ratios for the smallest of our galaxies. The *galaxy* threshold is identified as the green vertical line on Fig. 4.3, which displays the mass function for all the structures identified in the simulation (for comparison I have

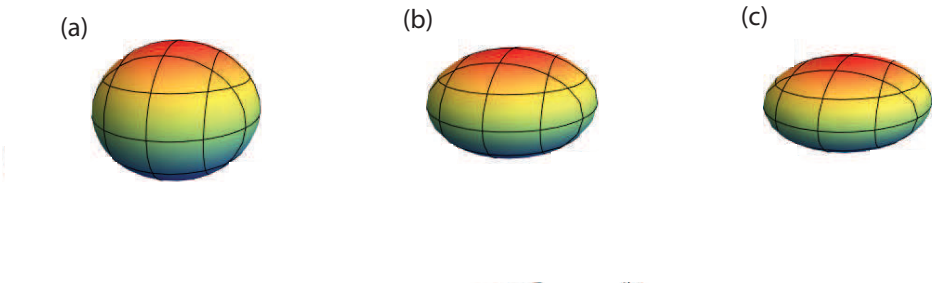

Figure 4.4: average ellipsoid for (a) the spheroid population, (b) the non-merger spheroid population after 1.5 Gyr, (c) the disk population

also plotted the mass function of the Horizon-noAGN simulation, which is the same simulation performed without BHs and, therefore, AGN feedback). As can be seen on the figure our sample is complete down to our strict selection threshold of $M_{\rm s} = 2 \times 10^8\,{\rm M}_\odot$, corresponding to galaxies with 100 star particles. Thus, the smallest mergers detectable for galaxies at the $M_{\rm s} < 5 \times 10^9\,{\rm M}_\odot$ threshold correspond to a mass ratio of $\delta m = 4.5\%$, which means that our merger classification is complete for our *galaxy* sample.

4.2.1 Characterizing the morphology of galaxies

As in Chapter 2, the inertia tensor I_{ij} of a galaxy is computed from its star particle distribution (indexed by l) and calculated at the centre of mass of the galaxy, according to the definition: $I_{ij} = \Sigma_l m^l(\delta_{ij}.(x^l_k.x^l_k) - x^l_i.x^l_j)$, where m_l is the mass of star particle l and x^l_i its position in the barycentric coordinate system of the galaxy. As a 3x3 real symmetric matrix, the inertia tensor can be diagonalized, with its eigenvalues $\lambda_1 > \lambda_2 > \lambda_3$ being the moments of inertia relative to the basis of principal axes e_1, e_2 and e_3. The lengths of the semi-principal axes a, b and c (with $a > b > c$) are straightforwardly derived from the moments of inertia:

$$a = (5/M_{0.5})\sqrt{\lambda_1 + \lambda_2 - \lambda_3}\,,\ \text{along e}_3\,,$$
$$b = (5/M_{0.5})\sqrt{\lambda_1 + \lambda_3 - \lambda_2}\,,\ \text{along e}_2\,,$$
$$c = (5/M_{0.5})\sqrt{\lambda_3 + \lambda_2 - \lambda_1}\,,\ \text{along e}_1\,.$$

In Chapter 2, I use the triaxiality ratio as a proxy for the shape of the galaxy. In this chapter, I want to be able to characterize more precisely the morphology of galaxies and to be able to trace their evolution over time, including through violent events such as mergers.

Therefore I rely on the axis ratios: $\xi_1 = c/a$, $\xi_2 = c/b$ and $\xi_3 = b/a$ and follow the variations

of these three parameters over time. As an example, a perfectly round and infinitely thin disk has $\xi_1 = 0$, $\xi_2 = 0$ and $\xi_3 = 1$. For a Milky Way like galaxy (including stars from the inner bulge+thin disk+bar), one gets $\xi_1 = 0.06$, $\xi_2 = 0.07$ and $\xi_3 = 0.98$.

The limited spatial resolution (1 kpc) of the Horizon-AGN simulation, prevents us from obtaining disks as thin as these. We therefore identify disks with our most flattened ellipsoids. More specifically, I adopt $\xi_1 < 0.45$ and $\xi_2 < 0.55$ as a definition for disks and $\xi_1 > 0.7$ and $\xi_2 \rangle 0.8$ to define spheroids. Other galaxies are simply classified as ellipsoids. Fig. 4.4 displays a visual representation of the ellipses that characterize the average member in the disk (panel c) and spheroid (panel a) samples.Though these cuts may appear a crude approximation, they are actually quite consistent with 3-D axis ratios reconstructed from observations (Lambas *et al.* , 1992). Note that I also define the morphology of our galaxies using star particles enclosed within their half mass radius sphere. We found that this is more robust than using all the star particles identified by our halo finder especially for post-merger remnants, as these can exhibit elongated tidal features which persist for a considerable amount of time.

4.2.2 Gas content of high-z galaxies

The gas content and its properties (density, metallicity, pressure, temperature) of each galaxy is extracted from the AMR grid, considering all cells within its effective radius.

Since the gas needs to be cold and dense enough to be eligible to form stars, let us define as "cold" gas (in the sense of star forming gas) the cells with a gas density higher than $n > 0.1\,\mathrm{H\,cm^{-3}}$ and a temperature $T \leq 10^4\,\mathrm{K}$(after subtracting the temperature from the polytropic equation of state). We also define the gas fraction $f_{\rm gas}$ of a galaxy as:

$$f_{\rm gas} = M_{\rm gas}^{\rm cold}/(M_{0.5} + M_{\rm gas}^{\rm cold})\,, \tag{4.12}$$

with $M_{\rm gas}^{\rm cold}$ the mass of cold gas and $M_{0.5}$ the mass of stars, both enclosed within the sphere of radius $r_{0.5}$. Fig. 4.5 displays a sketch of the systematic procedure used to extract gas content from AMR cells for all galaxies in Horizon-AGN .

As can be seen in Fig. 4.6, this quantity decreases with stellar mass and redshift due to star formation and feedback, older galaxies becoming more massive after they used the gas available to form stars and/or after it has been blown out of them by AGN/supernova feedback. This evolution is consistent with previous numerical studies (e.g. Dubois *et al.* , 2012b; Popping *et al.* , 2014).

For each galaxy in the sample, one can define the maximum radius $r_{\rm max}$ as the distance between the galactic center of mass (COM) and the furthest star particle, the effective radius $r_{0.5}$ as the half stellar mass radius and $\Delta r_{\rm cell} = r_{0.5}/10$. AMR cells with a size $d_{\rm cell}$ larger than $\Delta r_{\rm cell}$ are

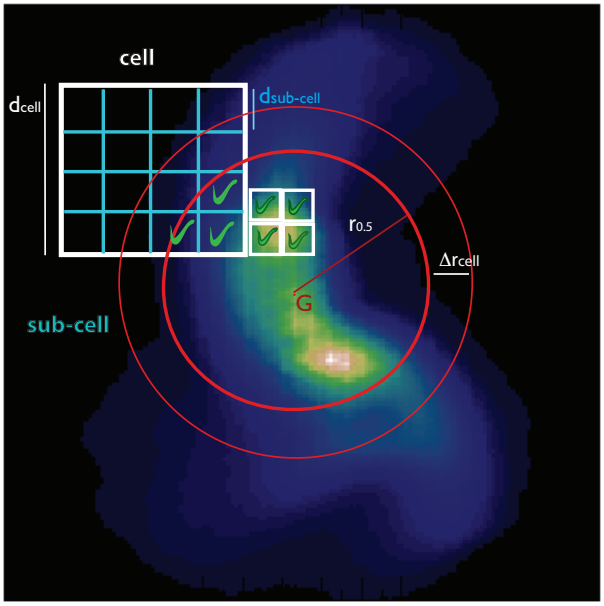

Figure 4.5: 2D sketch of the gas cell assignment procedure for one galaxy from Horizon-AGN (shown as a face-on projected gas density map). The thick red circle represents the effective radius $r_{0.5}$ around the galactic center of mass and the white squares the AMR grid with different levels of refinement. The green tick indicates when a cell or sub-cell is counted as belonging to the galaxy (see text for detail).

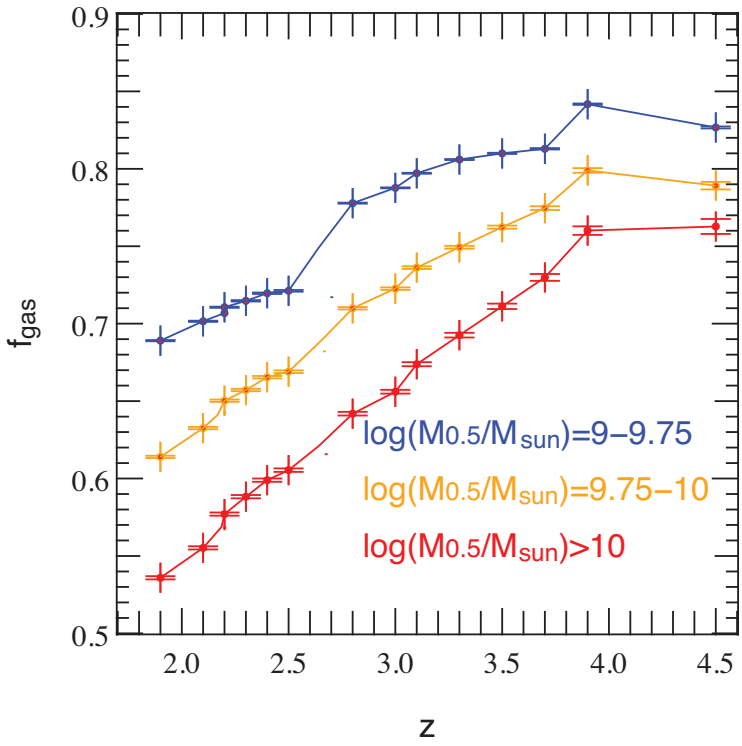

Figure 4.6: Evolution of the gas fraction $f_{\rm gas}$ in the redshift range $1.8 < z < 4.5$ for different mass bins, where $M_{0.5}$ is the stellar mass enclosed within the half mass sphere and $\mathrm{M}_{\odot}$ the mass of the sun. Results are consistent with previous simulations (e.g. Popping *et al.* , 2014). $f_{\rm gas}$ decreases with redshift as star formation consumes the available gas and/or feedback blows it out of the galaxies.

subdivided in 2^{3n_c} sub-cells with n_c such that $d_{\rm sub-cell} < \Delta r_{\rm cell}$. AMR cells counted as belonging to the galaxy are: 1) AMR cells with a size $d_{\rm cell} < \Delta r_{\rm cell}$ and a center within the sphere of radius $r_{0.5}$ centred on the COM 2) sub-cells of larger AMR cells with a length $d_{\rm cell} < \Delta r_{\rm cell}$ and a center within the sphere of radius $r_{0.5}$ centred on the galaxy COM. This procedure is illustrated in Fig. 4.5 which shows a 2D sketch of the cell selection process on a face on projected gas density map for a galaxy from Horizon-AGN with a post-merger sub-structure at $z = 3$.

Fig. 4.6 shows the evolution of the average gas fraction across the peak of cosmic star formation history for galaxies of different masses. Our results are consistent with previous numerical investigations (e.g. Popping *et al.* , 2014). Hence $f_{\rm gas}$ decreases with redshift as star formation consumes and feedback expels the available gas.

4.2.3 Merger rates: from observations to simulation

While it is now well established that mergers have a significant impact on $z < 1$ early-type galaxy sizes and kinematics, it is not yet clear whether (i) this extends to the galaxy population at high redshift and (ii) over which timescale they are of importance, as many galaxies may not merge at all for long periods of time. Observations of local galaxies not only suggest that early-type galaxies increased their size by 3–5 from $z \sim 2$, but also that, while most massive ones ($M_{\rm s} > 1.5 \times 10^{11}\,{\rm M}_{\odot}$) roughly doubled their size from $z \sim 1$, smaller ones underwent a more limited growth between $z \sim 1$ and z=0 (by a factor 1.1 to 1.3, Huertas-Company *et al.* , 2013). From these results, one can expect a growth by at least a factor $2 - 2.5$ between $z \sim 2 - 3$ and $z = 1$ (Nipoti *et al.* , 2012). To quantify the relative contribution of mergers and smooth accretion to the total mass budget of galaxies over the range of redshifts corresponding to the peak of cosmic star formation history down to $z = 1$, I therefore compute the rates of galaxies having undergone at least a merger within our mass fraction bins at these redshifts.

We find that, at $z = 1.2$, around 35% of galaxies with $M_{\rm s} > 10^{10}\,{\rm M}_{\odot}$ have undergone at least one major merger, 80% a minor merger, and 85% a very minor merger. These results are consistent with findings by Kaviraj *et al.* (2014a), (our minor merger rates are slightly inferior due to a coarser redshift sampling). Fig. 4.7 (left panel) presents the evolution of those rates with redshift, focusing on the sub-sample of galaxies in this mass range who possess a progenitor at $z = 5.2$ (sub-sample of 15 000 galaxies). It displays the evolution of the fraction of this sub-sample which remains free from mergers of a given type (major, minor and very minor) as a function of cosmic time. It shows that over this 4 Gyr period, $\sim 50\%$ of the sample undergoes a major merger and therefore that mergers, especially minor ones, are quite frequent over the whole redshift range. The sample is affected by mergers at an average rate around $1 - -2 \times 10^{-3}\,{\rm Gyr}^{-1}\,h^3\,{\rm Mpc}^{-3}$ and $3 - -5 \times 10^{-4}\,{\rm Gyr}^{-1}\,h^3\,{\rm Mpc}^{-3}$ for all mergers and major mergers respectively. Note that these values are consistent with observations by Lotz *et al.* (2011) and in good agreement with the cumulative merger rates per galaxy derived from the Illustris simulation (Rodriguez-Gomez *et al.* , 2015) .

The right panel of Fig. 4.7 focuses on galaxies which have had at least a merger between $z = 5.2$ and $z = 1.2$. It shows the probability distribution function (PDF) $P(n, > \delta m)$ for these galaxies to have undergone a number n of mergers of a given mass ratio, δm, between $z = 5.2$ and $z = 1.2$. This PDF indicates that, while most of these galaxies underwent at most a single major merger, on average they undergo two to three merger events.

Fig. 4.8 reveals that both mergers and smooth accretion ought to be taken into account to

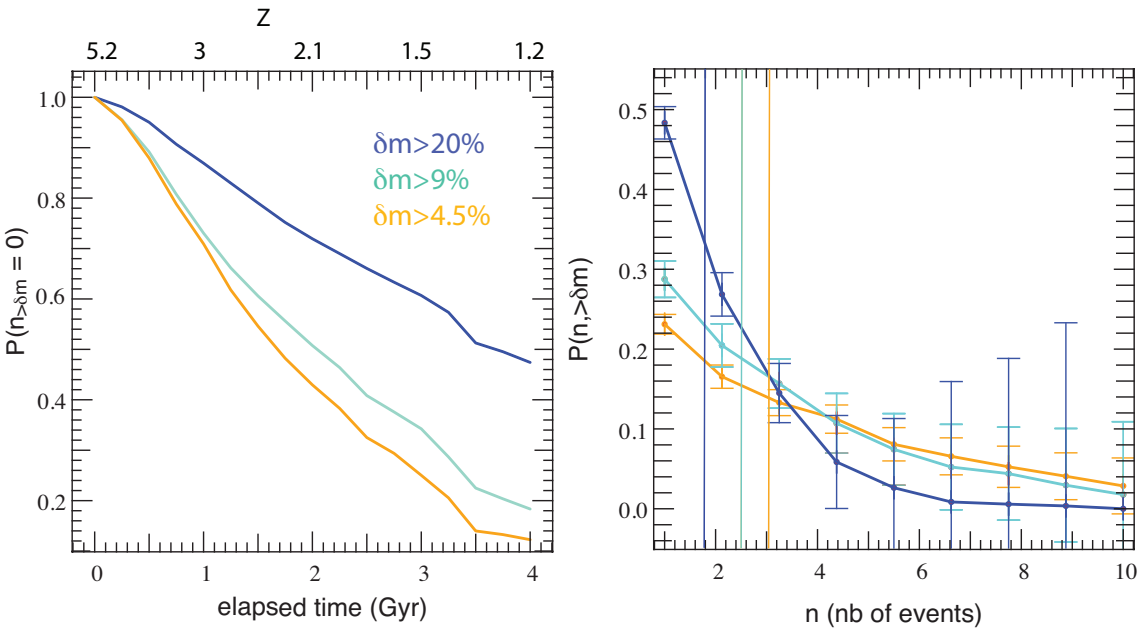

Figure 4.7: *Left panel*: evolution of a sub-sample of galaxies identified at $z = 1.2$ with $M_s > 10^{10}\,M_\odot$ and which can be tracked to $z = 5.2$. This panel shows the probability for galaxies *not* to undergo a major or minor merger during the redshift interval. *Right panel*: PDF of the number n_m of galaxy mergers of a given mass ratio, δm, undergone between redshifts $5.2 \geq z \geq 1.2$. This PDF is restricted to galaxies with at least one very minor merger. Vertical lines show the average value for each sample. It illustrates the paucity of major mergers: most galaxies which merged, have had at most one major merger across this cosmic time interval, while they go through on average 2 to 3 mergers.

attempt to understand the morphology distribution of galaxies. This figure shows the evolution of the smooth accretion and merger contributions to the mass budget of galaxies across the peak of cosmic star formation history. The first panel presents the evolution of $\Delta m/M_{\rm s}$ averaged for all galaxies with $M_{\rm s} > 10^{10}\,{\rm M}_{\odot}$ at $z = 1.2$, with Δm the mass accreted between two successive time steps (i.e. over a period of ~ 200 Myr) and $M_{\rm s}$ the stellar mass. The red and green curves correspond to the mass fraction accreted via smooth accretion of gas (green curve) and stars (red curve: gas+stars; i.e. including mergers with $M_{\rm s} < 2 \times 10^{8}\,{\rm M}_{\odot}$ galaxies), and the blue curve corresponds to the mass fraction accreted through mergers. While at high-redshift ($z \sim 5$) young and small galaxies undergo a rapid relative mass growth through accretion of gas and swift merging of very small structures close to the detection threshold, this activity settles around $z \sim 3-4$, when effects of smooth accretion and mergers on mass growth become comparable, until mergers slightly take over around $z \sim 1.5$. The net result is that at $z = 1.2$, $\sim 45\%$ of the galactic stellar mass can be attributed to in situ formation from smooth accretion of gas, as can be seen on Fig. 4.8 (second panel) .

In conclusion, mergers and smooth accretion contribute equivalently to the galactic mass budget over the peak of cosmic star formation history. It therefore seems that in order to understand the evolution of galactic sizes and morphologies over this period, one needs to account for the possibility that these two processes play different roles. This is what I will explore in the next sections.

4.3 Size growth of galaxies

4.3.1 Galactic stellar density

Fig. 4.9 shows the evolution of the stellar density, obtained by adding the masses of all star particles enclosed within the half mass radius of the galaxy. Since the shape of galaxies can vary significantly over the cosmic time interval spanned by our study, especially when galaxies merge, I take anisotropy into account. More specifically, the density ρ is defined as $\rho = 3M_{0.5}/(4\pi abc)$ with $a > b > c$ the lengths of the semi-principal axes of the galaxy derived from the eigenvalues of the inertia tensor and $M_{0.5}$ is the sum of all the masses of the star particles contained within its half mass radius. The left panel of the figure shows the PDF of the relative density growth $\mu = 2(\rho_{n+1} - \rho_n)/(\rho_n + \rho_{n+1})$, where ρ_n is the average density of the galaxy within its half mass radius at time step n, stacked for each time output of the simulation between $1.2 \leq z \leq 5.2$. Notice how mergers tend to widen the distribution, populating the high-compactions and high-dilatation tails of the distribution. Looking at this panel, one might think that smooth accretion and very minor mergers tend to lower the density of the merger remnant on average, while minor and major

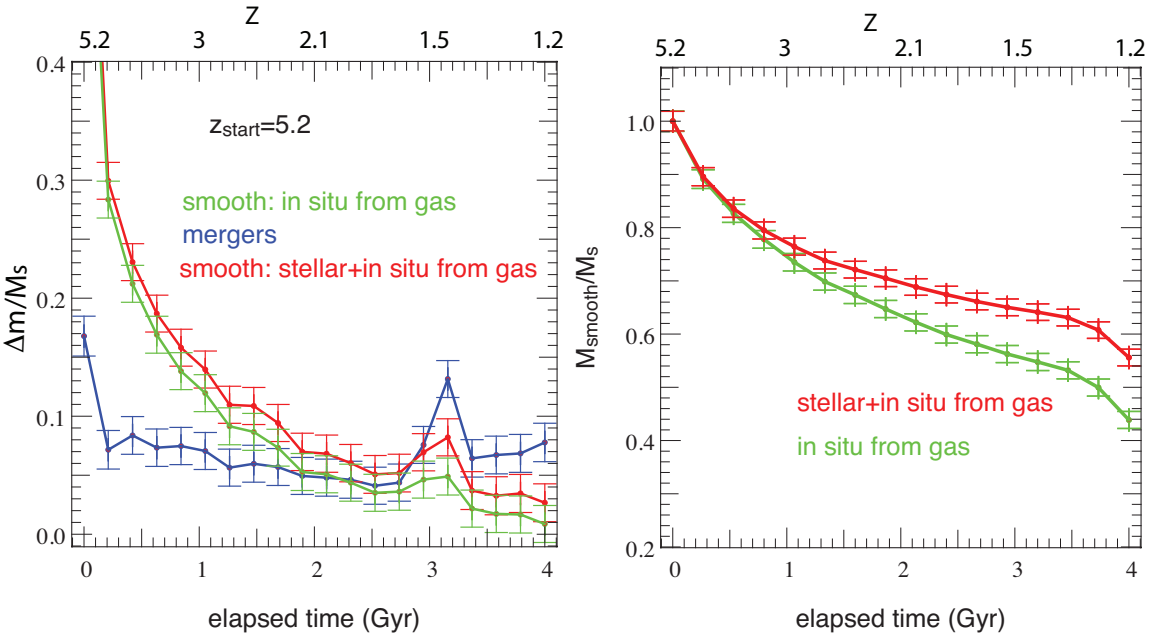

Figure 4.8: *Left panel*: evolution of $\Delta m/M_{\rm s}$ over cosmic time for galaxies with $M_{\rm s} > 10^{10}\,{\rm M}_{\odot}$ at $z = 1.2$, where Δm is the mass increase due to in situ formed stars (green), merger with a companion (blue), or in situ formed stars combined with the 'diffuse' accretion of stars (i.e. stars not identified as belonging to any galaxy, red) between two time steps ($\sim$ 200 Myr), and $M_{\rm s}$ is the stellar mass. We plot average values for all selected galaxies at every time output. Note that mergers and smooth accretion contribute similarly to the mass growth of galaxies from $z = 3$ onwards. *Right panel*: evolution of $M_{\rm smooth}/M_{\rm s}$ over cosmic time from $z = 5.2$ to $z = 1.2$, where $M_{\rm smooth}$ is the mass of stars either produced in situ from the gas component, or accreted 'smoothly' (i.e. star particles not associated with a galaxy above our mass resolution threshold), for galaxies with $M_{\rm s} > 10^{10}\,{\rm M}_{\odot}$ at $z = 1.2$. At $z = 1.2$, about half of the stellar mass of these galaxies comes from such smooth accretion processes.

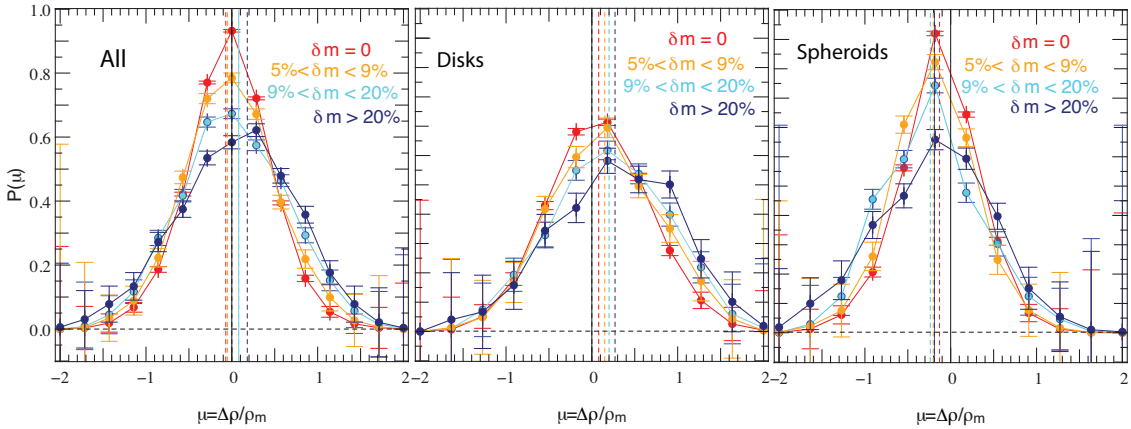

Figure 4.9: *Left panel:* PDF of the density growth ratio $\mu = 2(\rho_{n+1} - \rho_n)/(\rho_n + \rho_{n+1})$, where ρ_n is the density of the galaxy within its half mass radius at time step n, for different merger mass ratios. This ratio is calculated for galaxies with $M_s > 10^{9.5} M_\odot$ over each time step between $1.2 \leq z \leq 5.2$, and all these timesteps are then stacked. Each vertical dashed line shows the average value for the merger mass ratio bin of the corresponding color. Mergers have a tendency to widen the distribution and increase the stellar density, especially major mergers (vertical dashed line on the positive side of μ values). However, this behavior is actually different for galaxies which are disks prior to the merger (for which the stellar density rises: *middle panel*) and for those which are originally spheroids (for which the stellar density decreases: *right panel*).

mergers tend to increase it, but it is actually highly dependent on the initial morphology of the galaxy. This can be seen on the middle and right panels of Fig. 4.9. Galaxies that are initially disks show an increased stellar density after mergers, the effect being stronger the higher the mass ratio of the merger. On the other hand, galaxies which begin as spheroids tend to have their stellar density decreased by mergers, the effect being statistically stronger for minor mergers. 55% of spheroids which merge betray a decrease in stellar density after $\sim$ 200 Myr, and only 40% of the non-merger galaxies do the same. It is interesting to notice that, in both cases, this increase/decrease in average density is related to how skewed the distribution becomes and not only to a global drift towards positive/negative values. As a result, minor and major mergers of spheroids are much more likely to trigger important decreases in stellar density (by more than a factor 2) than smooth accretion: 16% of cases versus 5% respectively, and even as low as 3% if events where stars are accreted below our galaxy mass threshold are discarded. Around 8% of major mergers and even fewer minor mergers trigger dilatations by more than a factor 5.

Similarly, 73% of disk galaxies increase their density after merging (against 63% for non-mergers). However, and more importantly, 30% of these mergers increase it by at least a factor 2 as compared to only 9% for smooth accretion. Finally, only 10% of the major mergers and the minor mergers lead to compactions by more than a factor 5.

These results statistically support the claim that mergers turn disks into denser structures while they tend to lower the density of spheroids. Moreover, although major mergers are found to be quite rare, the ability of the more frequent minor mergers to trigger effects of comparable amplitude points towards an important role of multi-minor mergers in driving the size-mass relationship of early-type galaxies (Kaviraj, 2014).

4.3.2 Galactic half-mass radius

We further analyze the role of mergers in driving galaxy stellar density evolution by looking at the relation between growth in stellar mass and growth in stellar half-mass radius.

Evolution of the average radius over cosmic time The bottom panels show the evolution of the average half-mass radius $r_{0.5}$ as a function of redshift when splitting the galaxy sample in bins of "final" mass (i.e. galaxy masses at redshift $z = 1.2$; bottom left panel) and in bins of constant stellar mass (i.e. independent of redshift; bottom right panel). Once again, the results shown on Fig. 4.10 are consistent with the overall evolution of the size-mass relationship from observations such as Huertas-Company *et al.* (2013) (though our simulated galaxies are a factor of ~ 2 larger): galaxies of a given stellar mass display much larger radii at $z = 1.2$ than their counterparts of similar stellar mass at $z = 5.2$, most of the growth taking place between $z = 3$ and $z = 1.2$. More specifically, at $z = 1.2$ galaxies with $M_{\rm s} > 10^{10.5}\,{\rm M}_{\odot}$ display an average half-mass radius twice to 3 times bigger than their counterparts at $z = 3$. (see bottom right panel), while one can see on the bottom left panel that galaxies reaching $M_{\rm s} > 10^{10.5}\,{\rm M}_{\odot}$ at $z = 1.2$ have also seen their half-mass radius grow by a factor 2 to 3 since $z = 3$, and by a factor 4 since $z = 5.2$.

Dynamical analysis: Full Sample To do so, I compute the evolution of the logarithmic derivative of the half mass radius $r_{0.5}$ with respect to $M_{\rm s}$ as a function of the mass ratio $\delta m = \Delta m / M_{\rm s} \propto \Delta \log_{10} M_{\rm s}$, where Δm is the stellar mass accreted between two consecutive outputs through mergers (blue curve) or smooth accretion (red and green curves) for all galaxies and all time outputs between $z = 5.2$ and $z = 1.2$. Note that $M_{\rm s}$ or $M_{0.5}$ are equivalent for the purpose of this comparison so I use them interchangeably. The result is shown in the top left panel of Fig. 4.10. While mergers and smooth accretion drive a similar amount of mass growth (see the left panel of Fig. 4.8 in the previous section), mergers are much more efficient drivers of galaxy size growth. Ignoring the very shallow dependence on δm, smooth accretion processes lead to an average radius-mass relation $r_{0.5} \propto M_{\rm s}^{\alpha}$ with $\alpha = 0.1 \pm 0.05$. Slightly higher values of α are reached for higher δm (see left panel of Fig. 4.10), but always remain within a factor 2, i.e. $\alpha \leq 0.2$. This dependence on δm

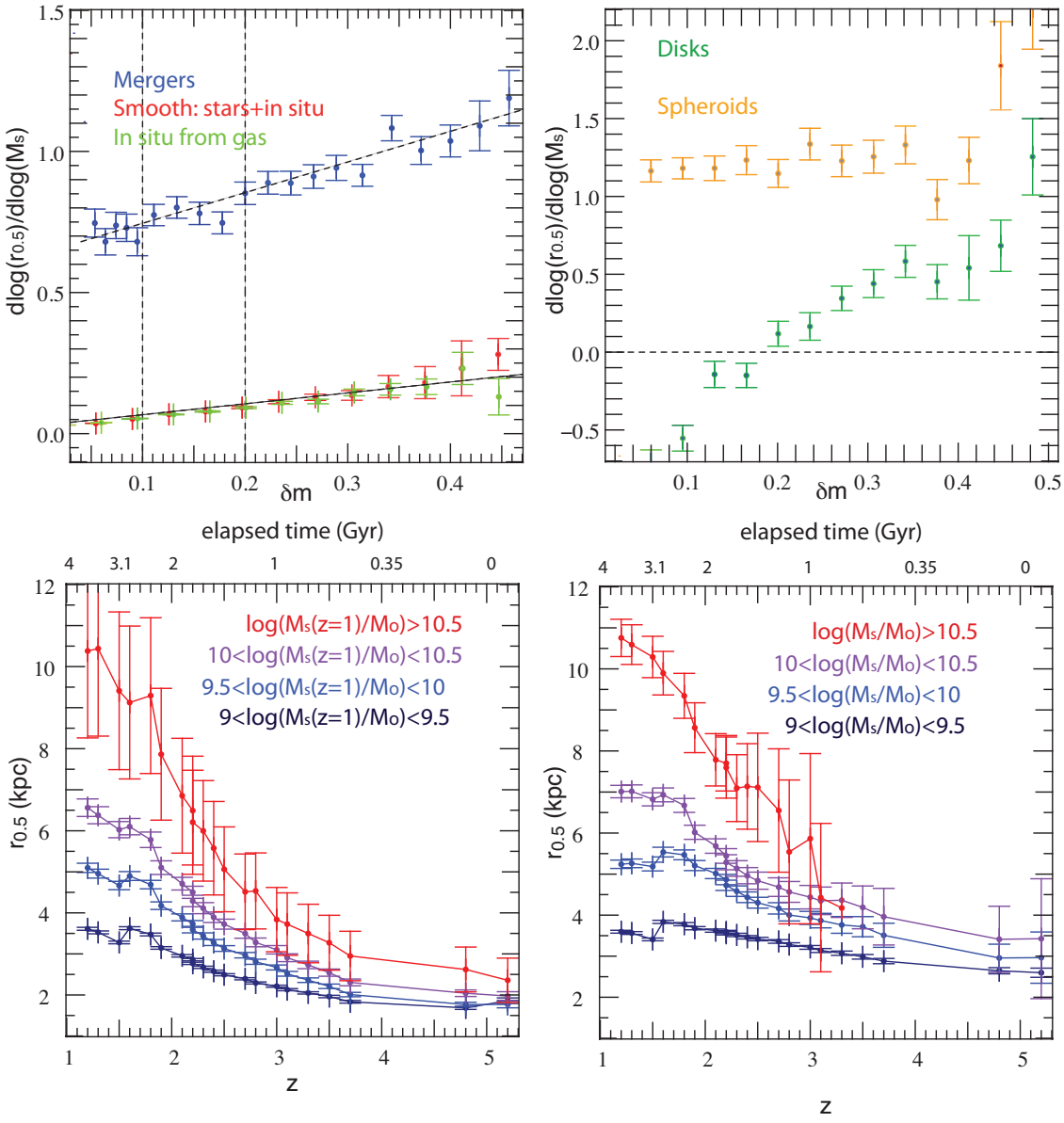

Figure 4.10: *Top left panel*: evolution of the logarithmic derivative of the half-mass radius $r_{0.5}$ with respect to the mass ratio $\delta m = \Delta m/M_s$ (Δm is the stellar mass gained between two consecutive outputs) of the merger or smoothly accreted material for all galaxies and all time outputs between $z = 5.2$ and $z = 1.2$. Filled blue symbols indicate mergers, red and light green ones represent smoothly accreted mass, including a stellar component (red) or gas only (green). Whilst the evolution is linear in each case, the dependence of radius growth on the mass ratio is found to be much steeper for mergers. *Top right panel*: same plot as the top left panel, except we have split the merger sample according to different pre-merger morphologies: disks (green) and spheroids (yellow). The steepness of the radius versus δm relation appears mainly caused by minor merger disruption of the disks. *Bottom left panel*: evolution of the half-mass radius as a function of redshift for galaxies split into bins of different mass at redshift $z = 1.2$. *Bottom right panel*: same plot as in the bottom left panel but for galaxies split into redshift independent mass bins.

can be explained by the fact that higher mass ratio values most often correspond to lower stellar masses, for which cold flows bring in more specific angular momentum than hot phase accretion in more massive galaxies (Kimm *et al.* , 2011). For mergers, I obtain $r_{0.5} \propto M_s^{\beta}$ with $\beta = 0.85 \pm 0.3$. β also increases with δm up to values ~ 1.2. These values are consistent with observations (e.g. Newman *et al.* , 2012; Cimatti *et al.* , 2012; Huertas-Company *et al.* , 2013; van der Wel *et al.* , 2014, who found a value of β around $\sim 0.6 - 0.8$ for early-type galaxies), and together with the smaller values of α, support the idea that the size growth of galaxies is mostly driven by mergers (Boylan-Kolchin *et al.* , 2006; Nipoti *et al.* , 2009; Feldmann *et al.* , 2010; Dubois *et al.* , 2013a).

4.3.3 Impact of initial gas fraction and morphology

However, Fig. 4.10 does not distinguish gas-rich and gas-poor mergers. This could be potentially important as gas-poor mergers are known to trigger intense size growth of local early type galaxies (e.g. Naab *et al.* , 2007; Feldmann *et al.* , 2010), whereas accretion of gas (by gas-rich mergers or smooth accretion) is thought not to be able to since their gas shocks radiatively and loses angular momentum, therefore piling up in the central region of the galaxy where it rapidly turns into stars and causes size contraction. The right panel of Fig. 4.11, lends statistical support to this claim. It shows the average value of the merger mass ratio δm which leads to a given relative variation of the half mass radius $\Delta r_{0.5}/r_{0.5}$, for mergers with $f_{\rm gas} > 0.6$ (blue data points) and $f_{\rm gas} < 0.6$ (yellow data points). From this data, one can see that radius contraction (negative values of $\Delta r_{0.5}/r_{0.5}$) is confined to gas rich minor mergers (blue data points with $0.09 < \delta m < 0.2$). The corresponding yellow data points for gas poor mergers are below – or very close to – the smooth accretion threshold (lower horizontal dashed line), indicating that smooth accretion of gas is in fact the leading advection process in those cases. Interestingly enough, major mergers $\delta m > 0.2$ statistically never lead to a compactification of galaxies, regardless of whether they are gas rich or not: the violent disruption that they occasion does not translate into a funelling of material to the central region as it does for minor mergers, but as an extended redistribution of it. Note that the threshold of $f_{\rm gas} = 0.6$ is chosen high compared to the values traditionally used to define wet and dry mergers at low redshift because galaxies are more gas rich on average in the redshift range of this study. One can get an idea of how much smaller the sample gets when this threshold is lowered to $f_{\rm gas} = 0.2$ by looking at the left panel of Fig. 4.11.

This panel presents the dependence of the logarithmic derivative of the half mass radius $r_{0.5}$ on the mass ratio δm for our sample of galaxies split into different pre-merger gas fraction bins. One can see that star rich mergers with $f_{\rm gas} < 0.6$ (in yellow), especially minor ones ($0.09 < \delta m < 0.2$)

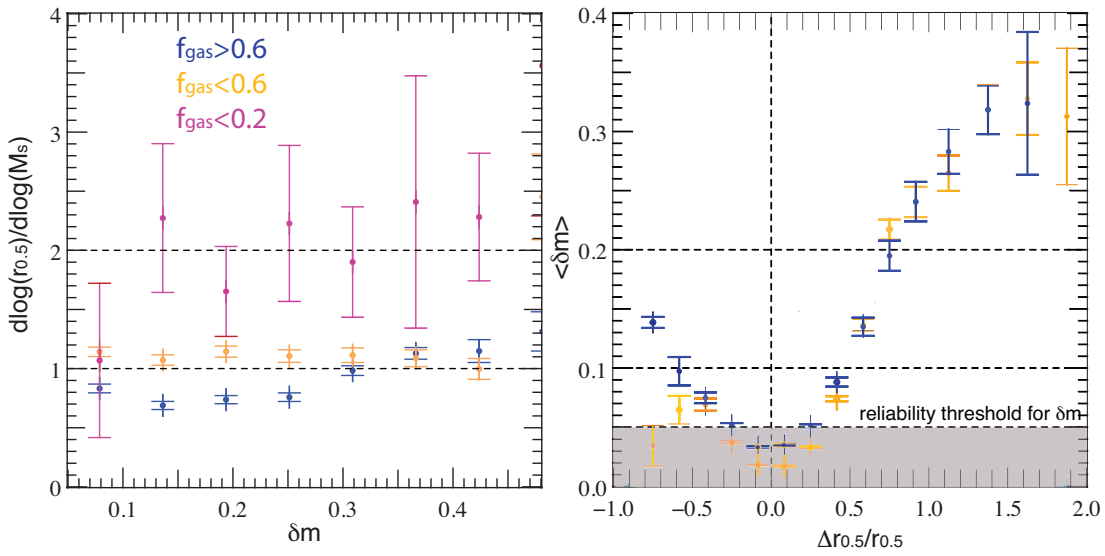

Figure 4.11: *Left panel*: evolution of the relative variation of the half-mass radius as a function of the merger mass ratio for all galaxies which undergo a merger between $z = 5.2$ and $z = 1.2$ and for different pre-merger gas fractions: $f_{\rm gas} < 0.2$ (pink symbols), $f_{\rm gas} < 0.6$ (yellow symbols) and $f_{\rm gas} > 0.6$ (blue symbols). The error bars plotted correspond to 1σ errors. Horizontal dashed lines represent $r_{0.5} \propto M_{\rm s}^{\gamma}$, with $\gamma = 1$ and $\gamma = 2$ which are predicted size-mass relations for (dry) major and minor mergers using the virial theorem (Hilz *et al.* , 2012; Dubois *et al.* , 2013a) . Note how the presence of gas limits the radius growth. *Right panel*: average mass ratio versus relative variation of the half-mass radius $\Delta r_{0.5}/r_{0.5}$ for mergers with gas fraction $f_{\rm gas} < 0.6$ (yellow) and $f_{\rm gas} > 0.6$ (blue). Horizontal dashed lines show major/minor/smooth accretion separation thresholds in δm. The vertical dashed line indicates the border between expansion (positive values) and contraction (negative values). Note how radius contraction is confined to wet minor mergers.

induce a more efficient radius growth than their gas dominated counterparts of similar mass ratio (in blue). Gas deprived mergers with $f_{\rm gas} < 0.2$ (pink curve), whether major or minor, lead to a rapid growth of the effective radius compatible with $r_{0.5} \propto M_{\rm s}^{\gamma}$ where $\gamma = 2 \pm 0.5$. This power law index is in excellent agreement with predictions from Hilz *et al.* (2012), and consistent with previous numerical studies (Boylan-Kolchin *et al.* , 2006; Nipoti *et al.* , 2009; Feldmann *et al.* , 2010), although slightly higher, which therefore lends extra support to the scenario involving multiple dry mergers to explain the loss of compacity of massive early-type galaxies at low redshifts.

Going back to the top right panel of Fig. 4.10, one can see that the dependence of the size-mass relationship on merger mass ratio can be interpreted as a morphological effect: galaxies that are spheroids prior to the merger (yellow data points) systematically grow in size almost indistinctively with mass ratio (except for the most extreme major mergers), whilst disks (green data points) exhibit a size growth proportional to the accreted mass ratio over the same range in δm. Note that van der Wel *et al.* (2014) find a different size-mass evolution for early-type and late-type galaxies with $\beta \simeq 0.75$ and $\beta \simeq 0.22$ respectively with negligible evolution with redshift. In our simulation, we find that spheroids (i.e. early-type galaxies) have $\beta = 1.2$ on average and disks (i.e. late-type galaxies) have $\beta \simeq -0.5$ for low values of δm and $\beta \simeq 0.5$ for large values of δm, which shows a similar discrepancy of the size-mass evolution between different galaxy morphologies to that observed in van der Wel *et al.* (2014). This stresses the need to study the morphology of our galaxies in further detail, so let us now turn to this issue.

4.4 Impact on morphologies

4.4.1 Smooth accretion

Focussing on more accurate morphological parameters, Fig. 4.12 displays the time evolution – for galaxies which do not merge – of the cumulative PDFs of the principal semi-axis ratios $\xi_1 = c/a$, $\xi_2 = c/b$ and $\xi_3 = b/a$ with $a > b > c$ of the inner half-mass stellar component, derived by calculating the inertia tensor of the galaxy. One can see from this figure that, while ξ_3 tends to remain constant over cosmic time, with a value strongly peaked at 1 (large axis equals to intermediate axis), both average values of ξ_1 and ξ_2 decrease at an average rate of almost 10% per Gyr, from 0.64 and 0.74 down to 0.54 and 0.64 respectively in the 4 Gyr which separate $z = 5.2$ and $z = 1.2$. For reference, note that an infinitely thin and homogeneous disk has $\xi_1 = \xi_2 = 0$ and $\xi_3 = 1$ while a perfect sphere has $\xi_1 = \xi_2 = \xi_3 = 1$. Our result indicates that smooth accretion and consecutive in situ star formation tend to flatten galaxies over time along the minor axis, which coincides with the spin axis. However, this accretion has no significant effect on the circularity of

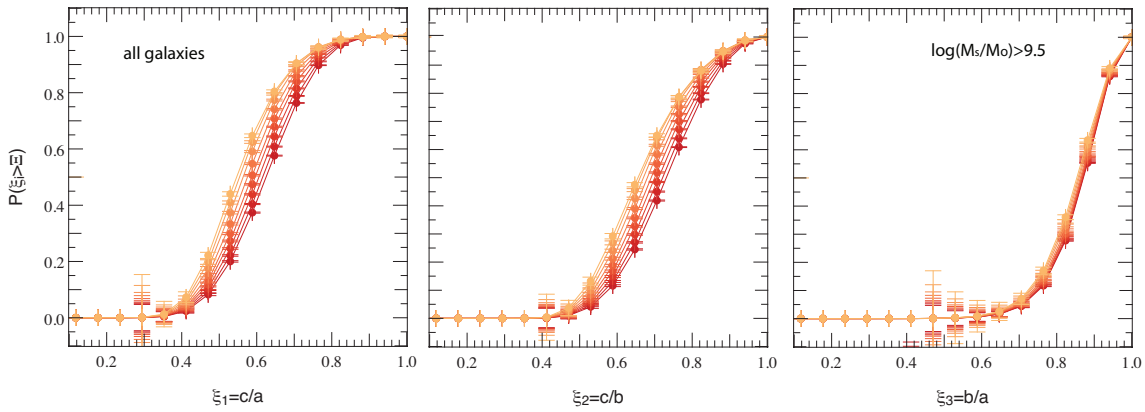

Figure 4.12: Cumulative PDFs of the principal semi-axis ratios ξ_i for all galaxies with $M_s > 10^{9.5} M_\odot$ which do not merge. Colors represent evolution with cosmic time from $z = 5.2$ (dark red) to $z = 1.2$ (light orange) with an average time step of ~ 200 Myr. The 1σ poissonian error bars are overplotted for all bins that have a non-zero probability. Smooth accretion tends to flatten galaxies over time.

galaxy disks.

This morphological transformation strongly depends on the mass and morphology of galaxies. As explained before, I define spheroids as galaxies with $\xi_1 > 0.7$ and $\xi_2 range 0.8$ and disks as galaxies with $\xi_1 < 0.45$ and $\xi_2 < 0.55$. Fig. 4.13 displays the evolution of the principal semi-axis ratio PDFs for galaxies classified as spheroids (blue curves and symbols) and disks (red curves and symbols) pre-merger (galaxies are excluded from the sample when they merge), and for two different mass bins. The upper panels focus on galaxies with a stellar mass comprised between $10^{9.5} M_\odot$ and $10^{10.5} M_\odot$, the lower panel on more massive galaxies with $M_s > 10^{10.5}\,\mathrm{M}_\odot$. This mass threshold corresponds to the transition mass above which galaxies embedded in filaments decouple from their vorticity quadrant and display a spin perpendicular to their closest filament (see Dubois *et al.* , 2014), and also to the transition in gas accreted onto the galaxy between cold and hot mode (e.g. Dekel & Birnboim, 2006; Ocvirk *et al.* , 2008). The figure reveals that the decrease rate in ξ_1 and ξ_2 is much faster, around 20% per Gyr for spheroids with masses below the transition mass (or from average values of $\xi_1 = 0.7$ and $\xi_2 = 0.8$ to 0.56 and 0.66 respectively). On the other hand, disks tend to thicken slightly on average (going from $\xi_1 = 0.46$ and $\xi_2 = 0.56$ to 0.5 and 0.64 respectively). This behaviour for the disks at least partially arises from the limited maximum spatial resolution of the simulation (1 kpc). By definition disks with scale heights below this value are artificially 'puffed up' to 1 kpc and any accretion of new material, no matter how dynamically cold, can only result in increasing this minimal numerical scale height. This especially alters the shape of small galaxies, for which the scale length is also poorly resolved. For galaxies with masses above the transition mass (bottom panels of Fig 4.13), I do not observe any significant impact of

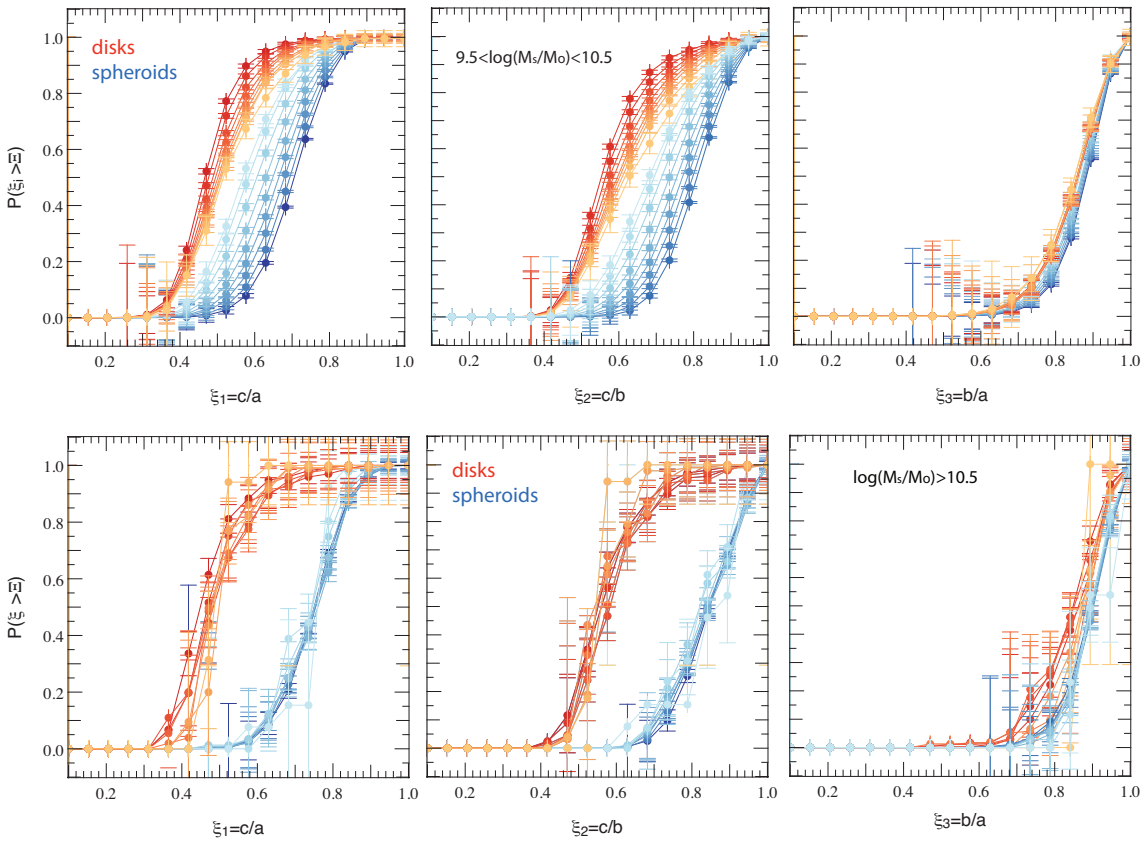

Figure 4.13: Cumulative PDFs of the principal semi-axis ratios ξ_i for galaxies which do not merge. Colors evolve with cosmic time from dark red ($z = 5.2$) to light orange ($z = 1.2$) for disks and navy blue ($z = 5.2$) to light blue ($z = 1.2$) for spheroids, with an average time step of ~ 200 Myr. The 1σ poissonian error bars are overplotted for all bins that have a non-zero probability. *Top panel*: galaxies with $9.5 < \log(M_s/M_\odot) < 10.5$. *Bottom panel*: galaxies with $\log(M_s/M_\odot) > 10.5$ (spin flip and cold/hot mode for accretion transition mass: see text for detail). Smooth accretion has little impact on the morphology of galaxies above the transition mass but clearly flattens galaxies below it.

smooth processes on the morphology indicators which remain constant on average.

Interpreting our results in the light of the scenario described by Codis *et al.* (2012) and Laigle *et al.* (2015), whereby small galaxies acquire their spin through angular momentum transfer from the vorticity quadrant they are embedded in, this "flattening" effect can be understood as the (re)-formation of disks in high vorticity regions at the heart of cosmic web filaments. In other words, smooth accretion tends to (re)-align galaxies with their nearest filament (Tillson *et al.* , 2012; Welker *et al.* , 2014; Danovich *et al.* , 2015; Pichon *et al.* , 2014) where the dominant component in this process, for galaxies below the transition mass, is coherent gas feeding from cold flows. At the opposite end of the mass spectrum, galaxies above the transition mass accrete material from multiple quadrants and/or smaller amounts of material along a unique filament. The angular

momentum streamed to the core of these massive galaxies from multiple directions is more likely to cancel out, which results in little to no effect of smooth accretion on the morphology of the galaxy. These results reinforce earlier findings that the underlying cosmic web plays a major role in shaping galaxy properties.

4.4.2 Mergers

As can be seen on Fig. 4.14 (and 4.16), mergers trigger very different evolutions for disk galaxies (respectively spheroids). This figure showcases a qualitative difference: contrary to smooth accretion, both minor and major mergers strongly change the galaxy morphology, leading to much more spheroidal/elliptical structures. However, this only occurs for disks: as can be seen in Fig. 4.16, for galaxies initially identified as spheroids, minor mergers behave more like smooth accretion, flattening the galaxy whereas major mergers preserve, by and large, their morphology. Looking at Fig. 4.14, there are quantitative differences between minor and major mergers. Whilst major mergers clearly destroy disks (the average value of the PDF of $\xi_1 = c/a$ shifts from 0.45 to 0.62, red and dark blue curves respectively), minor mergers have a more limited effect (ξ_1 PDF average value shifted from 0.45 to 0.52 only). Finally, the effect of very minor mergers (light orange curve) is closer to a thickening of the disks than an actual destruction of them and an alteration of the galaxy morphology. It is important to notice that all mergers also trigger an increase in the scatter of the distribution of galactic disks morphology indicators ξ_i, as the slope of the PDFs becomes shallower for mergers than smooth accretion. This effect is stronger for higher merger mass ratios.

These findings corroborate the view that major *and* multiple minor mergers can lead to galaxies with similar morphologies, destroying disks and turning them into spheroids (e.g. Bournaud *et al.* , 2007a). This allows to overcome the tension occasioned by the paucity of major mergers: minor mergers are much more frequent events, allowing for the formation of a much larger spheroid population. An illustration of this phenomenon is given in Fig. 4.17 which depicts rest-frame false color images of a sample of disk galaxies in the Horizon-AGN simulation before and after major/minor merging observed through the u, g and i filters.

Impact of initial morphology Fig. 4.15 shows the cumulative probability distributions of the morphologic ratio $\xi_1 = c/a$ over one time step, with all timesteps between $z = 5.2$ and $z = 1.2$ stacked, for different merger mass ratios. This is plotted for all galaxies regardless of their morphology. Fig. 4.16 displays the same quantity for galaxies identified as spheroids, i.e. with morphologic ratios $\xi_1 > 0.7$ and $\xi_2 \rangle 0.8$, before they merge.

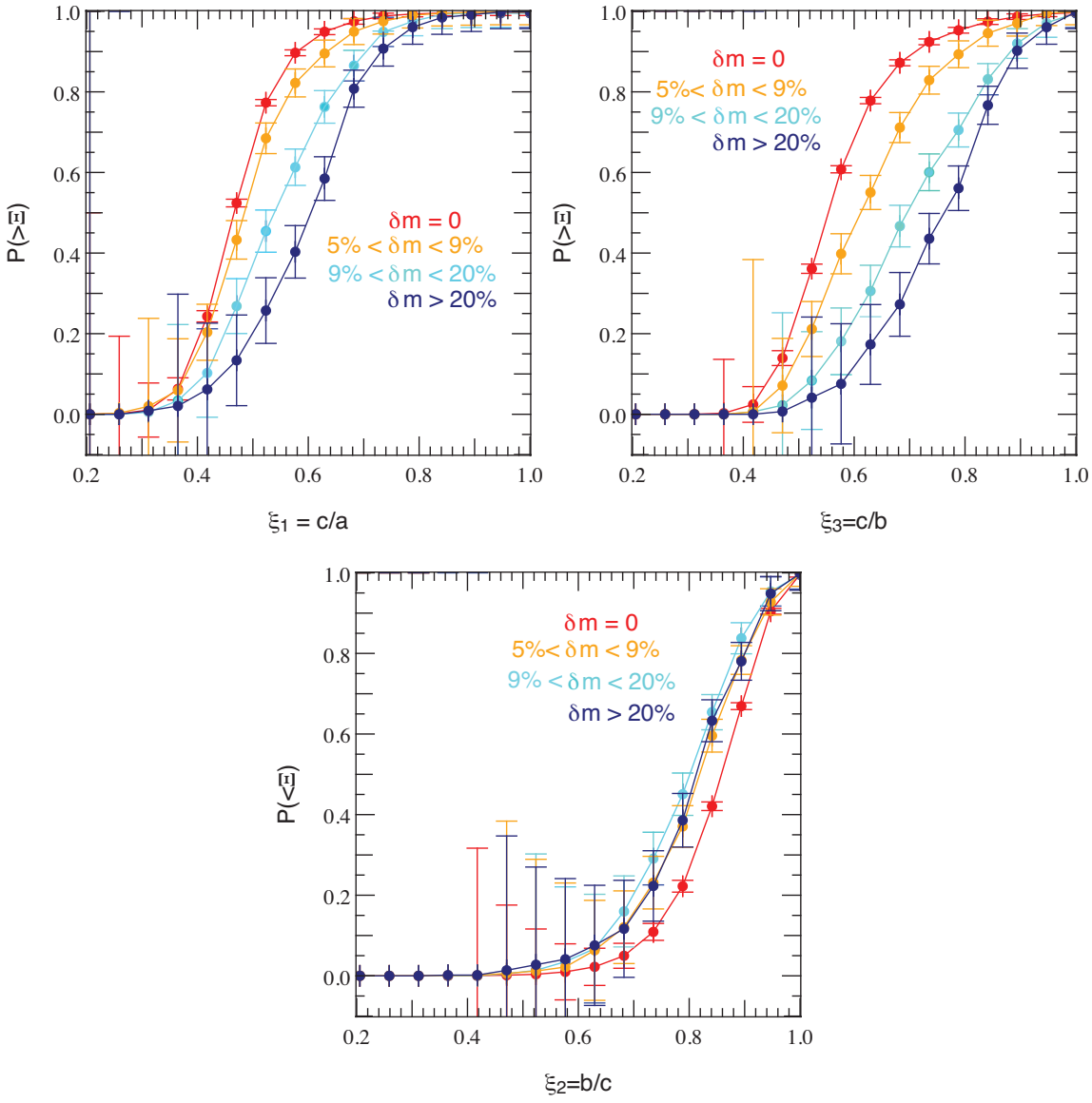

Figure 4.14: Cumulative PDFs of the morphology indicators ξ_i for different merger mass ratios and for galaxies with $M_s > 10^{10}\,M_\odot$ identified as pre-merger disks. The poissonian 1σ error bars are indicated for all bins with more than 10 galaxies. The results are stacked for each time output between $z = 5.2$ to $z = 1.2$. Mergers broaden the morphology distribution and quantitatively destroy disks. This effect strengthens with increasing merger mass ratios.

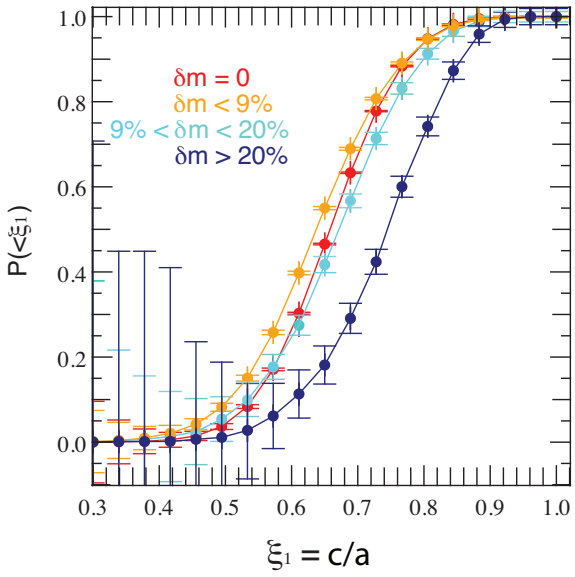

Figure 4.15: Cumulative PDF of $\xi_1 = c/a$ over one time step, with all timesteps between $z = 5.2$ and $z = 1.2$ stacked, for different merger mass ratios and for galaxies with $M_s > 10^{10}\mathrm{M}_\odot$.

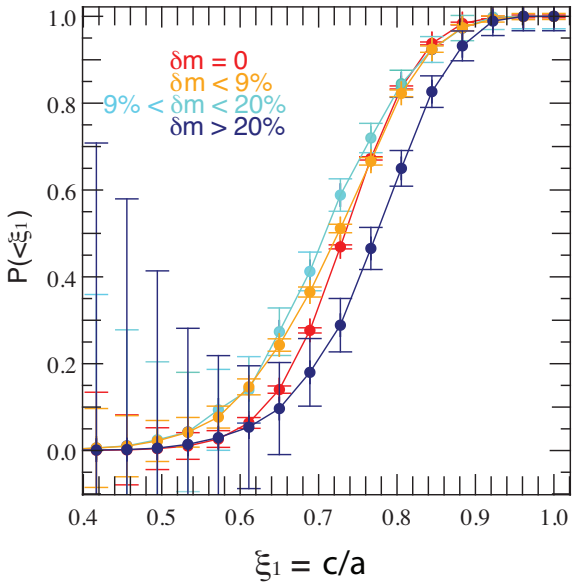

Figure 4.16: Same as Fig. 4.15 but for galaxies which are classified as spheroids before they merge (see text for detail).

4.5 Conclusion

Galaxy growth in the cosmic web involves a wide range of processes from anisotropic accretion to supernovae and AGN feedback whose effect can either add up or cancel one another, resulting in the observed diversity in morphologies, kinematics and colors of galaxies. While the interplay between these phenomena is undoubtedly complex, the approach I implemented in this work which consists in focussing on a couple of well defined processes (smooth accretion against mergers) and identify their impact – whether re-enforcing or competing – on specific galactic properties (size, morphology) still yields some interesting results:

- Mergers and smooth accretion augment galaxy masses across the peak of cosmic star formation history, in amounts that are statistically comparable. As a result, at $z = 1.2$, galaxies with $M_{\rm s} > 10^{10}\,{\rm M}_{\odot}$ have acquired 55% of their stellar mass via smooth accretion and 45% via mergers. However, while smooth accretion is a steady process with regular impact on stellar mass over cosmic history, mergers are violent processes which occur on average twice in the history of a galaxy over this epoch.

- Mergers and smooth accretion augment galaxy sizes across the peak of cosmic star formation history, especially major mergers, but this growth strongly depends on redshift and gas fraction. We also found that while mass is accreted, the mean density also rises for galaxies which are pre-merger disks, suggesting a gravitational contraction during the merger phase, while the inverse is true for pre-merger spheroids which on average expand after merging.

- For mergers of mass ratio δm, the relative increase in radius is found to evolve as a power law of the stellar mass $r_{0.5} = M_s^{0.65+\delta m}$ while smoothly accreted material of comparable mass ratio proves to be much less efficient in growing galaxy radii $r_{0.5} = M_s^{0.3\delta m}$. Moreover, while the growth of spheroid sizes shows little dependence on δm ($r_{0.5} \propto M_s$), – even for smallest minor mergers which is consistent with the idea that material is then smoothly accreted within the galactic plane –, disks show a stronger dependence on δm, even contracting trend when subjected to minor mergers. We interpret this result as the destruction of disks and redistribution of their stellar component in a more tightly packed spheroidal volume, which causes the effective half mass radius to decrease even though the amount of mass accreted actually increases.

- Gas fraction also plays an important part in determining the size growth consecutive to mass accretion. As expected, gas dominated mergers induce a much more limited growth in size than star dominated ones. In such gas rich mergers, the remnant appears to be more

compact. We interpret this as the result of gas shocking, losing angular momentum and being transported to the central parts of the galaxy where it forms stars, seemingly triggering a gravitational contraction of the galaxy. On the opposite, gas-poor mergers (with $f_{\rm gas} < 0.2$) induce an increased growth in radius with no significant dependence on merger mass fraction, but the steepest dependence on stellar mass that was measured ($r_{0.5} = M_{\rm s}^2$).

- These accretion processes are found to have a strong impact on galaxy morphologies. Smooth accretion tends to flatten small galaxies along their spin axis, consistent with the idea that those galaxies are embedded in a vorticity quadrant of cosmic filament which feeds them angular momentum coherently along the filament direction. This effect is even clearer for the sub-sample of spheroids fed by this smooth accretion which evolve to resemble the disk population in just over 2 Gyr. In contrast, mergers tend to destroy disks and form spheroids (see Fig. 4.17), except for very minor mergers – which only thicken them –, in agreement with the idea that in this case the satellite is slowly stripped from its gas and stars in the galactic plane of the main progenitor. But our main result is that minor mergers are responsible for a comparable amount of disk destruction than major mergers, coupled with a strong contraction effect when the minor merger happens to a gas-dominated ($f_{\rm gas} > 0.6$) galaxy.

- These results altogether statistically favor a scenario whereby galaxies grow their stellar mass by smooth accretion of gas, in situ formation and mergers in comparable amounts, but grow in size mostly through merging: disk (gas-dominated) galaxies merge to become more compact spheroids while spheroids lose their compactness through these same minor mergers. Occasionally, dramatic growth in size through rare major mergers and multiple, gas-deprived minor mergers happens. Non-merging spheroids with masses up to a transition mass around $10^{10.5}\,{\rm M}_\odot$ then rebuild disks from coherent smooth accretion. Above this mass the coherence of streams is lost and morphology is preserved.

Though this study supports – in a full cosmological context using the Horizon-AGN simulation – the consistent galaxy growth model that has emerged from previous numerical studies of different types of mergers, further investigation is required to extend these results down to $z = 0$ and to specify in detail the role played by galactic physics – more specifically supernovae and AGN feedback – in shaping these results. Analyzing more specific merger parameters such as the impact parameter and the orbital-to-intrinsic angular momentum transfer rate will also be necessary to understand the scattering of the morphology and size distributions induced by mergers and understand their overall impact on observed galaxies in the local Universe. Finally, the internal kinematics of the galaxy population also need to be examined more closely.

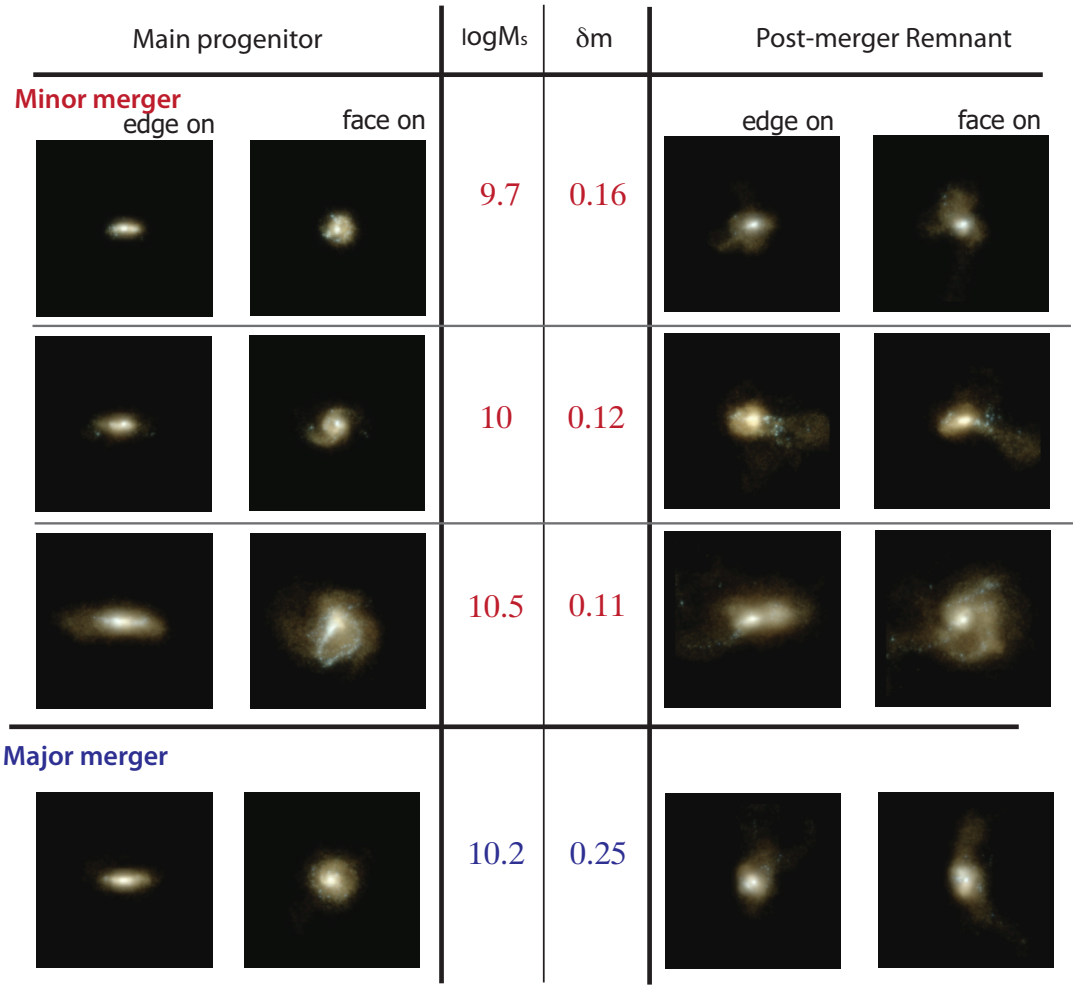

Figure 4.17: Rest-frame color images (u, g and i filters) of a sample of Horizon-AGN disk galaxies caught during their pre-merger phase at $z = 2.2$ (two leftmost columns) and their post-merger phase at $z = 1.9$ (two rightmost columns). The first and third columns are edge-on views, and the second and fourth columns are face-on views. Extinction by dust is not taken into account. Each frame is 100 kpc on a side. M_s is the stellar mass of the main progenitor in $M_\odot$ units and δm is the mass ratio of the merger (see text for exact definition). This figure illustrates the ability of mergers (major but also minor) to turn disk-like galaxies into spheroids.

Conclusion

Despite recent observational studies on the morphology of galaxies and its dependence on environment - conducted for galaxies up to redshift two and beyond (Lee *et al.* , 2013) -, the interplay between galaxies and their cosmic environment remains a puzzle. Galaxies are open dynamical systems and ever-changing products of a nature versus nurture confrontation. In this context, cosmological simulations are crucial to improve our understanding of their formation and evolution over a wide range of redshifts. My PhD focused on analyzing such simulations in order to gain some insight in probing these processes.This work was performed post-processing Horizon-AGN .

First, I focussed on the acquisition of the angular momentum of galaxies from redshift 5 down to redshift 1, as a key ingredient to explain their morphologies and physical properties as well as a vector quantity easy to relate to the underlying geometry.

Then, I characterized the distribution of satellites galaxies around their host and, building on these results on galactic orientations, I studied the competitive effects of smooth accretion and mergers as drivers of galactic properties such as their size and morphology.

I further performed the statistical analysis of the galactic gas content and inflows and their impact on galactic physical properties.

The common scope of those projects was to understand how - and to what extent - large-scale structure dynamics and kinematics cascade down to galactic scales, and how we can develop pseudo-observables to test those scenarios on real observations. The most significant results presented in this thesis are summarized in the next section, after which I detail prospects for future works.

4.6 Main results

Numerous simulations have established a clear orientation trend for the spin of dark haloes in the cosmic web: small mass haloes tend to display a spin aligned to their closest filament, while more massive haloes are more likely to maintain a perpendicular orientation of their spin. Codis *et al.*

(2012) confirmed this with high degree of significance and was able to estimate a transition mass around 10^{12} solar masses. My first goal was to understand if I could recover similar trends for galaxies using merger trees with a consistent stellar transition mass, and to define what physical properties could be used as tracers for this signal.

I recovered the alignment-perpendicular trends in the Horizon-AGN simulation down to $z = 1.2$, and found various galactic tracers of this signal such as colour, age, specific stellar formation rate or metallicity. In a nutshell, low-mass, young, centrifugally supported, metal-poor, bluer spiral galaxies tend to have their spin aligned to the closest filament, while massive, high velocity dispersion, red, metal-rich, old ellipticals are more likely to have a spin perpendicular to it (Dubois *et al.* , 2014). The mass-transition, confidently bracketed between $\log(Ms/M_{\odot}) = 10.25 - 10.75$, was also found to be consistent with the one for dark haloes. A first observational evidence was found in Tempel & Libeskind (2013), which identified a similar trend in the SDSS. As part of a collaboration with observers from the state-of-the-art $z \simeq 1$ VIPERS survey [1] from CFHTLS [2], I expect more significant observational imprints in a near future.

Codis *et al.* (2012) interpreted the orientation trend for dark haloes in terms of large-scale cosmic flows. Anisotropic tidal torque theory provides a natural lagrangian framework to account for the early acquisition of spin for dark haloes and recover this orientation trend. However similar correlations proved challenging to predict for galaxies, evolving on small non-linear scales and subject to a wide range of complex processes from gas dynamics and star formation to feedback from supernovae and AGN. To investigate this interplay, I relied on the Eulerian picture provided by the Horizon-AGN simulation. I argued that most small mass galaxies acquire their angular momentum from coherent accretion from vorticity-rich regions at the vicinity of filaments (Laigle *et al.* , 2015), leading to their parallel orientation. Massive galaxies (noticeably ellipticals) are more likely to be the product of mergers - occurring along the cosmic filament- and are therefore displaying a perpendicular orientation as a result of orbital-to-intrinsic angular momentum conversion.

Computing merger trees for all galaxies and haloes for 22 outputs from Horizon-AGN between $z = 5.2$ and $z = 1.2$ (average time-step of 250 Myr) and then computing merger rates and statistically analyzing correlations between the spin swings, I found strong evidence that mergers are responsible for spin swings - with distinctive features for minor and major mergers - and that they tend to swing the remnant s spin orthogonal to its surrounding filaments - along with increasing its overall angular momentum - while smooth accretion (re)-aligns small galaxies over cosmic time, building up their spin parallel to it (Welker *et al.* , 2014).

[1] http://vipers.inaf.it/
[2] http://www.cfht.hawaii.edu/Science/CFHTLS/

This led me to study the impact of both processes on the size and morphology of galaxies, noticeably by deriving axis ratios from the inertia tensor of all galaxies in the sample, systematically sorting out those galaxies in typical morphologies and following their evolution in different merger contexts. Consistently, my results suggest that smooth accretion flattens small non-merging galaxies along the spin axis while major and multiple minor mergers turn disk galaxies into spheroids. I also investigated the comparative effect on galactic size and shape of gas-rich and gas-poor mergers for both minor and major mergers, and the correlations between gas content, star formation and star migration in Horizon-AGN , which provided good statistics to conduct such an analysis. My results are consistent with a build-up of large massive spheroids observed at $z < 1$ from major mergers and gas-poor minor mergers, while smooth accretion is found to have a much fainter impact on galactic size growth.

Prior to galaxy mergers, small galaxies in sub-haloes that have been accreted by a more massive host form a collection of satellites orbiting around a massive central galaxy. I therefore investigated the statistical distribution of satellites around their host in Horizon-AGN at observed redshifts $0.3 < z < 0.8$ comparing the distribution of the angles between the separation vector of a satellite and the minor axis of its central galaxy on the one hand, the direction of the central′s closest filament on the other hand. I found it to be the result of an interplay between a tendency to be aligned in the filament they flowed from in the first place and a tendency to align in the galactic plane of their central galaxy. This trends can either add up (when filamentary ridge line lies in the galactic plane) or compete (when the central galactic plane is orthogonal to the filament), in which case the first trend dominates in the outskirt of the halo while the second takes over in the inner parts.

4.7 Prospects

4.7.1 Sorting out the merger zoo

Future studies will need to clarify the mergers distribution in cosmological simulations, especially identify specific types and their frequencies with respect to mass ratio (minor or major mergers), galactic types of the progenitors (disks, ellipticals, gas-rich, gas-poor), number of progenitors involved, impact parameter of the merger and the possible misalignments of the pair motion with its cosmic filament as well as variations with redshift. The impact parameter and orbital momentum of the pair are of particular interest and need to be analyzed conjointly with the gas fraction as it is expected to have a strong impact on the ability of low-z mergers to rebuild disks similar to those we observe in the Local Universe (Robertson *et al.* , 2006; Hammer & IMAGES Team, 2014). It

will be also necessary to investigate in greater details the variations of the velocity dispersion in galaxies undergoing mergers so as to confirm the role of specific types in building low-compacity spheroids or massive low-z disks, and produce robust pseudo-observables for observations.

Indeed, in observations mergers are only traced considering close pairs of interacting galaxies (Lotz *et al.* , 2008b). Precise information on the outcomes we can expect from a definite type of merger, along with its frequency at different redshifts could be tested directly on real catalogs and greatly improve our ability to test the relevance of this method, along with our understanding of spiral and elliptical abundances in observations. In order to produce a comprehensive set of predictions, analysis in morphology and size of the outcomes of mergers similar to the one presented here will need to be reproduced in similar simulations at lower redshifts and in simulations with different amounts of stellar and AGN feedback at all redshifts.

Close analysis of star migration processes and gas and baryons fluxes triggered by mergers will also be necessary to understand what signatures of such events have been imprinted on the Inter-Galactic Medium (IGM) and what percentage of intergalactic gas is left from those violent processes, and allows for comparison with observations.

4.7.2 Gas inflows: feeding galaxies into diverse morphologies ?

Another active field of research is the way gas inflows at high-redshift can feed galaxies with coherent streams, therefore transferring mass and angular momentum towards the core of the galaxy and connecting its morphology to the underlying cosmic web.

This is a highly debated topic as such colds flows are difficult to detect and strong feedback from AGN is thought to blow them away (Dubois *et al.* , 2013b; Nelson *et al.* , 2015), while supernovae feedback effect seems to be restricted to a partial fragmentation of the streams (Powell *et al.* , 2011). Recent numerical studies (Danovich *et al.* , 2015) have been conducted on small samples of well-resolved (down to 10 pc) galaxies to evaluate the geometry of the accretion of gas from filaments as well as the resulting tidal torques and pressure gradients. Although our resolution is limited to 1 kpc, cosmological simulations with and without AGN allow for a statistical analysis of the number of connected filaments - which is believed to have an impact on the strength of violent disk instabilities and on the internal features of disk galaxies (Cen, 2014) - , of their impact parameter, and eventually their corresponding advected mass and angular momentum on halo scales (0.3-0.5 virial radius).

Similar analysis on statistically relevant samples - such as those provided in hydrodynamical cosmological simulations - will be required to unravel the complex interactions between galaxies

and the surrounding IGM, its dependence on feedback from various types of supernovae and AGN - the contribution of which needs to be analyzed separately. It will provide statistical predictions to be tested in upcoming spectroscopic surveys at low and high redshift. Moreover, this would allow for the selection of typical haloes for further analysis in high-resolution, high-detail zooms of high-z haloes that would pave the way for next-generation observations of galactic inflows and outflows using $z \sim 5 - 7$ quasars. These quasars are primary targets for ALMA [3], which will measure the host's gas reservoir, star formation rate and kinematics. This would therefore enable the calculation of molecular gas masses, star formation rates and gas kinematics for comparison with the observations.

4.7.3 Distribution of satellites: tracing the distribution of dark matter in massive haloes ?

Eventually, results presented in Chapter 3 on the tendency of satellites to change their orientation dynamically in their host halo questions our ability to efficiently infer the triaxiality of a massive cluster from the mere distribution of its satellites. This will require further investigations in cosmological hydrodynamical simulations. Noticeably, we need to determine how well satellites follow the dark matter component of their host in specific ranges of host mass and color, satellite mass and color, central galaxy morphology, host-satellite separation and most importantly for haloes in different environments characterized by the number of filaments connected to the host structure, its distance to the ridge line defining the leading filament and its distance to closest nodes.

[3] http://www.almaobservatory.org/

List of Figures

1 The Hubble sequence 24

1.1 Morpholgical diversity in Horizon-AGN 38

1.2 Galaxy stellar mass function 39

1.3 Projected Maps of Horizon-AGN 41

2.1 Vorticity quadrants 50

2.2 Smooth accretion on spin 51

2.3 Mergers on spin 52

2.4 the numerical skeleton 54

2.5 distance to filament 55

2.6 Evolution of $V_{\rm rot}/\sigma$ with stellar mass 59

2.7 PDF of $\mu = \cos\theta$ for different masses 61

2.8 PDF of $\mu = \cos\theta$ for different $V_{\rm rot}/\sigma$ 63

2.9 PDF of $\mu = \cos\theta$ for different $g - r$ colors 63

2.10 Merger fraction and stellar mass 67

2.11 Examples of galactic spin flips 68

2.12 PDF of $\cos\Delta\alpha$ for different merger histories 70

2.13 PDF of μ for different merger histories 71

2.14 PDF of the spin contrast for different merger ratios. 73

2.15 PDF of the spin contrast for non-mergers. 74

2.16 PDF of μ for non-mergers 75

3.1 Tidal stripping: host-halo system . . . 81
3.2 Polar accretion onto haloes . . . 88
3.3 Sketch of the different angular biases . . . 91
3.4 Halo occupation in Horizon-AGN . . . 92
3.5 Distribution of the rest frame colors in Horizon-AGN . . . 94
3.6 2D projected angles . . . 96
3.7 Choice of variable: PDF of $\cos\alpha_{2D}$ . . . 98
3.8 minor axis-separation angle: PDF ξ of $\mu_1 = \cos\theta_1$ . . . 99
3.9 Sketch of the expected *filamentary trend* . . . 101
3.10 PDF ξ of $\mu_1 = \cos\theta_1$: evolution with separation . . . 102
3.11 Alignment trends: evolution with orientation of the central . . . 104
3.12 Evolution with separation for cases of competing trends . . . 105
3.13 Evolution with separation: central mass effects . . . 106
3.14 Corotation: satellites angular momentum and central spin . . . 110
3.15 Evolution of the satellite orbital momentum with separation . . . 111
3.16 Corotation: effects of the color of satellites . . . 112
3.17 Spin-spin correlations for satellites and central galaxy . . . 113
3.18 Minor axis-separation correlations for satellites . . . 114
3.19 Sketch: evolution of alignments with separation . . . 115
3.20 PDF of $\mu = \cos\theta$: evolution with central color . . . 117
3.21 Projected alignment trends . . . 118
3.22 Mean θ_x for color bins . . . 119
3.23 Alignment trends for color bins for centrals and satellites . . . 119
3.24 Alignment trends in sub-haloes . . . 120
3.25 Alignment trends in sub-haloes: effect of central color . . . 121
3.26 Alignment trends for oblate and prolate centrals . . . 123
3.27 Secondary alignment along the major axis . . . 124
3.28 PDF of $\mu = \cos(\theta)$: evolution with redshift . . . 124

3.29 Illustrated summary 125

4.1 A dynamical view on the Hubble sequence 137

4.2 Evolution of the average stellar mass with z 139

4.3 Galaxy stellar mass function in Horizon-AGN 140

4.4 Average ellipsoidal approximation of morphological types in Horizon-AGN 141

4.5 Gas cell assignment procedure 143

4.6 Evolution of the gas fraction with z 144

4.7 Evolution with time of post-merger fraction among galaxies 146

4.8 Compared mass budgets for mergers and smooth accretion 148

4.9 PDF of the density growth ratio for different merger ratios 149

4.10 Evolution of the galactic effective radius with mergers and smooth accretion 151

4.11 Evolution of the effective radius in mergers: effect of $f_{\rm gas}$ 153

4.12 Morphology: cumulative PDF of axis ratios with smooth accretion 155

4.13 Cumulative PDF of axis ratios with smooth accretion: effect of initial morphology 156

4.14 Cumulative PDF of axis ratios with mergers for initial disks 158

4.15 Cumulative PDF of $\xi_1 = c/a$ with mergers 159

4.16 Cumulative PDF of the $\xi_1 = c/a$ with mergers for initial spheroids 159

4.17 Rest-frame color images (u, g and i filters) of a sample of Horizon-AGN 162

Bibliography

Abazajian, K. N., Adelman-McCarthy, J. K., Agüeros, M. A., Allam, S. S., Allende Prieto, C., An, D., Anderson, K. S. J., Anderson, S. F., Annis, J., Bahcall, N. A., & et al. 2009. The Seventh Data Release of the Sloan Digital Sky Survey. *ApJ Sup.*, **182**(June), 543–558. 90

Agertz, O., Teyssier, R., & Moore, B. 2009. Disc formation and the origin of clumpy galaxies at high redshift. *MNRAS*, **397**(July), L64–L68. 131, 136

Agustsson, I., & Brainerd, T. G. 2010. Anisotropic Locations of Satellite Galaxies: Clues to the Orientations of Galaxies within their Dark Matter Halos. *ApJ*, **709**(Feb.), 1321–1336. 86

Aihara, H., Allende Prieto, C., An, D., & Anderson, et al. 2011. The Eighth Data Release of the Sloan Digital Sky Survey: First Data from SDSS-III. *ApJ Sup.*, **193**(Apr.), 29. 45, 64

Aragón-Calvo, M. A., van de Weygaert, R., Jones, B. J. T., & van der Hulst, J. M. 2007. Spin Alignment of Dark Matter Halos in Filaments and Walls. *ApJ Let.*, **655**(Jan.), L5–L8. 45

Aubert, D., Pichon, C., & Colombi, S. 2004. The origin and implications of dark matter anisotropic cosmic infall on ˜L$_*$ haloes. *MNRAS*, **352**(Aug.), 376–398. 35, 45, 53, 64, 87, 88, 89, 90, 100, 114, 138

Bailin, J., & Steinmetz, M. 2005. *ApJ*, **627**. 45

Bailin, J., Kawata, D., Gibson, B. K., Steinmetz, M., Navarro, J. F., Brook, C. B., Gill, S. P. D., Ibata, R. A., Knebe, A., Lewis, G. F., & Okamoto, T. 2005. Internal Alignment of the Halos of Disk Galaxies in Cosmological Hydrodynamic Simulations. *ApJ Let.*, **627**(July), L17–L20. 115

Bailin, J., Power, C., Norberg, P., Zaritsky, D., & Gibson, B. K. 2008. The anisotropic distribution of satellite galaxies. *MNRAS*, **390**(Nov.), 1133–1156. 87

Baldry, I. K., Balogh, M. L., Bower, R. G., Glazebrook, K., Nichol, R. C., Bamford, S. P., & Budavari, T. 2006. Galaxy bimodality versus stellar mass and environment. *MNRAS*, **373**(Dec.), 469–483. 93

Barnes, J., & Efstathiou, G. 1987. Angular momentum from tidal torques. *ApJ*, **319**(Aug.), 575–600. 86

Bédorf, J., & Portegies Zwart, S. 2013. The effect of many minor mergers on the size growth of compact quiescent galaxies. *MNRAS*, **431**(May), 767–780. 136

Bell, E. F., Wolf, C., Meisenheimer, K., Rix, H.-W., Borch, A., Dye, S., Kleinheinrich, M., Wisotzki, L., & McIntosh, D. H. 2004. Nearly 5000 Distant Early-Type Galaxies in COMBO-17: A Red Sequence and Its Evolution since z˜1. *ApJ*, **608**(June), 752–767. 93

Benson, A. J., Lacey, C. G., Frenk, C. S., Cole, S., & Baugh, C. M. 2003 (June). The Interplay Between Galaxy Formation and the IGM. *Pages 299–302 of:* Avila-Reese, V., Firmani, C., Frenk, C. S., & Allen, C. (eds), *Revista Mexicana de Astronomia y Astrofisica Conference Series*. Revista Mexicana de Astronomia y Astrofisica Conference Series, vol. 17. 17

Bernstein, G. M., & Norberg, P. 2002. Shape Alignments of Satellite Galaxies. *AJ*, **124**(Aug.), 733–736. 121

Berrier, J. C., Bullock, J. S., Barton, E. J., Guenther, H. D., Zentner, A. R., & Wechsler, R. H. 2006. Close Galaxy Counts as a Probe of Hierarchical Structure Formation. *ApJ*, **652**(Nov.), 56–70. 133

Bett, P. E., & Frenk, C. S. 2012. Spin flips - I. Evolution of the angular momentum orientation of Milky Way-mass dark matter haloes. *MNRAS*, **420**(Mar.), 3324–3333. 69

Binggeli, B. 1982. The shape and orientation of clusters of galaxies. *A&A*, **107**(Mar.), 338–349. 90, 107, 121

Binney, J. 1977. The physics of dissipational galaxy formation. *ApJ*, **215**(July), 483–491. 17

Binney, J., & Tabor, G. 1995. Evolving Cooling Flows. *MNRAS*, **276**(Sept.), 663. 17

Birnboim, Y., & Dekel, A. 2003. Virial shocks in galactic haloes? *MNRAS*, **345**(Oct.), 349–364. 52, 132

Blazek, J., Vlah, Z., & Seljak, U. 2015. Tidal alignment of galaxies. *ArXiv e-prints*, Apr. 127

Bodenheimer, P., Laughlin, G. P., Rózyczka, M., & Yorke, H. W. (eds). 2007. *Numerical Methods in Astrophysics: An Introduction*. 29

Bond, J. R., Kofman, L., & Pogosyan, D. 1996. How filaments of galaxies are woven into the cosmic web. *Nature*, **380**(Apr.), 603–606. 18, 23, 80

Booth, C. M., & Schaye, J. 2009. Cosmological simulations of the growth of supermassive black holes and feedback from active galactic nuclei: method and tests. *MNRAS*, **398**(Sept.), 53–74. 34, 136

Bournaud, F., Combes, F., & Jog, C. J. 2004. Unequal-mass galaxy merger remnants: Spiral-like morphology but elliptical-like kinematics. *A&A*, **418**(Apr.), L27–L30. 136

Bournaud, F., Jog, C. J., & Combes, F. 2005. Galaxy mergers with various mass ratios: Properties of remnants. *A&A*, **437**(July), 69–85. 136

Bournaud, F., Jog, C.J., & Combes, F. 2007a. Multiple minor mergers: formation of elliptical galaxies and constraints for the growth of spiral disks. *A&A*, **476**(Dec.), 1179–1190. 136, 157

Bournaud, F., Elmegreen, B. G., & Elmegreen, D. M. 2007b. Rapid Formation of Exponential Disks and Bulges at High Redshift from the Dynamical Evolution of Clump-Cluster and Chain Galaxies. *ApJ*, **670**(Nov.), 237–248. 132

Bower, R. G., Benson, A. J., Malbon, R., Helly, J. C., Frenk, C. S., Baugh, C. M., Cole, S., & Lacey, C. G. 2006. Breaking the hierarchy of galaxy formation. *MNRAS*, **370**(Aug.), 645–655. 17

Boylan-Kolchin, M., Ma, C-P., & Quataert, E. 2006. Red mergers and the assembly of massive elliptical galaxies: the fundamental plane and its projections. *MNRAS*, **369**, 1081–1089. 136, 152, 154

Brainerd, T. G. 2005. Anisotropic Distribution of SDSS Satellite Galaxies: Planar (Not Polar) Alignment. *ApJ Let.*, **628**(Aug.), L101–L104. 89

Brainerd, T. G., & Specian, M. A. 2003. Mass-to-Light Ratios of 2dF Galaxies. *ApJ*, **593**(Aug.), L7–L10. 87

Bridge, C., & Carlberg, R. 133

Brooks, A., Governato, F., Brook, C., Mayer, L., Willman, B., Jonsson, P., Stilp, A., Pope, L., Christensen, C., Wadsley, J., & Quinn, T. 2009a (May). The Formation of Large Galaxy Disks in Low z Major Mergers. *Page 308.05 of: American Astronomical Society Meeting Abstracts 214*. American Astronomical Society Meeting Abstracts, vol. 214. 136

Brooks, A. M., Governato, F., Quinn, T., Brook, C. B., & Wadsley, J. 2009b. The Role of Cold Flows in the Assembly of Galaxy Disks. *ApJ*, **694**(Mar.), 396–410. 52, 131

Bruzual, G., & Charlot, S. 2003. Stellar population synthesis at the resolution of 2003. *MNRAS*, **344**(Oct.), 1000–1028. 58, 93

Bryan, G. L., & Norman, M. L. 1998. Statistical Properties of X-Ray Clusters: Analytic and Numerical Comparisons. *ApJ*, **495**(Mar.), 80–99. 21

Bundy, K., Fukugita, M., Ellis, R. S., Kodama, T., & Conselice, C. J. 2004. A Slow Merger History of Field Galaxies since z ˜ 1. *ApJ Let.*, **601**(Feb.), L123–L126. 133

Cacciato, M., Dekel, A., & Genel, S. 2012. Evolution of violent gravitational disc instability in galaxies: late stabilization by transition from gas to stellar dominance. *MNRAS*, **421**(Mar.), 818–831. 131

Cattaneo, A., Dekel, A., Devriendt, J., Guiderdoni, B., & Blaizot, J. 2006. Modelling the galaxy bimodality: shutdown above a critical halo mass. *MNRAS*, **370**(Aug.), 1651–1665. 17

Cen, R. 2014. Evolution of Cold Streams and the Emergence of the Hubble Sequence. *ApJ Let.*, **789**(July), L21. 132, 166

Ceverino, D., Dekel, A., & Bournaud, F. 2010. High-redshift clumpy discs and bulges in cosmological simulations. *MNRAS*, **404**(June), 2151–2169. 132

Ceverino, D., Dekel, A., Mandelker, N., Bournaud, F., Burkert, A., Genzel, R., & Primack, J. 2012. Rotational support of giant clumps in high-z disc galaxies. *MNRAS*, **420**(Mar.), 3490–3520. 25, 131

Ceverino, D., Dekel, A., Tweed, D., & Primack, J. 2015. Early formation of massive, compact, spheroidal galaxies with classical profiles by violent disc instability or mergers. *MNRAS*, **447**(Mar.), 3291–3310. 132

Chandrasekhar, S. 1943. Dynamical Friction. I. General Considerations: the Coefficient of Dynamical Friction. *ApJ*, **97**(Mar.), 255. 84

Chang, J., Macciò, A. V., & Kang, X. 2013. The dependence of tidal stripping efficiency on the satellite and host galaxy morphology. *MNRAS*, **431**(June), 3533–3542. 82

Chen, C.C., Smail, I., Swinbank, A.M., & et al. 2014. An ALMA Survey of Submillimeter Galaxies in the Extended Chandra Deep Field South: Near-infrared morphologies and stellar sizes. *ArXiv e-prints*, Dec. 129, 131

Chen, D. N., Jing, Y. P., & Yoshikaw, K. 2003. Angular Momentum Distribution of Hot Gas and Implications for Disk Galaxy Formation. *ApJ*, **597**(Nov.), 35–47. 89

Chisari, N. E., Mandelbaum, R., Strauss, M. A., Huff, E. M., & Bahcall, N. A. 2014. Intrinsic alignments of group and cluster galaxies in photometric surveys. *MNRAS*, **445**(Nov.), 726–748. 114

Chisari, N. E., Codis, S., Laigle, C., Dubois, Y., Pichon, C., Devriendt, J., Slyz, A., Miller, L., Gavazzi, R., & Benabed, K. 2015. Intrinsic alignments of galaxies in the Horizon-AGN cosmological hydrodynamical simulation. *ArXiv e-prints*, July. 91, 107, 113, 121, 127, 128

Choi, E., Ostriker, J. P., Naab, T., Oser, L., & Moster, B. P. 2014. The impact of mechanical AGN feedback on the formation of massive early-type galaxies. *ArXiv e-prints*, Mar. 136

Choi, J.-H., Weinberg, M. D., & Katz, N. 2009. The dynamics of satellite disruption in cold dark matter haloes. *MNRAS*, **400**(Dec.), 1247–1263. 82

Cimatti, A., Nipoti, C., & Cassata, P. 2012. Fast evolving size of early-type galaxies at z gt 2 and the role of dissipationless (dry) merging. *MNRAS*, **422**(May), L62. 152

Ciotti, L., & Ostriker, J. P. 1997. Cooling Flows and Quasars: Different Aspects of the Same Phenomenon? I. Concepts. *ApJ Let.*, **487**(Oct.), L105–L108. 17

Codis, S., Pichon, C., Devriendt, J., Slyz, A., Pogosyan, D., Dubois, Y., & Sousbie, T. 2012. Connecting the cosmic web to the spin of dark haloes: implications for galaxy formation. *MNRAS*, **427**(Dec.), 3320–3336. 45, 46, 49, 62, 76, 87, 100, 108, 156, 163, 164

Codis, S., Gavazzi, R., Dubois, Y., Pichon, C., Benabed, K., Desjacques, V., Pogosyan, D., Devriendt, J., & Slyz, A. 2015. Intrinsic alignment of simulated galaxies in the cosmic web: implications for weak lensing surveys. *MNRAS*, **448**(Apr.), 3391–3404. 48, 50, 121

Cole, S. 1991. Modeling galaxy formation in evolving dark matter halos. *ApJ*, **367**(Jan.), 45–53. 17

Colless, M., Dalton, G., Maddox, S., Sutherland, W., Norberg, P., Cole, S., Bland-Hawthorn, J., Bridges, T., Cannon, R., Collins, C., Couch, W., Cross, N., Deeley, K., De Propris, R., Driver, S. P., Efstathiou, G., Ellis, R. S., Frenk, C. S., Glazebrook, K., Jackson, C., Lahav, O., Lewis, I., Lumsden, S., Madgwick, D., Peacock, J. A., Peterson, B. A., Price, I., Seaborne, M., & Taylor, K. 2001. The 2dF Galaxy Redshift Survey: spectra and redshifts. *MNRAS*, **328**(Dec.), 1039–1063. 18

Colpi, M. 1998. Accretion of a Satellite onto a Spherical Galaxy: Binary Evolution and Orbital Decay. *ApJ*, **502**(July), 167–176. 86, 114

Colpi, M., & Pallavicini, A. 1998. Drag on a Satellite Moving across a Spherical Galaxy: Tidal and Frictional Forces in Short-lived Encounters. *ApJ*, **502**(July), 150–166. 83

Colpi, M., Mayer, L., & Governato, F. 1999. Dynamical Friction and the Evolution of Satellites in Virialized Halos: The Theory of Linear Response. *ApJ*, **525**(Nov.), 720–733. 85

Cooper, M. C., Griffith, R. L., Newman, J. A., Coil, A. L., Davis, M., Dutton, A. A., Faber, S. M., Guhathakurta, P., Koo, D. C., Lotz, J. M., Weiner, B. J., Willmer, C. N. A., & Yan, R. 2012. The DEEP3 Galaxy Redshift Survey: the impact of environment on the size evolution of massive early-type galaxies at intermediate redshift. *MNRAS*, **419**(Feb.), 3018–3027. 129, 131

Cretton, N., Naab, T., Rix, H.-W., & Burkert, A. 2001. The Kinematics of 3:1 Merger Remnants and the Formation of Low-Luminosity Elliptical Galaxies. *ApJ*, **554**(June), 291–297. 25, 131, 136

Crighton, N. H. M., Hennawi, J. F., & Prochaska, J. X. 2013. Metal-poor, Cool Gas in the Circumgalactic Medium of a z = 2.4 Star-forming Galaxy: Direct Evidence for Cold Accretion? *ApJ Let.*, **776**(Oct.), L18. 53

Croton, D. J., Springel, V., White, S. D. M., De Lucia, G., Frenk, C. S., Gao, L., Jenkins, A., Kauffmann, G., Navarro, J. F., & Yoshida, N. 2006. The many lives of active galactic nuclei: cooling flows, black holes and the luminosities and colours of galaxies. *MNRAS*, **365**(Jan.), 11–28. 17, 40

Danovich, M., Dekel, A., Hahn, O., & Teyssier, R. 2012. Coplanar streams, pancakes and angular-momentum exchange in high-z disc galaxies. *MNRAS*, **422**(May), 1732–1749. 52, 56, 131

Danovich, M., Dekel, A., Hahn, O., Ceverino, D., & Primack, J. 2015. Four phases of angular-momentum buildup in high-z galaxies: from cosmic-web streams through an extended ring to disc and bulge. *MNRAS*, **449**(May), 2087–2111. 53, 102, 108, 127, 131, 156, 166

de Lapparent, V., Geller, M. J., & Huchra, J. P. 1986. A slice of the universe. *ApJ Let.*, **302**(Mar.), L1–L5. 18, 22

De Lucia, G. 2007. How 'Heredity' and 'Environment' Shape Galaxy Properties. *Cosmic Frontiers ASP Conference Series*, **379**(Dec.), 257. 136

De Lucia, G., & Blaizot, J. 2007. The hierarchical formation of the brightest cluster galaxies. *MNRAS*, **375**(Feb.), 2–14. 66

De Lucia, G., Kauffmann, G., Springel, V., White, S. D. M., Lanzoni, B., Stoehr, F., Tormen, G., & Yoshida, N. 2004. Substructures in cold dark matter haloes. *MNRAS*, **348**(Feb.), 333–344. 87

Dekel, A., & Birnboim, Y. 2006. Galaxy bimodality due to cold flows and shock heating. *MNRAS*, **368**(May), 2–20. 17, 52, 155

Dekel, A., & Birnboim, Y. 2008. Gravitational quenching in massive galaxies and clusters by clumpy accretion. *MNRAS*, **383**(Jan.), 119–138. 132

Dekel, A., & Silk, J. 1986. The origin of dwarf galaxies, cold dark matter, and biased galaxy formation. *ApJ*, **303**(Apr.), 39–55. 17

Dekel, A., Birnboim, Y., Engel, G., Freundlich, J., Goerdt, T., Mumcuoglu, M., Neistein, E., Pichon, C., Teyssier, R., & Zinger, E. 2009. Cold streams in early massive hot haloes as the main mode of galaxy formation. *Nature*, **457**(Jan.), 451–454. 25, 131, 132, 136

Delgado-Serrano, R., Hammer, F., Yang, Y. B., Puech, M., Flores, H., & Rodrigues, M. 2010. How was the Hubble sequence 6 Gyr ago? *A&A*, **509**(Jan.), A78. 131

Devriendt, J., Slyz, A., Powell, L., Pichon, C., & Teyssier, R. 2010a (Apr.). Modeling high-redshift galaxies: what can we learn from high and ultra-high resolution hydrodynamical simulations? *Pages 248–256 of:* Bruzual, G. R., & Charlot, S. (eds), *IAU Symposium*. IAU Symposium, vol. 262. 27

Devriendt, J., Rimes, C., Pichon, C., Teyssier, R., Le Borgne, D., Aubert, D., Audit, E., Colombi, S., Courty, S., Dubois, Y., Prunet, S., Rasera, Y., Slyz, A., & Tweed, D. 2010b. The dusty, albeit ultraviolet bright, infancy of galaxies. *MNRAS*, **403**(Mar.), L84–L88. 57

Devriendt, J. et al. 2011. . *in prep.*, **00**(00), 0–0. 52

Di Matteo, T., Colberg, J., Springel, V., Hernquist, L., & Sijacki, D. 2008. Direct Cosmological Simulations of the Growth of Black Holes and Galaxies. *ApJ*, **676**(Mar.), 33–53. 136

Dong, X. C., Lin, W. P., Kang, X., Ocean Wang, Y., Dutton, A. A., & Macciò, A. V. 2014. The Distribution of Satellites around Central Galaxies in a Cosmological Hydrodynamical Simulation. *ApJ Let.*, **791**(Aug.), L33. 86, 89, 90, 101, 115, 117

Doroshkevich, A., Tucker, D. L., Allam, S., & Way, M. J. 2004. Large scale structure in the SDSS galaxy survey. *A&A*, **418**(Apr.), 7–23. 18, 22

Doroshkevich, A. G. 1970. Spatial structure of perturbations and origin of galactic rotation in fluctuation theory. *Astrophysics*, **6**(Oct.), 320–330. 46, 47

Driver, S. P., Allen, P. D., Graham, A. W., Cameron, E., Liske, J., Ellis, S. C., Cross, N. J. G., De Propris, R., Phillipps, S., & Couch, W. J. 2006. The Millennium Galaxy Catalogue: morphological classification and bimodality in the colour-concentration plane. *MNRAS*, **368**(May), 414–434. 93

Dubois, Y., & Teyssier, R. 2008. On the onset of galactic winds in quiescent star forming galaxies. *A&A*, **477**(Jan.), 79–94. 33

Dubois, Y., Devriendt, J., Slyz, A., & Teyssier, R. 2010. Jet-regulated cooling catastrophe. *MNRAS*, **409**(Dec.), 985–1001. 35

Dubois, Y., Pichon, C., Haehnelt, M., Kimm, T., Slyz, A., Devriendt, J., & Pogosyan, D. 2012a. Feeding compact bulges and supermassive black holes with low angular momentum cosmic gas at high redshift. *MNRAS*, **423**(July), 3616–3630. 127

Dubois, Y., Devriendt, J., Slyz, A., & Teyssier, R. 2012b. Self-regulated growth of supermassive black holes by a dual jet-heating active galactic nucleus feedback mechanism: methods, tests and implications for cosmological simulations. *MNRAS*, Jan., 2188. 34, 35, 53, 136, 142

Dubois, Y., Gavazzi, R., Peirani, S., & Silk, J. 2013a. AGN-driven quenching of star formation: morphological and dynamical implications for early-type galaxies. *MNRAS*, **433**(Aug.), 3297–3313. 40, 136, 152, 153

Dubois, Y., Pichon, C., Devriendt, J., Silk, J., Haehnelt, M., Kimm, T., & Slyz, A. 2013b. Blowing cold flows away: the impact of early AGN activity on the formation of a brightest cluster galaxy progenitor. *MNRAS*, **428**(Feb.), 2885–2900. 132, 136, 166

Dubois, Y., Pichon, C., Welker, C., Le Borgne, D., Devriendt, J., Laigle, C., & Codis, S. 2014. Dancing in the dark: galactic properties trace spin swings along the cosmic web. *MNRAS*, **444**(Oct.), 1453–1468. 18, 26, 27, 46, 49, 57, 59, 60, 62, 64, 65, 72, 76, 89, 100, 101, 107, 138, 155, 164

Dunkley, J., Spergel, D. N., Komatsu, E., Hinshaw, G., Larson, D., Nolta, M. R., Odegard, N., Page, L., Bennett, C. L., Gold, B., Hill, R. S., Jarosik, N., Weiland, J. L., Halpern, M., Kogut, A., Limon, M., Meyer, S. S., Tucker, G. S., Wollack, E., & Wright, E. L. 2009. Five-Year Wilkinson Microwave Anisotropy Probe (WMAP) Observations: Bayesian Estimation of Cosmic Microwave Background Polarization Maps. *ApJ, 701, 1804.* 33

Efstathiou, G., Davis, M., White, S. D. M., & Frenk, C. S. 1985. Numerical techniques for large cosmological N-body simulations. *ApJ Sup.*, **57**(Feb.), 241–260. 22

Ellis, S. C., Driver, S. P., Allen, P. D., Liske, J., Bland-Hawthorn, J., & De Propris, R. 2005. The Millennium Galaxy Catalogue: on the natural subdivision of galaxies. *MNRAS*, **363**(Nov.), 1257–1271. 93

Elmegreen, B. G., Bournaud, F., & Elmegreen, D. M. 2008. Bulge Formation by the Coalescence of Giant Clumps in Primordial Disk Galaxies. *ApJ*, **688**(Nov.), 67–77. 25, 131, 132

Fakhouri, O., & Ma, C.-P. 2008. The nearly universal merger rate of dark matter haloes in ΛCDM cosmology. *MNRAS*, **386**(May), 577–592. 133

Faltenbacher, A., Jing, Y. P., Li, C., Mao, S., Mo, H. J., Pasquali, A., & van den Bosch, F. C. 2008. Spatial and Kinematic Alignments between Central and Satellite Halos. *ApJ*, **675**(Mar.), 146–155. 114

Feldmann, R., Carollo, C. M., Mayer, L., Renzini, A., Lake, G., Quinn, T., Stinson, G. S., & Yepes, G. 2010. The Evolution of Central Group Galaxies in Hydrodynamical Simulations. *ApJ*, **709**(Jan.), 218–240. 136, 152, 154

Forero-Romero, J. E., & González, R. 2015. The Local Group in the Cosmic Web. *ApJ*, **799**(Jan.), 45. 89

Forster Schreiber, N. M., Genzel, R., & Lehnert, M. D. et al. 2006. SINFONI Integral Field Spectroscopy of z ˜ 2 UV-selected Galaxies: Rotation Curves and Dynamical Evolution. *ApJ*, **645**(July), 1062–1075. 131

Gao, L., White, S. D. M., Jenkins, A., Stoehr, F., & Springel, V. 2004. The subhalo populations of ΛCDM dark haloes. *MNRAS*, **355**(Dec.), 819–834. 87

Gay, C., Pichon, C., Le Borgne, D., Teyssier, R., Sousbie, T., & Devriendt, J. 2010. On the filamentary environment of galaxies. *MNRAS*, **404**(June), 1801–1816. 57, 64

Geller, M. J., & Huchra, J. P. 1989. Mapping the universe. *Science*, **246**(Nov.), 897–903. 18

Genel, S., Vogelsberger, M., Springel, V., Sijacki, D., Nelson, D., Snyder, G., Rodriguez-Gomez, V., Torrey, P., & Hernquist, L. 2014. Introducing the Illustris project: the evolution of galaxy populations across cosmic time. *MNRAS*, **445**(Nov.), 175–200. 27

Genzel, R., & Burkert, A. et al. 2008. From Rings to Bulges: Evidence for Rapid Secular Galaxy Evolution at z ˜ 2 from Integral Field Spectroscopy in the SINS Survey. *ApJ*, **687**(Nov.), 59–77. 131

Ghigna, S., Moore, B., Governato, F., Lake, G., Quinn, T., & Stadel, J. 1999 (June). The Dark Matter Substructure of Clusters and Galaxies. *Page 140 of:* Giuricin, G., Mezzetti, M., & Salucci, P. (eds), *Observational Cosmology: The Development of Galaxy Systems*. Astronomical Society of the Pacific Conference Series, vol. 176. 86

Ghigna, S., Moore, B., Governato, F., Lake, G., Quinn, T., & Stadel, J. 2000. Density Profiles and Substructure of Dark Matter Halos: Converging Results at Ultra-High Numerical Resolution. *ApJ*, **544**(Dec.), 616–628. 87

Godunov, S. 1959. A Difference Scheme for Numerical Solution of Discontinuous Solution of Hydrodynamic Equations. *Math. Sbornik, JPRS*, **47**, 271–306. 30

Gottlöber, S., Klypin, A., & Kravtsov, A. V. 2001. Merging History as a Function of Halo Environment. *ApJ*, **546**(Jan.), 223–233. 133

Grazian, A., Fontana, A., Santini, P., Dunlop, J. S., Ferguson, H. C., & et al. 2014. The galaxy stellar mass function at 3.5 lt z lt 7.5 in the CANDELS/UDS, GOODS-South, and HUDF fields. *ArXiv e-prints*, Dec. 39, 140

Greggio, L., & Renzini, A. 1983. The binary model for type I supernovae - Theoretical rates. *A&A*, **118**(Feb.), 217–222. 34

Guo, Q., & White, S.D.M. 2008. Galaxy growth in the concordance ÎŻCDM cosmology. *MNRAS*, **384**(Feb.), 2–10. 136

Guzzo, L., Scodeggio, M., Garilli, B., Granett, B. R., Fritz, A., & Abbas, et al. 2014. The VIMOS Public Extragalactic Redshift Survey (VIPERS). An unprecedented view of galaxies and large-scale structure at 0.5 lt z lt 1.2. *A&A*, **566**(June), A108. 64

Haardt, F., & Madau, P. 1996. Radiative Transfer in a Clumpy Universe. II. The Ultraviolet Extragalactic Background. *ApJ*, **461**(Apr.), 20–+. 33

Haehnelt, M. G., Madau, P., Kudritzki, R., & Haardt, F. 2001. An Ionizing Ultraviolet Background Dominated by Massive Stars. *ApJ Let.*, **549**(Mar.), L151–L154. 33

Hahn, O., Carollo, C. M., Porciani, C., & Dekel, A. 2007. The evolution of dark matter halo properties in clusters, filaments, sheets and voids. *MNRAS*, **381**(Oct.), 41–51. 45, 76

Hahn, O., Teyssier, R., & Carollo, C. M. 2010. The large-scale orientations of disc galaxies. *MNRAS*, **405**(June), 274–290. 56

Hammer, F., & IMAGES Team. 2014. Formation of galactic disks through gas-rich mergers. *Memorie della Societa Astronomica Italiana*, **85**, 329. 165

Hammer, F., Flores, H., Puech, M., Yang, Y. B., Athanassoula, E., Rodrigues, M., & Delgado, R. 2009. The Hubble sequence: just a vestige of merger events? *A&A*, **507**(Dec.), 1313–1326. 131

Hawley, D. L., & Peebles, P. J. E. 1975. Distribution of observed orientations of galaxies. *AJ*, **80**(July), 477–491. 89

Helmi, A., & White, S. D. M. 1999. Building up the stellar halo of the Galaxy. *MNRAS*, **307**(Aug.), 495–517. 82

Henon, M. 1997. *Generating Families in the Restricted Three-Body Problem*. 82

Hidding, J., Shandarin, S. F., & van de Weygaert, R. 2014. The Zel'dovich approximation: key to understanding cosmic web complexity. *MNRAS*, **437**(Feb.), 3442–3472. 22

Hilz, M., Naab, T., Ostriker, J. P., Thomas, J., Burkert, A., & Jesseit, R. 2012. Relaxation and stripping - The evolution of sizes, dispersions and dark matter fractions in major and minor mergers of elliptical galaxies. *MNRAS*, **425**(Oct.), 3119–3136. 133, 153, 154

Hirata, C. M., Mandelbaum, R., Seljak, U., Guzik, J., Padmanabhan, N., Blake, C., Brinkmann, J., Budávari, T., Connolly, A., Csabai, I., Scranton, R., & Szalay, A. S. 2004. Galaxy-galaxy weak lensing in the Sloan Digital Sky Survey: intrinsic alignments and shear calibration errors. *MNRAS*, **353**(Sept.), 529–549. 121, 128

Hirata, C. M., Mandelbaum, R., Ishak, M., Seljak, U., Nichol, R., Pimbblet, K. A., Ross, N. P., & Wake, D. 2007. Intrinsic galaxy alignments from the 2SLAQ and SDSS surveys: luminosity and redshift scalings and implications for weak lensing surveys. *MNRAS*, **381**(Nov.), 1197–1218. 90

Hirschmann, M., Naab, T., Somerville, R. S., Burkert, A., & Oser, L. 2012. Galaxy formation in semi-analytic models and cosmological hydrodynamic zoom simulations. *MNRAS*, **419**(Feb.), 3200–3222. 136

Holmberg, E. 1969. A study of physical groups of galaxies. *Arkiv for Astronomi*, **5**, 305–343. 89, 107

Hopkins, A. M., & Beacom, J. F. 2006. On the Normalization of the Cosmic Star Formation History. *ApJ*, **651**(Nov.), 142–154. 129

Hopkins, P. F., Bahcall, N. A., & Bode, P. 2005. Cluster Alignments and Ellipticities in ΛCDM Cosmology. *ApJ*, **618**(Jan.), 1–15. 90

Hopkins, P. F., Bundy, K., Murray, N., Quataert, E., Lauer, T. R., & Ma, C.-P. 2009. Compact high-redshift galaxies are the cores of the most massive present-day spheroids. *MNRAS*, **398**(Sept.), 898–910. 136

Hoyle, F. 1949. *Problems of Cosmical Aerodynamics, Central Air Documents, Office, Dayton, OH.* Dayton, OH: Central Air Documents Office. 46, 47

Hubble, E. P. 1936. *Realm of the Nebulae.* 24

Huchra, J., Davis, M., Latham, D., & Tonry, J. 1983. A survey of galaxy redshifts. IV - The data. *ApJ Sup.*, **52**(June), 89–119. 18

Huertas-Company, M., Mei, S., Shankar, F., Delaye, L., Raichoor, A., Covone, G., Finoguenov, A., Kneib, J. P., Le, F. O., & Povic, M. 2013. The evolution of the mass-size relation for early-type galaxies from z 1 to the present: dependence on environment, mass range and detailed morphology. *MNRAS*, **428**(Jan.), 1715–1742. 132, 145, 150, 152

Huertas-Company, M., Kaviraj, S., Mei, S., O'Connell, R. W., Windhorst, R., Cohen, S. H., Hathi, . P., Koekemoer, A. M., Licitra, R., Raichoor, A., & Rutkowski, M. J. 2014. Measuring galaxy morphology at gt 1. I - calibration of automated proxies. *ArXiv e-prints*, June. 130

Hui, L., & Zhang, J. 2008. Density-Ellipticity Correlations, Galaxy-Galaxy Lensing, and the Importance of Non-Gaussianity in Intrinsic Alignment. *ApJ*, **688**(Dec.), 742–756. 121

Ibata, R. A., Lewis, G. F., Conn, A. R., Irwin, M. J., McConnachie, A. W., Chapman, S. C., Collins, M. L., Fardal, M., Ferguson, A. M. N., Ibata, N. G., Mackey, A. D., Martin, N. F., Navarro, J., Rich, R. M., Valls-Gabaud, D., & Widrow, L. M. 2013. A vast, thin plane of corotating dwarf galaxies orbiting the Andromeda galaxy. *Nature*, **493**(Jan.), 62–65. 87

Ivezic, Z., Tyson, J. A., et al., & for the LSST Collaboration. 2008. LSST: from Science Drivers to Reference Design and Anticipated Data Products. *ArXiv e-prints*, May. 127

Jing, Y. P., & Suto, Y. 2002. Triaxial Modeling of Halo Density Profiles with High-Resolution N-Body Simulations. *ApJ*, **574**(Aug.), 538–553. 86

Joachimi, B., Mandelbaum, R., Abdalla, F. B., & Bridle, S. L. 2011. Constraints on intrinsic alignment contamination of weak lensing surveys using the MegaZ-LRG sample. *A&A*, **527**(Mar.), A26. 90

Jost, J. 1995. *Riemannian Geometry and Geometric Analysis.* Adresse: Springer. 43

Kaiser, N. 1984. On the spatial correlations of Abell clusters. *ApJ Let.*, **284**(Sept.), L9–L12. 23

Kang, X., Jing, Y. P., Mo, H. J., & Börner, G. 2005. Semianalytical Model of Galaxy Formation with High-Resolution N-Body Simulations. *ApJ*, **631**(Sept.), 21–40. 93

Kauffmann, G., Colberg, J. M., Diaferio, A., & White, S. D. M. 1999. Clustering of galaxies in a hierarchical universe - I. Methods and results at z eq. 0. *MNRAS*, **303**(Feb.), 188–206. 17

Kaviraj, S. 2014. The importance of minor-merger-driven star formation and black hole growth in disc galaxies. *MNRAS*, **440**(June), 2944–2952. 150

Kaviraj, S., Cohen, S., & Ellis, R. S. et al. 2013a. Newborn spheroids at high redshift: when and how did the dominant, old stars in today's massive galaxies form? *MNRAS*, **428**(Jan.), 925–934. 132

Kaviraj, S., Cohen, S., Windhorst, R. A., Silk, J., O'Connell, R. W., Dopita, M. A., Dekel, A., Hathi, N. P., Straughn, A., & Rutkowski, M. 2013b. The insignificance of major mergers in driving star formation at z sime 2. *MNRAS*, **429**(Feb.), L40–L44. 131, 135

Kaviraj, S., Devriendt, J., Dubois, Y., Slyz, A., Welker, C., Pichon, C., Peirani, S., & Le Borgne, D. 2014a. Galaxy merger histories and the role of merging in driving star formation at z gt 1. *ArXiv e-prints*, Nov. 145

Kaviraj, S., Huertas-Company, M., Cohen, S., & Peirani, S. et al. 2014b. The role of major mergers in the size growth of intermediate-mass spheroids. *MNRAS*, **443**(Sept.), 1861–1866. 130

Kazantzidis, S., Magorrian, J., & Moore, B. 2004a. Generating Equilibrium Dark Matter Halos: Inadequacies of the Local Maxwellian Approximation. *ApJ*, **601**(Jan.), 37–46. 82

Kazantzidis, S., Kravtsov, A. V., Zentner, A. R., Allgood, B., Nagai, D., & Moore, B. 2004b. The Effect of Gas Cooling on the Shapes of Dark Matter Halos. *ApJ Let.*, **611**(Aug.), L73–L76. 82, 89, 101, 115

Keenan.D.W, & Innanen, K.A. 1975. *AJ*, **80**, 290. 82

Kennicutt, Jr., R. C. 1998. The Global Schmidt Law in Star-forming Galaxies. *ApJ*, **498**(May), 541–+. 33

Kereš, D., Katz, N., Weinberg, D. H., & Davé, R. 2005. How do galaxies get their gas? *MNRAS*, **363**(Oct.), 2–28. 136

Khandai, N., Di Matteo, T., Croft, R., Wilkins, S., Feng, Y., Tucker, E., DeGraf, C., & Liu, M.-S. 2015. The MassiveBlack-II simulation: the evolution of haloes and galaxies to z simeq 0. *MNRAS*, **450**(June), 1349–1374. 27

Khochfar, S., & Silk, J. 2006. A simple model for the size evolution of elliptical galaxies. *AJ*, **648**(Sept.), L21–L24. 136

Kimm, T., Devriendt, J., Slyz, A., Pichon, C., Kassin, S. A., & Dubois, Y. 2011. The angular momentum of baryons and dark matter halos revisited. *ArXiv e-prints*, June. 152

King, A. 2003. Black Holes, Galaxy Formation, and the Mbh-sigma Relation. *ApJ Let.*, **596**(Oct.), L27–L29. 17

King, I. 1962. The structure of star clusters. I. an empirical density law. *AJ*, **67**(Oct.), 471. 81

Knebe, A., Gill, S. P. D., Gibson, B. K., Lewis, G. F., Ibata, R. A., & Dopita, M. A. 2004. Anisotropy in the Distribution of Satellite Galaxy Orbits. *ApJ*, **603**(Mar.), 7–11. 87

Komatsu, E. et al, . 2011. Seven-year Wilkinson Microwave Anisotropy Probe (WMAP) Observations: Cosmological Interpretation. *ApJ Sup.*, **192**(Feb.), 18–+. 28

Krumholz, M. R., & Tan, J. C. 2007. Slow Star Formation in Dense Gas: Evidence and Implications. *ApJ*, **654**(Jan.), 304–315. 33

Lackner, C. N., Cen, R., Ostriker, J. P., & Joung, M. R. 2012. Building galaxies by accretion and in situ star formation. *MNRAS*, **425**(Sept.), 641–656. 136

Laigle, C., Pichon, C., Codis, S., Dubois, Y., Le Borgne, D., Pogosyan, D., Devriendt, J., Peirani, S., Prunet, S., Rouberol, S., Slyz, A., & Sousbie, T. 2015. Swirling around filaments: are large-scale structure vortices spinning up dark haloes? *MNRAS*, **446**(Jan.), 2744–2759. 45, 49, 50, 76, 100, 156, 164

Lambas, D. G., Maddox, S. J., & Loveday, J. 1992. On the true shapes of galaxies. *MNRAS*, **258**(Sept.), 404–414. 142

Laureijs, R., Amiaux, J., Arduini, S., Augueres, J. ., Brinchmann, J., Cole, R., Cropper, M., Dabin, C., Duvet, L., Ealet, A., & et al. 2011. Euclid Definition Study Report. *ArXiv e-prints*, Oct. 127

Law, D. R. 2009. *The Kiloparsec-Scale Structure and Kinematics of High-Redshift Star-Forming Galaxies*. Ph.D. thesis, California Institute of Technology. 135

Lee, Bomee, Giavalisco, Mauro, Williams, Christina C., Guo, Yicheng, Lotz, Jennifer, van der Wel, Arjen, Ferguson, Henry C, Faber, S M, Koekemoer, Anton, Grogin, Norman, Kocevski, Dale, Conselice, Christopher J, Wuyts, Stijn, Dekel, Avishai, Kartaltepe, Jeyhan, & Bell, Eric F.

2013. CANDELS: THE CORRELATION BETWEEN GALAXY MORPHOLOGY AND STAR FORMATION ACTIVITY AT z? 2. *ApJ*, **774**(1), 47. 163

Lee, J., & Pen, U. 2000. *ApJ*, **532**, L5. 45

Lee, J., & Yi, S. K. 2013. On the Assembly History of Stellar Components in Massive Galaxies. *ApJ*, **766**(Mar.), 38. 136

Lee, J., Rey, S. C., & Kim, S. 2014. Alignments of the Galaxies in and around the Virgo Cluster with the Local Velocity Shear. *ApJ*, **791**(Aug.), 15. 87

Leitherer, C., Schaerer, D., Goldader, J. D., González Delgado, R. M., Robert, C., Kune, D. F., de Mello, D. F., Devost, D., & Heckman, T. M. 1999. Starburst99: Synthesis Models for Galaxies with Active Star Formation. *ApJ Sup.*, **123**(July), 3–40. 34

Leitherer, C., Ortiz Otálvaro, P. A., Bresolin, F., Kudritzki, R.-P., Lo Faro, B., Pauldrach, A. W. A., Pettini, M., & Rix, S. A. 2010. A Library of Theoretical Ultraviolet Spectra of Massive, Hot Stars for Evolutionary Synthesis. *ApJ Sup.*, **189**(Aug.), 309–335. 34

Libeskind, N. I., Knebe, A., Hoffman, Y., Gottlöber, S., Yepes, G., & Steinmetz, M. 2011. The preferred direction of infalling satellite galaxies in the Local Group. *MNRAS*, **411**(Mar.), 1525–1535. 87

Libeskind, N. I., Knebe, A., Hoffman, Y., & Gottlöber, S. 2014. The universal nature of subhalo accretion. *MNRAS*, **443**(Sept.), 1274–1280. 80

Libeskind, N. I., Hoffman, Y., Tully, R. B., Courtois, H. M., Pomarede, D., Gottloeber, S., & Steinmetz, M. 2015. Planes of satellite galaxies and the cosmic web. *ArXiv e-prints*, Mar. 87, 89

Lin, L., Koo, D. C., Willmer, C. N. A., Patton, D. R., Conselice, C. J., Yan, R., Coil, A. L., Cooper, M. C., Davis, M., Faber, S. M., Gerke, B. F., Guhathakurta, P., & Newman, J. A. 2004. The DEEP2 Galaxy Redshift Survey: Evolution of Close Galaxy Pairs and Major-Merger Rates up to z eq. 1.2. *ApJ Let.*, **617**(Dec.), L9–L12. 133

Lin, L., Cooper, M. C., Jian, H.-Y., Koo, D. C., Patton, D. R., Yan, R., Willmer, C. N. A., Coil, A. L., Chiueh, T., Croton, D. J., Gerke, B. F., Lotz, J., Guhathakurta, P., & Newman, J. A. 2010. Where do Wet, Dry, and Mixed Galaxy Mergers Occur? A Study of the Environments of Close Galaxy Pairs in the DEEP2 Galaxy Redshift Survey. *ApJ*, **718**(Aug.), 1158–1170. 129, 131

López-Sanjuan, C., Le Fèvre, O., Tasca, L. A. M., Epinat, B., Amram, P., Contini, T., Garilli, B., Kissler-Patig, M., Moultaka, J., Paioro, L., Perret, V., Queyrel, J., Tresse, L., Vergani, D., & Divoy, C. 2013. MASSIV: Mass Assembly Survey with SINFONI in VVDS. V. The major merger rate of star-forming galaxies at 0.9 lt z lt 1.8 from IFS-based close pairs. *A&A*, **553**(May), A78. 129, 131

Lotz, J. M., Jonsson, P., Cox, T. J., & Primack, J. R. 2008a. Galaxy merger morphologies and time-scales from simulations of equal-mass gas-rich disc mergers. *MNRAS*, **391**(Dec.), 1137–1162. 133

Lotz, J. M., Davis, M., Faber, S. M., Guhathakurta, P., Gwyn, S., Huang, J., Koo, D. C., Le Floc'h, E., Lin, L., Newman, J., Noeske, K., Papovich, C., Willmer, C. N. A., Coil, A., Conselice, C. J., Cooper, M., Hopkins, A. M., Metevier, A., Primack, J., Rieke, G., & Weiner, B. J. 2008b. The Evolution of Galaxy Mergers and Morphology at z lt 1.2 in the Extended Groth Strip. *ApJ*, **672**(Jan.), 177–197. 133, 166

Lotz, J. M., Jonsson, P., Cox, T. J., & Primack, J. R. 2010a. The effect of gas fraction on the morphology and time-scales of disc galaxy mergers. *MNRAS*, **404**(May), 590–603. 51, 133

Lotz, J. M., Jonsson, P., Cox, T. J., & Primack, J. R. 2010b. The effect of mass ratio on the morphology and time-scales of disc galaxy mergers. *MNRAS*, **404**(May), 575–589. 51, 133

Lotz, J. M., Jonsson, P., Cox, T. J., Croton, D., Primack, J. R., Somerville, R. S., & Stewart, K. 2011. The Major and Minor Galaxy Merger Rates at z lt 1.5. *ApJ*, **742**(Dec.), 103. 145

Lynden-Bell, D. 1967. Statistical mechanics of violent relaxation in stellar systems. *MNRAS*, **136**, 101. 134, 135

Lynden-Bell, D., & Kalnajs, A. J. 1972. On the generating mechanism of spiral structure. *MNRAS*, **157**, 1. 85

Madau, P., Pozzetti, L., & Dickinson, M. 1998. The Star Formation History of Field Galaxies. *ApJ*, **498**(May), 106–116. 129

Maller, A., Katz, N., Keres, D., DavÃĺ, R., & Weinberg, D. 2006. Galaxy Merger Statistics and Inferred Bulge-to-Disk Ratios in Cosmological SPH Simulations. *ApJ*, **647**(Aug.), 763–772. 136

Mancini, C., Forster Schreiber, N. M., Renzini, A., & Cresci, G. et al. 2011. The zCOSMOS-SINFONI Project. I. Sample Selection and Natural-seeing Observations. *ApJ*, **743**(Dec.), 86. 131

Mandelbaum, R., Hirata, C. M., Ishak, M., & Seljak, U. 2006 (Dec.). A Detection of Large-scale Intrinsic Alignments and Implications for Cosmic Shear. *Page 1001 of: American Astronomical Society Meeting Abstracts*. Bulletin of the American Astronomical Society, vol. 38. 90, 121

Mao, S. 2004 (July). Lensing Diagnostics of Halo Substructure. *Page 85 of:* Ryder, S., Pisano, D., Walker, M., & Freeman, K. (eds), *Dark Matter in Galaxies*. IAU Symposium, vol. 220. 87

Martel, H., & Shapiro, P. R. 1998. A convenient set of comoving cosmological variables and their application. *MNRAS*, **297**(June), 467–485. 28

Mayer, L. 2005. The environment of dwarf spheroidal satellites; ram pressure, tides and external radiation fields. *Pages 220–228 of:* Jerjen, H., & Binggeli, B. (eds), *IAU Colloq. 198: Near-fields cosmology with dwarf elliptical galaxies*. 83

Meneghetti, M., Bartelmann, M., & Moscardini, L. 2001. Constraining cosmological models using arc statistics in future SZ cluster surveys. *ArXiv Astrophysics e-prints*, Sept. 86

Monaghan, J. J. 1992. Smoothed particle hydrodynamics. *ARA&A*, **30**, 543–574. 35

Mortlock, A., Conselice, C. J., Hartley, W. G., Ownsworth, J. R., Lani, C., Bluck, A. F. L., Almaini, O., Duncan, K., van der Wel, A., Koekemoer, A. M., Dekel, A., Davé, R., Ferguson, H. C., de Mello, D. F., Newman, J. A., Faber, S. M., Grogin, N. A., Kocevski, D. D., & Lai, K. 2013. The redshift and mass dependence on the formation of the Hubble sequence at z gt 1 from CANDELS/UDS. *MNRAS*, **433**(Aug.), 1185–1201. 131

Mortlock, A., Conselice, C. J., Hartley, W. G., Duncan, K., Lani, C., & et al. 2015. Deconstructing the galaxy stellar mass function with UKIDSS and CANDELS: the impact of colour, structure and environment. *MNRAS*, **447**(Feb.), 2–24. 39, 140

Naab, T., & Burkert, A. 2003. Statistical Properties of Collisionless Equal- and Unequal-Mass Merger Remnants of Disk Galaxies. *ApJ*, **597**(Nov.), 893–906. 25, 131, 136

Naab, T., & Trujillo, I. 2006. Surface density profiles of collisionless disc merger remnants. *MNRAS*, **369**(June), 625–644. 136

Naab, T., Khochfar, S., & Burkert, A. 2006a. Properties of Early-Type, Dry Galaxy Mergers and the Origin of Massive Elliptical Galaxies. *ApJ*, **636**(Jan.), L81–84. 136

Naab, T., Jesseit, R., & Burkert, A. 2006b. The influence of gas on the structure of merger remnants. *MNRAS*, **372**(Oct.), 839–852. 25, 131, 136

Naab, T., Johansson, P.H., & Jeremiah, P.and Efstathiou, G. 2007. Formation of Early-Type Galaxies from Cosmological Initial Conditions. *ApJ*, **658**(Apr.), 710–720. 136, 152

Naab, T., Johansson, P. H., & Ostriker, J. P. 2009. Minor Mergers and the Size Evolution of Elliptical Galaxies. *ApJ Let.*, **699**(July), L178–L182. 133

Nagai, D., & Kravtsov, A. V. 2005. The Radial Distribution of Galaxies in Λ Cold Dark Matter Clusters. *ApJ*, **618**(Jan.), 557–568. 87

Nakamura, T. K. 2000. Statistical Mechanics of a Collisionless System Based on the Maximum Entropy Principle. *ApJ*, **531**(Mar.), 739–743. 134

Nelson, D., Genel, S., Vogelsberger, M., Springel, V., Sijacki, D., Torrey, P., & Hernquist, L. 2015. The impact of feedback on cosmological gas accretion. *MNRAS*, **448**(Mar.), 59–74. 53, 132, 166

Newman, A. B., Ellis, R. S., Bundy, K., & Treu, T. 2012. Can Minor Merging Account for the Size Growth of Quiescent Galaxies? New Results from the CANDELS Survey. *ApJ*, **746**(Feb.), 162. 152

Nierenberg, A. M., Auger, M. W., Treu, T., Marshall, P. J., Fassnacht, C. D., & Busha, M. T. 2012. Luminous Satellites. II. Spatial Distribution, Luminosity Function, and Cosmic Evolution. *ApJ*, **752**(June), 99. 89

Nipoti, C., Treu, T., Auger, M. W., & Bolton, A. S. 2009. Can Dry Merging Explain the Size Evolution of Early-Type Galaxies? *ApJ Let.*, **706**(Nov.), L86–L90. 136, 152, 154

Nipoti, C., Treu, T., Leauthaud, A., Bundy, K., Newman, A. B., & Auger, M. W. 2012. Size and velocity-dispersion evolution of early-type galaxies in a Λ cold dark matter universe. *MNRAS*, **422**(May), 1714–1731. 132, 145

Novikov, D., Colombi, S., & Doré, O. 2006. Skeleton as a probe of the cosmic web: the two-dimensional case. *MNRAS*, **366**(Mar.), 1201–1216. 40

Ocvirk, P., Pichon, C., & Teyssier, R. 2008. Bimodal gas accretion in the Horizon-MareNostrum galaxy formation simulation. *MNRAS*, **390**(Nov.), 1326–1338. 136, 155

Okumura, T., & Jing, Y. P. 2009. The Gravitational Shear-Intrinsic Ellipticity Correlation Functions of Luminous Red Galaxies in Observation and in the ΛCDM Model. *ApJ Let.*, **694**(Mar.), L83–L86. 90

Omma, H., Binney, J., Bryan, G., & Slyz, A. 2004. Heating cooling flows with jets. *MNRAS*, **348**(Mar.), 1105–1119. 35

Oser, L., Ostriker, J. P., Naab, T., Johansson, P. H., & Burkert, A. 2010. The Two Phases of Galaxy Formation. *ApJ*, **725**(Dec.), 2312–2323. 66, 136

Paranjape, A., & Sheth, R. K. 2012. Peaks theory and the excursion set approach. *MNRAS*, **426**(Nov.), 2789–2796. 49

Patton, D. R., Pritchet, C. J., Carlberg, R. G., Marzke, R. O., Yee, H. K. C., Hall, P. B., Lin, H., Morris, S. L., Sawicki, M., Shepherd, C. W., & Wirth, G. D. 2002. Dynamically Close Galaxy Pairs and Merger Rate Evolution in the CNOC2 Redshift Survey. *ApJ*, **565**(Jan.), 208–222. 133

Pawlowski, M. S., Kroupa, P., Angus, G., de Boer, K. S., Famaey, B., & Hensler, G. 2012. Filamentary accretion cannot explain the orbital poles of the Milky Way satellites. *MNRAS*, **424**(July), 80–92. 89

Paz, D. J., Stasyszyn, F., & Padilla, N. D. 2008. *MNRAS*, **389**, 1127P. 45, 87

Paz, D. J., Sgró, M. A., Merchán, M., & Padilla, N. 2011. Alignments of galaxy group shapes with large-scale structure. *MNRAS*, **414**(July), 2029–2039. 87

Peacock, J. A., & Heavens, A. F. 1990. Alternatives to the Press-Schechter cosmological mass function. *MNRAS*, **243**(Mar.), 133–143. 49

Peebles, P. J. E. 1969. Origin of the Angular Momentum of Galaxies. *ApJ*, **155**(Feb.), 393–+. 18, 46, 47

Peirani, S., Mohayaee, R., & de Freitas Pacheco, J. A. 2004. The angular momentum of dark haloes: merger and accretion effects. *MNRAS*, **348**(Mar.), 921–931. 45

Peirani, S., Crockett, R. M., Geen, S., Khochfar, S., Kaviraj, S., & Silk, J. 2010. Composite star formation histories of early-type galaxies from minor mergers: prospects for WFC3. *MNRAS*, **405**(July), 2327–2338. 136

Peng, Y., Maiolino, R., & Cochrane, R. 2015. Strangulation as the primary mechanism for shutting down star formation in galaxies. *Nature*, **521**(May), 192–195. 93

Phillips, J. I., Cooper, M. C., Bullock, J. S., & Boylan-Kolchin, M. 2015. Are rotating planes of satellite galaxies ubiquitous? *ArXiv e-prints*, May. 89

Pichon, C., Pogosyan, D., Kimm, T., Slyz, A., Devriendt, J., & Dubois, Y. 2011. Rigging dark haloes: why is hierarchical galaxy formation consistent with the inside-out build-up of thin discs? *MNRAS*, Oct., 1739–+. 50, 76, 87, 108, 131, 136

Pichon, C., Codis, S., Pogosyan, D., Dubois, Y., Desjacques, V., & Devriendt, J. 2014. Why do galactic spins flip in the cosmic web? A Theory of Tidal Torques near saddles. *ArXiv e-prints*, Sept. 156

Pisano, D. J. 2014. Green Bank Telescope Observations of Low Column Density H I around NGC 2997 and NGC 6946. *AJ*, **147**(Mar.), 48. 53

Planck Collaboration, Ade, P. A. R., Aghanim, N., Armitage-Caplan, C., Arnaud, M., Ashdown, M., Atrio-Barandela, F., Aumont, J., Baccigalupi, C., Banday, A. J., & et al. 2014. Planck 2013 results. XVI. Cosmological parameters. *A&A*, **571**(Nov.), A16. 28

Plionis, M., & Basilakos, S. 2002. The cluster substructure-alignment connection. *MNRAS*, **329**(Jan.), L47–L51. 90

Popping, G., Somerville, R. S., & Trager, S. C. 2014. Evolution of the atomic and molecular gas content of galaxies. *MNRAS*, **442**(Aug.), 2398–2418. 142, 144

Porciani, C., Dekel, A., & Hoffman, Y. 2002a. Testing tidal-torque theory - I. Spin amplitude and direction. *MNRAS*, **332**(May), 325–338. 46, 48

Porciani, C., Dekel, A., & Hoffman, Y. 2002b. Testing tidal-torque theory - II. Alignment of inertia and shear and the characteristics of protohaloes. *MNRAS*, **332**(May), 339–351. 18, 46, 47

Powell, L. C., Slyz, A., & Devriendt, J. 2011. The impact of supernova-driven winds on stream-fed protogalaxies. *MNRAS*, **414**(July), 3671–3689. 53, 166

Press, W. H., & Schechter, P. 1974. Formation of Galaxies and Clusters of Galaxies by Self-Similar Gravitational Condensation. *ApJ*, **187**(Feb.), 425–438. 17, 21, 22, 49

Prunet, S., Pichon, C., Aubert, D., Pogosyan, D., Teyssier, R., & Gottloeber, S. 2008. Initial Conditions For Large Cosmological Simulations. *ApJ Sup.*, **178**(Oct.), 179–188. 28

Qu, Y., Di Matteo, P., Lehnert, M. D., & van Driel, W. 2011. Characteristics of thick disks formed through minor mergers: stellar excesses and scale lengths. *A&A*, **530**(June), A10. 25, 131, 136

Quinn, P. J., Hernquist, L., & Fullagar, D. P. 1993. Heating of galactic disks by mergers. *ApJ*, **403**(Jan.), 74–93. 136

Rasera, Y., & Teyssier, R. 2006. The history of the baryon budget. Cosmic logistics in a hierarchical universe. *A&A*, **445**(Jan.), 1–27. 33

Read, J. I., Wilkinson, M. I., Evans, N. W., Gilmore, G., & Kleyna, J. T. 2006. The tidal stripping of satellites. *MNRAS*, **366**(Feb.), 429–437. 82

Robertson, B., Bullock, J. S., Cox, T. J., Di Matteo, T., Hernquist, L., Springel, V., & Yoshida, N. 2006. A Merger-driven Scenario for Cosmological Disk Galaxy Formation. *ApJ*, **645**(July), 986–1000. 165

Rodriguez-Gomez, V., Genel, S., Vogelsberger, M., Sijacki, D., Pillepich, A., Sales, L. V., Torrey, P., Snyder, G., Nelson, D., Springel, V., Ma, C.-P., & Hernquist, L. 2015. The merger rate of galaxies in the Illustris Simulation: a comparison with observations and semi-empirical models. *ArXiv e-prints*, Feb. 145

Sales, L., & Lambas, D. G. 2004. Anisotropy in the distribution of satellites around primary galaxies in the 2dF Galaxy Redshift Survey: the Holmberg effect. *MNRAS*, **348**(Mar.), 1236–1240. 89

Sales, L. V., Navarro, J. F., Schaye, J., Dalla Vecchia, C., Springel, V., Haas, M. R., & Helmi, A. 2009. The origin of extended disc galaxies at z = 2. *MNRAS*, **399**(Oct.), L64–L68. 89

Sales, L. V., Vogelsberger, M., Genel, S., Torrey, P., Nelson, D., Rodriguez-Gomez, V., Wang, W., Pillepich, A., Sijacki, D., Springel, V., & Hernquist, L. 2015. The colours of satellite galaxies in the Illustris simulation. *MNRAS*, **447**(Feb.), L6–L10. 87

Salpeter, E. E. 1955. The Luminosity Function and Stellar Evolution. *ApJ*, **121**(Jan.), 161. 34

Santini, P., Maiolino, R., Magnelli, B., & et al. 2014. The evolution of the dust and gas content in galaxies. *A&A*, **562**(Feb.), A30. 136

Schaye, J., Crain, R. A., Bower, R., & et al. 2015. The EAGLE project: simulating the evolution and assembly of galaxies and their environments. *MNRAS*, **446**(Jan.), 521–554. 27

Schneider, M. D., & Bridle, S. 2010. A halo model for intrinsic alignments of galaxy ellipticities. *MNRAS*, **402**(Mar.), 2127–2139. 121, 127

Schneider, M. D., Cole, S., Frenk, C. S., Kelvin, L., Mandelbaum, R., Norberg, P., Bland-Hawthorn, J., Brough, S., Driver, S., Hopkins, A., Liske, J., Loveday, J., & Robotham, A. 2013. Galaxy And Mass Assembly (GAMA): galaxy radial alignments in GAMA groups. *MNRAS*, **433**(Aug.), 2727–2738. 114, 121

Schweizer, F. 1982. Colliding and merging galaxies. I - Evidence for the recent merging of two disk galaxies in NGC 7252. *ApJ*, **252**(Jan.), 455–460. 25

Shakura, N. I., & Sunyaev, R. A. 1973. Black holes in binary systems. Observational appearance. *A&A*, **24**, 337–355. 35

Shandarin, S. F., & Zeldovich, Y. B. 1989. The large-scale structure of the universe: Turbulence, intermittency, structures in a self-gravitating medium. *Reviews of Modern Physics*, **61**(Apr.), 185–220. 18, 22, 80

Shankar, F., Salucci, P., Granato, G. L., De Zotti, G., & Danese, L. 2004. Supermassive black hole demography: the match between the local and accreted mass functions. *MNRAS*, **354**(Nov.), 1020–1030. 135

Shankar, F., Marulli, F., Bernardi, M., Mei, S., Meert, A., & Vikram, V. 2013. Size evolution of spheroids in a hierarchical Universe. *MNRAS*, **428**(Jan.), 109–128. 136

Shapiro, K. L., Genzel, R., & Forster Schreiber, N. M. et al. 2008. Kinemetry of SINS High-Redshift Star-Forming Galaxies: Distinguishing Rotating Disks from Major Mergers. *ApJ*, **682**(July), 231–251. 131

Sharma, S., & Steinmetz, M. 2005. The Angular Momentum Distribution of Gas and Dark Matter in Galactic Halos. *ApJ*, **628**(July), 21–44. 89

Sifón, C., Hoekstra, H., Cacciato, M., Viola, M., Köhlinger, F., van der Burg, R. F. J., Sand, D. J., & Graham, M. L. 2015. Constraints on the alignment of galaxies in galaxy clusters from ˜14 000 spectroscopic members. *A&A*, **575**(Mar.), A48. 114

Sijacki, D., Springel, V., Di Matteo, T., & Hernquist, L. 2007. A unified model for AGN feedback in cosmological simulations of structure formation. *MNRAS*, **380**(Sept.), 877–900. 17, 136

Silk, J., & Rees, M. J. 1998. Quasars and galaxy formation. *A&A*, **331**(Mar.), L1–L4. 17

Singh, S., & Mandelbaum, R. 2014 (June). Intrinsic Alignments of galaxies in SDSS-III BOSS LOWZ sample. *Page 423.04 of: American Astronomical Society Meeting Abstracts 224*. American Astronomical Society Meeting Abstracts, vol. 224. 90

Smargon, A., Mandelbaum, R., Bahcall, N., & Niederste-Ostholt, M. 2012. Detection of intrinsic cluster alignments to 100 h^{-1} Mpc in the Sloan Digital Sky Survey. *MNRAS*, **423**(June), 856–861. 90

Sousbie, T. 2013 (Feb.). *DisPerSE: Discrete Persistent Structures Extractor*. Astrophysics Source Code Library. 40

Sousbie, T, Pichon, C, Colombi, S, & Pogosyan, D. 2008. The 3D skeleton: tracing the filamentary structure of the Universe. *MNRAS*, **383**(4), 1655–1670. 40, 45, 80

Sousbie, T., Colombi, S., & Pichon, C. 2009. The fully connected N-dimensional skeleton: probing the evolution of the cosmic web. *MNRAS*, **393**(Feb.), 457–477. 40, 43, 46

Sousbie, T., Pichon, C., & Kawahara, H. 2010. The persistent cosmic web and its filamentary structure II: Illustrations. *ArXiv e-prints*, Sept. 40, 43

Spergel, D., Gehrels, N., & et al. 2013. WFIRST-2.4: What Every Astronomer Should Know. *ArXiv e-prints*, May. 127

Springel, V., & Hernquist, L. 2003. The history of star formation in a Λ cold dark matter universe. *MNRAS*, **339**(Feb.), 312–334. 33

Springel, V., Di Matteo, T., & Hernquist, L. 2005. Black Holes in Galaxy Mergers: The Formation of Red Elliptical Galaxies. *ApJ Let.*, **620**(Feb.), L79–L82. 135

Springel, V., Frenk, C. S., & White, S. D. M. 2006. The large-scale structure of the Universe. *Nature*, **440**(Apr.), 1137–1144. 22

Stewart, K. R. 2009. *Merger histories of dark matter halos in ΛCDM and implications for the evolution of Milky Way-size galaxies.* Ph.D. thesis, University of California, Irvine <EMAIL>stewartk@uci.edu</EMAIL>. 133

Strateva, I., Ivezić, Ž., Knapp, G. R., Narayanan, V. K., Strauss, M. A., Gunn, J. E., Lupton, R. H., Schlegel, D., Bahcall, N. A., Brinkmann, J., Brunner, R. J., Budavári, T., Csabai, I., Castander, F. J., Doi, M., Fukugita, M., Győry, Z., Hamabe, M., Hennessy, G., Ichikawa, T., Kunszt, P. Z., Lamb, D. Q., McKay, T. A., Okamura, S., Racusin, J., Sekiguchi, M., Schneider, D. P., Shimasaku, K., & York, D. 2001. Color Separation of Galaxy Types in the Sloan Digital Sky Survey Imaging Data. *AJ*, **122**(Oct.), 1861–1874. 93

Sutherland, R. S., & Dopita, M. A. 1993. Cooling functions for low-density astrophysical plasmas. *ApJ Sup.*, **88**(Sept.), 253–327. 32

Szebehely, V., & Peters, C. F. 1967. A new periodic solution of the problem of three bodies. *AJ*, **72**(Nov.), 1187. 82

Tacconi, L. J., Genzel, R., Neri, R., & et al. 2010. High molecular gas fractions in normal massive star-forming galaxies in the young Universe. *Nature*, **463**(Feb.), 781–784. 136

Tempel, E., & Libeskind, N. I. 2013. Galaxy Spin Alignment in Filaments and Sheets: Observational Evidence. *ApJ*, **775**(Sept.). 45, 64, 75, 164

Tempel, E., Guo, Q., Kipper, R., & Libeskind, N. I. 2015. The alignment of satellite galaxies and cosmic filaments: observations and simulations. *MNRAS*, **450**(July), 2727–2738. 87

Tenneti, A., Singh, S., Mandelbaum, R., Matteo, T. D., Feng, Y., & Khandai, N. 2015a. Intrinsic alignments of galaxies in the MassiveBlack-II simulation: analysis of two-point statistics. *MNRAS*, **448**(Apr.), 3522–3544. 121, 127

Tenneti, A., Singh, S., Mandelbaum, R., Matteo, T. D., Feng, Y., & Khandai, N. 2015b. Intrinsic alignments of galaxies in the MassiveBlack-II simulation: analysis of two-point statistics. *MNRAS*, **448**(Apr.), 3522–3544. 127

Teyssier, R. 2002. Cosmological hydrodynamics with adaptive mesh refinement. A new high resolution code called RAMSES. *A&A*, **385**(Apr.), 337–364. 26, 28, 30, 31

Tillson, H., Devriendt, J., Slyz, A., Miller, L., & Pichon, C. 2012. Angular momentum transfer to a Milky Way disk at high redshift. *ArXiv e-prints*, Nov. 52, 156

Tillson, H., Devriendt, J., Slyz, A., Miller, L., & Pichon, C. 2015. Angular momentum transfer to a Milky Way disc at high redshift. *MNRAS*, **449**(June), 4363–4379. 108

Toomre, A. 1964. On the gravitational stability of a disk of stars. *ApJ*, **139**(May), 1217–1238. 132

Toomre, A., & Toomre, J. 1972. *Astrophysical Journal*, **178**, 623. 25, 82

Tormen, G., Bouchet, F. R., & White, S. D. M. 1997. The structure and dynamical evolution of dark matter haloes. *MNRAS*, **286**(Apr.), 865–884. 87

Toro, E.F.and Spruce, M., & Speares, W. 1994. Restoration of the contact surface in the Harten-Lax-van Leer Riemann solver. *Shock Waves*, **4**, 25–34. 31

Tremaine, S., & Ostriker, J. P. 1999. Relaxation in stellar systems, and the shape and rotation of the inner dark halo. *MNRAS*, **306**(July), 662–668. 82

Tremaine, S., & Weinberg, M. D. 1984. Dynamical friction in spherical systems. *MNRAS*, **209**(Aug.), 729–757. 83, 85, 86

Trujillo, I., Carretero, C., & Patiri, S. G. 2006. Detection of the Effect of Cosmological Large-Scale Structure on the Orientation of Galaxies. *ApJ Let.*, **640**(Apr.), L111–L114. 132

Tweed, D., Devriendt, J., Blaizot, J., Colombi, S., & Slyz, A. 2009. Building merger trees from cosmological N-body simulations. Towards improving galaxy formation models using subhaloes. *A&A*, **506**(Nov.), 647–660. 35, 36, 53, 65, 90, 138

Valtonen, M., & Karttunen, H. 2006. *The Three-Body Problem*. 82

van den Bosch, F. C., Abel, T., Croft, R. A. C., Hernquist, L., & White, S. D. M. 2002. The Angular Momentum of Gas in Protogalaxies. I. Implications for the Formation of Disk Galaxies. *ApJ*, **576**(Sept.), 21–35. 89

van den Bosch, F. C., Norberg, P., Mo, H. J., & Yang, X. 2004. Probing dark matter haloes with satellite kinematics. *MNRAS*, **352**(Aug.), 1302–1314. 87

van den Bosch, F. C., Yang, X., Mo, H. J., & Norberg, P. 2005. The abundance and radial distribution of satellite galaxies. *MNRAS*, **356**(Feb.), 1233–1248. 87

van den Bosch, F. C., Aquino, D., Yang, X., Mo, H. J., Pasquali, A., McIntosh, D. H., Weinmann, S. M., & Kang, X. 2008. The importance of satellite quenching for the build-up of the red sequence of present-day galaxies. *MNRAS*, **387**(June), 79–91. 93

van der Wel, A., Franx, M., van Dokkum, P. G., & et al. 2014. 3D-HST+CANDELS: The Evolution of the Galaxy Size-Mass Distribution since z = 3. *ApJ*, **788**(June), 28. 152, 154

van Dokkum, P. G., Franx, M., Kriek, M., Holden, B., Illingworth, G. D., Magee, D., Bouwens, R., Marchesini, D., Quadri, R., Rudnick, G., Taylor, E. N., & Toft, S. 2008. Confirmation of the Remarkable Compactness of Massive Quiescent Galaxies at z ˜ 2.3: Early-Type Galaxies Did not Form in a Simple Monolithic Collapse. *ApJ Let.*, **677**(Apr.), L5–L8. 132

van Haarlem, M., & van de Weygaert, R. 1993. Velocity Fields and Alignments of Clusters in Gravitational Instability Scenarios. *ApJ*, **418**(Dec.), 544. 87

Velazquez, H., & White, S. D. M. 1999. Sinking satellites and the heating of galaxy discs. *MNRAS*, **304**(Apr.), 254–270. 136

Vogelsberger, M., Genel, S., Springel, V., Torrey, P., Sijacki, D., Xu, D., Snyder, G., Nelson, D., & Hernquist, L. 2014. Introducing the Illustris Project: simulating the coevolution of dark and visible matter in the Universe. *MNRAS*, **444**(Oct.), 1518–1547. 27

von Hoerner, S. 1957. Internal structure of globular clusters. *ApJ*, **125**(Mar.), 451. 81

Walker, I. R., Mihos, J. C., & Hernquist, L. 1996. Quantifying the Fragility of Galactic Disks in Minor Mergers. *ApJ*, **460**(Mar.), 121. 136

Wang, H. Y., Jing, Y. P., Mao, S., & Kang, X. 2005. The phase-space distribution of infalling dark matter subhaloes. *MNRAS*, **364**(Dec.), 424–432. 86, 87

Wang, Y., Park, C., Hwang, H. S., & Chen, X. 2010. Distribution of Satellite Galaxies in High-redshift Groups. *ApJ*, **718**(Aug.), 762–767. 89

Warren, M. S., Quinn, P. J., Salmon, J. K., & Zurek, W. H. 1992. Dark halos formed via dissipationless collapse. I - Shapes and alignment of angular momentum. *ApJ*, **399**(Nov.), 405–425. 86

Weinberg, M. D. 1986. Orbital decay of satellite galaxies in spherical systems. *ApJ*, **300**(Jan.), 93–111. 83

Weinberg, M. D. 1989. Self-gravitating response of a spherical galaxy to sinking satellites. *MNRAS*, **239**(Aug.), 549–569. 83, 84

Welker, C., Devriendt, J., Dubois, Y., Pichon, C., & Peirani, S. 2014. Mergers drive spin swings along the cosmic web. *MNRAS*, **445**(Nov.), L46–L50. 46, 49, 100, 101, 156, 164

Wellons, S., Torrey, P., Ma, C.-P., Rodriguez-Gomez, V., Vogelsberger, M., Kriek, M., van Dokkum, P., Nelson, E., Genel, S., Pillepich, A., Springel, V., Sijacki, D., Snyder, G., Nelson, D., Sales, L., & Hernquist, L. 2015. The formation of massive, compact galaxies at z = 2 in the Illustris simulation. *MNRAS*, **449**(May), 361–372. 135

White, S. D. M. 1984. Angular momentum growth in protogalaxies. *ApJ*, **286**(Nov.), 38–41. 18, 46, 47

White, S. D. M., & Frenk, C. S. 1991. Galaxy formation through hierarchical clustering. *ApJ*, **379**(Sept.), 52–79. 17

White, S. D. M., & Rees, M. J. 1978. Core condensation in heavy halos - A two-stage theory for galaxy formation and clustering. *MNRAS*, **183**(May), 341–358. 17

Wong, T., & Blitz, L. 2002. The Relationship between Gas Content and Star Formation in Molecule-rich Spiral Galaxies. *ApJ*, **569**(Apr.), 157–183. 33

Yang, X., Mo, H. J., van den Bosch, F. C., Weinmann, S. M., Li, C., & Jing, Y. P. 2005. The cross-correlation between galaxies and groups: probing the galaxy distribution in and around dark matter haloes. *MNRAS*, **362**(Sept.), 711–726. 87

Yang, X., van den Bosch, F. C., Mo, H. J., Mao, S., & Kang, X. 2006. The alignment between the distribution of satellites and the orientation of their central galaxy. *MNRAS*, **369**(July), 1293–1302. 86, 89, 90, 117, 118

Yoshida, N., Springel, V., White, S. D. M., & Tormen, G. 2000. Collisional Dark Matter and the Structure of Dark Halos. *ApJ Let.*, **535**(June), L103–L106. 86

Younger, J. D., Cox, T. J., Seth, A. C., & Hernquist, L. 2007. Antitruncated Stellar Disks via Minor Mergers. *ApJ*, **670**(Nov.), 269–278. 136

Zaritsky, D., Smith, R., Frenk, C., & White, S. D. M. 1993. Satellites of spiral galaxies. *ApJ*, **405**(Mar.), 464–478. 87

Zaritsky, D., Smith, R., Frenk, C. S., & White, S. D. M. 1997. Anisotropies in the Distribution of Satellite Galaxies. *ApJ Let.*, **478**(Apr.), L53–L56. 107

Zel'dovich, Y. B. 1970. Gravitational instability: An approximate theory for large density perturbations. *A&A*, **5**(Mar.), 84–89. 18, 22, 80

Zentner, A. R., Kravtsov, A. V., Gnedin, O. Y., & Klypin, A. A. 2005. The Anisotropic Distribution of Galactic Satellites. *ApJ*, **629**(Aug.), 219–232. 87

Zhang, Y., Yang, X., Wang, H., Wang, L., Mo, H. J., & van den Bosch, F. C. 2013. Alignments of Galaxies within Cosmic Filaments from SDSS DR7. *ApJ*, **779**(Dec.), 160. 87